



HAL
open science

Toward nanofiltration membranes with layer-by-layer assembled and nano-reinforced separation layers

Xiaofeng Lin

► **To cite this version:**

Xiaofeng Lin. Toward nanofiltration membranes with layer-by-layer assembled and nano-reinforced separation layers. Chemical Physics [physics.chem-ph]. Université de Strasbourg, 2016. English. NNT : 2016STRAE012 . tel-01578150

HAL Id: tel-01578150

<https://theses.hal.science/tel-01578150>

Submitted on 28 Aug 2017

HAL is a multi-disciplinary open access archive for the deposit and dissemination of scientific research documents, whether they are published or not. The documents may come from teaching and research institutions in France or abroad, or from public or private research centers.

L'archive ouverte pluridisciplinaire **HAL**, est destinée au dépôt et à la diffusion de documents scientifiques de niveau recherche, publiés ou non, émanant des établissements d'enseignement et de recherche français ou étrangers, des laboratoires publics ou privés.



THÈSE



En vue de l'obtention du

Doctorat de Chimie-Physique

ECOLE DOCTORALE de Physique et Chimie-Physique

Institut Charles Sadron (UPR22-CNRS)

Titre:

Toward nanofiltration membranes with Layer-by-Layer assembled and nano-reinforced separation layers

Xiaofeng LIN

Le 17 Juin 2016

Thèse dirigée par:

Professeur Gero DECHER, Université de Strasbourg

Jury

Rapporteurs:

M. Lars WAGBERG	Professeur	KTH Royal institute of technology
Mme Karine GLINEL	Professeur	Université Catholique de Louvain

Autres membres:

M. Vincent BALL	Professeur	Université de Strasbourg
-----------------	------------	--------------------------

Acknowledgements

The work of the present dissertation was carried out at the Institut Charles Sadron (ICS) in Strasbourg, France under the supervision of Professor Gero Decher. First of all, I would like to express my sincere gratitude to Prof. DECHER for having given me the precious opportunity to carry out my PhD thesis in his outstanding team in the field of Layer-by-layer assembly.

It was such a pleasure spending my PhD time in such a lovely group where I learned a lot - from scientific knowledge to how to be more organized in the lab. I am extremely grateful to our lovely supervisor Olivier Félix for his continuous help during my work and especially for his help with the correction of this manuscript. I would like also to thank to all the lovely team members whose names are (in no particular order): Marek Twardoch, Pauline Barrois, Hebing Hu, Marvin Motay, Paul Rouster, Jonas Bär, Rémi Merindol, Vincent Lemaire, Matthias Pauly, Michel Tschopp, David Martel, Sribharani Sekar, Teruhiko Umehara, Remi Merindol, Seydina Diabang, Christophe Higy, Alliny Naves, Heveline Follmann, Florian Schmidt, Yulia Sergeeva, Tongtong Huang, Charly Ou, Maria Alice Wit, Rahul dev Jayant, Akkiz Bekel, De Souvick, etc. for their kind support and help during this period. I would like to express my deepest gratitude to the mechanical team of Professor Christian Gauthier and in particularly Leandro Jacomine, Damien Favier and Vincent Le Houerou for their help with the mechanical tests and for their valuable contributions to this manuscript. In addition, I also would like to thank Marc Schmutz for his help with the SEM imaging, and Christophe Contal and Mounir Maaloum for their help with AFM imaging. I would like to express my gratitude to administration people who helped me a lot with the paperwork especially during the beginning of my thesis, thank you Odile Lemble, Magali Meyer, Katia Bruzzone, Paule Vannson, Isabelle Colrat, Charlotte Schaeffer, etc.!

Some work of this thesis was performed in collaboration with partners within the European project LbLBRANE. I would like to thank all partners for the nice project we had together, especially Carlos and Jens who performed the tests on membrane performances.

I want to thank my family and friends for their support during my study. Without them, I could never finish my work. Finally, I want to give my special thank to my

beloved wife Tongtong: your company has always been the most powerful source for my strength! Thank you darling!

TABLE OF CONTENTS

Acknowledgements	3
TABLE OF CONTENTS	1
Résumé de thèse en français	5
List of abbreviations.....	16
Introduction	19
I. State of the art.....	23
I-A. LbL-assembly technique.....	23
I-A-1. Introduction to the LbL-assembly technique	23
I-A-2. Growth mechanism of LbL-assembled films	25
I-B. Conventional synthetic separation membrane	29
I-B-1. Different types of membrane	32
I-B-1.1. Microfiltration membranes	32
I-B-1.2. Ultrafiltration membranes.....	32
I-B-1.3. Reverse osmosis membranes	33
I-B-1.4. Nanofiltration	35
I-B-2. Disadvantages of TFC membranes	36
I-C. LbL-assembly modified membranes	39
I-C-1. LbL-assembly modified membranes with polyelectrolytes	39
I-C-2. LbL-assembly modified membranes reinforced with nanofibers.....	42
I-C-2.1. Nanofibers used for improving membrane permeability	42
I-C-2.2. Nanofibers used for reinforcing mechanical properties.....	47
II. Materials and methods	59
II-A. Materials	59
II-A-1. Polyelectrolytes.....	59
II-A-2. Nanofibers suspension.....	60
II-A-2.1. Carbon nanotubes (CNTs)	60
II-A-2.2. Cellulose nanofibrils (CNFs).....	61
II-A-3. Surface preparation.....	62
II-A-3.1. Hydrophilic surface preparation	62
II-A-3.2. Hydrophobic surface preparation	62
II-A-3.3. Membrane-like surface preparation	63
II-A-4. Freestanding films preparation	63
II-A-5. Membrane preparation.....	64
II-A-5.1. Single fiber module preparation.....	67

II-A-5.2. Membrane conditioning.....	68
II-A-6. LbL-assembly	69
II-A-6.1. Dipping LbL-assembly	69
II-A-6.2. Spin-assisted LbL-assembly	69
II-A-6.3. Spray-assisted LbL-assembly.....	70
II-A-6.4. Grazing-incidence spray-assisted LbL-assembly	71
II-A-7. Membrane coating by LbL-assembly	72
II-A-7.1. Flat sheet membrane coating.....	72
II-A-7.2. Hollow fiber membrane coating.....	72
II-B. Methods.....	73
II-B-1. Ellipsometry.....	73
II-B-1.1. Single wavelength ellipsometry.....	73
II-B-1.2. Spectroscopic ellipsometry.....	74
II-B-2. UV-Vis spectroscopy	74
II-B-2.1. UV-Vis spectroscopy in transmission.....	75
II-B-2.2. UV-Vis spectroscopy in reflection	76
II-B-3. Quartz Crystal Microbalance dissipation (QCM-d)	78
II-B-4. Microscopy	80
II-B-4.1. Atomic Force Microscopy (AFM).....	80
II-B-4.2. Transmission Electronic Microscopy (TEM).....	82
II-B-4.3. Scanning Electronic Microscopy (SEM).....	83
II-B-4.4. Cross-polarized microscopy	85
II-B-5. Membrane performance test.....	87
II-B-5.1. Membrane Retention/Permeability Measurement.....	87
II-B-6. Mechanical test.....	88
II-B-6.1. Tensile test.....	88
II-B-6.2. Digital image correlation	89
II-B-6.3. Nanoindentation.....	90
III. LbL-assembly of separative polyelectrolyte film on model and real membrane surfaces	94
III-A. LbL-assembled coating on model surfaces	94
III-A-1. LbL-assembly on Si-wafer followed by ellipsometry	95
III-A-2. LbL-assembly on quartz slides followed by UV-Vis absorption spectroscopy	98
III-A-3. LbL-assembly on quartz crystal followed by QCM-D	99
III-A-4. Comparison of the three characterization methods.....	100
III-B. LbL-assembled coating on membrane-like model surface.....	102
III-B-1. Membrane-like surfaces.....	103
III-B-2. Comparison of LbL-film growth on Si-Wafers and membrane-like surfaces by ellipsometry.....	104

III-C. LbL-assembled coating on real membrane surfaces.....	106
III-C-1. UV-Vis reflection spectroscopy measurement of LbL-assembly on flat sheet real membrane surface.....	106
III-C-2. Permeability and retention measurement of LbL-assembly on hollow fiber real membrane surfaces.....	108
III-D. Comparison of different LbL-assembled film growth on real membrane surfaces and on model surfaces	110
III-D-1. Non-linear regime both on model surfaces and on real membranes.....	110
III-D-2. Surface effect on LbL-assembled film growth.....	112
IV. LbL-assembly of CNTs and CNFs based films	116
IV-A. LbL-assembled CNTs based films.....	116
IV-A-1. Preparing CNTs aqueous dispersion by physical wrapping with poly(styrene sulfonated) (PSS).....	118
IV-A-1.1. UV-Vis spectroscopic monitoring of the PSS-wrapped CNTs suspensions.....	119
IV-A-1.2. Purification of the PSS wrapped CNTs suspensions by ‘Salt-out’	120
IV-A-2. Characterization of LbL-assembled CNTs based films.....	124
IV-A-2.1. LbL-assembly of CNTs based films on Si-wafer followed by ellipsometry	124
IV-A-2.2. LbL-assembly of CNTs based films on quartz slide followed by UV-Vis absorption spectroscopy.....	125
IV-A-2.3. LbL-assembly of CNTs based film on quartz crystal metalized with gold electrodes followed by QCM-D	126
IV-A-2.4. Micron-thick CNTs based LbL-assembled films	127
IV-B. LbL-assembled CNFs based films	129
IV-B-1. LbL-assembly of CNFs based film on Si-wafer followed by ellipsometry.....	130
IV-B-2. LbL-assembly of CNFs based film on quartz crystal followed by QCM-D.....	133
IV-B-3. Comparison between QCM-D and ellipsometry results for CNFs based LbL- assembled films	134
IV-B-4. Micron-thick CNFs based LbL-assembled films.....	136
V. Nanofibers reinforced LbL-assembly modified nanofiltration membranes	140
V-A. Selection of polyelectrolytes for making nanofiltration membranes.....	140
V-B. LbL-assembled coatings for the membranes	144
V-B-1. SEM characterization	145
V-B-2. Small dye molecules separation by LbL-assembly modified nanofiltration membranes	145
V-B-3. UV-Vis reflection spectroscopy measurements.....	147
V-C. Performance of LbL-assembly modified membranes.....	148
V-D. Performance of LbL-assembly modified membranes reinforced with nanofibers	150

V-D-1. Performance of LbL-assembly modified membranes reinforced with CNTs	150
V-D-2. Performance of LbL-assembly modified membranes reinforced with CNFs	154
VI. Mechanical properties of LbL-assembled films reinforced with nanofibers...	157
VI-A. Mechanical properties of LbL-assembled films of polyelectrolytes	157
VI-B. Mechanical properties of LbL-assembled films reinforced with CNTs	158
VI-B-1. Effect of salt on the mechanical properties of film	159
VI-B-2. Comparing mechanical properties of LbL-assembled films made with and without CNT	162
VI-B-3. Alignment of CNTs by LbL-assembly	163
VI-B-3.1. Alignment of CNTs by grazing-incidence spray-assisted LbL-assembly	164
VI-B-3.2. Alignment of CNTs by spin-assisted LbL-assembly	166
VI-B-3.3. Impact of CNTs alignment on the mechanical properties	168
VI-C. Mechanical properties of LbL-assembled films reinforced with CNFs	172
VI-C-1. Mechanical properties of CNFs based film	175
VI-C-1.1. Influence of polyelectrolyte matrix on the mechanical properties of the film	180
VI-C-1.2. Influence of humidity on the mechanical properties of CNFs based films	184
VI-C-1.3. Influence of fiber alignment on the mechanical properties	188
Conclusions and perspectives	193
References	201
Appendix 1	217
Appendix 2	220

Vers des membranes de nanofiltration avec des couches de separation nano-renforcées et assemblées couche-par-couche

La pénurie d'eau potable dans de nombreuses régions de la planète constitue un réel problème d'importance croissante avec l'accroissement de la population mondiale. De ce fait, la purification de l'eau de mer, des eaux usées et des eaux insalubres pour la consommation humaine est devenue au cours des dernières années une alternative viable pour le futur. Parmi les techniques développées pour le traitement de l'eau, les systèmes de séparation membranaire (microfiltration, ultrafiltration, osmose inverse et nanofiltration) sont les plus rentables, les plus performantes et les plus respectueuses de l'environnement. De plus, elles offrent également des conditions de fonctionnement plus simples et la production de rendement élevé avec une consommation de produits chimiques et d'énergie plus faible que les méthodes conventionnelles (sédimentation, coagulation, ...). Cependant, en dépit des améliorations technologiques des membranes pour la récupération de l'eau, les systèmes de séparation membranaire souffrent d'un problème majeur: l'encrassement des membranes qui réduit significativement leurs performances. Les inconvénients principaux de l'encrassement des membranes sont une augmentation inévitable des coûts d'exploitation et d'entretien ainsi qu'un effet négatif sur la durée de vie des membranes (traitements agressifs). Pour contourner cette limitation, le dépôt d'une couche de séparation ultra-mince régénérable sur un support très perméable et robuste mécaniquement semble être la seule façon de concevoir des membranes de séparation régénérables combinant un flux élevé avec une sélectivité élevée.

Le sujet de ma thèse s'intègre dans le cadre du projet européen LbLBRANE dont l'objectif est de développer des membranes de nanofiltration pour le traitement de l'eau en utilisant la technique couche-par-couche (abrégée LbL pour Layer-by-Layer) (Figure 1, à gauche).[1] Cette méthode d'assemblage, développée dans les années 90 par le professeur G. Decher, est un outil puissant pour la modification de surface et la

préparation de membranes composites avec une précision nanométrique.[2] Le film multicouche envisagé dans ce projet est constitué d'une couche intermédiaire de renforcement au contact de la membrane et d'une couche active de séparation déposée sur la couche intermédiaire (Figure 1, à droite). Cette approche devrait permettre d'obtenir des membranes performantes combinant un flux élevé, une rétention élevée et la possibilité de pouvoir régénérer la couche active après encrassement.[3] Dans le cadre de ce projet, mon travail de thèse a consisté plus particulièrement à développer une couche intermédiaire performante en terme de flux et de résistance mécanique. En effet, le dépôt d'une couche intermédiaire avec une structure en maille de porosité contrôlée entre la surface de la membrane et la couche active de séparation devrait empêcher le blocage des pores de la membrane, permettre un flux élevé par diffusion latérale et améliorer la résistance mécanique des membranes.

Les nanotubes de carbone (CNT) et les nanofibrilles de cellulose (CNF), en raison de leur structure rigide en fil et de leur haute résistance à la traction (jusqu'à 63 GPa), sont des candidats idéaux pour concevoir une couche intermédiaire poreuse et résistante sur les membranes.[4] Par conséquent, au cours de ce travail, nous avons contrôlé à travers les conditions d'assemblage LbL la composition et la structure de la couche intermédiaire afin d'étudier les relations structure-propriété de ces membranes.

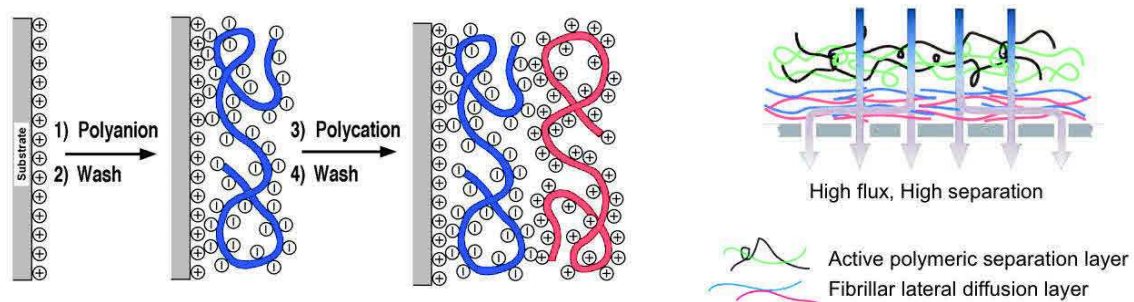


Figure 1. (à gauche) Représentation schématique du principe d'assemblage couche-par-couche de polyélectrolytes. (à droite) Représentation schématique d'une membrane de nanofiltration composée d'une couche de séparation active déposée sur une couche intermédiaire fibrillaire. La structure en maille de la couche intermédiaire permet d'accroître le flux par diffusion latérale de la solution lors de la filtration.

Dans un premier temps, nous avons étudié la construction et les propriétés de la couche active qui nous a servi de système de référence avant d'investiguer la couche intermédiaire proprement dite. Pour ce faire, un criblage des polyélectrolytes réalisé par les différents partenaires du projet a permis d'identifier ceux (poly(styrène-4-sulfonate) (PSS) et poly(diallyldiméthylammonium chloride) (PDDA)) qui permettent de remplir les exigences imposées par l'application du dispositif à l'échelle industrielle (rétention élevée, perméabilité élevée, résistance au chlore et régénéralité).

Comme il est très difficile de caractériser le dépôt de couche mince sur des surfaces non homogène comme les membranes, nous avons d'abord étudié la construction de films $(PSS/PDDA)_n$ sur des surfaces modèles (cristal de quartz, wafer de silicium, lame de quartz) en utilisant des techniques classiques d'analyse de surface telles que l'ellipsométrie, la spectroscopie UV-Visible et la microbalance à cristal de quartz (Figure 2). Comme décrit dans la littérature,[5] les films $(PSS/PDDA)_n$ en présence de sels montrent une croissance superlinéaire quelque soit la technique utilisée. Ce régime de croissance a été expliqué par la diffusion du PDDA et du PSS dans le film.

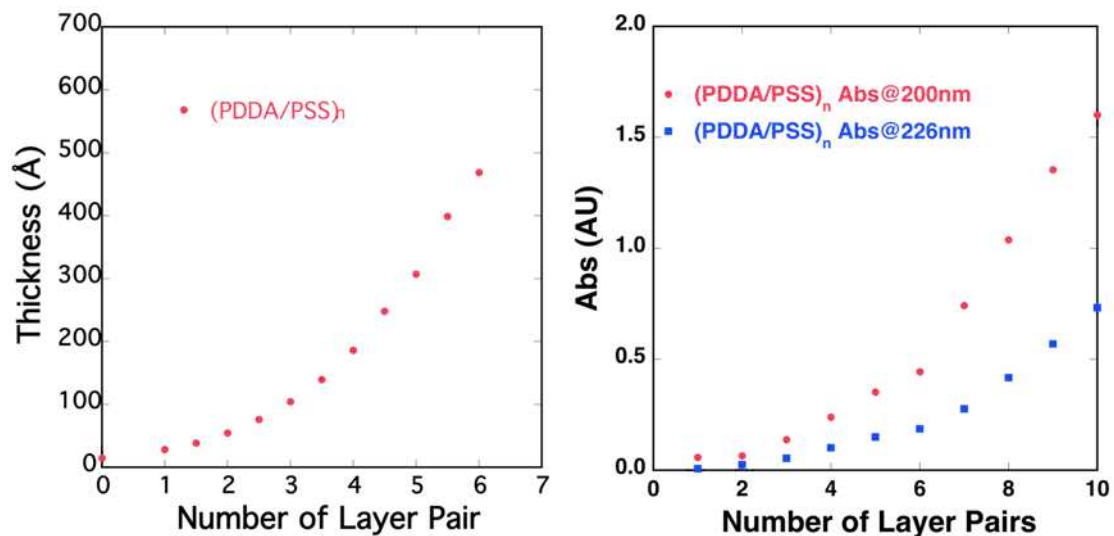


Figure 2. (à gauche) Variation de l'épaisseur d'un film $(PDDA/PSS)_n$ construit sur wafer de silicium en fonction de nombre de paires de couches caractérisée par ellipsométrie. (à droite) Variation de l'absorbance d'un film $(PDDA/PSS)_n$ construit sur une lame de quartz en fonction de nombre de paires de couches caractérisée par spectroscopie UV-Visible en transmission.

La prochaine étape a consisté à vérifier la croissance de ces films sur des membranes en polyéthersulfone sulfoné (SPES). Pour ce faire, la construction des films $(\text{PDDA}/\text{PSS})_n$ sur les membranes a été suivie par spectroscopie UV-Visible en réflexion diffuse en utilisant une sphère d'intégration (Figure 3). Nous avons observé que les films construits sur les membranes montraient une croissance superlinéaire similaire à celle observée sur les surfaces modèles.

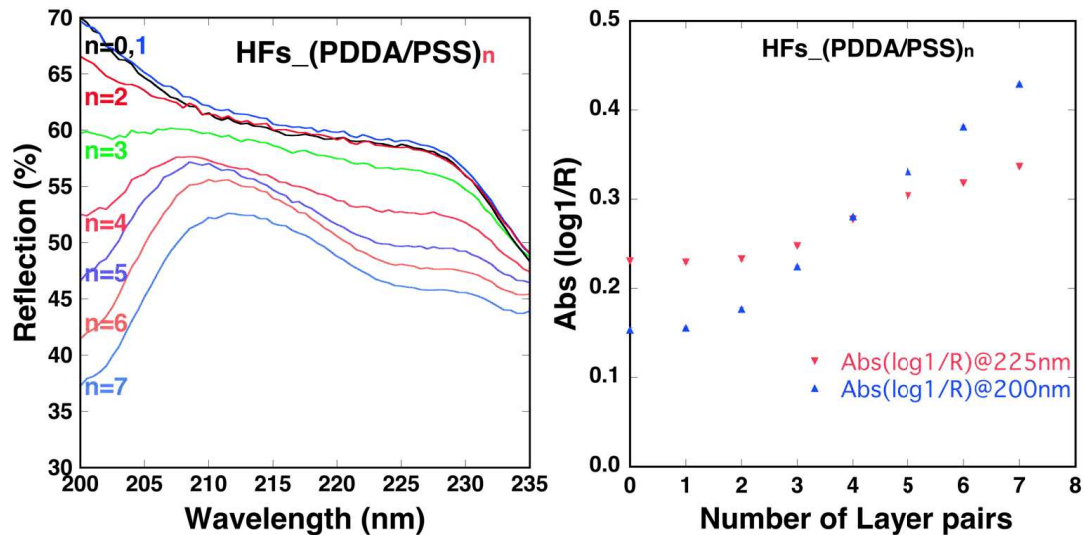


Figure 3. (à gauche) Variation de la réflexion diffuse d'un film $(\text{PDDA}/\text{PSS})_n$ construit sur une membrane en fonction de la longueur d'onde et du nombre de couches caractérisée par spectroscopie UV-Visible en réflexion diffuse. (à droite) Variation de $\text{Log } 1/R$ à 200 et 225 nm en fonction de nombre de paires de couche.

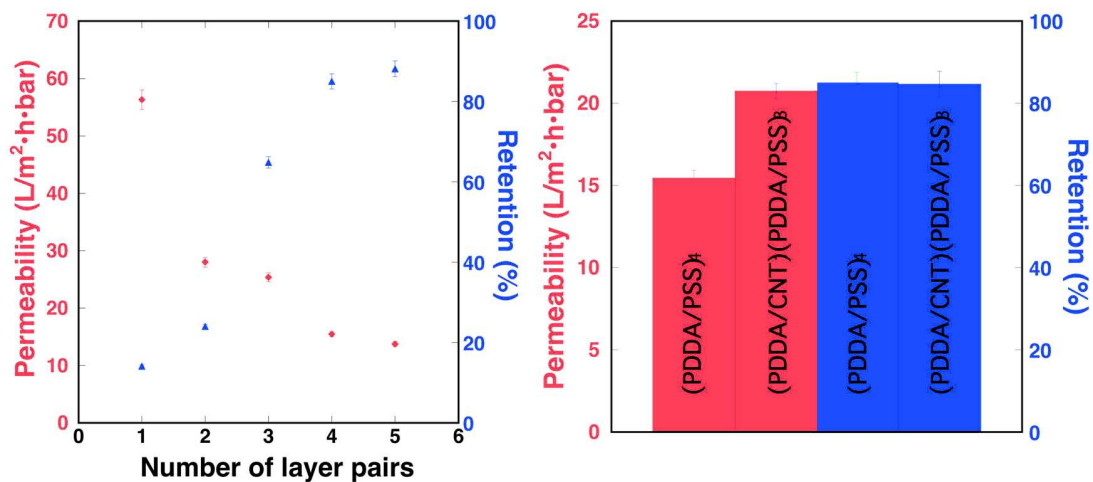


Figure 4. (à gauche) Variation du flux et de la rétention de MgSO_4 en fonction du nombre de paires de couches $(\text{PDDA}/\text{PSS})_n$ déposé sur les membranes. (à droite) Comparaison du flux et de la rétention de MgSO_4 pour des membranes modifiées avec et sans CNTs.

Sur la base de ces résultats, nous avons ensuite investigué l'influence du nombre de paires de couches déposées sur les membranes sur le flux et la rétention des ions MgSO_4 (Figure 4, à gauche). Ces mesures ont été réalisées par le partenaire industriel en charge de la production et de l'analyse des performances des membranes.

Comme attendu, les résultats montrent que le flux diminue et la rétention de MgSO_4 augmente avec le nombre de paires de couche. Une rétention maximale de 85% et un flux de $15 \text{ L/m}^2 \cdot \text{h} \cdot \text{bar}$ sont atteints pour un film de 4 paires de couches. Le dépôt d'une paire de couche additionnelle n'améliore pas significativement la rétention mais diminue légèrement le flux.

Après avoir validé la construction et les performances de la couche active, nous nous sommes ensuite intéressés à la fabrication et à la caractérisation de la couche intermédiaire à base de nanofibres sur des surfaces modèles et sur les membranes. La préparation de dispersions aqueuses stables de CNT et CNF, condition préalable indispensable à l'assemblage LbL de nano-objets, a été d'abord réalisée par différentes approches. Puis, la construction de films à base de CNT et CNF a été caractérisée par ellipsométrie (CNT et CNF) et spectroscopie UV-visible (CNT) respectivement sur wafers de silicium et lames de quartz. Compte tenu des performances observées pour la couche active, nous avons décidé dans un premier temps de remplacer le PSS de la première paire de couches par une couche de CNT (nommé P3) et d'étudier son influence sur la construction d'un film (PSS/PDDA) (Figure 5, à gauche).

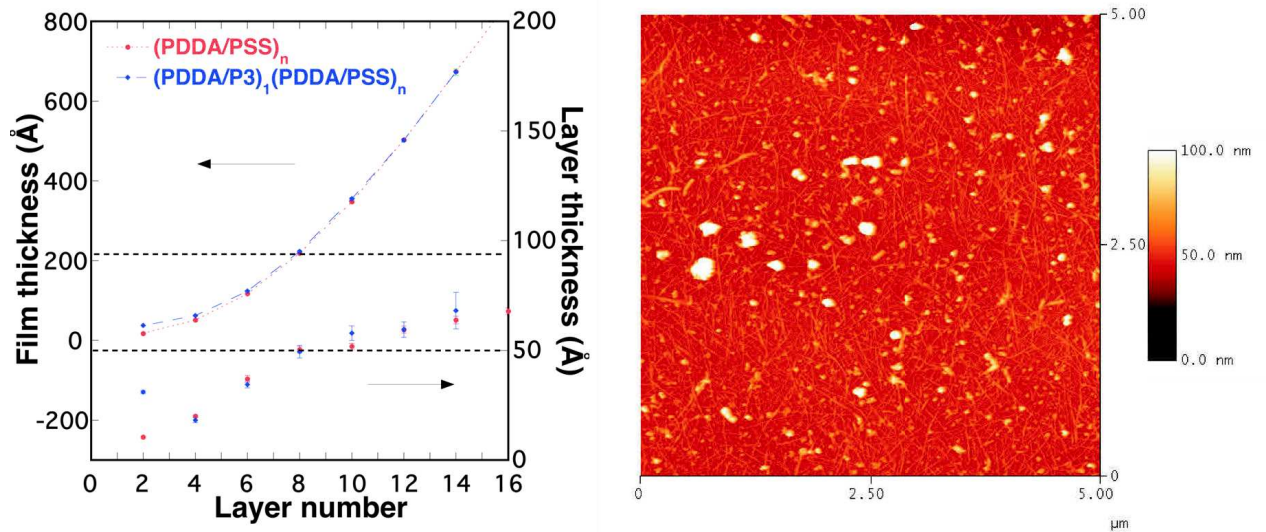


Figure 5. (à gauche) Variation de l'épaisseur des films $(PSS/PDDA)_n$ et $(PDDA/P3)_1(PDDA/PSS)_n$ (axe à gauche) et de chaque couche de PSS(ou CNTs) (axe à droite) en fonction de nombre de couches. (à droite) Image AFM d'une couche de CNT déposée sur un wafer de silicium fonctionnalisé avec une couche de PDDA.

On observe que le remplacement de la première couche de PSS par des CNTs (P3) ne change pas l'épaisseur totale du film et son régime de croissance superlinéaire malgré la structure poreuse de la couche de CNT (Figure 5, à droite). Par ailleurs, l'incorporation des CNTs dans la première couche se traduit bien par une augmentation significative de l'épaisseur de celle-ci par rapport à celle contenant du PSS.

Compte tenu de ces résultats et de ceux obtenus pour la couche active, nous avons déposé sur la membrane un film multicouche composé d'une couche intermédiaire comportant une couche de CNTs recouverte d'une couche active comportant 3 paires de couches $(PDDA/PSS)$ dans le but d'étudier l'influence de la couche intermédiaire sur les propriétés de la membrane (Figure 4, à droite). L'addition d'une couche intermédiaire à base de CNT permet d'augmenter le flux de 30% tout en conservant la même rétention par rapport à la membrane de référence $(PDDA/PSS)_4$. Il semble que la structure en maille de la couche CNT permette une diffusion latérale du liquide et de ce fait d'augmenter significativement le flux à travers la membrane sans compromettre la rétention de $MgSO_4$ de la couche active. L'étude des films à base de

CNT nous a permis de valider le concept de la couche intermédiaire mais elle a été interrompue, malgré les résultats préliminaires prometteurs, compte tenu du coût, de la faible solubilité et de la toxicité potentiel des CNTs. C'est la raison pour laquelle nous nous sommes alors tournés vers un produit naturel peu cher et disponible en grande quantité, les CNF. Cependant, la voie à base de CNF n'a pu être explorée qu'au niveau des propriétés mécaniques compte tenu de l'avancement du projet.

Afin d'évaluer le renforcement mécanique induit par les CNTs et CNFs dans les films multicouches, nous avons été obligé de préparer des films micrométriques auto-supportées à base de CNT et CNF pour être en mesure de déterminer leurs propriétés mécaniques à l'aide d'une machine de traction en fonction de leur composition, de leur structure, des conditions de préparation et de l'humidité relative. L'étude des propriétés mécaniques des films multicouches a été réalisée en collaboration avec l'équipe de C. Gauthier à l'Institut Charles Sadron. La construction des différents films a été réalisée par le biais d'un dispositif automatique de trempage et a nécessité plusieurs jours. A titre d'exemple, la Figure 6 (à gauche) montre que les films renforcés par des CNTs ont un module de Young environ quatre fois supérieur à celui des films non-renforcés mais avec une déformation similaire. La Figure 6 (à droite) montre que le remplacement des CNTs par CNFs dans les films nous a permis d'obtenir des revêtements avec des valeurs "record" en terme de résistance mécanique. En effet, le film (chitosan/CNF)₁₅₀ présente une contrainte à la rupture de 450 MPa, ce qui est comparable à de l'acier. Par conséquent, ces résultats indiquent clairement l'importance de la composition et de la structure d'un matériau sur ses propriétés.

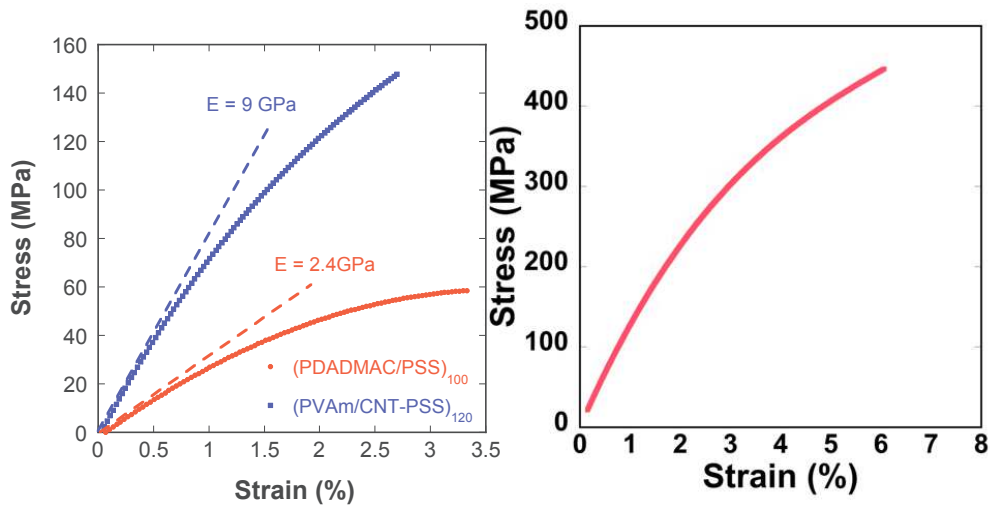


Figure 6. (à gauche) Courbes de contrainte/déformation observées pour des films (PDADMAC/PSS)₁₀₀ and (PVAm/CNT-PSS)₁₂₀ films. (à droite) Courbe de contrainte/déformation observée pour un film (Chitosan/CNF)₁₅₀.

L'eau étant connue pour avoir un fort effet plastifiant sur les complexes de polyélectrolytes, (Hariri, H. H.; Lehaf, A. M.; Schlenoff, J. B. Mechanical Properties of Osmotically Stressed Polyelectrolyte Complexes and Multilayers: Water as a Plasticizer. *Macromolecules* 2012, 45, 9364–9372) nous avons étudié l'influence de l'humidité relative de l'environnement sur les propriétés mécaniques du film (Chitosan/CNF)_n par nanoindentation en collaboration avec l'équipe du professeur Christian Gauthier. La Figure 7 montre qu'une augmentation progressive de l'humidité relative de 5% à 33% conduit à une diminution progressive de la valeur du module de Young du film atteignant une diminution de 40% à 33% d'humidité. Ce résultat peut être expliqué par le fait que l'eau qui pénètre dans le film diminue les interactions entre les différents constituants du film, favorise le déplacement des polyélectrolytes au sein du film et diminue ainsi ses propriétés mécaniques.[6]

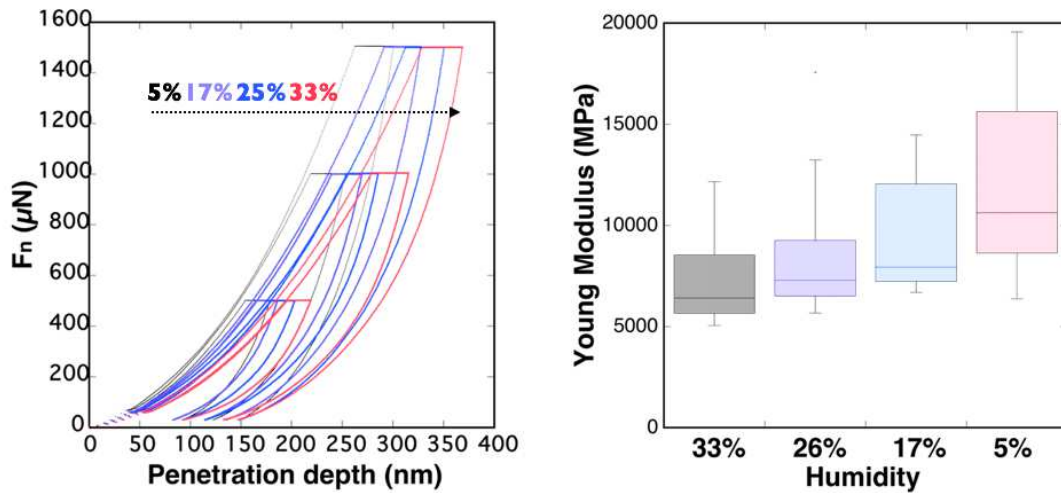


Figure 7. (à gauche) Courbes de nanoindentation force/profondeur en fonction de l'humidité relative. (à droite) Modules de Young calculé à partir des courbes observées pour des films $(\text{Chitosan/CNF})_{150}$ exposées à différentes humidités.

Finalement, en comparant les propriétés mécaniques des films $(\text{Chitosan/CNF})_n$ et $(\text{PVAm/CNF})_n$, nous avons observé que la contrainte à la rupture des films $(\text{Chitosan/CNF})_n$ était presque deux fois plus grande que pour les films $(\text{PVAm/CNF})_n$ indépendamment de l'humidité relative (Figure 8). Cette différence de propriétés est induite par la plus grande rigidité des chaînes de chitosan par rapport au PVAm et par la maximisation des interactions électrostatiques et hydrogènes entre chitosan et CNF compte tenu de leur nature polysaccharide.[7] De plus, en augmentant l'humidité relative de 5 à 33%, on observe dans chaque cas une diminution de la contrainte à la rupture et une augmentation de la déformation du film. Cette dernière est d'ailleurs plus importante pour les films à base PVAm que pour les films à base de chitosan pour les mêmes raisons évoquées précédemment.

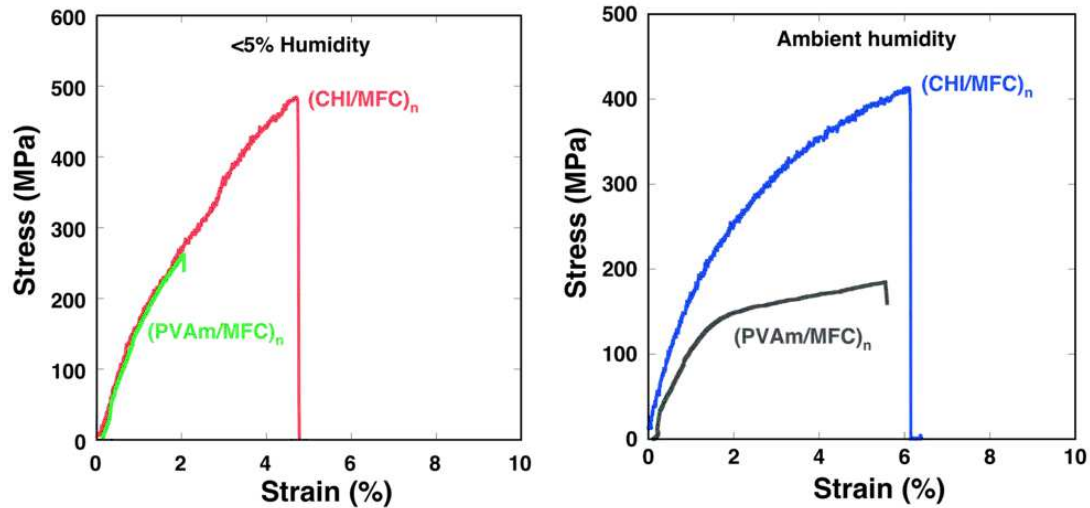


Figure 8. (à gauche) Courbes de contrainte/déformation observées pour des films (Chitosan/CNF)₁₅₀ et (PVAm/CNF)₁₅₀ avec une humidité relative de 5%. (à droite) Courbes de contrainte/déformation observées pour des films (Chitosan/CNF)₁₅₀ et (PVAm/CNF)₁₅₀ avec une humidité de 33% (humidité ambiante).

Pour résumé, nous avons contribué au cours de ce travail au développement de membranes de nanofiltration pour le traitement de l'eau en utilisant la technique couche-par-couche. Plus précisément, nous nous sommes intéressés à l'incorporation d'une couche intermédiaire entre la membrane et la couche active dans le but d'accroître le flux à travers la membrane et de renforcer mécaniquement la membrane. Au préalable, nous avons défini les conditions optimales pour la construction du système de référence à savoir une membrane recouverte uniquement de la couche active. Ainsi, nous avons pu établir que 4 paires de couches de (PDDA/PSS) étaient suffisantes pour atteindre un maximum de rétention de MgSO_4 (85 %) avec un flux raisonnable ($15 \text{ L/m}^2 \cdot \text{h} \cdot \text{bar}$). Ensuite, nous avons étudié la construction et les propriétés de la couche intermédiaire à base de CNT ou de CNF. Après l'obtention de suspensions stables de CNT et CNF, nous avons montré qu'il était possible de construire de tels films sur des surfaces modèles (CNT et CNF) et sur des membranes (CNT uniquement). De plus, nous avons démontré que l'addition d'une couche intermédiaire à base de CNT entre la membrane et la couche active permettait d'augmenter le flux à travers la membrane de 30 % sans modification de la rétention de MgSO_4 . Compte tenu de l'avancement du projet, il n'a pas été possible d'investiguer les propriétés des membranes à base de CNF.

Parallèlement à l'étude du flux et de la rétention des membranes composites, nous avons également étudié les propriétés mécaniques des films multicouches à base de CNT et de CNF. Pour des raisons techniques, ce travail a été réalisé sur des films micrométriques auto-suspendus impliquant le développement de méthodes de préparation et d'analyse. Il a été montré que l'ajout de CNT ou de CNF dans les films permet d'augmenter significativement leurs propriétés mécaniques, en particulier ceux à base de CNF qui atteignent des valeurs "record" en terme de contrainte à la rupture (environ 500 MPa). Ces propriétés mécaniques peuvent être contrôlées en jouant sur la composition, la structure, les conditions de préparation et l'humidité relative. Les propriétés mécaniques extraordinaires obtenues pour les films à base de nanofibrilles de cellulose assemblés par LbL suggèrent un futur prometteur pour ces matériaux composites dans de nombreux domaines d'applications.[8], [9]

Références :

- [1] L. Krasemann, A. Toutianoush, and B. Tieke, "Self-assembled polyelectrolyte multilayer membranes with highly improved pervaporation separation of ethanol/water mixtures," *J. Memb. Sci.*, vol. 181, no. 2, pp. 221–228, 2001.
- [2] G. Decher, "Fuzzy Nanoassemblies: Toward Layered Polymeric Multicomposites," *Science (80-.)*, vol. 277, no. 5330, pp. 1232–1237, 1997.
- [3] R. Blell, "Microfibrillated cellulose based nanomaterials," *Thèse soutenue à l'Université de Strasbourg*, 2012.
- [4] A. A. Mamedov, N. A. Kotov, M. M. Prato, D. M. Guldi, J. P. Wicksted, and A. A. Hirsch, "Molecular design of strong single-wall carbon nanotube/polyelectrolyte multilayer composites.," *Nat. Mater.*, vol. 1, no. 3, pp. 190–194, 2002.
- [5] R. A. Ghostine, M. Z. Markarian, and J. B. Schlenoff, "Asymmetric growth in polyelectrolyte multilayers.," *J. Am. Chem. Soc.*, vol. 135, no. 20, pp. 7636–7646, 2013.

-
- [6] R. Merindol, S. Diabang, O. Felix, T. Roland, C. Gauthier, and G. Decher, “Bio-inspired multiproperty materials: strong, self-healing, and transparent artificial wood nanostructures.,” *ACS Nano*, vol. 9, no. 2, pp. 1127–36, Feb. 2015.
- [7] J. P. De Mesquita, C. L. Donnici, and F. V. Pereira, “Biobased nanocomposites from layer-by-layer assembly of cellulose nanowhiskers with chitosan,” *Biomacromolecules*, vol. 11, pp. 473–480, 2010.
- [8] D. Klemm, F. Kramer, S. Moritz, T. Lindström, M. Ankerfors, D. Gray, and A. Dorris, “Nanocelluloses: A new family of nature-based materials,” *Angewandte Chemie - International Edition*, vol. 50, no. 24, pp. 5438–5466, 2011.
- [9] I. Siró and D. Plackett, “Microfibrillated cellulose and new nanocomposite materials: A review,” *Cellulose*, vol. 17, pp. 459–494, 2010.

List of abbreviations

AFM	Atomic Force Microscopy
HFs, HFc	Hollow Fiber Ultrafiltration membranes
IP	Interfacial Polymerization
K-M	Kubelka-Munk
LbL	Layer-by-Layer
MF	Microfiltration
NF	Nanofiltration
NIPS	Non-solvent induced phase separation
PEM	Polyelectrolyte Multilayer
QCM-D	Dissipation enhanced Quartz Crystal Microbalance
RMS	Root Mean Square
RO	Reverse Osmosis
SEM	Scanning Electron Microscopy
Si-wafer	Silicon wafer
SWNT	Single Wall Carbon Nanotubes
TFC	Thin Film Composite
TFNC	Thin Film Nanofibrous Composite
TFN	Thin Film Nanocomposite
TIPS	Thermally induced phase separation
TOC	Total Organic Content
UF	Ultrafiltration
UV	UltraViolet
UV-Vis	Ultraviolet-visible

CaCO₃	Calcium Carbonate
CA	Cellulose Acetate
CNFs	Cellulose Nanofibril
HA	Hyaluronan
HF	Hydrofluoric acid
MgSO₄	Magnesium sulfate
MPD	M-PhenyleneDiamine
NaCl	Sodium chloride
NaOCl	Sodium hypochlorite
PA	Polyamide
PAA	Poly(acrylic acid)
PAN	Poly(acrylonitrile)
PAH	Poly(allylamine hydrochloride)
PDADMAC	Poly(diallyldimethylammonium chloride)
PE	Polyethylene
PEC	Polyelectrolyte Complex
PEI	Poly(ethylenimine)
PES	Polyethersulfone
PET	Poly(ethyleneterephthalate)
PLL	Poly(L-lysine)
PP	Polypropylene
PSF	Polysulfone
PSS	Poly(sodium 4-styrenesulfonate)
PVA	Poly(vinyl alcohol)
PVP	Poly(vinylpyrrolidone)
PVS	Poly(vinylsulfonic acid)

SPES	Sulfonated poly(ethersulfone)
THM	Trihalomethane
TiO₂	Titanium dioxide
TMC	Trimesoyl Chloride

Introduction

Water scarcity is an increasingly serious issue around the world due to many reasons such as water pollution, growing populations or diminishing supplies of fresh water, which causes various problems such as diseases, poverty or sanitation issues. Among all available techniques for water treatment to settle these problems, thin film composite (TFC) membranes especially nanofiltration (NF) TFC membranes have become one of the most promising innovations for water purification or desalination.¹ TFC membranes are semipermeable membranes manufactured typically by forming a thin and dense selective or active layer of polyamide (< 200 nm) through interfacial polymerization (IP) reaction on a porous membrane support. The TFC membrane separation process can achieve a high rejection of multivalent ions and dissolved organic matter combined with different removal of monovalent ions while requiring much less energy compared to conventional thermal separation process such as distillation or sublimation, which makes them the state of the art membranes. However, despite their prominent market and increasing applications in various domains, TFC membranes face always some fatal problems. The inherent properties of the polyamide selective film determine the high fouling potential and poor chlorine resistance of the TFC membranes. Besides these two important issues TFC membranes have extra drawbacks such as relatively low permeability, high cost and environmental unfriendly (due to their preparation conditions). Therefore, a new generation of membrane is highly desired to replace the current problematic TFC membranes.

Ideally, the water flux/permeability of the new membranes should be as high as possible in order to reduce operation cost while maintaining robust mechanical properties to withstand operation pressure, which requires not only a strong membrane support but also more importantly the selective separation film to be simultaneously ultrathin and mechanically strong. Membranes with such record properties have been prepared by Peng et al.,² who succeeded in making membranes with ultra high flux and strong mechanical properties by depositing a thin layer of film (60 nm) made of crosslinked globular proteins onto a porous support (alumina filter). This approach, however, is totally unsuitable for large scale applications for

example for water purification. Various other efforts have also been made (see discussion of page 25-26), however no significant break-through has taken place until the finding of Tieke et al. and other researchers who demonstrated a new kind of TFC-like membranes made through modification of existing commercial ultrafiltration membranes with Layer-by-layer assembly technique (Figure 1A).³⁻⁵ Layer-by-layer (LbL) assembly is a very versatile technique for the construction of multicomposite thin films in an ordered and controlled manner by alternating deposition of charged polyelectrolytes or other materials with a nanometer precision.⁶ This technique allows the deposition of a thinner defect-free separation layer (< 50 nm)⁷ compared to conventional membranes (> 50 nm)⁸. Furthermore, the thickness, composition and/or architecture of the separation layer built by LbL-assembly can easily be controlled. Thus, LbL-assembly permits the development of separation membranes possessing a higher flux and selectivity compared to conventional membranes.^{7,9-11}

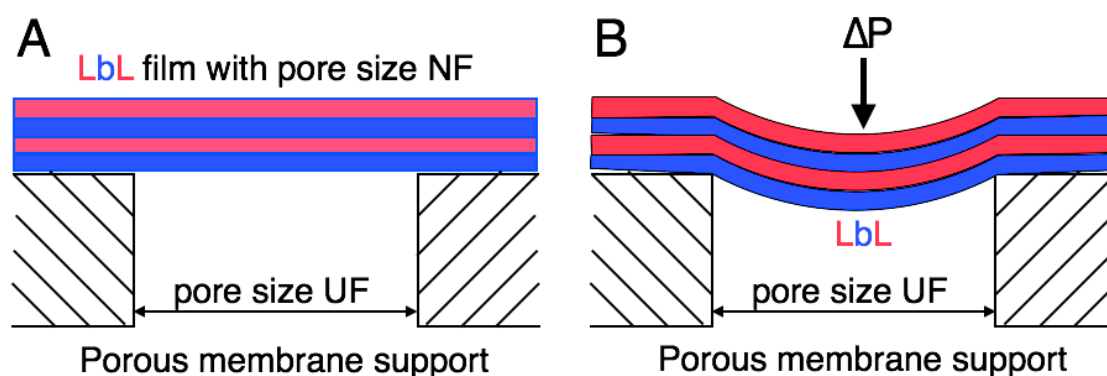


Figure 1. A) Over-simplified schematic representation of the LbL-assembly modified membranes where the pores of the membrane support (ultrafiltration membrane - UF) are covered by LbL-assembled films with pore size of NF; B) Over-simplified schematic depiction of the LbL-assembly modified membranes described in A when applying pressure on top of it, the LbL-assembled film is deformed resulting in mechanical shear. (Please note that this is an idealized scenario, the LbL deposition may also occur inside of the pores, see discussion page 34-35)

This PhD thesis work, carried out within the European project LbLBRANE, aimed at co-developing a new generation of TFC nanofiltration membranes with high membrane performance (high flux and high retention) and of mechanical robustness

using the LbL-assembly technique for water treatment. More precisely, among all the objectives of the LbLBRANE project, my purpose was to control through the LbL-assembly conditions the composition and the structure of an intermediate layer deposited between the membrane support and the separation layer and to investigate the structure-property relationships of such composite membranes. The controlled porous structure of this intermediate layer should prevent the blocking of the membrane pores, allow high flux and improve mechanical strength of membranes.

The development of new NF membranes equipped with an intermediate reinforcing layer and a separation layer requires a detailed understanding of polyelectrolyte multilayers and separation membranes, and basic concepts regarding mechanical properties of common structural materials. The first chapter of this thesis will introduce consecutively the LbL-assembly technique, conventional synthetic separation membranes, and LbL-modified membranes. The second chapter will be dedicated to materials and methods used in this work.

Prior to investigate the preparation and the properties of the intermediate layer, it was first necessary to establish the composition and the structure of the separation layer that will serve as a reference for the membrane performance tests (chapter 3). As real membranes only allow to employ a very limited set of characterization techniques because they are porous objects, the parameters controlling the assembly and the quality (thickness and homogeneity) of the LbL-coatings were investigated on model and membrane-like surfaces prior to coat real membranes. The use of membrane-like surfaces was motivated by the fact that LbL films must be grown on surfaces that are similar to the bulk surfaces to fully characterize them using classical characterization techniques. The investigations of the LbL-assembly on the various surfaces and the results on filtration properties of LbL-coated membranes allowed to determine the best composition and structure for the separation layer with respect to membrane performances and to get a better understanding of the structure-property relationships of the LbL-assembly modified membranes.

The next step was to study the LbL-deposition of an intermediate layer with a mesh structure of customizable porosity between the membrane surface and the active separation layer to prevent the blocking of the membrane pores, allow high flux and improve mechanical strength of membranes. Carbon nanotubes (CNTs) and cellulose nanofibrils (CNFs), owing to their unique ultrahigh mechanical properties, are ideal

candidates as reinforcing agents to design such intermediate layer on membranes. Ma et al. showed also that the deposition of nanofiber layer spanning over the membrane pores produces membranes showing high permeability while maintaining a high selectivity.¹² Beside the filtration efficiency, the intermediate layer offers also extra mechanical properties to the coated membrane that should be stable when exposed to high pressure during operation (Figure 1B). A prerequisite for the LbL-assembly of LbL-based nanofibers films was to make stable suspensions of these nanofibers. Chapter 4 describes how stable nanofiber suspensions were prepared and used for the LbL-assembly of nanofiber reinforced coatings on model surfaces as a function of deposition conditions (salt concentration, polycation nature, ...). As the evaluation of the mechanical benefit of nanofiber incorporation in the intermediate layer requires freestanding micron-thick films, the LbL-assembly of thick nanofiber-based multilayer films was studied.

As we could successfully build nanofiber-based coatings on model surfaces, the LbL-assembly of an intermediate layer on real membranes was carried out and the properties (water permeability and retention towards MgSO_4) of these LbL coated membranes were determined as a function of the composition and the structure of the intermediate layer (chapter 5). The membrane performances were compared to bare membrane and membrane coated with either only a separation layer or with an intermediate layer and a separation an intermediate layer

In chapter 6, freestanding thick nanofiber reinforced films were prepared and characterized, and their mechanical properties were measured by tensile strength and nano-indentation experiments as a function of film composition and architecture, and experimental conditions (ionic strength, deposition method, humidity, ...). Different mechanisms of film failure, i.e. nanofiber-polymer matrix interface rupture or nanofiber rupture, were observed and discussed. Mechanics models for conventional composite materials and the shear-leg model for nanofibers based nanocomposite materials were used to interpret the mechanical properties of these nanofibers based LbL-assembled films.

I. State of the art

This chapter first introduces the Layer-by-Layer (LbL) assembly technique and then overviews the two main growth regimes that are linked with semi-permeable property of LbL-assembled films. This semi-permeable property of the LbL-assembled films can be used for making separation membranes of high permeability and good retention. Before looking into how the LbL-assembly technique can be applied to fabricating LbL-assembly modified membranes of new generation, some basic concepts of conventional synthetic membranes and their drawbacks will be described. Finally, after giving an overview of the LbL-assembly modified membranes, the roles of an intermediate layer made of nanofibers in the LbL-assembly modified membranes will be introduced, which covers their effect on improving membrane performance and the role as mechanical reinforcing agent. These two aspects of using LbL-assembled nanofibers as intermediate layer of LbL-assembly modified membranes will be discussed separately. On the one hand, a ‘three layer structure’ model will be introduced to explain how the membrane performance could be enhanced with intermediate layer made of LbL-assembled nanofibers, and on the other hand, the characterization of the mechanical reinforcement of the LbL-assembled films by nanofibers will be discussed in the light of mechanical tests of thick LbL-assembled nanofibers based films.

I-A. *LbL-assembly technique*

I-A-1. Introduction to the LbL-assembly technique

Layer-by-layer assembly is a versatile surface assisted nanoscopic assembly technique for the construction of multicomposite films of molecules bearing ionic groups such as synthetic polyelectrolytes,⁶ biomacromolecules,¹³ inorganic nanoparticles and platelet,¹⁴ carbon nanotubes or cellulose nanofibrils with a nanometer precision.^{15,16} Typically this technique involves alternate adsorption of polycations and polyanions (or other above mentioned molecules) on a charged (or uncharged polar) surface which leads to formation of self-assembled multilayered films mainly through electrostatic interactions combined with some other interactions such as hydrogen

bonding,¹⁷ donor/acceptor (or charge transfer) interactions,¹⁸ stereocomplex,¹⁹ Van der Waals,²⁰ Pi-Pi stacking or hydrophobic interactions.^{21–23} Figure I-1 shows the principle of LbL-assembly technique using polyelectrolytes as an example. When a polyelectrolyte adsorbs onto an oppositely charged surface, charge reversal on the surface typically occurs and allows the adsorption of an oppositely charged polyelectrolyte. Every adsorption of polyelectrolyte is usually followed by rinsing steps to remove the excess and weakly adsorbed polyelectrolytes. This cyclic process can be repeated until the desired number of layers is obtained. Apart from the conventional dipping method, spray-assisted²⁴ and spin-assisted^{25–28} LbL-assemblies were also developed. Compared to dipping, these two methods can not only accelerate the assembly process but also afford possibilities for coating on larger surface and for making oriented structures.^{25,29}

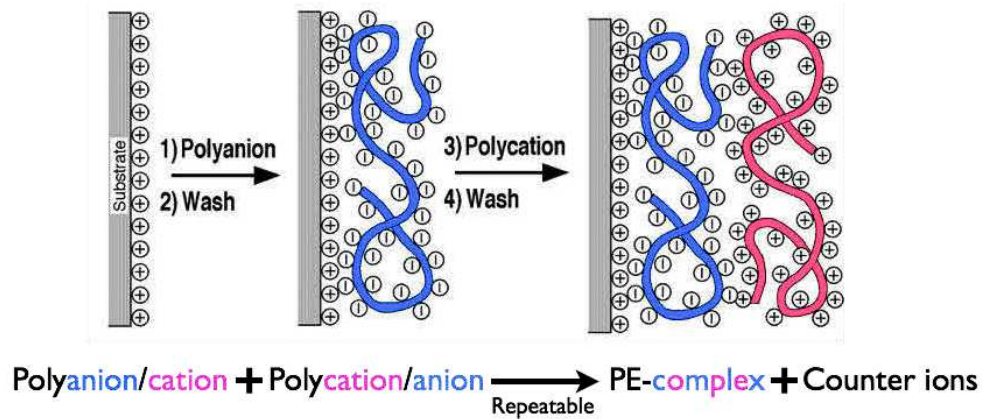


Figure I-1. Schematic representation of the principle of LbL-assembly technique. Steps 1 and 3 represent respectively the adsorption of a polyanion and polycation, and steps 2 and 4 are washing steps.

LbL-assembled films, owing to their tunable and well-controlled nano- and microscale structures combined with ease of production and industrial scalability, have attracted significant interdisciplinary interest leading to considerable applications such as light emitting diodes,³⁰ nonlinear optics,³¹ biosensors,¹³ corrosion protective coating,³² anti-reflection coating,^{33,34} conducting and/or antistatic coating,³⁵ antifouling coating for membranes^{36,37} or nanofiltration membranes.^{38,39,10} Among these applications, LbL-assembly technique for making separation membranes is one of the most valuable specific implementations. In the next part, we will overview the

two main growth regimes of LbL-assembled films and their link with the applications of LbL-assembly modified separation membranes.

I-A-2. Growth mechanism of LbL-assembled films

Fundamental understanding of the growth mechanism of LbL-assembled films, especially the ions transport behavior and permeability, is essential for the applications of LbL-assembly modified membranes. In general, two basic growth regimes can be defined for LbL-assembled films, which are linear and non-linear (also called superlinear or exponential) respectively. It is known that rigid polyelectrolytes and/or nanoparticles usually form films where molecules are of flat conformation and kinetically trapped in solid glassy state, which leads to a linear film growth as a function of the number of deposited layers of materials.⁴⁰ Whereas, polyelectrolytes of low glass transition temperature (T_g) form films of fluid coacervate state,^{41,42} which enables the diffusion of at least one of the deposited polyelectrolytes into the underlayered films and toward the upcoming deposited polyelectrolytes and thus results in non-linear film by increasing the number of deposited layers. Meanwhile, for certain polyelectrolytes, the film growth regime can be altered from linear to non-linear by increasing the ionic strength of the polyelectrolytes solutions. For example, LbL-assembled films of Poly(diallyldimethylammonium) chloride (PDADMAC)/Poly(styrene sulfonate) (PSS) showed linear growth in absence of salt or at low salt concentration in the starting solutions, while the films show non-linear growth when 0.5M of NaCl was added to the solutions (Figure I-2). Such influence of salt have been observed in many other studies,^{27,42,43} where it is believed that: at low ionic strength, the polyelectrolyte charges repel each other due to electrostatic repulsion and force the polymer chains to adopt an extended flat conformation and form a thin quasi-monolayer on the substrate; whereas at high ionic strength, the polyelectrolyte charges are effectively screened by the counter ions leading to polymers chains of coiled conformation and resulting thick absorption layer of polyelectrolytes with loops and tails structure. These loops and tails can penetrate into several adjacent layers of films to form more interdigitated structure, which results in thicker film with non-linear growth regime.

The shift of film growth behaviors from linear to non-linear by adding of a certain amount of salt for a similar system of (PDADMAC/PSS) was attributed to phase

transition from solid glassy state at low ionic strength to fluid complex-coacervate state at high ionic strength where polyelectrolytes can diffuse throughout the film.³⁴ This argument seems quite original and is in large agreement with the ‘diffusion in and out’ model that will be discussed shortly,³⁸ however, one should notice that the conditions of LbL-assembly in their study were quite different from ours. First, the deposition of the LbL-assembled films was realized ‘in situ’ without drying step, which makes the films constantly stay in wet condition differing from our films made with drying step after each circle of deposition. Second, rinsing solutions were also different from ours. In our case, we use water as rinsing solutions, whereas in their work, the authors used an aqueous NaCl solution with the same NaCl concentration as in the polyelectrolyte solutions for rinsing. These conditions, however, are similar to that were used for the interpretation of ‘diffusion in and out’ model that is overviewed in the next paragraph.

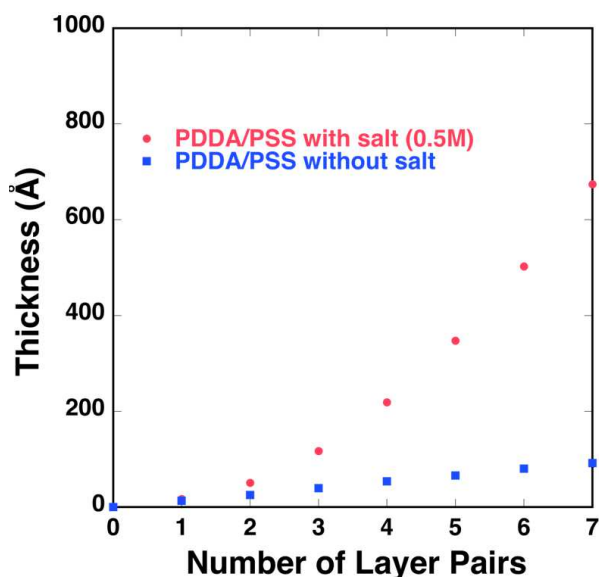


Figure I-2. Thickness vs number of layer pairs of (PDADMAC/PSS) with 0.5M NaCl (red dots) and without salt (blue dots) in the solutions. (rinsing process with water was carried out after each deposition of polyelectrolytes and drying step with compressed air was performed after each layer pair of deposition)

Since the first observation of Elbert et al. for poly(L-lysine) (PLL) and alginate (AG) polyelectrolytes pair,⁴¹ LbL-assembled films of non-linear regime have been extensively studied.^{40,44–47} A common accepted model of “diffusion in and out” were suggested and experimentally proved by Lavalle et al.^{46,47} Their studies suggest that

the mechanism of non-linear growth is strongly related to the diffusion throughout the film of at least one of the polyelectrolytes that comprise the film. Such diffusion occurs “into” the film when it is brought into contact with the solution of polyelectrolytes that are able to diffuse into the film, and “out” of the film when it is brought into contact with the rinsing solution, as well as with the solution of polyelectrolytes of opposite charge, during each cycle of deposition (Figure I-3).

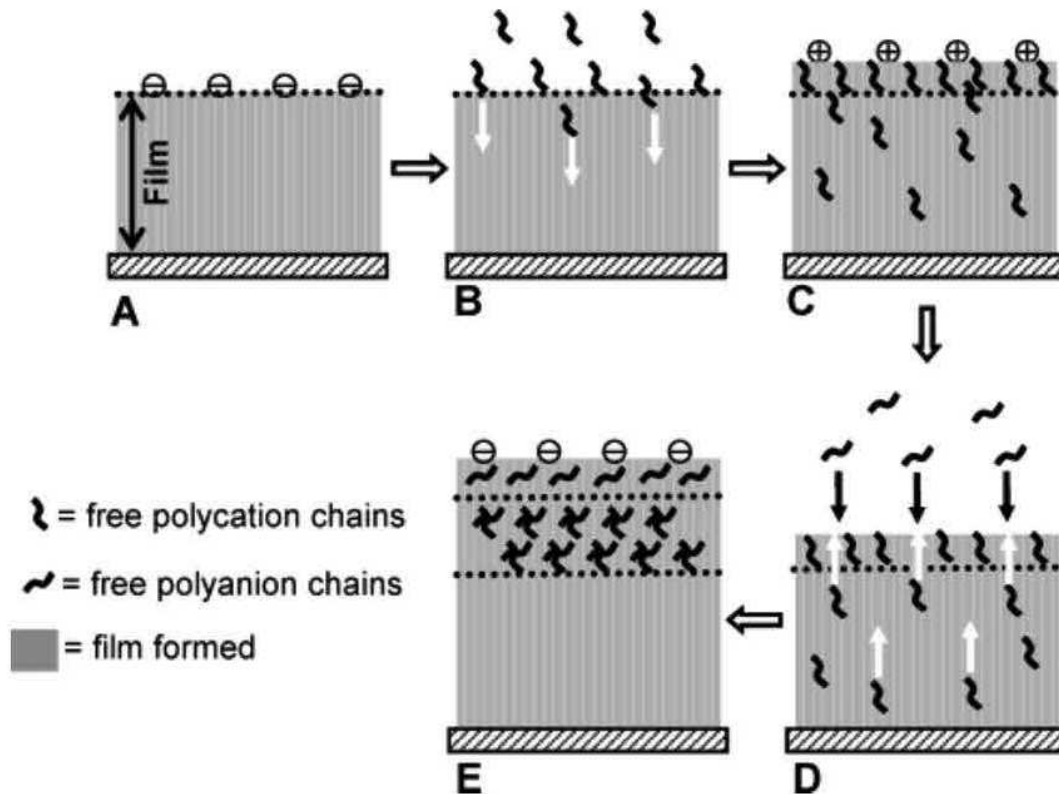


Figure I-3. Schematic representation of the “diffusion in and out” build-up mechanism of a Poly(L-lysine) (PLL)/Hyaluronan (HA) LbL-assembled film, based on the diffusion of the polycation PLL: (A) assuming that mechanism started with a negatively HA terminated film; (B) the film is put in contact with the polycation solution (PLL) (most of the chains diffuse “into” the film; some chains, however, adsorb on top of the film, leading to positive charge overcompensation in the film); (C) after a rinsing step, some free polycations remain in the film; (D) contact between the positively terminated film and the polyanion solution, followed by diffusion of the free polycation chains “out” of the film; (E) end of step D, resulting in negative charge overcompensation. The adsorption cycle results in a negatively terminated film thicker than that in step A.⁴⁶

This diffusion in and out model, also called diffusion-reaction model, based on the “inward” and “outward” diffusion process of at least one of the components of LbL-

assembly, successfully explain the non-linear growth mechanism, as well as the case of linear growth where none of the components of LbL-assembly diffuse within the film. It also described an energy barrier that is formed during the LbL-assembly, which stops and/or prevents further diffusion in and out of the polyelectrolytes. This barrier, together with the Donnan effect arising from the noncompensated “fixed” charge (also called extrinsic charge) inside the film, are responsible for the semi-permeability of the LbL-assembled films.

The presence of extrinsic charge in the LbL-assembled films of non-linear growth have been confirmed by Ghostine et al. (Figure I-4).⁴⁸ In this study of LbL-assembled films of (PDADMAC/PSS), using radio-labeled constituents, they found that the superlinear growth of the (PDADMAC/PSS) films assembled at high ionic strength could be mostly explained by the diffusion-reaction model however with some exceptions in terms of the mechanism of charge overcompensation. They found that after a certain number of layer pairs, the excess PDADMA positive charge was no longer compensated by the addition of PSS, which resulted in permanent presence of positive extrinsic charge of PDADMAC with its counter ions of sodium. This was ascribed to the different diffusion-reaction distances for PDADMAC and PSS through the film. When the film is capped with a last layer of PSS, a glassy and stoichiometric complex is formed, which freezes the PSS in place and results in the uncompensation of certain PDADMAC sites. Whereas when the last layer is PDADMAC, the large diffusion range of PDADMAC through the film complex with the PSS leads to the overcompensation. Such layering strongly influences the fundamental properties of LbL-assembled films, ions permeability, for instance. The excess extrinsic charge in the as-prepared films can includes or excludes ions through a classical Donnan mechanism, which might lead to unexpectedly high permeability and high selectivity (retention) for ions and small charged molecules.⁴⁸ This is why LbL-assembly technique is so attractive for making separation membranes whose two most important characters are high permeability and good retention. In addition, the rinsing and drying conditions used in our study of film growth behavior of LbL-assembly are quite similar to that used in this study, which will be further discussed in the chapter III.

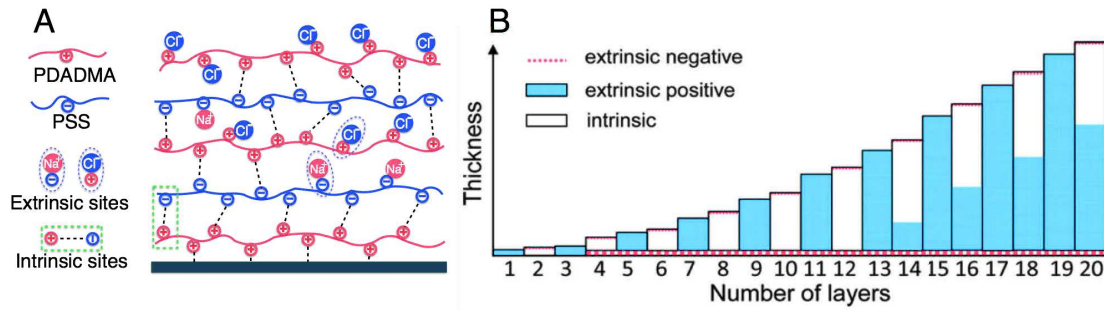


Figure I-4. A) Internal charge balance in LbL-assembled films maintained by a combination of extrinsic charges (polymer/counterion Pairs) and intrinsic charges (polymer/polymer ion pairs); B) Approximate asymmetric distribution of positive (PDADMAC) and negative (PSS) excess polyelectrolyte charge following each layer during buildup of a (PDADMAC/PSS) multilayer at 0.5 M NaCl.⁴⁸

Up to now, we have described the film growth behaviors and their link with the semipermeable property of resulting LbL-assembled films, which could lead to new generation of separation membranes with high permeability and good retention. Before looking into how LbL-assembly technique could be applied for making separation membranes, in the next part we will overview some basic concepts of conventional synthetic membranes and their drawbacks that could be overcome by making new generation membranes through Layer-by-Layer (LbL) assembly technique.

I-B. *Conventional synthetic separation membrane*

Separation membranes are based on a long-known phenomenon. Since the eighteenth century, the concept of a membrane has been noted, but not until end of nineteenth century and beginning of twentieth century this concept was only well studied and applied to drinking water supplies during the second World War in Europe. Like biological membranes such as mucous membrane and basement membranes, synthetic membrane is a selective semi-permeable barrier that allows the passage of certain constituents and retains other constituents in the liquid.

Membrane's basic performances are characterized by its permeability and retention. Permeability (J) is the volume (V) of pure water or solution that pass through the

membrane per unit area of membrane surface (A) per unit time (t). J is calculated using the following equation:

$$J = \frac{V}{A \times t} \quad \text{Equation I-1}$$

The permeability of pressure-driven membrane-separation processes has been given by the following semi-empirical mathematical model:¹

$$J = K \frac{\Delta P}{t_e} \quad \text{Equation I-2}$$

where K is the membrane permeability coefficient constant defined by the diffusivity of the permeate in the membrane, ΔP the pressure difference across the membrane and t_e the effective membrane thickness. The effective thickness t_e is roughly determined by the thickness of the densest layer of the membrane that serves for the separation. The importance of the effective thickness of the membrane is evident from Equation I-2 since flux is inversely proportional to thickness.

The retention of membrane is evaluated in most cases by the rejection (R) that is calculated by the following equation:

$$R = \left(1 - \frac{C_p}{C_f}\right) \times 100\% \quad \text{Equation I-3}$$

where C_p and C_f are the concentration of the permeation and the feed respectively. Molecular weight cut-off (MWCO) of a membrane refers to the lowest molecular weight solute (in daltons) in which retention of at least 90% of the solute is obtained by the membrane.

Depending on the type of raw materials, artificial membranes are mainly composed of two categories: organic and inorganic membranes. While inorganic membranes are slowly replacing some traditional organic membranes because of their superior mechanical strength and better chemical resistance, organic membranes remain the most used and studied membranes due to their low cost and high packing density. In this thesis, only organic membranes will be considered. According to the pore size, synthetic organic membrane can be classified as reverse osmosis (RO), nanofiltration (NF), ultrafiltration (UF) and microfiltration (MF) membranes (Figure I-5).

I-B-1. Different types of membrane

I-B-1.1. Microfiltration membranes

Microfiltration (MF) is the oldest membrane process and remains a very important application. MF membranes are prepared by sintering, track-etching or by phase inversion. They are usually symmetric unlike UF membranes with a well-defined pore size in the range 0.05-10 μm . The most common polymers used for MF are polytetrafluoroethylene (PTFE), polyvinylfluoridine (PVDF), polypropylene (PP), polysulphone (PS), CA/CN, CTA, polyethylene (PE), polycarbonate, polyester, polyester imide and nylon 6. Some alumina and zirconia based ceramic membranes are also developed in multi-tube sheet and monolith honeycomb modules.⁴⁹ MF is primarily used for clarifying liquids, whereas UF is used for fractionating solutions, in food and municipal applications.

I-B-1.2. Ultrafiltration membranes

Ultrafiltration (UF) membrane is defined as a membranes with a pore size of 1-50 nm, smaller than MF. UF membranes are also manufactured by the phase-inversion process, which results in an asymmetric structure. The most widely used polymer is PS, but also some other polymers such as CA, polyethersulfone (PES), polyacrylonitrile (PAN) and PVDF. In general, hydrophilic membranes such as CA, PE, polyvinylpyrrolidone (PVP) and inorganic alumina are less susceptible to fouling than hydrophobic membranes such as PVDF, PS, PES and PP. Some charged functionalization are introduced to the hydrophobic membrane in order to increase its hydrophilicity and resistance to fouling for example sulfonated polyethersulfone (SPES). The solvent along with microsolute permeates through the UF membrane while macrosolute (emulsified oils, metal hydroxides, colloids, emulsified oil, endotoxins, pyrogens, viruses and bacteria) and other large molecular weight materials are retained by the UF membranes. UF has been introduced in the mid-1990s for municipal water treatment applications including treatment of surface water for production of safe drinking water and advanced tertiary treatment of municipal wastewater for recovery and reuse.⁵⁰ UF is also often used in the dairy and beverage industry as well as in high-purity water production for microelectronics and pharmaceuticals as the final polishing step. Ultrafiltration owing to its homogeneous

and suitable pore size, are usually used as the porous substrate for the fabrication of polyamide reverse osmosis membranes.

I-B-1.3. Reverse osmosis membranes

Reverse osmosis (RO) is a process often used for removing solutes such as dissolved ions from a solution by utilizing a semipermeable membrane. The semipermeable membrane can serve as a barrier to separate water from a concentrated solution, by which water passes through the membrane to the concentrated solution with the help of osmosis that tends to even out the water concentration. Due to the fact that water has lower chemical potential at the side of more concentrated solution, it continues moving from the less concentrated side to the more concentrated side until equilibrium where sufficient osmotic pressure builds up on the concentrated solution side to prevent further flow of water up the concentration gradient. As illustrated in Figure I-6, when hydraulic pressure greater than the osmotic pressure is applied on the concentrated solution side, the flow of water is reversed. This process called “reverse osmosis” results in a concentrated salt solution on the feed side of the membrane and a purified solution on the other side of the membrane. RO is used for retain solutes having a molecular weight more than 300 Da or effective size smaller than 1 nm, which includes heavy metal ions, carcinogens such as trihalomethane (THM), bacteria, germs, etc.

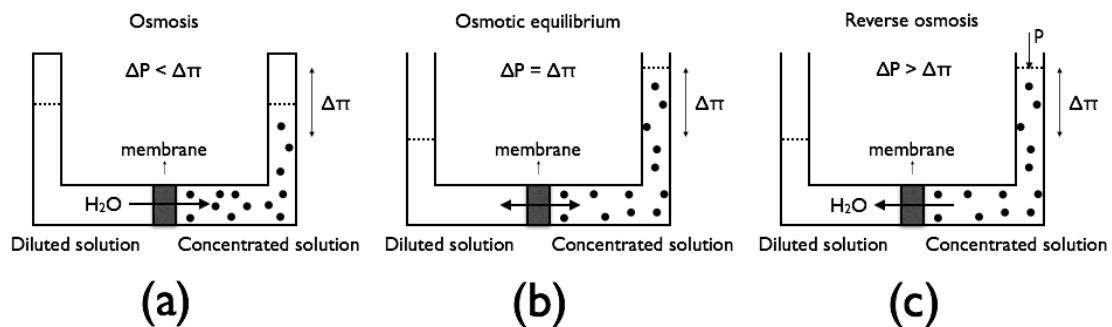


Figure I-6. a) Osmosis process where water flows from diluted solution to concentrated solution; b) osmotic equilibrium when hydraulic pressure (ΔP) equals to the osmotic pressure ($\Delta \pi$); c) reverse osmosis when a pressure (p) is applied to the concentrated solution side resulting in $\Delta P > \Delta \pi$.

Although semipermeable membrane phenomena have been recorded by the French Abbe Nollet more than two centuries ago,¹ first successful man-made osmosis membranes were only discovered in the late-1950s, where Sourirajan found that cellulose acetate was semipermeable to sea water electrolytes.⁵¹ After that, membranes made of homogeneous isotropic (symmetric) film of cellulose acetate (CA) (Figure I-7A) became available however with very low water permeability. The extremely low water permeability was ascribed to the symmetric structure of this CA membrane of which the effective membrane thickness (t_e) approached the total thickness of the isotropic CA film of as high as 6 μm . This high t_e thus resulted in the low permeability according to Equation I-2. Indeed later accidental finding of much higher permeability for an asymmetric/anisotropic CA membrane made using phase inversion method (Figure I-7B) confirms this.⁵¹ It was found that compared to symmetric membrane, the asymmetric membrane had a 13-fold higher total membrane thickness (100 μm), yet it had more than 40-fold higher permeability because of its much smaller t_e arising from its very thin top skin layer of the asymmetric structure. This principle of increasing permeability by forming a thin skinned top layer on more porous support of the asymmetric membrane inspired a new class of RO membrane called thin film composite (TFC) membrane (Figure I-7C). Owing to its much higher intrinsic water permeability and stronger chemical resistance than CA membrane combined with high salt retention, TFC membranes are now the state-of-the-art membranes and dominate the reverse osmosis commercial market with CA membranes a distant second.⁵² The TFC membranes have a special structure that consists of an extremely thin (about 100 nm) salt-rejecting polyamide selective layer made by interfacial polymerization (IP) reaction onto surface of suitable finely porous substrate such as polysulfone (PSF) or polyethersulfone (PES) UF membranes. The polyamide film made by the IP reaction could be as thin as less than 100 nm and is defect free, which ensures the TFC membranes' much higher permeability and higher retention compared to the other membranes such as symmetric or asymmetric membranes.

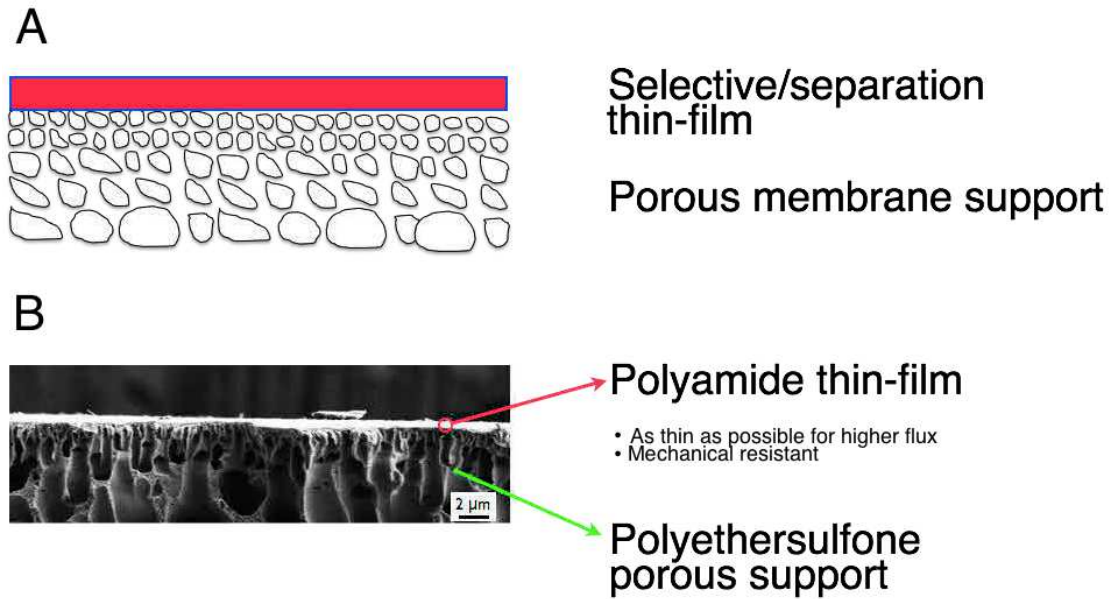


Figure I-8. A) Schematic representation of the TFC membranes composed of one selective/separation thin film covering on a porous membrane support; B) A cross-sectional SEM image of a polyamide TFC membrane with polyethersulfone ultrafiltration membrane as the support.

I-B-2. Disadvantages of TFC membranes

Among all these membranes, TFC membranes (Figure I-8) of RO and NF are the most efficient and economical method for removing more than 95% of all contaminants for the purification of water including all particles, bacteria and organics having molecular weight of more than 200 Dalton. Therefore, in the last 20 years TFC membranes (i.e. RO and its closely related NF - sometimes called “loose RO”) have evolved as important technologies for municipal and industrial water treatment. However, in spite of their prominent market and increasing applications in various domains, RO and NF face always some fatal problems.

One of the few shortcomings is that they are susceptible to degradation by chlorine due to the attack on the amide nitrogen and aromatic rings.⁵⁴ Nevertheless, chlorine is critical for membrane washing and for removing scaling (CaCO_3 deposits on the surface) and fouling (deposits of organics or colloids on the surface) of membranes. The lack of chlorine resistance of RO/NF membranes induces lost service time, a loss in water flux and quality, reduced operating efficiency, premature membrane replacement and higher operating costs. Therefore, prevention and reduction in the

rate of fouling is crucial in the design of the TFC membranes. Most fouling substances are hydrophobic and carry a surface charge.⁵⁵ Proteins such as bovine serum albumin (BSA) are more readily adsorbed onto the surface of hydrophobic membranes than hydrophilic membranes due to hydrophobic interactions. In addition, surface roughness also increases the adhesion of substances to the membrane surface. Hence, fabricating new membranes that are hydrophilic and homogeneous, and therefore, less prone to fouling with the added benefit of enhanced flux, has been a key priority.

Currently, pre-treatment procedures are taken for the feed prior to TFC membranes filtration in order to reduce fouling problem. These pre-treatment procedures include coagulation, sedimentation and flocculation, which serve as prefiltration to remove particles and colloids so as to reduce fouling. However these procedures are economically undesirable and are highly problematic for continuous operation. It doesn't change the fundamental source of fouling that is due to the surface properties of membranes. Different strategies have been introduced to make fouling resistant membranes through membrane surface modification. One of the main techniques for avoiding fouling is through the development of membranes with charged hydrophilic surface. For example, sulfonation of bulk polysulfone could impart negatively charged functions of sulfon and hydrophilic surface to polysulfone membranes.⁵⁶ In contrast to the direct functionalization of membrane bulk polymers, hydrophilic-hydrophobic blend membranes are manufactured by blending hydrophilic polymer to bulk hydrophobic polymer, which results in membranes of more hydrophilic. For instance, hydrophilic polyvinylpyrrolidone (PVP) is frequently used as a blending agent for hydrophobic PS or PES polymers.⁵⁷⁻⁵⁹ In addition, among the surface modification techniques investigated is surface fluorination. Fluorination renders the membranes with hydrophilic surface of which the contact angle could be reduced dramatically. Fluorinated TFC membranes showed almost an order of magnitude increase in flux without any reduction in rejection.^{60,61} Other surface modification techniques include grafting of hydrophilic polymer as brush layer, gas plasma treatment, various water soluble solvents activation and hydrophilic coating.⁶²⁻⁶⁵

Despite enormous works during the last 30 years either on enhancing the properties of existing TFC membranes by improving fouling resistance and/or chlorine resistance, or on making new TFC membranes, the problems of fouling and low chlorine resistance still remain largely unsolved. This is either due to the fact that most works

require complicated chemical/physical treatment and expensive materials, which limit their applications only to small lab scale; or due to less competitive membrane performance (e.g. much lower water permeability and/or lower retention) of new TFC membranes involving thick selective film far beyond the order of conventional TFC membrane's thin film (about 100 nm). Therefore, in order to be able to be competitive with conventional TFC membranes, the challenges on making new generation membranes with low fouling and high chlorine resistance are on:

1. making thinner separation film than that of the conventional TFC membranes, which means several dozens nm, without compromising the membrane performance and the mechanical properties for resisting high pressure membrane operation conditions;
2. using techniques that are inexpensive and easy to scale-up for industrial production.

One of the approaches used for making membranes with ultrahigh permeability and strong mechanical properties was achieved by Peng et al.,² who reported a new type of filtration membrane made of crosslinked proteins that are mechanically robust and contain nano-channels with diameters of less than 2.2 nm (Figure I-9). The resulting membranes had surprisingly two to three orders of magnitude higher flux than commercial membranes with similar rejection properties, which was ascribed to the presence of a large number of nano-channels (Figure I-9B) surrounded by the proteins. Nanoindentation tests were performed on as-made freestanding protein membranes, which gave an average Young's modulus of 4.4 ± 0.4 GPa.

Despite this remarkable achievement in making robust membranes with high permeability and good rejection properties, the technique used in this approach could not unfortunately be applied to making commercial membrane modules that require low cost and industrial scalability. Layer-by-Layer (LbL) assembly technique developed by Prof. Gero DECHER appears to be an ideal candidate for making new generation nanofiltration membranes though modification of existing commercial ultrafiltration membranes with LbL-assembled films, which can result in TFC-like membranes with high membrane performance and good mechanical properties^{6,66}

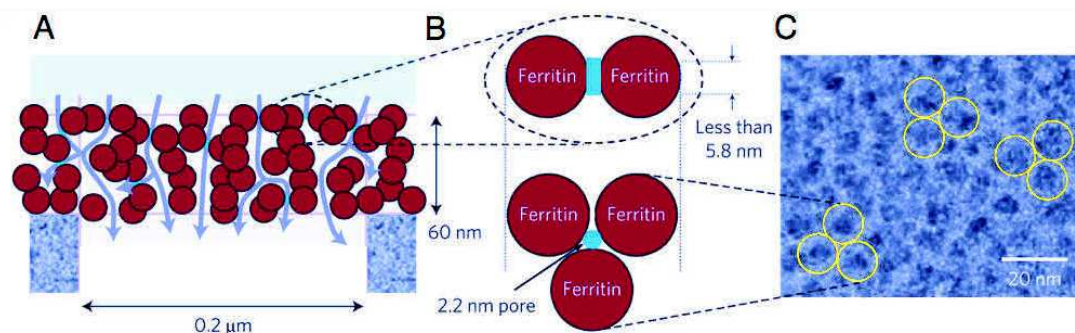


Figure I-9. Water permeation through protein-surrounded channels. A) A cross-sectional representation of a protein membrane on a porous alumina support. The scale of the ferritin is 1.5 times larger than that of the rest of the drawing. B) Side and top views of a protein-surrounded channel. Ultrafast water permeation is made possible by the presence of a large number of channels with effective lengths of less than 5.8 nm. C) ATEM image of a thin protein membrane. Some ferritin units are marked with yellow circles (which have diameters of 12 nm).²

I-C. *LbL-assembly modified membranes*

I-C-1. **LbL-assembly modified membranes with polyelectrolytes**

LbL-assembled films are particularly attractive for making selective membrane coatings due to their ultra-low thickness, high hydrophilicity, ionic crosslinked structures and tunable film architecture. Tieke et al. were among the first who prepared LbL-assembly modified membranes on porous supports.³ By depositing 60 layer pairs of poly(allylamine hydrochloride) (PAH) and PSS LbL-assembled film on a porous supporting membrane of PAN/PET (a polyethyleneterephthalate fleece coated with a thin layer of polyacrylonitrile), the authors obtained hybrid (or composite) membranes of remarkable selectivity towards ethanol/water and toluene/heptane. Since then, both the substrates and the LbL-assembly components have been greatly expanded. For example, the porous substrates of alumina, cellulose acetate, ceramic, polyethersulfone, polyamide and so on, were explored.⁶⁷ The same group studied the impact of ionic density of the polyelectrolytes components on the selectivity of water/ethanol and permeability of the LbL-assembly modified

composite membranes (Figure I-10).⁶⁸ It was demonstrated that under similar assembly conditions (without salt in the solutions), the denser the charge density of the polyelectrolytes components are, the lower permeability and higher ethanol retention the composite membranes modified with 60 layer pairs are. This indicates that the separation mechanism of as-prepared composite membranes is mainly related to the effect of size exclusion arising from the densely packed LbL-assembled films, which can be confirmed by the relatively low permeability of all the membranes. Despite their considerable selectivity, low permeability and time consuming process due to such a large number of layers (60 layer pairs), have prohibited these membranes from real applications.

Malaisamy et al.⁶⁹ successfully shortened the LbL-assembly procedure with as few as 2.5 layer pairs of PSS/PAH or 3.5 layer pairs of PSS/PDADMAC coated on a porous UF support membrane of polyethersulfone (PES) while excellent separation performance could still remain. They deposited 3.5 layer pairs of polyanions/polycations on surface of ultrafiltration membranes made by PES, and the prepared multilayer NF membranes have excellent separation performance, which showed a greater than 90% rejections of Na_2SO_4 along with a permeability of higher than $14 \text{ L/m}^2\cdot\text{h}\cdot\text{bar}$. The LbL-assembly reduces the molecular weight cut-off of polyethersulfone ultrafiltration supports from 50 kDa to $< 500 \text{ Da}$ and the permeability of the LbL-assembly modified membranes are about twice those of commercial membranes with a similar MWCO. Although the authors ascribed the observed remarkable membrane performance of the LbL-assembly modified composite membranes with only less than 4.5 layer pairs of coating simply to Donnan exclusion effect, they did not explain in details. Indeed, the use of polyelectrolytes solution with high ionic strength (0.5M NaCl or 2.5M MnCl_2) was the major difference compared to the works of Tieke et al. where no salt were used for starting solutions of same type of polyelectrolytes. The differed growth mechanism with presence of salt could have changed the separation mechanism of the membranes from size exclusion in the case of the works of Tieke et al.³ to Donnan exclusion dominant mechanism combined with small contribution of size exclusion depending on the type of polyelectrolytes. For membranes coated with PSS/PAH whose charge density is high, the contribution of size exclusion become higher than that of membranes coated with polyelectrolytes of low charge density - PSS/PDADMAC.

This explains why the membranes coated with PSS/PAH had lower permeability than that coated with the same layer pairs of PSS/PDADMAC. Therefore, in order to produce LbL-assembly modified membranes of high flux, low charge density PSS/PDADMAC are preferred pair of polyelectrolytes and should be used at high ionic strength.

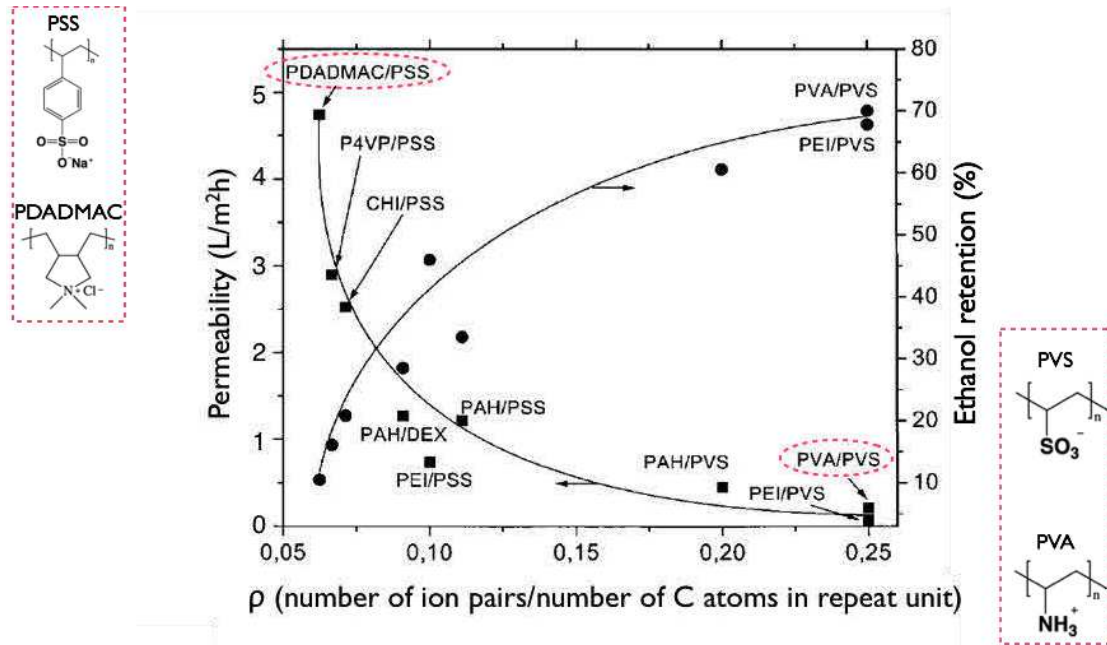


Figure I-10. Dependence of permeability and ethanol retention on charge density ρ of various polyelectrolyte systems. ρ refers to the number of ion pairs per number of carbon atoms in repeat unit of polyelectrolytes. The insets on the left and right show the molecular structures of the least and most dense polyelectrolytes pairs PDADMAC/PSS and PVS/PVA respectively.⁶⁸

To conclude, through careful selection of the type of polyelectrolytes (charge density) and adjustment of the parameters of LbL-assembly such as ionic strength, capping polyelectrolyte, number of coating layer pairs, the LbL-assembly modified composite membranes could eventually possess excellent membranes performance. However, the LbL-assembled films made of purely polyelectrolytes have two main drawbacks. Firstly, due to relatively weak electrostatic interactions of the polyelectrolytes, the LbL-assembled films of solely polyelectrolytes have very weak mechanical properties,¹⁵ while good mechanical properties are required for the membranes to withstand high operation pressure conditions. The other drawback lies in the inverse relation between the permeability and the retention of the membranes. As

demonstrated by Malaisamy et al.⁶⁹, the permeability of LbL-assembly modified membranes decreases and the retention increases with increasing number of layer pairs of polyelectrolytes coated. Therefore, in order to obtain membranes with best retention, the permeability has to be compromised, which results in restrained and unsatisfying flux for the resulting membranes. Fortunately, these two drawbacks could be overcome at the same time by introducing nanofibers into the LbL-assembled films.

I-C-2. LbL-assembly modified membranes reinforced with nanofibers

Nanofibers, owing to their unique properties, such as large surface areas, outstanding mechanical properties, ability of forming nanofibers network structures of high porosity, have been used to prepare LbL-assembled films with reinforced mechanical properties,^{15,16,70} and to increase the permeability of the LbL-assembly modified membranes.²⁹ In this section, we will first present the concept of improving membrane permeability via introduction of porous intermediate film layer formed between the membrane support and top selective film layer using nanofibers, which we call ‘three layers structure’. After this, mechanical reinforcement of LbL-assembled films by nanofibers will be discussed in terms of the preparation of thick free-suspended LbL-assembled films and the methods for characterizing the mechanical properties of such thick films.

I-C-2.1. Nanofibers used for improving membrane permeability

Nanofibers have been shown to be capable of improving the permeability of TFC membranes either by forming an additional intermediate layer of nanofibrous scaffold between thin selective layer and the membrane support (Figure I-11A) or by incorporating nanofibers into the selective barrier layer (Figure I-11B).^{71,72} The first approach came from the team of Chu⁷² who fabricated a new kind of high flux thin film nanofibrous composite (TFNC) membranes by taking advantages of the natural formation of the interface between an interconnected nanofibrous scaffold made of

carbon nanotubes and the polymer matrix of the selective barrier made of cross-linked poly(vinyl alcohol) (PVA), where the interface can be used to guide water transport and to exclude pre-designed contaminant molecules (Figure I-11B). Compared with similar membranes made without adding carbon nanotubes, the TFNC membranes exhibited substantially higher permeability and unaffected excellent retention of oil/surfactant emulsion (>99.8%). This was attributed to the interconnected external nanochannels formed by the nanofibers, through which water molecules travel a significantly shorter distance than through the tortuous path via molecular cavities in the polymer matrix of the barrier layer.

After this first approach, the same team expanded their concept of TFNC membranes to a new achievement, where, instead of embedding the nanofibers into the barrier matrix, they made an separate intermediate layer (mid-layer) of nanofibers between the membrane support and the selective barrier layer of the conventional TFC membranes, resulting in a TFNC membrane with “three-layer-structure”.⁷³ Compared to conventional TFC membranes with the same chemical compositions, the resulting TFNC membranes of three-layer-structure exhibited over 2.4 times more permeate flux while keeping comparable retention towards MgSO_4 .

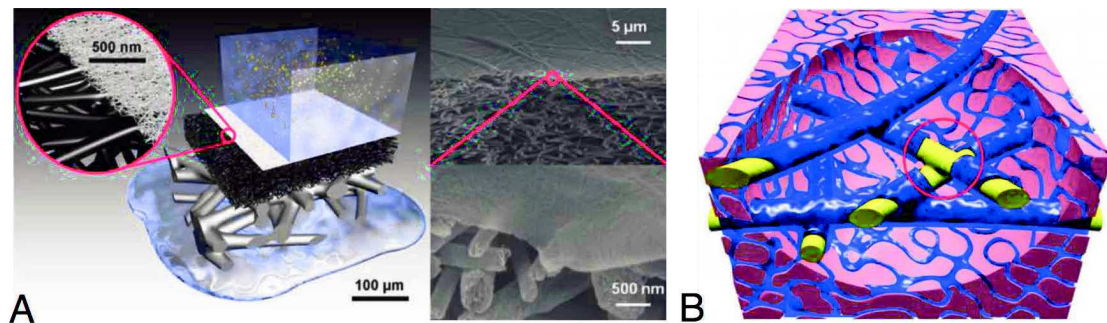


Figure I-11. A) On the left: Schematic hierarchical structure of thin-film nanofibrous composite (TFNC) membrane containing threr-layers-structure; On the right: Cross-sectional SEM micrographs of the barrier layer and nanofibrous scaffold in a typical TFNC membrane with the barrier layer deposited onto a nanofibers scaffold. B) Schematic representation of the nature of water nanochannels in the selective nanocomposite barrier layer. A skeleton of overlapped nanofibers (yellow) guides a continuously connected system of directed water channels (blue) formed by the connected hollow cylindrical gaps between the nanofibers and the polymer matrix (pink). The cut-out in the red circle sketches the cross-linked nature of the nanofiber interconnects. Nondirected molecular cavities in the polymer matrix also contribute to the overall water flow through the barrier layer.^{71,72}

Despite their remarkable achievements on improving membrane permeability by incorporating nanofibers, the methods they used such as casting or electrospinning, have some main drawbacks such as the use of organic solvents and limited control of the pore structure,^{74,75} which prohibit the TFNC membranes from real applications.

Blell R.²⁹ studied LbL-assembly modified membranes with similar “three layers structure”, where a porous intermediate layer made of LbL-assembled cellulose nanofibrils (CNFs) was incorporated between the selective/active top separation layer made of purely polyelectrolytes and the membrane support (Figure I-12). It was demonstrated that compared to membranes modified with only polyelectrolytes, the incorporation of intermediate layer made of CNFs could enhance the resulting membranes’ permeability without affecting the retention. This was attributed to the porous mesh structure of the intermediate layer formed by the CNFs, which bring lateral water transportation nanochannels that were far less tortuous than the molecular cavities in the dense polyelectrolyte selective layer, resulting in higher permeability for the modified membranes. Besides, the membrane’s high retention could be retained due to the intact dense selective top layer that is responsible for the separation properties (retention) of TFC like membranes.

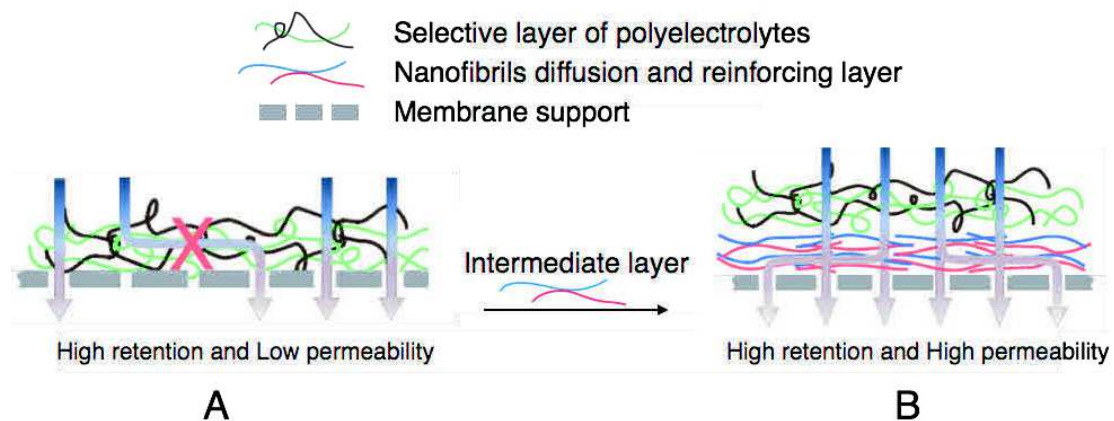


Figure I-12. A) Schematic representation of LbL-assembly modified membranes with pure polyelectrolytes deposited onto a membrane support; B) Nanofibers reinforced (CNFs) LbL-assembly modified membranes of “three-layer-structure” with an intermediate nanofibrous diffusion and mechanical reinforcing layer made of nanofibers for increasing the membrane’s flux while keeping high retention.²⁹

In addition, as the polyelectrolyte molecules in solutions are generally soft and have short persistence length and small size, when they are deposited onto porous

membrane support, the pores of membrane support are prone to be blocked because of the penetration and coating of the polyelectrolytes inside the pores, which leads to reduced porosity and thus lower permeability. The penetration or infiltration of polyelectrolytes in the confined porous have been demonstrated on silicon nanochannels by Kim et al. (Figure I-13).⁷⁶ It was shown that LbL-assembly took place within the channels whose initial gap size was from about 240-300 nm and stopped at a nanochannel gap size of 55 nm for the PVS/TiO₂ polyelectrolyte-nanoparticle hybrid system. As for the infiltration of pure polyelectrolytes systems, Wang et al. synthesized nanoporous polymer-based spheres via LbL-assembly deposition of PAH/PAA polyelectrolytes in mesoporous silica particles with 3-40 nm pores followed by removal of the silica template.^{77,78} The experiments showed that stable nanoporous polymer spheres could only be formed using porous silica particles with pore size > 2-3 nm, which suggested that the polyelectrolytes could not infiltrate into the pores of size smaller than 2-3 nm.

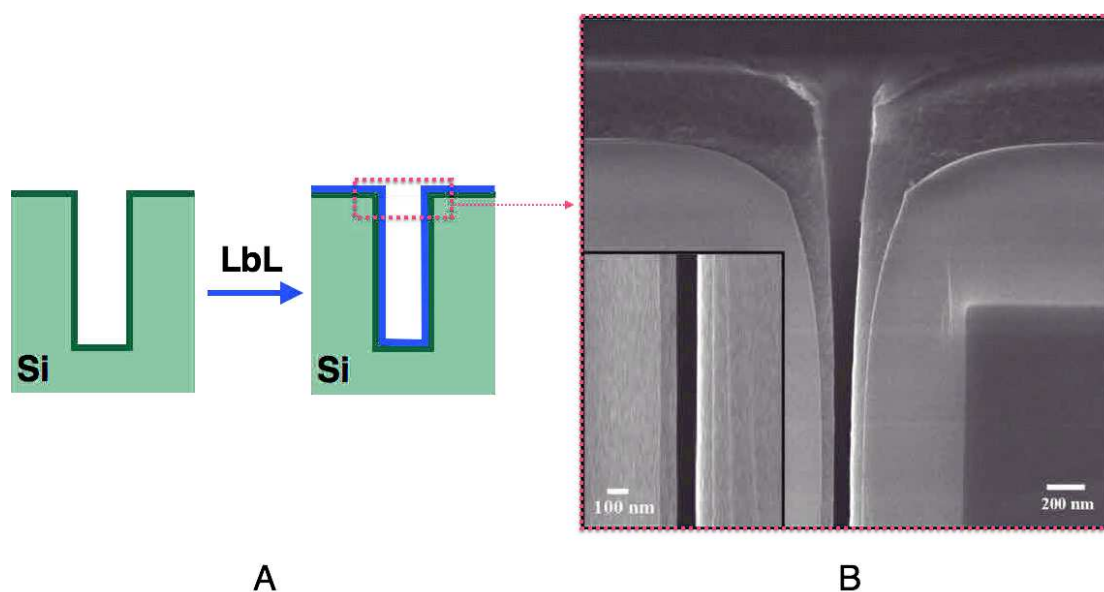


Figure I-13. A) Schematic representation of silicon nanochannel coated by LbL-assembly of poly(vinylsulfonic acid)/titania (PVS/TiO₂) (blue line); B) Cross-sectional SEM image of the nanochannel coated with 120 layer pairs of PVS/TiO₂, the inset shows a magnified view of the uniform, conformal multilayer within the nanochannel.⁷⁶

Nevertheless, LbL-assembled films spanning over the gap or pores could be possible. For example, direct preparation of ultrathin free suspended arrays of LbL-assembled films spanning across the gaps of TEM grids has been demonstrated by Laschewsky

and his group (Figure I-14).⁷⁹ By skipping the rinsing and drying steps during the initial steps of LbL-assembly, multilayered (PAA/PAH) spanning across 100 μm wide gaps of TEM grids were constructed. It was shown that the obtained ultrathin freestanding LbL-assembled (PAA/PAH)₈ film was unstable against physical or chemical stresses, however, crosslinking by amidation rendered the film much more resistant.

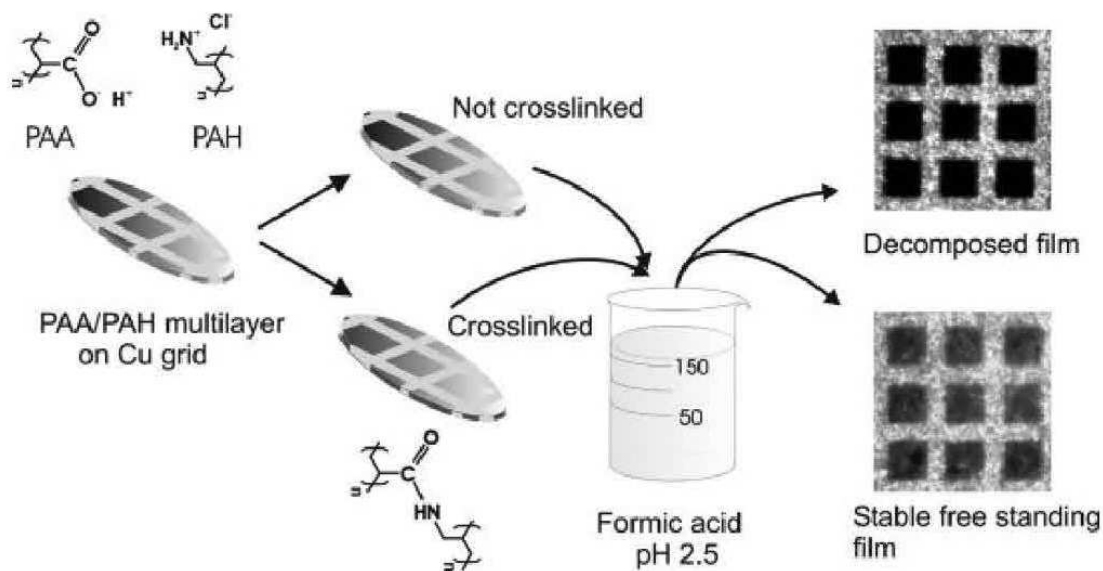


Figure I-14. Schematic of the formation of a freestanding, self-assembled (PAA/PAH)₈ film on a copper EM grid before and after incubation in formic acid. The crosslinked film was stable, whereas the non-crosslinked film decomposed after the incubation. The right-hand side shows microscopy images of decomposed and stable freestanding films (mesh size: 100 μm x 100 μm).⁷⁹

Therefore, stable and mechanically strong films are needed for the LbL-assembled films to be able to span over gaps or pores including the membrane supports. This could be achieved by the very intermediate layer of nanofibers of the abovementioned three layers structure for the reason that the nanofibers of the intermediate layer, owing to the long persistence length and high rigidity, could lie flat on top of the membrane support's pores and cover them by forming a rigid scaffold of interconnected nanofibers without blocking them as the polyelectrolytes do. Therefore, the top/separation layer of polyelectrolytes can then cover on this intermediate layer of high surface area reducing infiltration into the pores, so that the porosity of the membrane support and so as the permeability of the membrane can stay unaffected.

To conclude, inspired by the work of Chu⁷², LbL-assembly modified membranes bearing the so-called ‘three layers structure’ with an intermediate layer made of nanofibers can be prepared, which allows us not only to improve the permeability of the membranes via the less tortuous water nanochannels formed by the interconnected nanofibers, but also to span the LbL-assembled films over the membrane support’s pores without blocking them by the infiltration of polyelectrolytes.

Although Blell R. has demonstrated the proof of concept of this three layers structure in the fashion of LbL-assembly, its application for making real membranes especially nanofiltration membranes has never been done. In the present thesis, we studied the effect of this three layers structures on the membrane performance of LbL-assembly modified nanofiltration membranes using two different nanofibers of carbon nanotubes (CNTs) and cellulose nanofibrils (CNFs). Besides, as the mechanical properties of the LbL-assembled films are important for spanning on the membrane support’s pores, the nanofibers reinforcement on the mechanical properties was also investigated.

I-C-2.2. Nanofibers used for reinforcing mechanical properties

In order to investigate the reinforcement of mechanical properties of LbL-assembled films by incorporating nanofibers, thick freestanding or freely suspended LbL-assembled films are required for conventional mechanical measurement such as tensile tests. In this part, we overview the preparation of freestanding LbL-assembled films and mechanical measurement techniques that will be used for testing the mechanical properties of the LbL-assembled films.

I-C-2.2.1. Freestanding LbL-assembled films

Actually, the LbL-assembly modified membranes can be considered as composite membranes, of which the porous membrane support is covered with an ultra-thin LbL-assembled freely suspended (or freestanding) film that is suspending on top of each man-sized pores of the support. This is similar to the traditional TFC polyamide membranes where freestanding thin film is produced by interfacial polymerization reaction taking place between the water-oil interfaces above the membrane support.

Freely suspended ultrathin films have been a theoretical curiosity and experimental challenge for several decades.⁸⁰ Compared to existing synthetic routes to freely suspended films, such as polymerization at fluid-fluid interfaces (flat liquid-air or liquid-liquid interfaces and interfaces of liquid droplets in liquids)⁸¹ or polymerization of lipid bilayers, LbL-assembled freely suspended films, owing to its defect-free uniformness, aqueous assembly environment and capability of assembly on surface of large-area, have attracted increasing attentions.^{79,82-87} Hereby, we review some of these important approaches for making LbL-assembled freely suspended films.

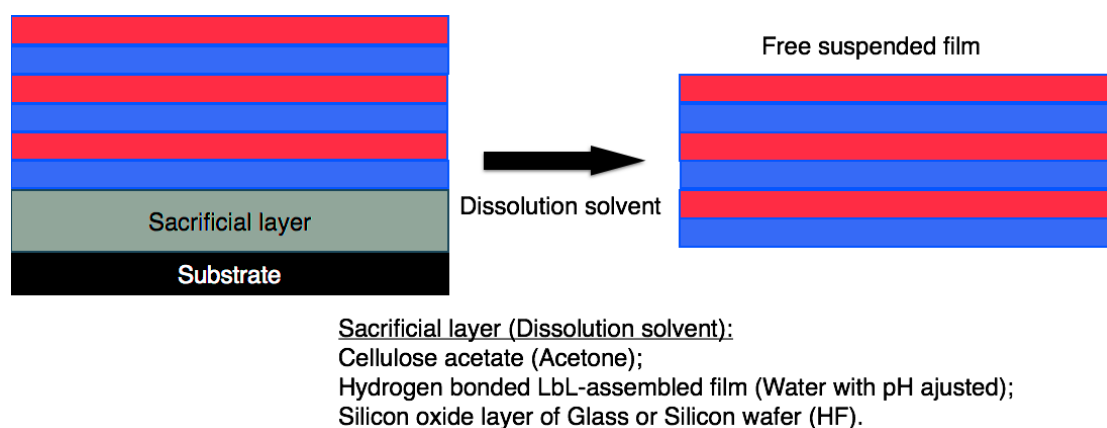


Figure I-15. Schematic representation of the process for making free suspended LbL-assembled film by dissolving a precursor sacrificial layer.

Inspired by the fabrication of LbL-assembled freely suspended hollow spheres through dissolution of sacrificial substrate (PS latex particles),⁸² Mamedov et al. successfully constructed freely suspended flat LbL-assembled films in 2000, where freestanding films were released from a sacrificial layer of spin-coated cellulose acetate that is dissolved in acetone afterward.⁸⁸ Since then, different sacrificial substrate and dissolution systems have been used for making freestanding LbL-assembled films (Figure I-15). For example, preparation of ultrathin self-standing polyelectrolyte multilayer membranes at physiological conditions using pH-responsive film segments as sacrificial layers has been demonstrated by Ono et Decher.⁸⁵ Another particular example concerns dissolution of the silicon oxide layer at the surface of glass slides and/or silicon wafers with hydrofluoric acid (HF) to release the freestanding films.⁸⁹ In this case, the silicon oxide layer could be considered as sacrificial layer for the assembly. Apart from some other planar freestanding films developed by several groups,⁸⁶ ultrathin robust freestanding LbL-

assembled films in other form were also demonstrated, for example, freestanding LbL-assembled films have been further extended to in the form of microcantilevers⁹⁰ and microtubes.⁹¹

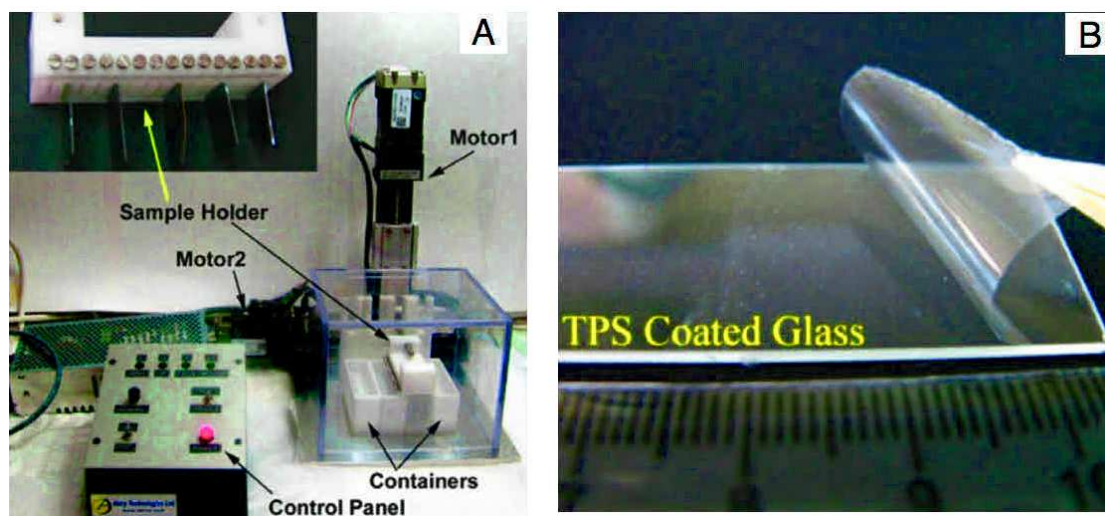


Figure I-16. A) Optical photograph of an automatic LbL-assembly set-up showing the motors, sample holder, solution containers and the control panel; B) Peeling off a 100 layer pairs freestanding LbL-assembled film (about 5 μm thick) from a trichloro(1H, 1H, 2H, 2H-perfluorooctyl)silane (TPS) monolayer-coated glass slide.⁸⁷

Another approach toward the production of free-standing LbL-assembled films consists in mechanical delamination of the film from a highly hydrophobic surface.⁸⁷ Using an automatic set-up (Figure I-16A), Patro and Wagner constructed micron-thick LbL-assembled PVA/Laponite films on glass slides or silicon wafers that were coated with a monolayer of functional silane (trichloro (1H, 1H, 2H, 2H-perfluorooctyl)silane (TPS)). The fluoroalkyl chains of the TPS endowed the substrates with hydrophobic surfaces, on which the LbL-assembled films can still grow. The weak interactions between the assembled films and the substrates allows a 100 layer pairs LbL-assembled film of about 5 μm thick to be peeled off by a plastic tweezer (Figure I-16B). Compared to the other methods mentioned above, this method has several advantages, such as:⁸⁷

1. It allows the films to be lifted off without sacrificial layer;
2. No harsh conditions like HF etching which could damage the LbL-assembled films;

3. LbL-assembled films with thickness as small as a few tens of nanometers may be produced with this method.
4. It allows the construction of LbL-assembled films of well-defined size and shape, which is a prerequisite for many applications and also for preparing samples for classic tensile test.

The freestanding LbL-assembled films fabricated using this method are suitable for investigation of their mechanical properties by classic mechanical characterization methods such as tensile test. In this work, mechanical reinforcement of LbL-assembled films by nanofibers was studied by tensile tests of freestanding LbL-assembled films and nanoindentation tests of thick LbL-assembled films assembled on Si-wafers.

I-C-2.2.2. Mechanical characterization of freestanding LbL-assembled films

I-C-2.2.2.1. Tensile test

One of the simplest ways of assessing the reinforcement of polymers upon the addition of nanofibers is through tensile tests. Tensile test, namely, stress-strain test, is the easiest and the most used characterization technique for measuring mechanical properties of solid materials.⁹² The basic idea of a tensile test is to place a sample of regular shape (mostly rectangular) between two fixtures called “grips” which clamp the sample (Figure I-17). The initial length of the sample (L_0) and its cross-sectional area (A) are known before the test. Then force F is loaded at one end of the sample while the other end is fixed. The force is increased and recorded as a function of the strain ϵ which is equal to $(L_1-L_0)/L_0$, where L_1 is the length of sample after stretching.

The stress applied on the sample is:

$$\sigma = \frac{F}{A} \quad \text{Equation I-4}$$

The result of this tensile test is a curve of stress versus displacement (strain). Typically, three main mechanical features can be obtained from this curve (**Figure I-18**):

1. Young's modulus (E) is defined by the initial slope of the uniaxial stress-strain curve, where the strains are recoverable (elastic), it corresponds to the property of the material to resist to a deformation.
2. The stress at breaks also called ultimate tensile stress (σ_u) that corresponds to the tensile strength of the material.
3. The strain at breaks (ϵ_u) that corresponds to the maximum strain the material can handle.

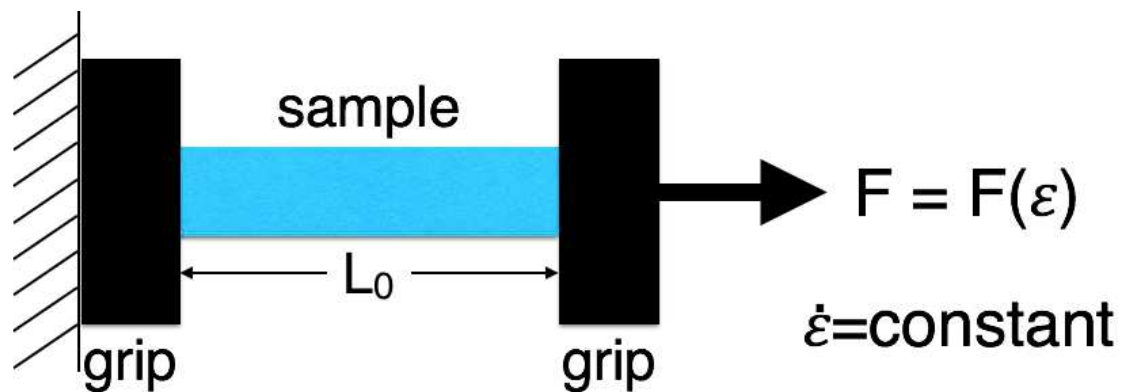


Figure I-17. Schematic representation of tensile test. The sample having an initial length of L_0 clamped between two grips is pulled at a constant speed with applied loading force (F) which is recorded as a function of the strain (ϵ).

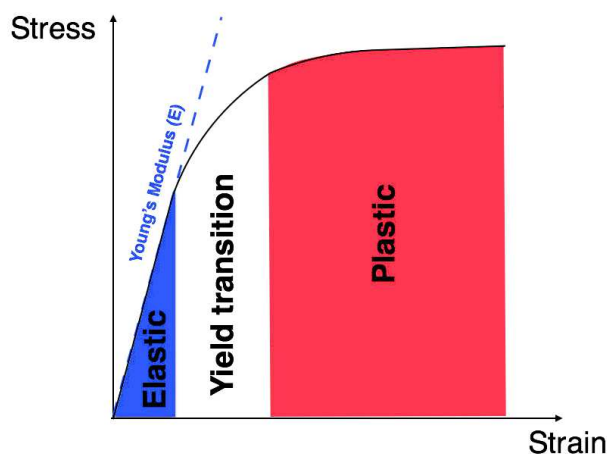


Figure I-18. Schematic representation of a stress-strain curve.

Typically, depending on the properties of material, stress-strain curve could be divided in three parts.⁹² The first initial part corresponds to elastic region at low strain, where the stress is proportional to the strain and material behaves elastically with reversible deformation. The Young's modulus obtained by calculating the slope of the elastic region is related to stiffness of the material. The second part is the so called "yield transition" region, where material's behavior transits from elastic to plastic of the last part due to non-perfect elastic properties. Except for elastomers possessing an elastic behavior, most polymers have a plastic region as the last part of the stress-strain curve. In the plastic region, material starts to undergo irreversible deformation and the stress continues increasing non-elastically due to strain hardening. The failure of the material happens in the plastic region, in which the stress at break corresponds to the tensile strength of the material. The total energy required to break the material can be assessed in terms of the area under the stress-strain curve, which defines another mechanical feature of the material – toughness. The toughness measures resistance of the material to fracture, which obviously depends not only on its Young's modulus in the elastic region but also on the yield transition and more importantly plastic region.

I-C-2.2.2.2. Tensile test of freestanding LbL-assembled films

Tensile test on freestanding LbL-assembled films have been demonstrated by several groups.^{15,87,93} For example, Mamedov et al.¹⁵ improved the yield stress of LbL-

assembled films of purely polyelectrolytes by more than 20 times through incorporation of single wall carbon nanotubes (SWNT) into the films (Figure I-19). Merindol et al.⁹³ made strong, self-healing and transparent LbL-assembled films using cellulose nanofibrils (CNFs). These films showed tensile strength of up to 250 MPa and Young's moduli of up to 18 GPa (Figure I-20).

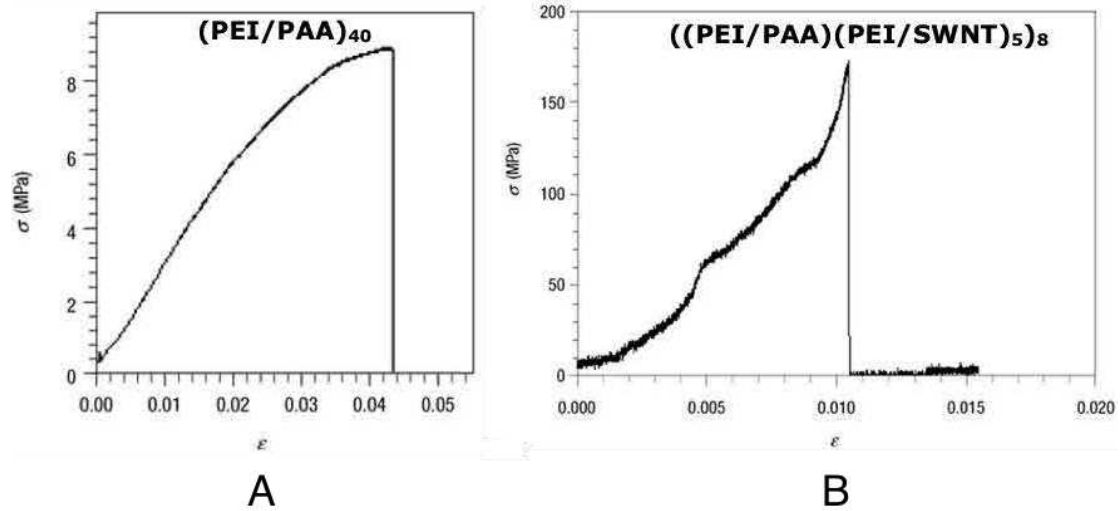


Figure I-19. A) Stress-strain curve of freestanding LbL-assembled films made of solely polyelectrolytes of (PEI/PAA); B) Stress-strain curve of similar films reinforced with SWNT.¹⁵

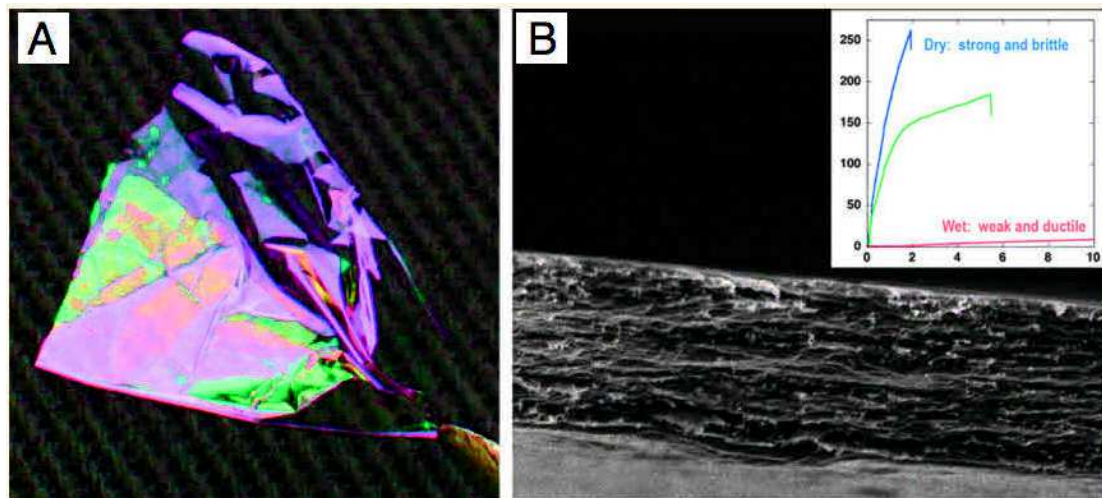


Figure I-20. A) Optical graph of freestanding LbL-assembled films reinforced with CNFs; B) Cross-sectional SEM image of a CNFs based film; Inset shows Stress-strain curves of the CNFs based films at different humidity conditions.⁹³

As these studies showed feasibility of improving mechanical properties of LbL-assembled films using CNTs and CNFs, which will be of benefit to the LbL-assembly

modified membranes that require good resistance to operation conditions such as high pressure or high shear force. Therefore understanding the mechanical properties of the nanofiber reinforced LbL-assembled films is naturally important and became a part of this thesis study. Constrained by the precision limit of force sensor of the tensile test machine, micron-thick freestanding LbL-assembled films were required. To this end, a similar automatic set-up to the Figure I-16A was used for constructing thick LbL-assembled films.

I-C-2.2.2.3. Nanoindentation

Another supplementary mechanical characterization method for testing LbL-assembled films is the nanoindentation technique. Nanoindentation testing is a simple method that consists essentially of touching the material of interest whose mechanical properties such as elastic modulus and hardness are unknown using a hard tip of known mechanical properties. Nanoindentation is simply an indentation test in which the length scale of the penetration is measured in nanometers rather than micron or millimeters, the latter being common in classic harness tests. Apart from the displacement scale involved, the distinguishing feature of most nanoindentation tests is the indirect measurement of the contact area between the indenter and the specimen. In conventional indentation tests, the area of contact is calculated from direct measurements of the dimensions of the residual impression left in the specimen surface upon the removal of load. Whereas, in nanoindentation tests, the size of the residual impression is of the order of microns which is too small to be measured directly. Thus, the projected area of contact of nanoindentation tests (A_c) is commonly determined by measuring the depth of penetration of the indenter into the specimen surface (h). This, together with the known geometry of the indenter, provides an indirect measurement of contact area at full load.⁹⁴

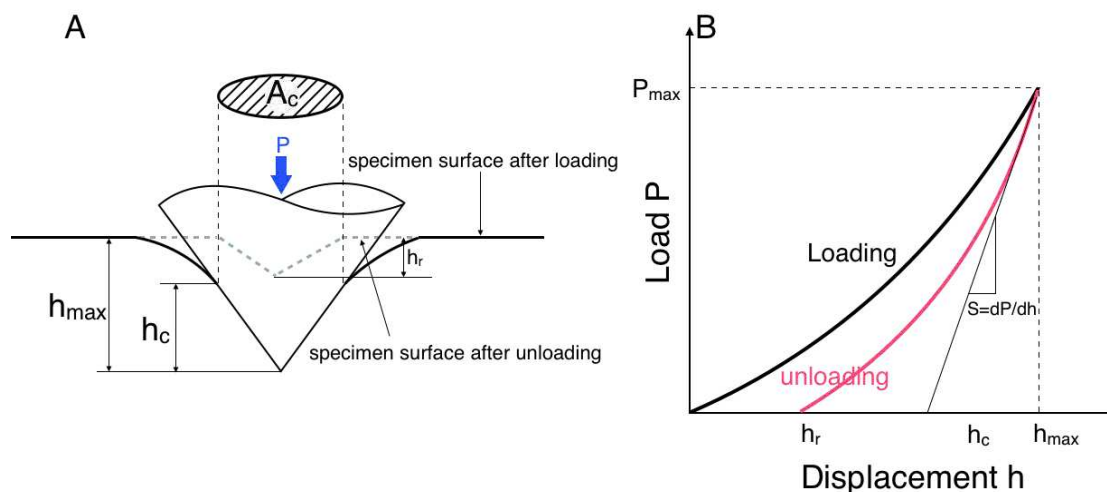


Figure I-21. A) Schematic representation of nanoindentation test; B) Schematic representation of typical load(P)-displacement(h) curve of the nanoindentation test showing loading curve (in black) and unloading curve (in red). h_c , h_{max} and h_r are the contact depth, maximum penetration depth and residual depth after unloading, respectively; S is the contact stiffness determined as the slope of the unloading curve at the beginning of unloading dP/dh ; A_c is the projected contact area.

During the nanoindentation tests, the load placed on the indenter tip is increased as the tip penetrates into the specimen following a user-defined protocol. While indenting, various parameters such as load (P) and depth of penetration (or displacement h) can be measured. A record of these values can be plotted to create a load-displacement curve (Figure I-21), from which several mechanical properties of the specimen material can be extracted, i.e. Young's modulus and hardness (detailed in the next chapter).⁹⁵

I-C-2.2.2.4. Nanoindentation of freestanding LbL-assembled films

Nanoindentation tests on LbL-assembled films have been demonstrated by several groups.^{96–98} Fan et al.⁸⁰ tested hardness and Young's modulus of LbL-assembled montmorillonite (M)/poly(diallyldimethylammonium chloride) (P) films of 50 and 100 layer pairs with average thickness per layer pair of about 4 nm. They found that, contrary to the hardness of pure silicon wafer that has a constant hardness value of about 12.5 GPa, both films of 50 and 100 layer pairs showed similar 3-stage curve

pattern: early decrease and ultimate increase with a plateau in between (Figure I-22A). The hardness values of the plateau in the middle were considered to be the authentically representative data. It was also found that the hardness values of the plateau for both films were different, showing higher hardness for the 50 layer pairs film compared to the thicker 100 layer pairs film. Similar results were obtained for the Young's modulus (Figure I-22B).

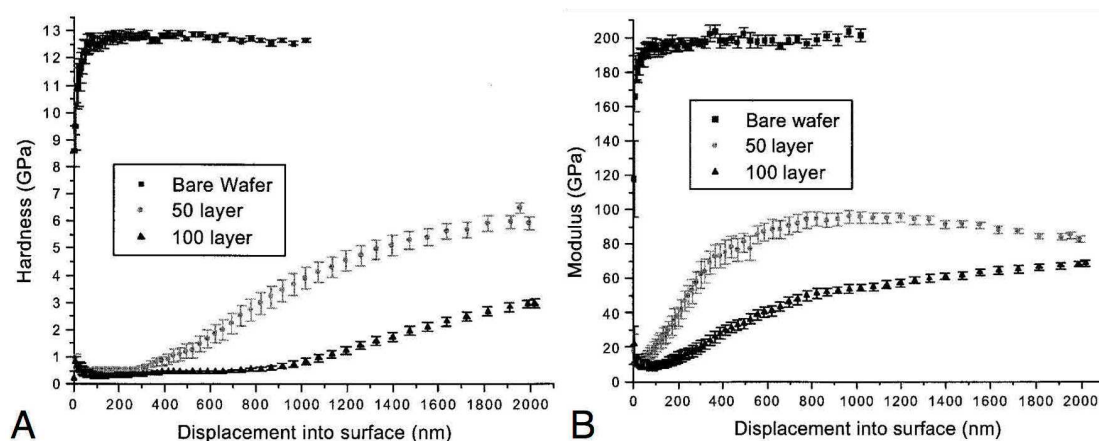


Figure I-22. A) Hardness and B) Young's modulus versus indent depth relationship of bare silicon wafer and LbL-assembled films of 50 and 100 layer pairs of M/P.⁸⁰

This was attributed to the substrate effect on the indentation. Indeed, during nanoindentation tests, substrate can contribute to the resulting values of the mechanical properties of the tested films depending on the film thickness (Figure I-23). In order to avoid the influence of the substrate, it is common to restrict the maximum depth of penetration in a test to no more than 10% of the film thickness.⁹⁴ Therefore, for the film of 50 layer pairs of M/P whose thickness is about 200 nm, the maximum depth of penetration should be less than 20 nm in order to avoid the substrate's influence. However, since the indenter tip is never perfectly sharp, a minimum depth of penetration is usually required for the tip to be able to see the specimen, which is called tip defect. As we can see from the curves of the bare wafer, at about 40 nm of penetration, the hardness and the Young's modulus reached to a plateau, which is caused presumably by the tip defect. Consequently, there is no available zone of penetration depth where the measured values of mechanical properties of the film of 200 nm thick do not undergo neither substrate influence nor the tip defect. On the other hand, for the film of 100 layer pairs of M/P whose

thickness is about 400 nm, it possesses a small zone of penetration depth around 40 nm where the obtained values of mechanical properties should be less influenced by the substrate and the tip defect. To increase this ‘uninfluenced zone’ of penetration depth and to get more accurate measurements, much thicker films should have been prepared for nanoindentation tests during this work.

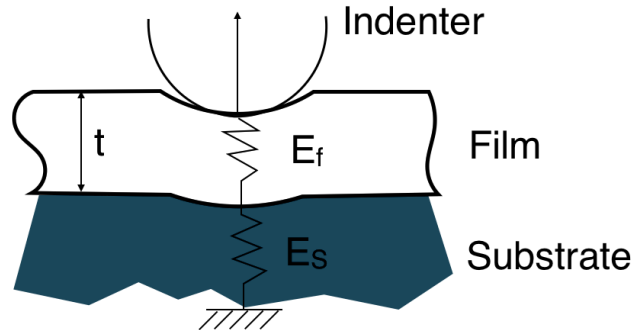


Figure I-23. Schematic representation of the contribution of the Young's modulus of substrate (E_s) to the measured Young modulus of a film with a Young's modulus of E_f by nanoindentation test.⁹⁴ (t is the film thickness)

Similar substrate effect has been observed by Wang et al.⁹⁹ who studied thickness dependence of elastic modulus and hardness of ultrathin polytetrafluoroethylene films of various thickness from about 50 nm up to 1 μm . They found that the mechanical properties became thickness independent when the film was thicker than 500 nm, where there is no more or negligible substrate effect.

Therefore, in order to avoid the unintentional influence of the substrate and to obtain real mechanical properties of thin films by nanoindentation tests, films of at least 500 nm should be prepared in order to eliminate the substrate effect. Considering that maximum depth of penetration in a nanoindentation test should be restricted to no more than 10% of the film thickness,⁹⁴ and that at least 100 nm of penetration depth is required for eliminating tip defect, films thicker than 2 μm were constructed for all the indentation tests in the present work so as to make sure that the measured values of mechanical properties of the LbL-assembled films are not subject to the influence of either the substrate or the tip defect.

Additionally, nanoindentation tests can be also used to quantitatively determine the viscoelastic properties of materials.⁹⁴ A small oscillatory force or displacement is

imparted to the indenter. The phase shift (δ) between the resulting load and displacement sinusoidal curves can be obtained, which can be used to study the viscoelastic properties of the materials.

Summary

In summary, tensile tests and nanoindentation tests are the two suitable and complementary methods for investigating the mechanical properties of LbL-assembled films. Using these methods, the reinforcement of mechanical properties by incorporation of nanofibers such as CNTs or CNFs was studied in this thesis. This verified the role as mechanical reinforcement agents of these nanofibers in addition to their role of improving membrane permeability of the LbL-assembly modified composite membranes via the three layers structure.

Prior to the discussion of the experimental results, the materials and methods used in the present work will be first addressed in the next chapter.

II. Materials and methods

II-A. *Materials*

II-A-1. **Polyelectrolytes**

Ultrapure water (will be called Milli-Q water for the rest of this thesis) with a resistivity of 18.2 M Ω .cm was obtained by purification with the Milli-Q Gradient System from Millipore (Molsheim, France). This ultrapure water was used directly after production.

Chitosan (\geq 75% deacetylated, No. 417963 from shrimp shells, practical grade, average M_w about 190-370kDa) was purchased from Sigma-Aldrich and was firstly dissolved in water at concentration of 1g/L with pH adjusted to 4 by adding drop by drop of 8% w/w acetic acid aqueous solution. The obtained solution is kept in a sealed beaker overnight under agitation at about 300Rpm before being filtrated with cotton (Laboratoires Euromedic, France). To get Chitosan solution of pH 6, the filtrated solution's pH is adjusted by titrating with 1% w/v NaOH solution. The ionic strength of the solution is modified by adding 0.25M of NaCl before the adjustment of pH.

Poly(vinyl amine) (trade name LUPAMIN 9095, PVAm, 20% in water, average M_w about 340,000 g/mol, more than 90% hydrolysed) was freely supplied by BASF. PVAm was diluted into Milli-Q water to obtain a solution with concentration of 1 g/L. The ionic strength of the solution is changed by adding certain amount of NaCl.

Poly(dimethyldiallylammonium chloride) (PDADMAC 20% in water, average M_w about 100,000-200,000 g/mol) and Poly(sodium 4-styrenesulfonate) (PSS powder, average M_w about 70,000 g/mol) were purchased from Sigma-Aldrich and were diluted in Milli-Q water to obtain solutions at 1g/L. The ionic strength of the solutions were changed by adding certain amount of NaCl.

II-A-2. Nanofibers suspension

II-A-2.1. Carbon nanotubes (CNTs)

Purified single wall carbon nanotubes designated P2-CNTs and P3-CNTs were purchased from Carbon Solution, Inc. All the carbon nanotubes bought from Carbon Solution, Inc were synthesized using the electric arc discharge method with nickel/yttrium catalyst. The P2-CNTs have >90% of carbonaceous purity and has been purified by air oxidation and subsequently treated to remove the catalyst. The P2-CNTs are closely approximates the pristine state of carbon nanotubes and have very low functionality, while the P3-CNTs have 1-3 atomic% carboxylic acid functional groups. To prepare stable CNTs dispersion in water, PSS was used as dispersing agents.¹⁰⁰⁻¹⁰² 20 mg of CNTs were pre-dispersed into 10 mL aqueous solution of PSS with a concentration of 0.4% with the help of a bath sonicator (Figure II-1 a), which was followed by ultrasonication for 2 hours at amplitude of 20% with a tip sonicator (Vibra cell 75042 from Bioblock Scientific, illkirch, France). After the ultrasonication, a highly homogeneous suspension of the PSS wrapped CNTs in water was obtained and can be kept stable in ambient environment for at least three months. AFM image of the obtained PSS wrapped P3-CNTs suspensions dropped onto a Si-wafer (Figure II-1 c) shows individually separated PSS wrapped P3-CNTs, which proves successful dispersion of the CNTs in water.

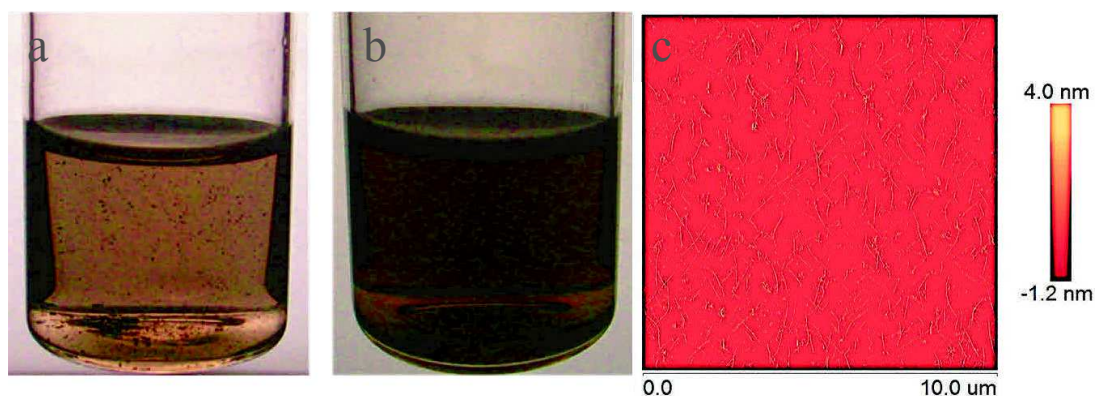


Figure II-1. a) A pre-dispersive PSS wrapped P3-CNTs in water before tip sonication; b) a homogeneous suspension of P3-CNTs in water after tip sonication; c) AFM image of the P3-CNTs suspension after being dropped on to a Si-wafer.

II-A-2.2. Cellulose nanofibrils (CNFs)

Carboxylated Cellulose nanofibrils (CNFs also referred to as Microfibrillated cellulose MFC) were given as gift by Innventia AB (Stockholm, Sweden) as a pulp containing about 2.5% fibers in water. These CNFs of 1-2 micrometers long and 5-20 nm in diameter have the appearance of a highly viscous and shear-thinning transparent gel (Figure II-2). They were produced as described previously by professor Wagberg,^{16,103,104} which consisted in a step of carboxymethylation with monochloroacetic acid followed by a conversion of carboxyl groups into sodium form with NaHCO_3 before being homogenized using a high-pressure microfluidizer.

The as-received pulp (never-dry) state CNFs were firstly dispersed in Milli-Q water to obtain a suspension at 2 g/L before put into a tip sonicator (Vibra cell 75042 from Bioblock Scientific, Illkirch, France) for one hour of sonication at 20% of amplitude. After sonication, the suspension was then centrifuged for 3 hours at 5,000 Rpm (centrifuge 4K10 with rotor Nr 12254 from Sigma, Lyon, France). The resulting supernatant was carefully decanted and used for LbL-assembly after filtration with cotton wool (Laboratoires Euromedic, France). Typical transparent CNFs solution's concentration was in the range of 0.9 g/L as determined from dry mass measurements (Figure II-2 b). TEM image shows individually dispersed single cellulose nanofibril indicating successful dispersion of the CNFs in water (Figure II-2c).



Figure II-2. A) Photograph of the viscous and transparent gel pulp formed by the cellulose nanofibrils (images credited to Dr. Rémi Merindol); B) transparent solution of CNFs obtained after the ultrasonication, centrifugation and filtration;¹⁰³ C) TEM image of the CNFs solution described in B, the scale bar is 500 nm.¹⁰³

II-A-3. Surface preparation

II-A-3.1. Hydrophilic surface preparation

Si-wafer was purchased from Wafernet, Inc., San Jose, CA. The cut Si-wafer slides were cleaned using ethanol and then Milli-Q water both for 10 min in a ultrasound bath. After the ultrasound bath cleaning, the slides were dried using compressed air flow and then activated for 3 min in a Plasma Cleaner (Harrick Plasma, Ithaca, NY) at medium intensity.

The QCM-d sensors were rinsed with Milli-Q water and then dried with compressed air before activated with UV-Ozone for 15 min in UV-Ozone cleaner (UV/Ozone ProCleaner BioForce Nanoscience, Inc., Ames, IA).

II-A-3.2. Hydrophobic surface preparation

The activated Si-wafer was dipped in a freshly prepared solution of Octadecyltrichlorosilane (OCS $\geq 90\%$ assay, Aldrich) in toluene at 0.1% for one hour. Then the modified substrates were rinsed successively with toluene, ethanol and Milli-Q water before rubbed with dust free cloth (Ko-ton, Chicopee Europe, AA Cuijk, The Netherlands). Typical thickness of the OCS layer was about 2.4 nm according to ellipsometry measurement, which corresponded well to the theoretical thickness of a monolayer of OCS.¹⁰⁵ Typical hydrophobic surfaces with contact angle of 105° were obtained (**Figure II-3**).

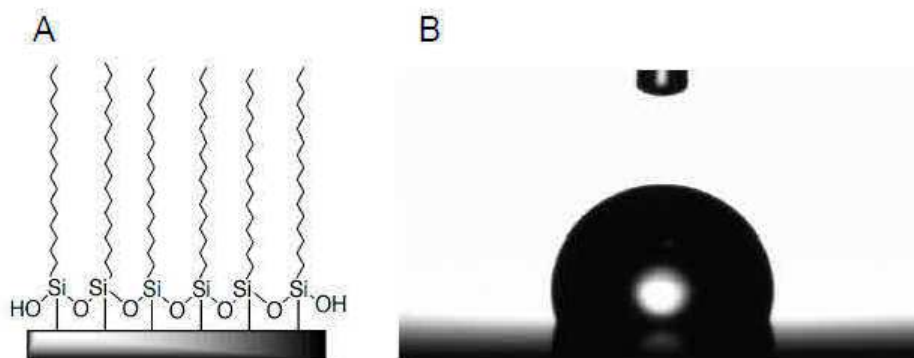


Figure II-3. A) Schematic representation of an octadecyltrichlorosilane coated Si-wafer; B) photograph of a water droplet on the modified Si-wafer surface during contact angle measurements (observed contact angle of 105°).

II-A-3.3. Membrane-like surface preparation

Raw membrane polymer sulfonated Polyethersulfone (SPES) was dissolved in organic solvent DMSO at a concentration of 10wt% and then was spin-casted on Si-wafer with a speed of rotation at 3000 Rpm and acceleration speed of 1500 Rpm/min. Two different types of SPES films, of which their thickness are around 90nm and 200 nm respectively were prepared using or not the ventilation. To get rid of the residual solvent in the SPES film, the films were baked in the oven at 120°C for at least 24 hours.

II-A-4. Freestanding films preparation

It has been shown that the hydrophilic LbL-assembled thick films can be easily delaminated from the hydrophobic surface of octadecyltrichlorosilane coated Si-wafer.^{16,87} For preparing freestanding films, micron thick LbL-assembled films were first constructed on octadecyltrichlorosilane coated hydrophobic Si-wafer with the help of an automated dipping robot as shown in Figure II-4 below.

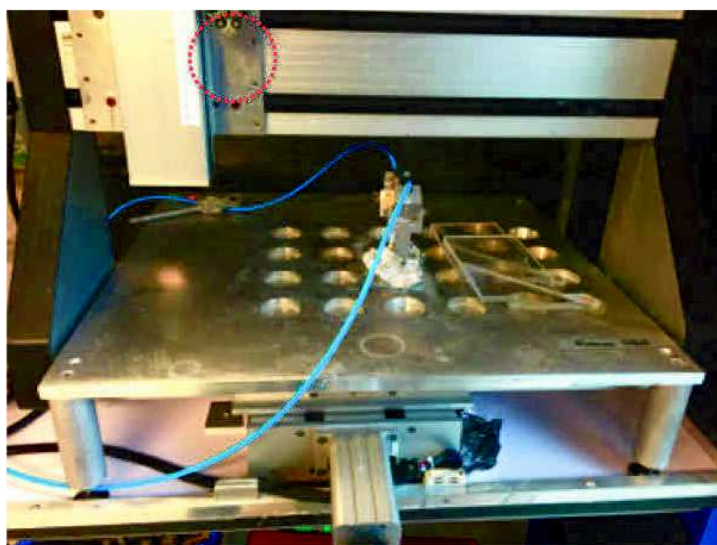


Figure II-4. Programmable automated dipping robot that is used for constructing thick films. (Solutions and rinsing water for the LbL-assembly will be placed in the concave slots arrays; the blue tube brings compressed air to the air blade for drying the films; Silicon wafer substrate is fixed with the help of a metal clip labeled in red dotted circle.)

A homemade LabVIEW[®] application was used to control the dipping robot. With this application, the sample immersion time and speed, dipping, rinsing and drying time as

well as their deposition sequences can be adjusted and programmed. Typical dipping time was set at 3 min. Each dipping step of polyelectrolytes (or nanofibrils dispersions) was followed by three consecutive rinsing step of 1 min with water. As we can see in Figure II-5A, a homogeneous film was successfully assembled on the hydrophobic Si-wafer with a size of about 2-3 cm wide and 8-10 cm long. Figure II-5B shows a piece of freestanding film being peeled off from the surface with a plastic tweezer.

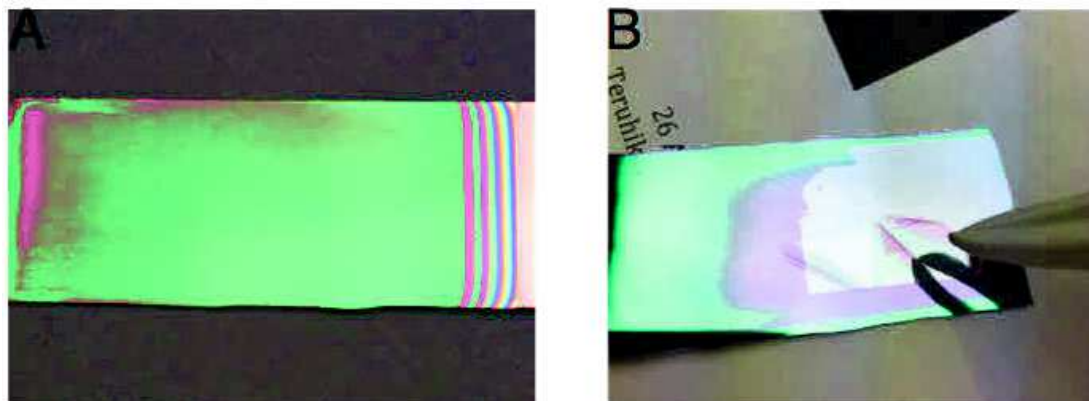


Figure II-5. A) Photograph of LbL-assembled film (Chitosan/CNFs)₁₅₀ having a thickness of about 1.05 μm (the rainbow on the right is due to the evaporation of the solution during assembly; B) another film of (Chitosan/CNFs)₁₅₀ being peeled off with a plastic tweezer.

II-A-5. Membrane preparation

Phase inversion or phase separation is among the principal and most versatile methods for preparing polymeric membranes, which is based on the existence of a miscibility gap in the phase diagram. Within the miscibility gap, the polymer/solvent system is no longer stable, and phase separation, mainly consisting of liquid–liquid demixing, takes place and leads to a cellular structure with pore formation deriving from the polymer-poor phase surrounded by the membrane structure formed from the polymer-rich phase. There are four main different techniques for the preparation of polymer membranes by phase inversion/separation originating from different desolvation mechanism^{53,106–111}:

- Thermally induced phase separation (TIPS). This method is based on the phenomenon that the solvent quality usually decreases when the temperature is decreased. After demixing is induced, the solvent is removed by extraction, evaporation or freeze-drying.

- Air-casting of a polymer solution. In this process, the polymer is dissolved in a mixture of a volatile solvent and a less volatile non-solvent. During the evaporation of the solvent, the solubility of the polymer decreases, and then phase separation can take place.

- Precipitation from the vapor phase. During this process, phase separation of the polymer solution is induced by penetration of non-solvent vapor in the solution.

- Immersion precipitation also called non-solvent induced phase separation (NIPS). A polymer solution is cast as a thin film on a support (flat sheet) or extruded through a die (hollow fiber), and is subsequently immersed in a non-solvent bath. Precipitation can occur because the good solvent in the polymer solution is exchanged for non-solvent (Figure II-6).

Most of the commercially available membranes are prepared by non-solvent induced phase separation (NIPS) method, as it offers simplicity and flexibility to scale-up the membrane manufacture in addition to its well developed and optimized polymer dope chemistry and fabrication parameters.

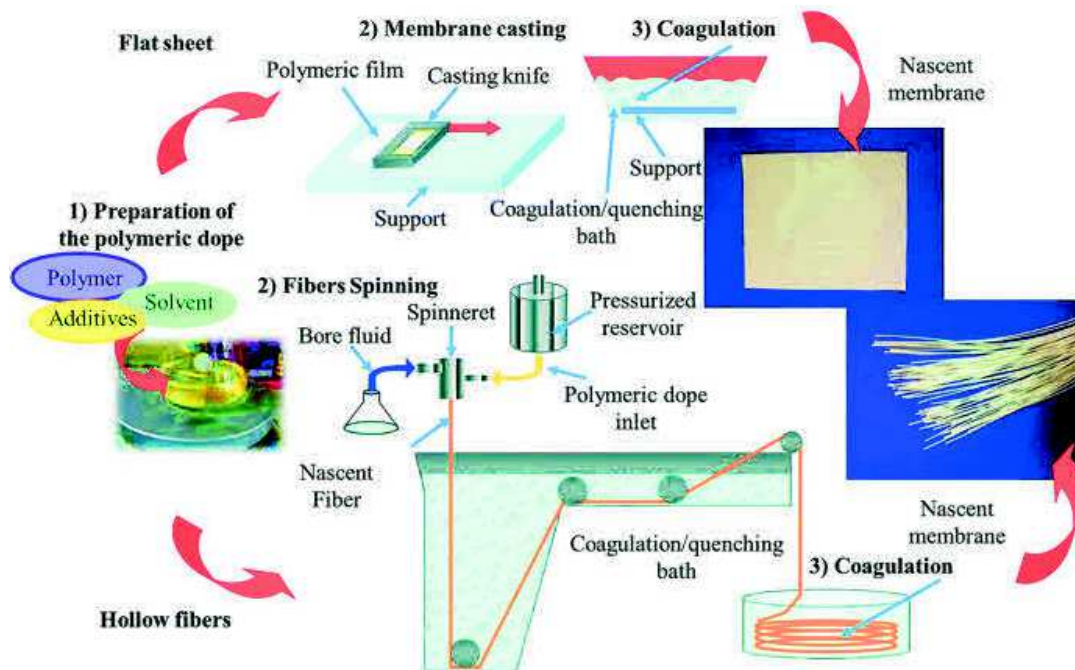


Figure II-6. Schematic representation of flat sheet and hollow fiber membranes produced by NIPS.¹¹²

The flat sheet and hollow fiber membranes made of polyether sulfone (PES) and sulfonated polyether sulfone (SPES) are produced by NIPS and provided by project partner. A hollow-fiber membrane is a capillary having an inside diameter of $>25\ \mu\text{m}$ and an outside diameter $<1\ \text{mm}$ and whose wall functions as a semipermeable membrane. The fibers can be employed singly or grouped into a bundle that may contain tens of thousands of fibers and up to several million fibers as in reverse osmosis (Figure II-7). In most cases, hollow-fibers are used as cylindrical membranes that permit selective exchange of materials across their walls.

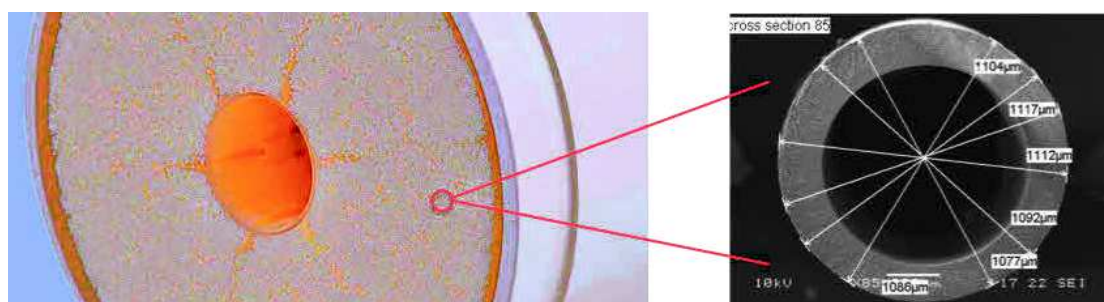


Figure II-7. a) Photograph of a eight inches membrane cartridge filled with thousands of hollow fiber membranes; b) a close-up SEM image of the single hollow fiber membrane shows an average outer diameter of $1100\ \mu\text{m}$ and an average wall thickness of $150\ \mu\text{m}$ (images from project partner).

Compared to the flat-sheet membrane, hollow-fiber configuration has the following advantages: (1) a much larger membrane area per unit volume of membrane module and, hence, resulting in a higher productivity; (2) self-mechanical support that can be back flushed for liquid separation; and (3) good flexibility and easy handling during module fabrication, membrane repair, and system operation.¹¹³

Hollow fiber membranes (Figure II-8b) designated HFs were used for LbL-assembled coating and their membrane performance including the retention of salts (NaCl , MgSO_4) and water permeability were characterized.

Flat sheet membranes (Figure II-8a), owing to their large flat surface and ease of characterization by traditional methods such as AFM, contact angle measurements and UV-Vis reflection spectroscopy, were used mainly for the physic-chemical characterization of the LbL-assembled film's growth on the membranes in addition to the characterization of the membranes themselves.



Figure II-8. a) Photograph of a typical flat sheet membrane made by non-solvent induced phase separation (NIPS); b) photograph of hollow fiber membranes HF from project partner.

II-A-5.1. Single fiber module preparation

Preparing materials:

- 1 x Festo T junction
- 2 x plastic tubes with a diameter of 8 mm
- Membranes
- 2-component glue (Araldite[®] Multi prise usages rapide)
- syringe
- nippers

Module preparation:



Figure II-9. a) Photograph of a t-junction and two 8 mm tubes; b) photograph of the two tubes connected by the t-junction; c) photograph of a single hollow fiber membrane inserted into the two tubes connected by t-junction (images taken by project partner).

1. First the two 8 mm tubes have to be connected with the t-junction (Figure II-9a, b);

2. Then the membrane is inserted into the tubing. The membrane has to stick out the tubing for a few centimeters ((Figure II-9c);
3. Now the membrane has to be potted into the module. This is done with a 2-component glue from Araldite[®] (Multi prise usages rapide). The glue is prepared in a plastic cup and the two components are mixed at the ratio of 1:1. Approximately 2 grams of glue is needed per module. After mixing the two components the resin stays workable for about half an hour.
4. After mixing the two components together, the glue can be filled in a syringe (25 ml). Pay attention that no air is in the syringe after filling.
5. With the syringe the glue can be filled about 2 cm in the module to glue the membrane. Let the resin harden for 24 h. After 24 h of hardening the modules can be cut off and the modules are ready for use.
6. The membrane should be placed in the middle of the potting (Figure II-10).

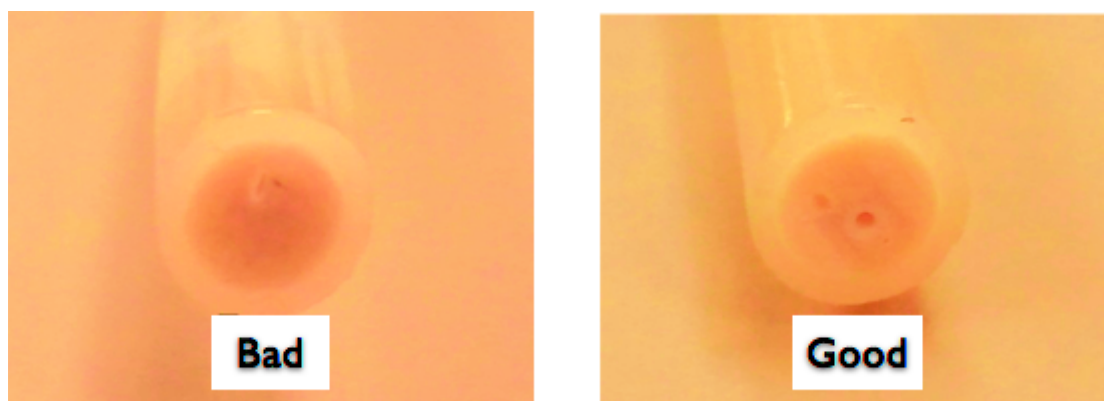


Figure II-10. Photograph of a glued module with a) the hollow fiber not in the middle and b) the hollow fiber well placed in the middle of the module (images taken by project partner).

II-A-5.2. Membrane conditioning

For the reason that membranes from Project partner have to be stored in an aqueous solution containing glycerin and sodium metabisulfite, they have to be conditioned before being used for LbL-assembled coating.

The conditioning of HF's membranes is performed with a mixture of 18wt% ethanol in water. The membranes/modules have to be soaked for 5 hours in a closed vessel/container.

II-A-6. LbL-assembly

II-A-6.1. Dipping LbL-assembly

The process of dipping LbL-assembly is illustrated in Figure II-11. All the dipping experiments (including the preparation of micron thick freestanding films using dipping robot) had immersing time of polyelectrolytes and/or nanofibers for 3 min followed by three times of water rinsing of 1 min, unless specified otherwise. After rinsing, the samples are submitted for a drying step in order to remove excess water.

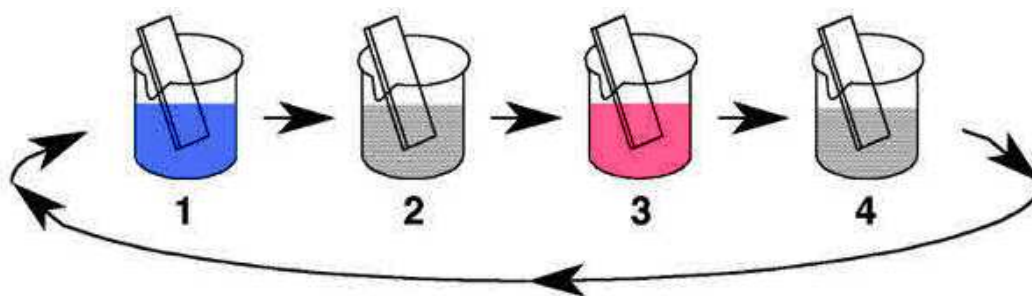


Figure II-11. Illustration of different steps of the dipping LbL-assembly method. Step 1: dipping of polyelectrolytes; Step 2: rinsing with water; Step 3: dipping of another oppositely charged polyelectrolytes; Step 4: rinsing with water. Steps 1,2,3,4 constitute one circle of dipping process, which can be repeated multiple times as demanded.

II-A-6.2. Spin-assisted LbL-assembly

Spin-assisted LbL-assembly process is illustrated in Figure II-11. A spin coater (model WS-50H7-8NPP/A8/AR, Laurell Technology Corporation, North Wales, PA) was used for the spin-assisted LbL-assembly. Each cycle of deposition consists in four steps. Step 1 and 3 concern the deposition of typically ten drops (about 0.3 mL) of polyelectrolytes or nanofibers suspensions during rotating. The substrate was immediately rinsed with about 1 mL of Milli-Q water and left rotating until dry before repeating the next deposition of polyelectrolytes or nanofibers suspensions. The rotation speed was defined kept constant during the entire build-up.

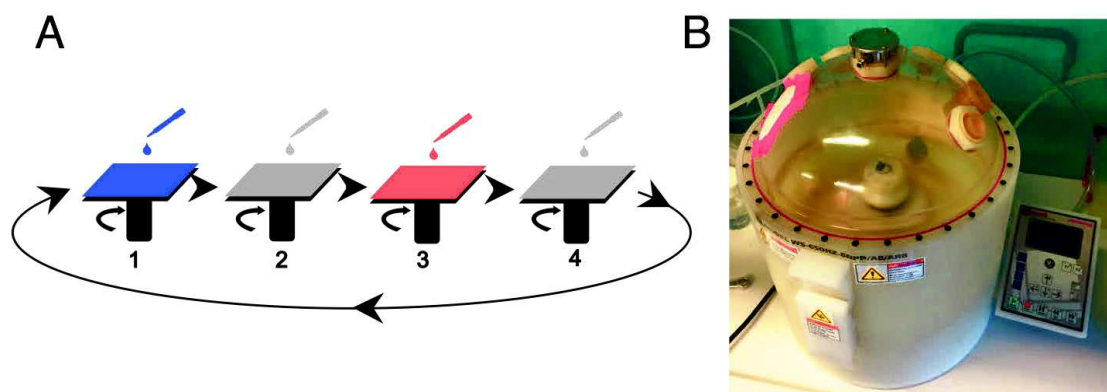


Figure II-12. A) Illustration of different steps of the dipping LbL-assembly method. Step 1: spin-coating of polyelectrolytes; Step 2: rinsing with water; Step 3: spin-coating of another oppositely charged polyelectrolytes; Step 4: rinsing with water. Steps 1,2,3,4 constitute one circle of spin-coating process, which can be repeated multiple times as demanded; B) Optical graph of the spin coater used for LbL-assembly. The substrate is fixed on the little round plate in the device. Solutions can be dropped on the rotating substrate with a pipette through a hole in the cap of the device.

II-A-6.3. Spray-assisted LbL-assembly

Spray-assisted LbL-assembly was carried out using AIR-BOY spraying bottles (Figure II-12). Similar to the spin-assisted LbL-assembly, each cycle of the assembly consists in four steps. Typically, ten seconds of spraying of the polyelectrolytes or nanofibers suspensions was performed onto a vertically fixed substrate, which was followed immediately with another ten seconds of rinsing with Milli-Q water. Drying with compressed air took place after each rinsing step.

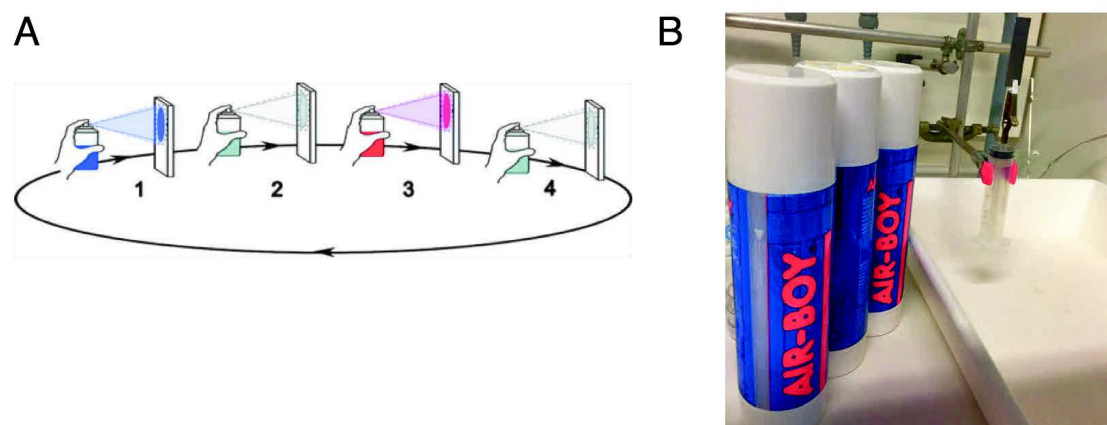


Figure II-13. a) Illustration of different steps of the spray-assisted LbL-assembly method. Step 1: spraying of polyelectrolytes; Step 2: rinsing with water; Step 3: spraying of another

oppositely charged polyelectrolytes; Step 4: rinsing with water. Steps 1,2,3,4 constitute one circle of spin-coating process, which can be repeated multiple times as demanded; b) Spray-assisted LbL-assembly setup. On the right a fixed substrate on which the films shall be assembled. On the left three “AIR-BOY” spraying devices with which the polymer solutions and the rinsing water can be sprayed on the substrate.

II-A-6.4. Grazing-incidence spray-assisted LbL-assembly

Compared with classical orthogonal spraying method (Figure II-14a), the technique called “Grazing Incidence Spraying” and initially developed by R. Blell, has a different incident angle (Figure II-14b). Grazing Incidence Spraying involves a spray jet of which the axis is almost parallel to the receiving surface inducing a liquid shear in the direction of the spray away from the nozzle. A customized robot in the team of Prof. G. Decher was mainly used to form oriented multilayered films. This air-assisted robot could yield a jet of solution accelerated by a jet of high airflow rate. Both the flow rate of the solution and that of air are programmable. All the films are prepared with spraying time of 10 sec followed by 10 sec of rinsing with Milli-Q water, unless specified elsewhere. Drying with compressed air was operated after every step of rinsing. Such system was used for constructing LbL-assembled films of aligned carbon nanotubes.

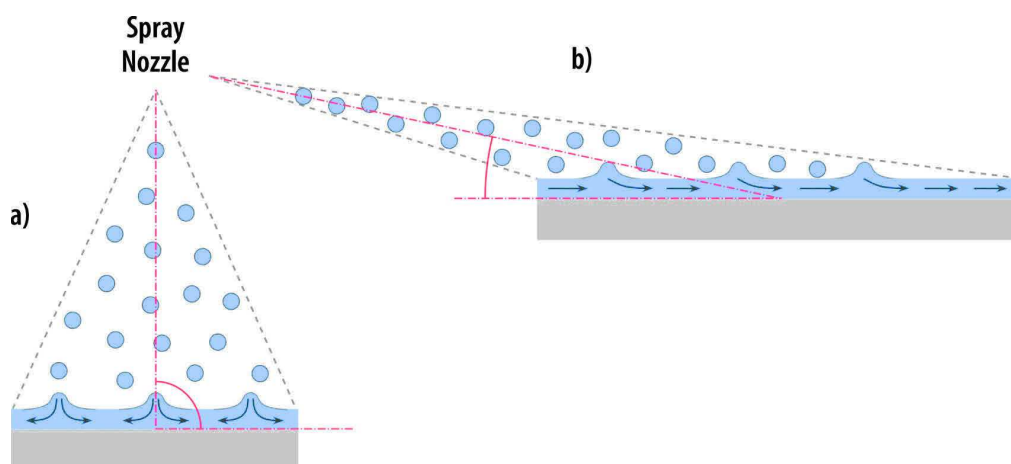


Figure II-14. a) Classic Orthogonal Spraying: the axis of the spray jet is parallel to the layer normal and the spray droplets arriving on the receiving surface do not cause a directional shear in the liquid; b) Grazing Incidence Spraying: the axis of the spray jet is almost parallel to the receiving surface and a liquid shear in the direction of the spray away from the nozzle

is induced.

II-A-7. Membrane coating by LbL-assembly

II-A-7.1. Flat sheet membrane coating

Layer-by-layer multilayer coating films have been assembled on flat sheet membranes HF with the help of a spin coater (model WS-50H7-8NPP/A8/AR, Laurell Technology Corporation North Wales, PA). Flat sheet membrane HF was cut into a square of $3 \times 3 \text{ cm}^2$ after being conditioned and then placed on the sample holder in the middle of the spin coater with its smooth separation layer side on top for the LbL assembly. The rotating speed was defined and kept constant at 300 rpm. Typically ten drops (about 0.3ml) of a given polyelectrolyte solution were deposited with a pipette on the center of a rotating membrane before the membrane was kept rotating for one minute. After each coating step of polyelectrolytes, the membrane was rinsed thoroughly with 20 drops of Milli-Q water in order to remove excess polyelectrolytes.

II-A-7.2. Hollow fiber membrane coating

The LbL-assembly on hollow fiber membranes was carried out by using a peristaltic pump system (model XX8000000, Millipore®) as shown in Figure II-15a.

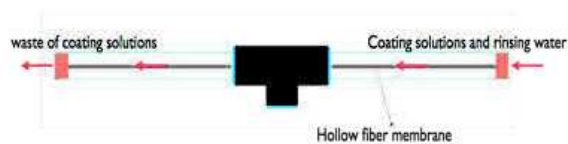


Figure II-15. a) Photograph of a single hollow fiber membrane module connected by a peristaltic tubing that is installed on a peristaltic pump; b) schematic representation of a single hollow fiber membrane module marked with red arrows indicating the flow direction of the coating/rinsing solutions.

As shown in Figure II-15b, a single fiber membrane module is placed horizontally and its right side was connected to the outlet of the peristaltic pump, while the inlet of the pump was immersed in a given polyelectrolyte solution and/or Milli-Q water for their injection to the membrane module. The pump rotation speed was set to 50 rpm and the flow in the tube was measured to be about 12 mL/min. 0.5 mL of polyelectrolyte solution was pumped into the membrane module for the static coating of the single fiber for fifteen minutes followed immediately by three times of pumping of Milli-Q water for the rinsing step where for each step 0.5mL of water is injected to the module and kept static for one minute.

Figure II-16 shows a cross section SEM image of a hollow fiber membrane HF with colored circles illustrating the cationic polyelectrolyte (blue) layer and the anionic polyelectrolyte (red) layer.

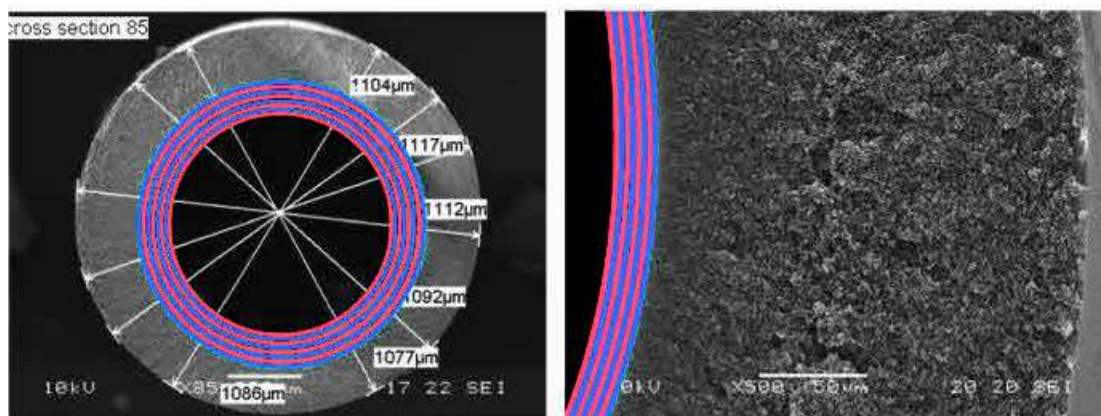


Figure II-16. a) A SEM image of a hollow fiber membrane HF with colored circles illustrating the cationic polyelectrolyte (blue) layer and the anionic polyelectrolyte (red) layer; b) a close-up of the SEM image in a. (The colored circles are only for better viewing and their thickness is not to scale)

II-B. Methods

II-B-1. Ellipsometry

II-B-1.1. Single wavelength ellipsometry

A single wavelength ellipsometry Plasmos SD 2100 was used for measuring the thickness of multilayered films. Plasmos SD 2100 was operated by setting the

incident light at a single wavelength of 632.8 and a constant angle of 45°. For simplicity, the refractive index of the film was fixed to $n = 1.465$ and the multilayer performed as a stack covering one layer of Silicon dioxide activated by plasma on the substrate of Si-wafer. 10 random points were measured for each sample to obtain an average film thickness and to determine the film homogeneity in a rough manner.

II-B-1.2. Spectroscopic ellipsometry

A spectroscopic ellipsometer SE800 from SENTECH in Germany was utilized later to get a more precise thickness of the films and their refractive index using software SENpro supplied by SENTECH. The ellipsometry technique measures changes in polarization of light upon reflection at an optical interface. The primary data obtained by ellipsometry are the ellipsometric angles ψ and Δ . They are related to the complex reflectance ratio through **Equation II-1**:

$$\tan\psi e^{i\Delta} = R_p/R_s \quad \text{Equation II-1}$$

where $\tan \psi$ corresponds to the amplitude ratio of the reflection in the direction parallel and perpendicular to the plane of incidence, and Δ corresponds to the phase difference between them.¹¹⁴

A four-layer model (silicon, silicone dioxide, multilayered polymer film, air) was employed in order to determine the thickness and the refractive index of the adsorbed film, assuming homogeneous layers. The software SENpro then calculated the thickness and refractive index of the multilayered polymer film on the basis of the obtained values of ψ and Δ .

II-B-2. UV-Vis spectroscopy

Ultraviolet–visible (UV-Vis) spectroscopy is a measurement of the attenuation of a beam of light after it passes through (absorption) or reflects from (reflection) a material. Ultraviolet and visible radiation of a single wavelength or over an extended spectral range interacts with the sample, which causes electronic transitions by promoting electrons from the ground state of highest occupied molecular orbital

(HOMO) to a higher energy state of lowest unoccupied molecular orbital (LUMO). Materials that can absorb UV-Vis light of wavelength typically from about 200 nm to 800 nm (this extends slightly into the near infra-red as well) include pi-electron functions and hetero atoms having non-bonding valence-shell electron pairs. Such light absorbing groups are referred to as chromophores.

II-B-2.1. UV-Vis spectroscopy in transmission

UV-Vis absorption spectroscope is the most common type of UV-Vis spectroscope. Figure II-17 shows a diagram of the components of a typical UV-Vis absorption spectroscope of double beams. A beam of light from UV and visible lamp sources is focused on to a gradually rotating diffraction grating that allows light of a very narrow range of wavelengths (single wavelength beam called monochromatic) in the whole spectrum of UV-Vis range through into the rest of the spectrometer. Each monochromatic beam is split into two equal intensity beams by a half-mirrored device, of which, one sample beam passes through a transparent sample (liquid or solid), and the other beam (reference beam) passes through a reference (solvent or quartz/glass slide). The detectors convert the incoming light into a current. The higher the current the greater the intensity of the light is. For each wavelength of light passing through the spectrometer, the intensity of the light passing through the reference is measured and is usually referred to as I_0 . The intensity of the light passing through the sample is also measured for that wavelength given the symbol I . If I is less than I_0 , then obviously the sample has absorbed some of the light.

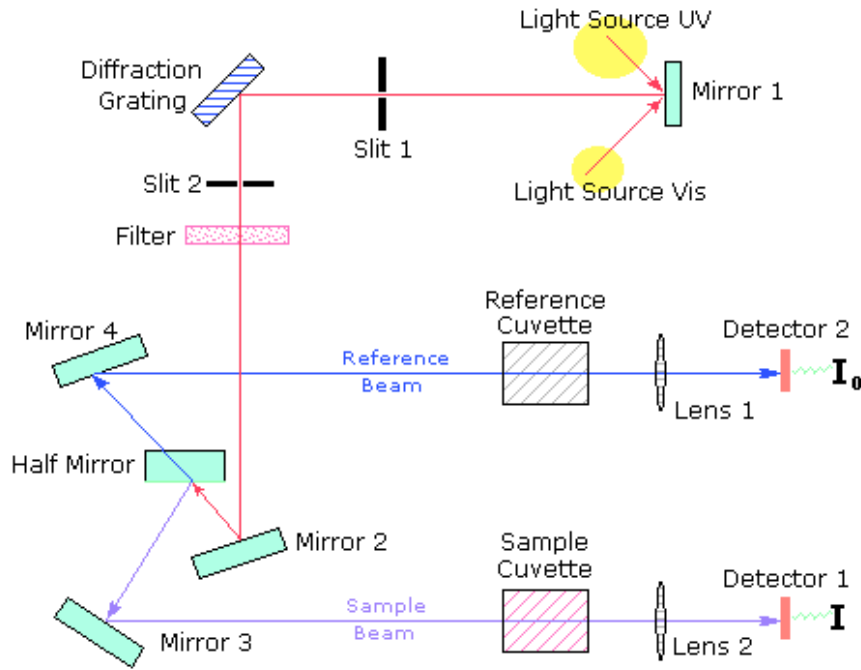


Figure II-17. Schematic representation of the components and principle of the UV-Vis spectroscopy with double beam.¹¹⁵

According to the Beer-Lamber law (**Equation II-2**):

$$A = -\log_{10}(I/I_0) = \varepsilon \cdot c \cdot L \quad \text{Equation II-2}$$

where A is absorbance, ε is a proportionality constant called absorptivity, c is sample concentration and L is the distance of light path through the sample (film's thickness for solid film samples), we assume the concentration of the chromophores in the film remains constant, thus the absorbance A is proportional to the film's thickness. By calculating the absorbance we thereby can quantify the film's thickness by UV-Vis absorption spectroscopy.

II-B-2.2. UV-Vis spectroscopy in reflection

As shown in Figure II-18, when incident light is excited onto non-homogeneous solid sample, it has two kinds of reflectance, specular and diffuse. Specular reflection refers to the part of the incident beam that is reflected in the direction of the same angle as that of incidence light. Diffuse reflection is the part of the reflected light in all directions.

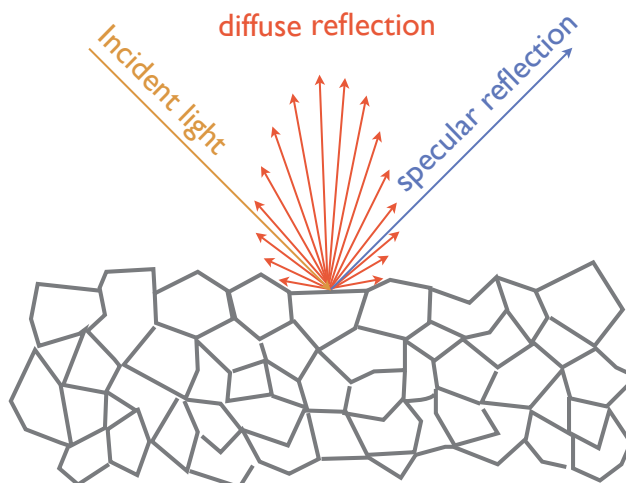


Figure II-18. Schematic representation of specular and diffuse reflection of incident light on non-homogeneous surface.

To collect all the reflected light including specular and diffused light, UV-Vis reflection spectroscope uses an accessory called integrating sphere. As we can see in Figure II-19 that an integrating sphere is actually a hollow sphere with internal chamber coated with white material of diffuse reflectance close to 1 usually made of barium sulfate (BaSO_4). Using this sphere, we can measure the reflectance R_∞ . According to Kubelka-Munk (K-M) function (**Equation II-3**):

$$F(R_\infty) = \frac{(1 - R_\infty)^2}{2R_\infty} = \frac{K}{S} \quad \text{Equation II-3}$$

where K and S stand for the absorption and scattering coefficient respectively. The K-M function $F(R_\infty)$ is proportional to and almost exclusively depends on the concentration of the colored chromophores. Usually S differs little among matrices of white with a low percentage of the colored materials. We can approximately quantify the concentration of chromophores contained on the sample's surface by applying the K-M function. Alternatively, we can simply convert the total reflectance (specular and diffuse reflectance) to absorbance using the equation: $\text{Log}1/R_\infty$, which is equivalent to absorbance A.

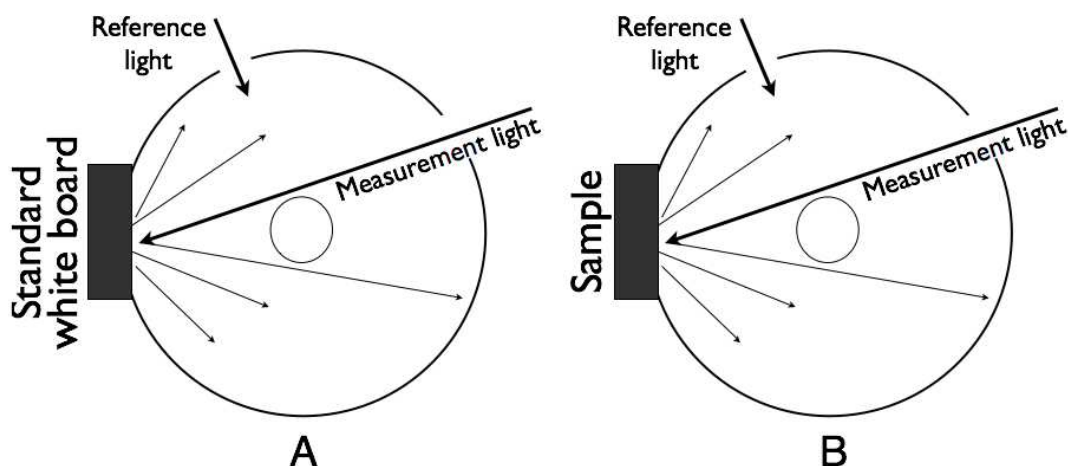


Figure II-19. Schematic representation of the integrating sphere of UV-Vis reflection spectroscope showing A) a standard white board of high diffuse reflection is placed on the sample holder for baseline measurement; B) a sample is placed on the holder and being measured with the measurement incident light on its surface.

II-B-3. Quartz Crystal Microbalance dissipation (QCM-d)

Quartz crystal microbalance (QCM) is a very powerful technique for studying molecular absorption/desorption and binding kinetics to different surfaces in a very precise way. This technique is based on piezoelectric effect in quartz crystals first discovered in 1880 by the Curie brothers. An alternating potential causes the crystal to oscillate owing to piezoelectric effect. With a properly cut crystal and an appropriate alternating potential, a standing shear wave is formed at the resonant frequency of quartz crystal, which can be used for the determination of a small resonant frequency shift when a small amount of matter (ng/cm^2) is placed on the quartz crystal surface. This technique was first used in a sensing application when Sauerbrey reported a linear relationship between the decrease of resonant frequency f of an oscillating quartz crystal and the bound elastic mass of adhering metal.^{116,117} By using the Sauerbrey equation (**Equation II-4**), we can precisely quantify, with nanogram sensitivity, the amount of elastic mass absorbed onto the electrode surface (Au):

$$\Delta f = -2\Delta m f^2 / A(\mu\rho_q)^{0.5} = -nC_f\Delta m \quad \text{Equation II-4}$$

Where Δf is the measured resonant frequency decrease (Hz), Δm is the elastic mass change (g), f is the intrinsic crystal frequency, A is the electrode area (0.79 cm² for Q-sense sensors), μ is the shear modulus, ρ_q is the density of quartz. n is the overtone, C_f is constant about $5.65 \cdot 10^{-2}$ Hz cm²/ng.

QCM-d, standing for quartz crystal microbalance with dissipation monitoring, was developed by Rodahl based on ring-down analysis rather than conventional impedance analysis.^{118,119} As shown in Figure II-20, the crystal was driven at its resonant frequency with an oscillator that can be intermittently disconnected causing the crystal oscillation amplitude to decay exponentially, from which the dissipation can be obtained, in addition to the frequency of the freely oscillating crystal, by calculating from the decay time constant.

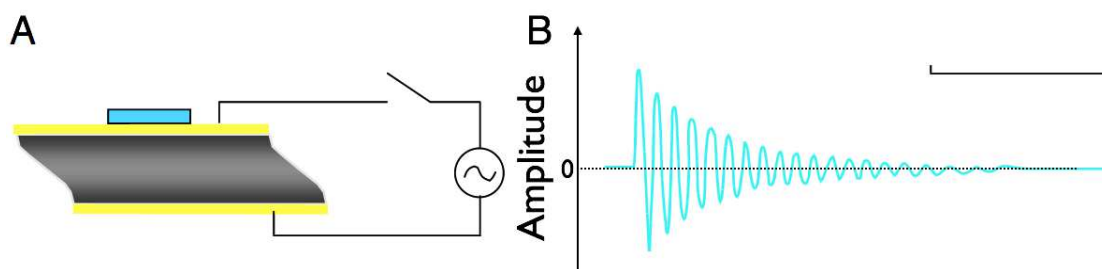


Figure II-20. A) Simplified schematic representation of the QCM-d electrical circuit; B) a typical decay curve of the QCM-d showing the exponential decrease of the amplitude over time of decay.¹¹⁸

For all the QCM-d measurements, a QCM-d E4 (Q-Sense AB, Göteborg, Sweden) was used. The overtone 5 was used for monitoring the frequency shifts. Typically 600 μ l of a given solution was injected with the help of a peristaltic pump at a flow speed of 600 μ l/min. Dipping and rinsing time was set at three and one minutes respectively where rinsing step was repeated for three times.

II-B-4. Microscopy

II-B-4.1. Atomic Force Microscopy (AFM)

To investigate electrically neutral materials, atomic force microscopy (AFM) was developed as an alternative of the scanning tunneling microscopy (STM) technique that was limited to imaging conductive samples because of the need to establish a tunneling current. After having invented STM in 1981 and earned the Nobel prize in physics together with Heinrich Rohrer in 1986, Gerd Binnig and his coworkers demonstrated for the first time the ideas of AFM. Since then it has drawn increasing attentions as an entirely new approach in the investigation of the surface topography especially for the non-conductive materials such as proteins or polymers.¹²⁰⁻¹²⁴

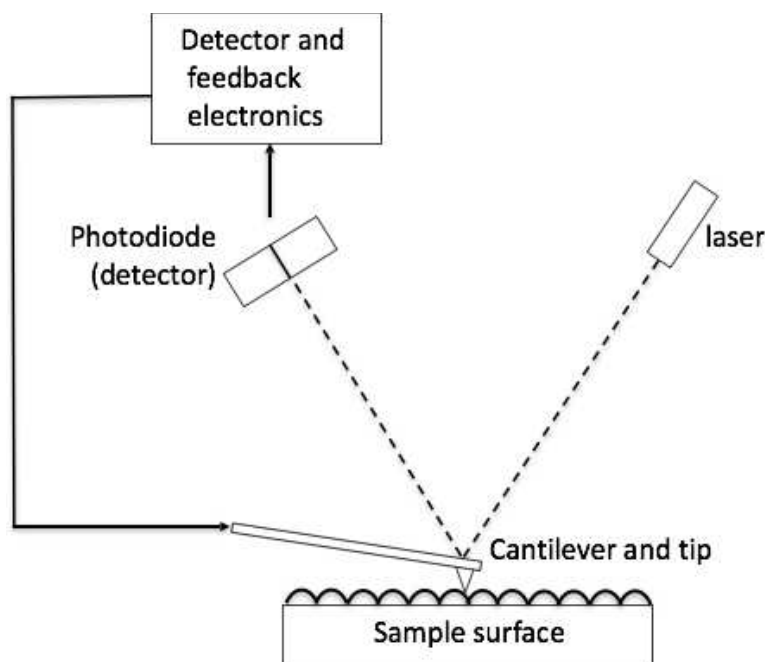


Figure II-21. Schematic representation of the principle of AFM.

As shown in Figure II-21, AFM images are obtained using a spring-like probe (tip) with a radius of curvature on the order of nanometers for monitoring the sample's surface by measuring the force between the tip and the surface. When the tip is brought into proximity of a sample surface, the interaction between the tip and the surface contributes to a deflection of the cantilever according to Hooke's law. Several interatomic forces act between the apex of the tip and atoms of the sample surface as the tip is scanned over the surface.¹²⁵ With the help of a piezoelectric scanner on

which the sample is mounted, the displacement of the sample surface can be precisely controlled in three dimensions. A laser beam is projected on the cantilever where the deflection owing to the tip deflection can be monitored by a position sensitive photoelectric detector.

Depending on the nature of the tip motion, AFM has two main basic operation modes. The first mode is the 'contact mode', where the tip almost touches the sample and interacts with the surface under a dominating repulsive force originating from the 'exchange interactions' due to the overlap of the electronic orbitals at atomic distances. The contact mode has several advantages including no problem with surface pollution (imaging in air and liquid is possible), highest resolution and fastest measurement of all the topographic modes. However it is not suitable for soft and delicate samples like polymers, because the tip could damage the sample or displace the soft part of the sample due to friction or adhesion between the tip and surface. Moreover, the AFM tip is very brittle and can be easily broken owing to the high contact pressure.

The second mode is the 'non-contact mode' that was first developed by Martin et al in 1987.¹²⁶ In non-contact mode, the tip oscillates at either its resonant frequency (frequency modulation) or just above (amplitude modulation) rather than contacts the sample surface. Opposite to the contact mode where repulsive force dominates, the non-contact mode measures surface topography by utilizing the attractive interatomic force between the tip and the sample surface. While the non-contact mode can avoid the frictional and adhesive forces that can damage samples and distort image data which is encountered in the contact mode, it can only provide low resolution owing to not sufficient high Z-servo performance that is required for tracking the changes caused by tip-sample interaction and can also be hampered by the contaminant layer of fluid covering most surfaces under ambient air conditions. In order to overcome these limitations, Zhong et al introduced a deliberate 'tapping mode', in which the tip alternately contacts with the surface to provide high resolution and then is lifted off the surface to avoid being dragged across the surface.¹²⁷ Unlike contact and non-contact mode, when the tip contacts the surface, it has sufficient oscillation amplitude to overcome the tip-sample adhesion force and also the surface material is not pulled sideways by shear force since the applied force is mainly vertical.

The AFM images presented in this thesis were performed in tapping mode on an AFM Multimode from Bruker Nano Surface (Palaiseau, France) with the controller Nanoscope IV from Veeco (Mannheim, Germany) and non-coated silicon cantilevers (resonance frequency 300 kHz, resonance constant of 40 N/m, and radius below 10 nm). Phase and height modes were recorded simultaneously using a constant scan rate of 1.3 Hz with a resolution of 512 x 512 pixels. The samples were fixed on metallic supports with either cyanoacrylate glue for large samples or microscopy tape for small substrates.

II-B-4.2. Transmission Electronic Microscopy (TEM)

The transmission electron microscope (TEM) is a very powerful technique that is first developed by Ernst Ruska and Max Knolls in 1931. It operates on the same basic principles as the light microscope except that it uses electrons instead of optical light and electromagnetic lenses instead of glass lenses. With a maximum potential magnification of one nanometer owing to the small de Broglie wavelength of electrons, TEM is the most powerful microscope and has a wide range of applications in different fields (life science, nanotechnology, medical, material science...). A TEM produces a high-resolution, black and white image from the interaction that takes place between a thin sample and energetic electrons in a high vacuum chamber.

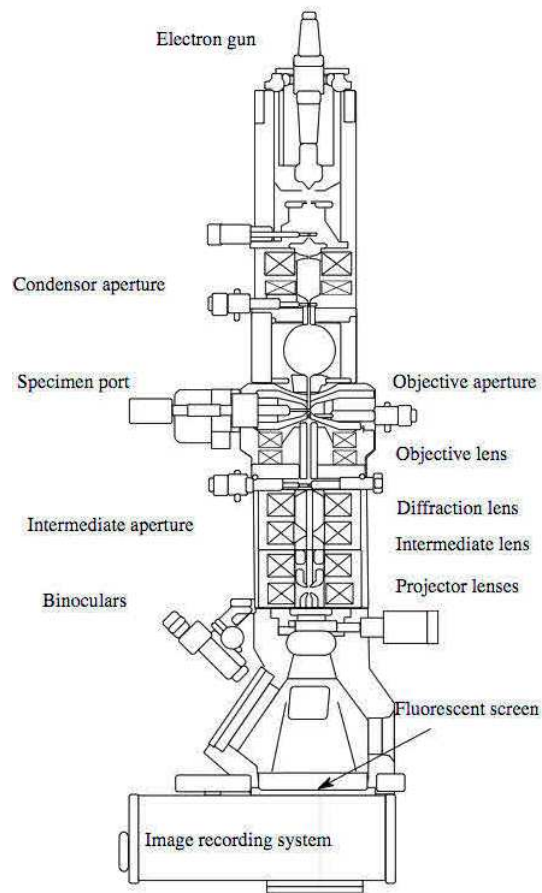


Figure II-22. Layout of optical components in a basic TEM.¹²⁸

As shown in Figure II-22, TEM consists of an emission source of electron gun that is connected to a high voltage source (typically 100-300 kV) and emits electrons either by thermionic or field electron emission into the vacuum, which then travels through the specimen. Depending on the density of the material present, some of the electrons are scattered and disappear from the beam. At the bottom of the microscope the unscattered electrons hit a fluorescent screen, which gives rise to a "shadow image" of the specimen with its different parts displayed in varied darkness according to their density. The image can be studied directly by the operator or photographed with a image recording system.

II-B-4.3. Scanning Electronic Microscopy (SEM)

A scanning electron microscope (SEM), like a transmission electron microscope, consists of an electron optical column, a vacuum system, electronics, and software.

The column is considerably shorter because the only lenses needed are those above the specimen used to focus the electrons into a fine spot ranging from approximately 5 microns to 1 cm on the specimen surface. The specimen chamber, however, is larger because the SEM technique does not impose any restriction on specimen size other than chamber size (Figure II-23).

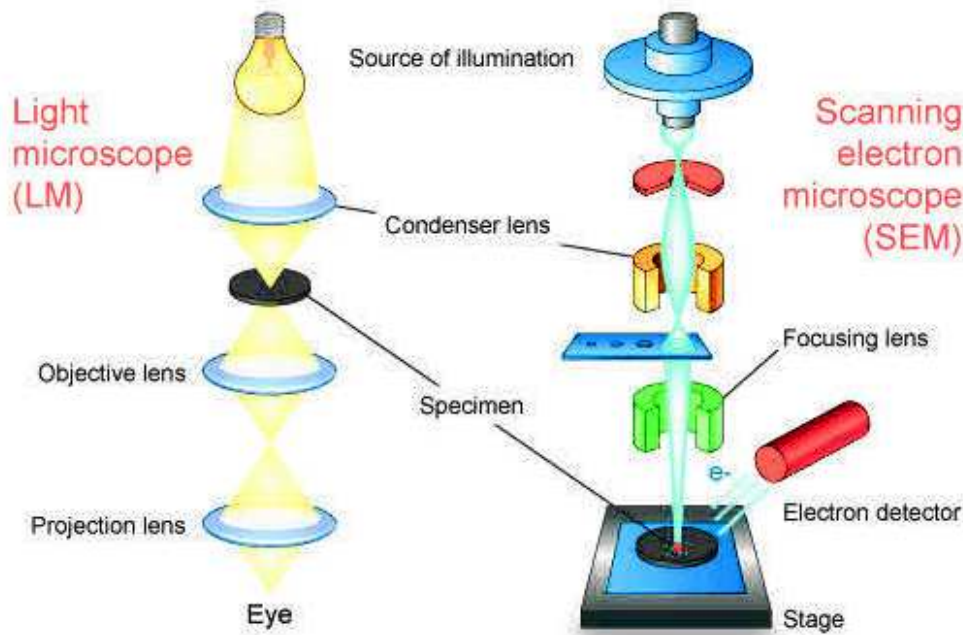


Figure II-23. Schematic representation of the main components of the typical SEM compared with that of light microscope (LM).¹²⁹

The electron gun at the top of the column produces an electron beam that is focused into a fine spot as small as 1 nm in diameter on the specimen surface. This beam is scanned in a rectangular raster over the specimen and the intensities of various signals created by interactions between the beam electrons and the specimen are measured and stored in computer memory. The stored values are then mapped as variations in brightness on the image display. The signals include secondary electrons (that produce SEM images), backscattered electrons, diffracted backscattered electrons that are used to determine crystal structures and orientations of minerals, photons (characteristic X-rays that are used for elemental analysis and continuum X-rays), visible light (cathodoluminescence—CL), and heat. Secondary electrons and backscattered electrons are commonly used for imaging samples: secondary electrons are most valuable for showing morphology and topography on samples and

backscattered electrons are most valuable for illustrating contrasts in composition in multiphase samples (i.e. for rapid phase discrimination). The ratio of the size of the displayed image to the size of the area scanned on the specimen gives the magnification.

II-B-4.4. Cross-polarized microscopy

The cross-polarized light microscope (cPIM) is designed to observe and photograph specimens that are visible primarily due to their optically anisotropic character. In order to accomplish this task, the microscope must be equipped with both a polarizer, positioned in the light path somewhere before the specimen, and an analyzer (a second polarizer), placed in the optical pathway between the objective rear aperture and the observation tubes or camera port.

Image contrast arises from the interaction of plane-polarized light with a birefringent (or doubly-refracting) specimen to produce two individual wave components that are each polarized in mutually perpendicular planes. The velocities of these components are different and vary with the propagation direction through the specimen. After exiting the specimen, the light components become out of phase with each other, but are recombined with constructive and destructive interference when they pass through the analyzer.

When an anisotropic specimen is brought into focus and rotated through 360 degrees on a circular polarized light microscope stage, it will sequentially appear bright and dark (extinct), depending upon the rotation position. When the specimen long axis is oriented at a 45-degree angle to the polarizer axis, the maximum degree of brightness will be achieved, and the greatest degree of extinction will be observed when the two axes coincide (Figure II-24). During rotation over a range of 360 degrees, specimen visibility will oscillate between bright and dark four times, in 90-degree increments. This is due to the fact that when polarized light impacts the birefringent specimen with a vibration direction parallel to the optical axis, the illumination vibrations will coincide with the principal axis of the specimen and it will appear isotropic (dark or extinct). If the specimen orientation is altered by 45 degrees, incident light rays will

be resolved by the specimen into ordinary and extraordinary components that are then united in the analyzer to yield interference patterns.

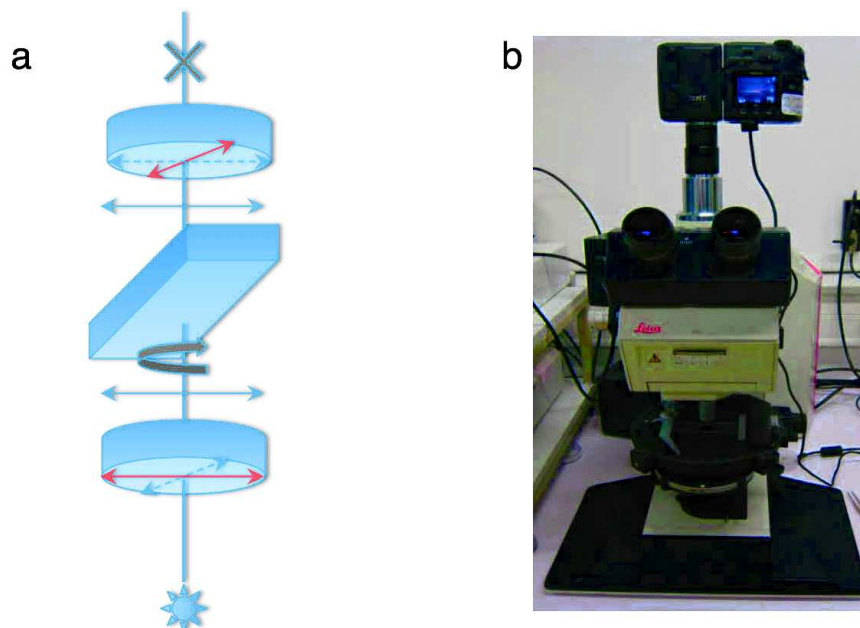


Figure II-24. a) Schematic representation of the light path in a cPIM showing a rotating sample placed between two polarizers of which the polarizer axis directions are perpendicular to each other; b) Photograph of the utilized cross-polarized microscope (image credited to M. Jonas Bär).

A digital camera was connected with cPIM for capturing pictures. The microscope was set up at reflection mode because of the opacity of the Si-wafer substrate used for building the films. The camera is operated at Manuel Mode with 1 second of exposure time and F3.1 of zooming. The pictures obtained were then transferred to a computer and treated with two software named GraphicConverter and ImageJ for acquiring the intensity of light reflected by the films. The arbitrary units for the intensity of birefringence were assigned from the grey values. The difference in the intensity of birefringence is obtained for that later use in comparing the degree of orientation of different sample or different point of the same sample by subtracting the intensity at the minimum from that at the maximum.

II-B-5. Membrane performance test

II-B-5.1. Membrane Retention/Permeability Measurement

5 mM aqueous solution of MgSO₄ was prepared and used as test solution for the retention and permeability measurements of the LbL-assembly modified nanofiltration membrane. Before starting the measurements, the active length (L) of the membrane was measured for calculating the membrane surface. Then the membrane was flushed for 60 minutes with the 5 mM solution before starting collecting the permeate (V in volume) and counting the collecting time (t). After having collected reasonable amounts of permeate, we measured the conductivity of the collected permeate solution (C_p) and also that of the feed solution (C_f). The feed pressure was recorded as P.

The retention R was calculated by the Equation I-3:

$$R = \left(1 - \frac{C_p}{C_f}\right) \times 100\%$$

And the permeability was obtained using the Equation I-1:

$$J = \frac{V}{A \times t}$$

where A is the active surface area of the membrane that is equal to the active length L multiplied by the perimeter of the membrane with a diameter of 0.8 mm.

To minimize concentration polarization and to achieve an optimum retention, a Reynolds number of >3500 was needed, which required a mass flow of > 6 kg/h per fiber on a 0,8 mm HFs. (12 kg/h per 2 fibers). Each sample was measured for three times. Figure II-25 is photograph of a typical set-up for the membrane retention and permeability tests.



Figure II-25. Photograph of a typical set-up for the membrane retention and permeability tests (image from project partner).

II-B-6. Mechanical test

II-B-6.1. Tensile test

In order to perform the tensile tests on LbL-assembled films, freestanding LbL-assembled films were prepared as described in II-A-4. . Micron thick LbL-assembled films were cut to a rectangular shape using a scalpel blade and then carefully peeled-off from the hydrophobic surface of Si-wafer. Typically rectangular stripes of films with 1.5 mm wide and 15 mm long were cut directly and then labeled with colored powder before put into a tensile test machine with the help of an U-shape paper consisting of a 25 x 20 mm piece of paper with a 5 x 10 mm gap in the middle (Figure II-26C). A load cell, connected in series with the specimen which is clamped at its other end, provides an electronic reading of the changing force that pulls the sample at a certain speed (Figure II-26B). All samples were equilibrated before test in a desiccator cabinet with freshly activated silica gel for at least 24 hours. Tensile tests run in dry conditions at relative humidity (RH) of <5% (below the detection limit of the humidity sensor) were carried out in a confined environment under a flow of dry filtered compressed air with an actual RH in the range of 2-3%. Tensile tests performed in ambient conditions were run with the sample chamber open and without the compressed air (typical RH ranges from 35% to 50%). The cross-sectional area of the film surface was calculated by multiplying the film's width by the film's thickness

which was obtained by AFM, SEM and/or spectroscopic ellipsometry. Then the stress can be obtained using Equation I-4. A camera was installed for capturing the movement of the film, according to which image correlation and then the real deformation of the sample (strain) could be calculated. Finally a stress-strain curve is obtained.

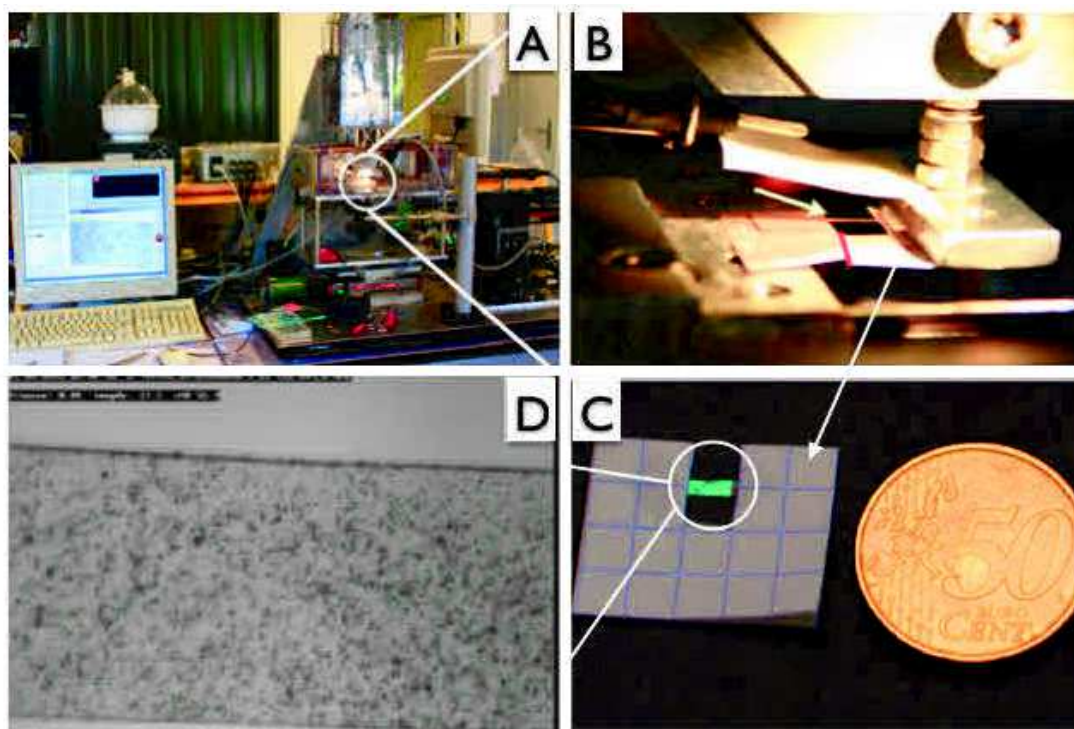


Figure II-26. A) Photograph of the experimental set-up of the tensile tests; B) Close-up image on the sample set-up; C) photograph of the sample with a piece of film taped onto a U-shaped paper support; D) typical powder patterns shaped on the film observed under the installed camera (image credited to Dr. Rémi Merindol).

II-B-6.2. Digital image correlation

Because of the compliance of the machine and deformation of the tape used to fix the sample, direct measurement of the true strain of the film by the machine was impossible.⁹³ In order to obtain the film's actual deformation in real time, a technique called digital image correlation was employed.^{130,131} This technique tracks the displacement of a random gray scale pattern on a sequence of images and a correlation algorithm is used to calculate the strain by derivation of the displacement.

A video camera of 0.5 Megapixel was installed to record the painted color powders on the film at a shutter speed of 6 frames per second with an image size of 1.86*1.40 mm. After each measurement, sequenced images were extracted from the recorded video with software called GraphicConverter®. Afterwards these grey-scaled images were imported into commercial digital image correlation software designated CORRELI^{STC}. Using CORRELI^{STC}, each image was subdivided into elements of more than 16 pixels (usually 32 pixels was chosen if the image quality is good enough) in order to reduce the mean displacement error and corresponding standard deviation. A cumulative strain map can be obtained by comparing each current deformation image with the initial image, while an incremental strain map can be computed by comparing the image at the current load step with the image recorded just before the current load increment (Figure II-27).

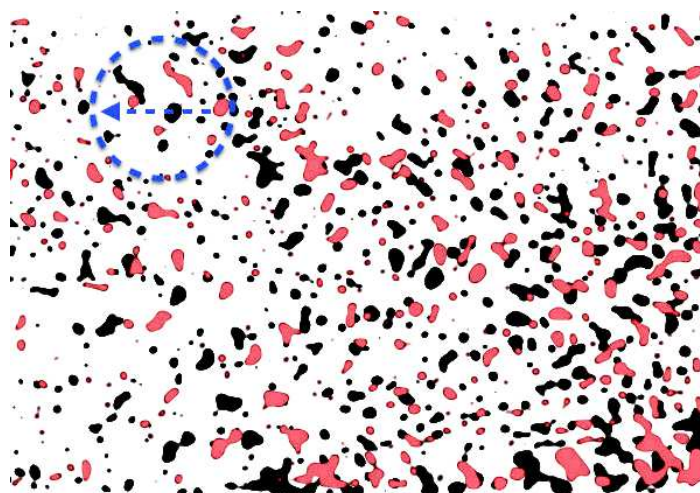


Figure II-27. Two images of a same painted sample of the film (CHI/CNFs)₁₅₀ recorded at two different stages (red and black) showing the displacement of the powders with the moving direction labeled with the blue dashed arrow.

II-B-6.3. Nanoindentation

II-B-6.3.1. Static nanoindentation tests

In order to eliminate substrate effect, micron-thick LbL-assembled films were constructed on silicon wafers and were tested in the platform of MINAMEC of Institut Charles Sadron using a nanoindenter machine from CSM-Instrument (Figure II-28). A three-sided pyramid shaped indenter (Berkovich) was used. For the nanoindentation tests under each relative humidity condition ranging from 5% to 72%, the film was first placed in a desiccator cabinet with freshly activated silica gel

for one week before being moved to the sealed nanoindentation machine chamber filled with nitrogen. A heating cycle was performed to eliminate any moisture absorption during the transportation of the films from desiccator to the machine chamber. To do so, the sample was slowly heated from ambient temperature of 25 °C to 100 °C for 1 hour and then kept at 100 °C for 30 min before being slowly cooled down back to 25 °C for 1 hour. Then, the relative humidity of the chamber was adjusted to the relevant testing value by introducing a controlled amount of water vapor. The film was kept under this testing relative humidity for at least 1 hour before the launching of nanoindentation tests.

The method of Oliver and Pharr⁹⁵ was used to determine the contact depth h_c by the following equation:

$$h_c = h_{\max} - \varepsilon \frac{P_{\max}}{S} \quad \text{Equation II-5}$$

where h_{\max} is the maximum penetration depth, ε is geometric constant of an indenter (0.75 for a Berkovich indenter) and S is the slope of load versus depth curve (dP/dh) during unloading.

The contact area A_c of the indenter and the sample is:

$$A_c = 24.5h_c^2 + \sum_{i=0}^7 C_i h_c^{1/2^i} \quad \text{Equation II-6}$$

Which can be used to calculate the hardness H and the reduced Young's modulus E_r :

$$H = \frac{P_{\max}}{A_c} \quad \text{Equation II-7}$$

$$E_r = \frac{\sqrt{\pi}}{2\beta} \frac{S}{\sqrt{A_c}} \quad \text{Equation II-8}$$

where β is the geometry correction factor (1.034 for Berkovich indenter). The Young's modulus of the specimen E_s thus can be obtained through the following relationship:

$$E_r = \left[\frac{1-\nu_s^2}{E_s} + \frac{1-\nu_i^2}{E_i} \right]^{-1} \quad \text{Equation II-9}$$

where

E_s, ν_s : Young's modulus and Poisson ratio of the specimen;

E_i, ν_i : Young's modulus and Poisson ratio of the indenter.

To calculate the modulus of the sample material, a modulus and Poisson ratio of $E_i = 1141$ GPa and $\nu_i = 0.07$ were used for the diamond indenter, and a Poisson ratio of $\nu_s = 0.3$ was used for all the tested specimens. For each sample, at least 5 indents were made to achieve reliable statistics of the data.

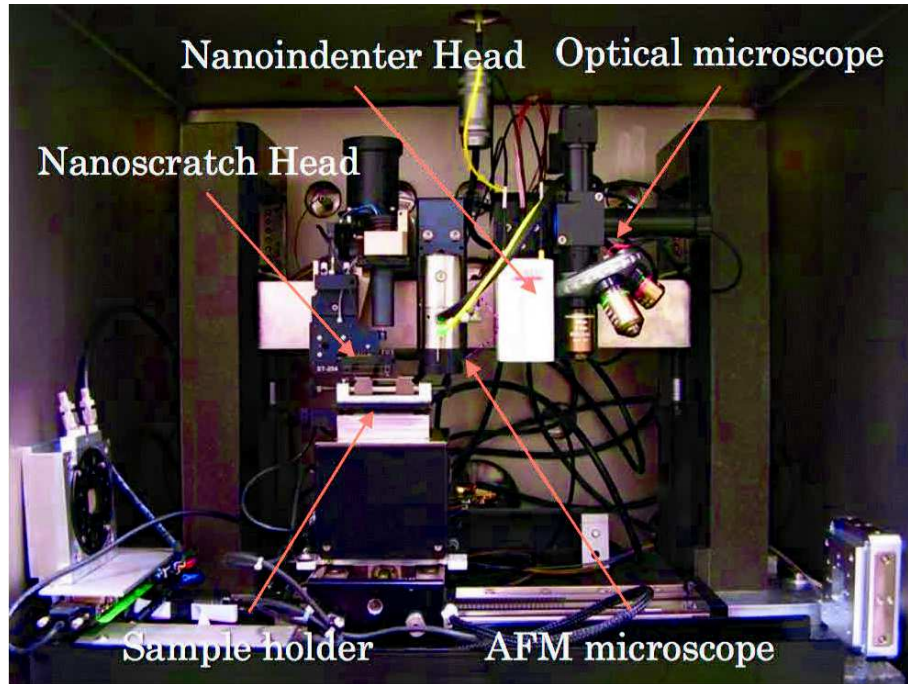


Figure II-28. Optical graph of the nanoindenter from CSM® (image credited to Dr. Jacomine).

II-B-6.3.2. Dynamic nanoindentation tests

Dynamic nanoindentation tests were undertaken on the LbL-assembled films. A sinusoidal stress is applied and the strain in the material is measured, which allows plotting elastic modulus versus displacement as well as the study of viscoelastic properties of the specimen at relative humidity conditions ranging from 5% to 72% in intervals of between 4% and 9%. A series (20 points) of dynamic nanoindentation tests was performed on the films for each relative humidity. The conditioning of the film samples and the controlling of humidity of the chamber were both carried out by following the same procedures of the static nanoindentation tests. The test conditions of the dynamic nanoindentation are summarized in Table II-1.

Maximum force (mN)	2
Loading rate (mN/min)	0.5
Unloading rate (mN/min)	20
Amplitude (mN)	0.05
Frequency (Hz)	1

Table II-1. Test conditions of dynamic nanoindentation tests.

With the Load-displacement data of the dynamic Nanoindentation tests, we can obtain the phase shift (δ) between load curves and displacement (Figure II-29) for each relative humidity condition. Then a plot of phase shift (δ) or $\tan(\delta)$ can be obtained.

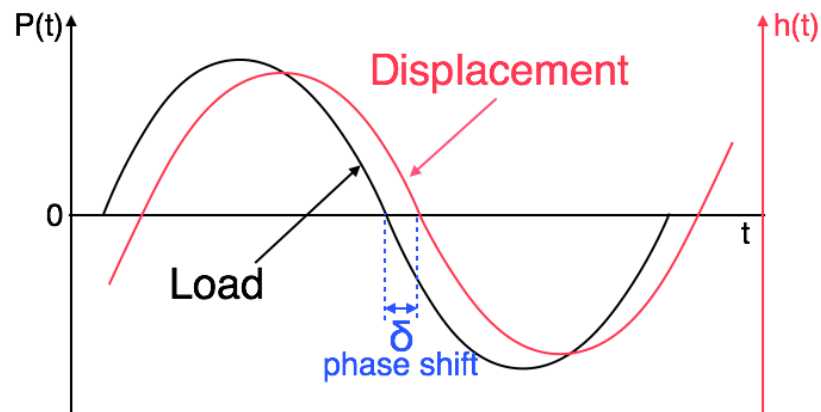


Figure II-29. Schematic representative sinusoidal force $P(t)$ and displacement $h(t)$ curves as a function of time (t) showing a phase shift of δ .

III. LbL-assembly of separative polyelectrolyte film on model and real membrane surfaces

Over the last two decades, researchers have focused on studying the internal structure, dynamics, and growth mechanism of LbL-assembly for the reason that these are important factors that determine the properties of LbL-assembled films.³³ For example, superlinear or non-linear growth mechanism of LbL-assembled films of (PDADMAC/PSS)_n was considered to be responsible for their high selectivity of multivalent ions,⁴⁸ which is highly interesting for the construction of LbL-assembly modified membranes. Therefore, understanding the growth behavior of this kind of films and its connections with the ions selectivity and permeability became the first part of our investigations.

In this thesis, LbL-assembly of (PDADMAC/PSS)_n at high ionic strength (0.5M) was chosen as main system for the separative/selective layer of the LbL-assembly modified membranes for twofold reasons. First, similar system of LbL-assembly has already been proven to be promising for making membranes of high permeability and good retention in several other studies.^{50,58} Second, both polyelectrolytes were demonstrated to have remarkable resistance to chlorine within the work of our project, which is important for enhancing chlorine resistance of the resulting membranes (see chapter V-A). Thus, this chapter is dedicated to the study of the growth behavior of LbL-assembled (PDADMAC/PSS)_n films. In order to study the effect of surface properties on the film growth behavior, different substrates were used for the construction of films, including tool surfaces, membrane-like surfaces and real membrane surfaces. Comparison of film growth behaviors on these surfaces will be performed.

III-A. *LbL-assembled coating on model surfaces*

We started our investigations on model surfaces, i.e., Si-wafers, quartz slide and quartz crystal, on which the deposition of (PDADMAC/PSS)_n films could be precisely

monitored using traditional characterization methods, i.e., ellipsometry, UV-Vis spectroscopy and QCM-D, are commonly used for the study of LbL-assembled films.

III-A-1. LbL-assembly on Si-wafer followed by ellipsometry

Ellipsometry, thanks to its non-destructive feature, is a widely used technique for the characterization of thin films. Here we first studied the construction of LbL-assembled films of (PDADMAC/PSS)_n at 0.5M of NaCl prepared on plasma activated Si-wafer with three different assembly methods including dipping, spray-assisted and spin-assisted methods. Film's thickness was measured with an ellipsometer by following the protocol described previously in section II-B-1.

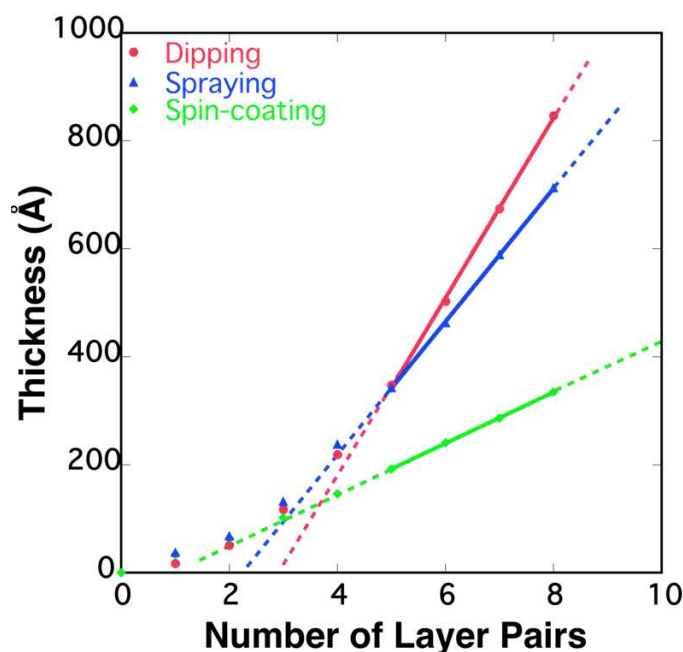


Figure III-1. Thickness variation of the LbL-assembled films (PDADMAC/PSS)_n on Si-wafer by dipping (Red), spray-assisted (Blue) and spin-assisted (Green) as a function of number of layer pairs (data for n=5 to 8 were linearly fitted, the slope is about 16.7 nm (Red), 12.4 nm (Blue) and 4.7 nm (Green) per layer pair respectively).

Figure III-1 shows the results of film thickness as a function of the number of layer pairs of (PDADMAC/PSS) and the deposition method. We can see that for all the three different assembly methods, film's growth becomes linear (steady state) though with different growth rate after a certain number of layer pairs, which is in agreement

with previous investigation on the similar system of (PDADMAC/PSS)_n films.^{24,43,132,133}

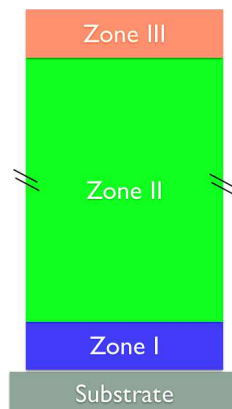


Figure III-2. Schematic representation of the zone model for polyelectrolyte multilayers with Zone I that is adjacent to the substrate, Zone II forming the “bulk” of the multilayer and Zone III that is adjacent to the film/solution or film/air interface.¹³⁴ The interface between the zones is diffuse rather than a sharp plane, which is indicated here for clarity.

The non-linear transitional growth region at the beginning of both the dipping and spray-assisted assembly process corresponds to the precursor zone 1 of the conventional ‘zone model’ for polyelectrolyte multilayer films first proposed by G. Ladam et al (see Figure III-2).¹³⁴ Inside this zone I the thickness of each layer pair measured by ellipsometer is lower than that in the linear region referring to the core zone II, which has been confirmed previously by UV–vis spectroscopy,¹³⁵ quartz crystal microbalance measurements,¹³⁶ X-ray reflectometry¹³⁷ and surface force microscopy (SFM).¹³⁸ This phenomenon is however caused by two main reasons.¹³⁴

First, the substrate has important influence on the adsorption of polyelectrolytes especially on the conformation of polyelectrolytes on the first layer. It has been proved that the conformation of polyelectrolytes of the first layer is a weak function of polyelectrolytes or salt concentration, however, interactions, including hydrogen bonding, dipolar, or hydrophobic forces between the substrate and the polyelectrolytes, may be responsible for controlling the conformation and the thickness of this initial layer.^{139,140} A rather flat conformation is usually formed for the initial layer polyelectrolytes due to entropy-induced adsorption mechanism, originating from the increment of entropy of the counter-ions that release into the

solution after the binding of polyelectrolytes to the naked solid or much less rougher substrate after a few layers of LbL-coating.^{138,40,141}

Second, according to the ‘diffusion in and out’ theory,^{46,47} the polyelectrolyte chains can diffuse in and out through the film during the buildup leading to interdigitation of the adjacent polyelectrolytes layers. Because the diffusion during the beginning of the buildup is limited by the non-penetratable solid substrate, the conformation of polyelectrolytes thus probably tends to be flat instead of vertically stretched globules, which results in thinner film. As the substrate is gradually covered by increasing layers of polyelectrolytes, the polyelectrolyte chains can diffuse more and more into the film and reach more binding points to form increasingly thicker film layers until the film’s thickness becomes thicker than the reaction-diffusion ability zone of the polyelectrolytes, after which film’s buildup comes to the steady zone II where film’s thickness increases linearly based on the full diffusion of the polyelectrolytes.

Therefore, from the dipping and spraying film’s thickness growth data shown in Figure III-1, we can conclude that around 22 nm corresponds to the thickness of zone I, which is in line with previous study of the asymmetric growth of similar (PDADMAC/PSS)_n system carried out by Ghostine et al.⁴⁸ A slightly slower growth at the steady state was obtained for the spraying method when compared with the dipping method. This is due to the self-limiting (also termed “self-assembling”) absorption process of the polyelectrolytes that results in slow rearrangement of the absorbed polymers and thus requires several minutes of contact time in order to achieve maximum or steady-state coverage for a given polymer solution, which limits the absorption of polyelectrolytes deposited for a short time (about 10 seconds) contact of the spraying method.¹⁴²⁻¹⁴⁴ Increasing the spraying contact time and/or solution concentration could lead to faster growth.¹⁴⁵

Unlike the other two methods of non-linear behavior, the spin-assisted method shows unique linear growth with much slower growth from the beginning of the film’s construction, which can be also explained by the self-limiting process of polyelectrolytes absorption on the rotating substrate due to even shorter contact time (about 2-10 seconds) at high rotation speed (3000 Rpm). In addition, the high shear forces exerted by the external shear flow will flatten and elongate on the plane the conformation of the polyelectrolytes and thus reduce their diffusion effect, which results in less interdigitation and thus thinner film.¹⁴⁶

In summary, these results provide preliminary basic information of our LbL-assembly system of (PDADMAC/PSS) including film growth behavior (zone model) and growth rate, diffusion in and out of the polyelectrolytes chains, interdigitation degree of the adjacent layers, etc. In order to verify these results obtained by measuring thickness of films constructed on Si-wafer by ellipsometry and to provide further information on the film's construction, we turned to investigate LbL-assembly of (PDADMAC/PSS) on other substrates with supplementary characterization methods. Since spin-coating and spraying are difficult to be utilized for the LbL-assembly in the hollow fiber membranes, we will only focus on the dipping methods for the following experiments.

III-A-2. LbL-assembly on quartz slides followed by UV-Vis absorption spectroscopy

UV-Vis absorption spectroscopy has been extensively applied to the characterization of LbL-assembled films containing chromophores because of its non-destructiveness, high accuracy and ease of sample preparation.¹⁴⁷⁻¹⁵⁴ Here we studied the dipping LbL-assembly of the same system of (PDADMAC/PSS)_n films by dipping on quartz slides using a UV-Vis spectrophotometer Cary5000 from Agilent. The substrates and the coating process have been prepared as described in II-A-3.1.

In the Figure III-3A, the deposition of each PSS layer leads to an increase of the absorption band at 226 nm. As expected, similarly to the results obtained by ellipsometry, Figure III-3B reveals non-linear regime of the increase of absorbance as a function of number of the number of layer pairs of coated (PDADMAC/PSS) on the quartz slides. Although the UV-Vis absorbance indicates only the amount of absorbed chromophores of PSS, we can still find that compared with previous results of ellipsometer there is a slight difference in the zone I as shown in Figure III-3B, which implies that the zone I ends at the 6th layer pair instead of the 4th layer pair for the aforementioned observation by ellipsometry. This difference is most probably due to the different substrate properties, which will be discussed further in details in the following section III-A-4.

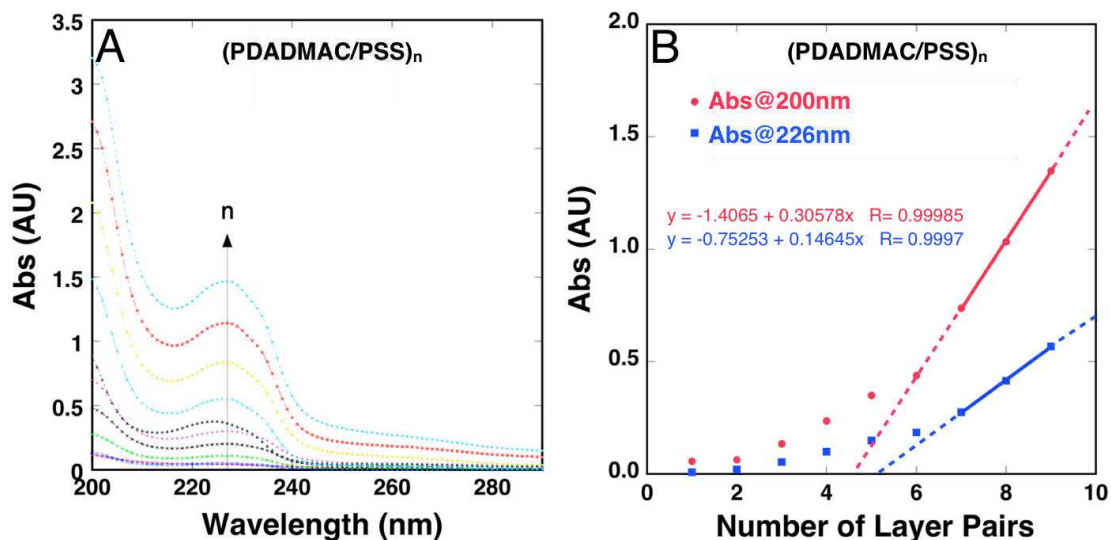


Figure III-3. A) UV-Vis absorbance of the coated (PDADMAC/PSS)_n as a function of wavelength for increasing number of layer pairs; B) Absorbance at the wavelength of 226 nm (blue) and of 200 nm (red) as a function of number of layer pairs (data for n=7 to 9 were linearly fitted, the slope is 0.30 A.U. and 0.15 A.U. per layer pair).

III-A-3. LbL-assembly on quartz crystal followed by QCM-D

Quartz crystal microbalance (QCM) is a powerful method for precise sensing of LbL-assembled films notably in wet state thanks to its extreme sensitivity based upon piezoelectric effect.^{20,44,149,150,155–161} Two different QCM-D sensors coated either with gold (Au) or SiO₂ respectively were UV-ozone activated and coated as described in II-A-3.1.

Figure III-4 shows the raw data and the plot of frequency shift against number of layer pairs of (PDADMAC/PSS) measured by QCM-D machine on gold and SiO₂ coated crystals. We can see likewise similar non-linear regime for both substrates, which is in accordance with previous observations by ellipsometry of the same polyelectrolytes system coated on Si-wafer. This can be easily understood since films are coated on very similar substrate of Si-wafer even though the oxidized layer of SiO₂ on the QCM-D sensor is much thicker (about 100 nm) than the one on the Si-wafer (about 1.6 nm). The similarity of growth between gold and SiO₂ indicates similar substrate properties of these two substrates.¹⁶²

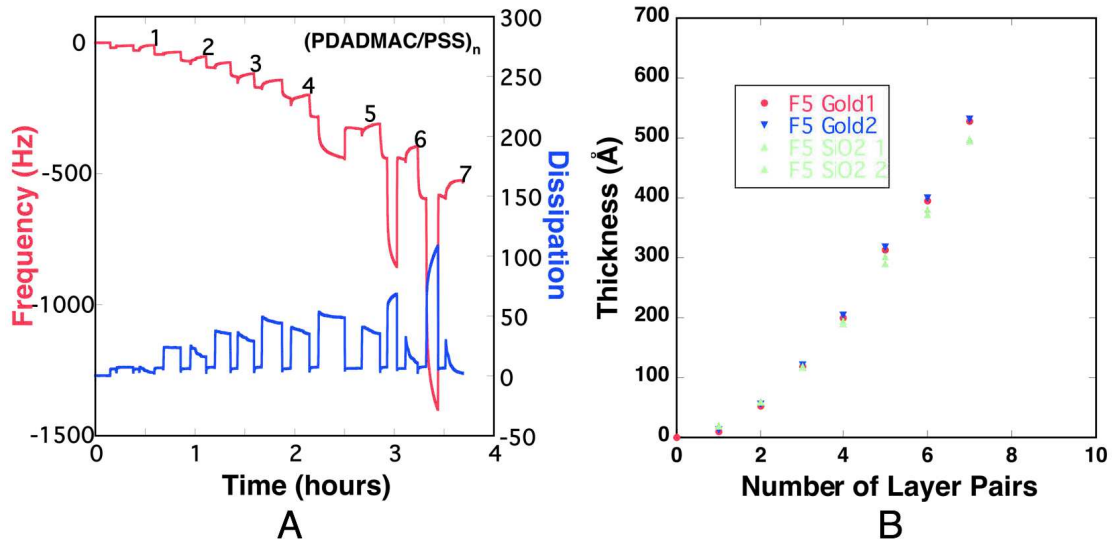


Figure III-4. A) Frequency and dissipation shift against time of deposition of $(\text{PDADMAC/PSS})_n$ on the activated gold surface of the QCM-d, number of layer pairs is marked at corresponding end of the relevant cycle; B) Frequency shift as a function of number of layer pairs of (PDADMAC/PSS) on Gold and SiO_2 surfaces.

III-A-4. Comparison of the three characterization methods

Although non-linear regime was found on all the tested different surfaces with various characterization methods, differences in the effect of surface arising from different properties of these surfaces led to different growth behavior at the beginning of film construction (zone I).

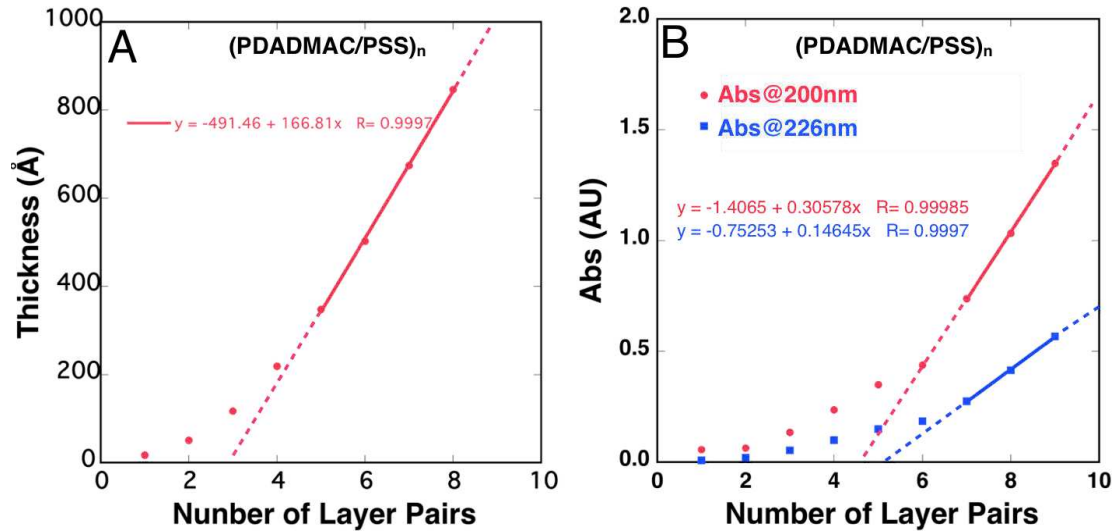


Figure III-5. A) Thickness variation of film (PDADMAC/PSS)_n assembled with 0.5M NaCl in the solutions as a function of number of layer pairs obtained by ellipsometry (data for $n=5$ to 8 were linearly fitted, the slope is about 16.7 nm per layer pair) (see **Figure III-1**); B) UV-Vis absorbance at wavelength of 200 nm (red) and 226 nm (blue) as a function of number of layer pairs obtained by UV-Vis absorption spectroscopy (data for $n=7$ to 9 were linearly fitted, the slope is 0.30 A.U. (red) and 0.15 A.U. (blue) per layer pair respectively) (see **Figure III-3B**).

Figure III-5 suggests that LbL-assembled films of (PDADMAC/PSS)_n on Si-wafer and quartz slide both have similar non-linear regime however with different behaviors in zone I, which is hard to explain in view of similar components of both surfaces. Since it has been commonly known and proved by AFM measurements that the surface roughness of Si-wafer and quartz slide are very similar and both have very smooth Å level surface with root mean square (RMS) roughness less than 0.4nm,^{44,163} we can basically exclude the contribution of the surface roughness to the different growth behavior in the zone I, which leaves us with only one possible conclusion that a difference in surface charge density and/or surface zeta potential between Si-wafer and quartz slide would be the reason. One may doubt about the existence of difference in surface charge density and/or surface zeta potential between these two surface, which is reasonable if we consider their shared same main component of silicon dioxide. However there is indeed some difference of surface zeta potential that have been found experimentally, which suggested a zeta potential of -100 mV for quartz and about -65 mV for silica in a neutral pH environment.¹⁶⁴⁻¹⁶⁶ The difference may originate from the different crystalline form of SiO₂ that results in different refractive

index and compact density (Appendix 2),¹⁶⁷ which gives higher charge density and zeta potential for the quartz. As we know that higher zeta potential will force polyelectrolytes to form more flattened and extended conformation and thus will slow the film's thickness growth,¹⁶⁸ which explains why the films coated on quartz requires more layer pairs (6 layer pairs) than the films on Si-wafer (4 layer pairs) for constructing the zone I. These findings of surface charge effect on the build-up of LbL-assembled films could have an important impact on the design and characterization of LbL-assembled films modified membranes and other LbL-assembly based devices. This will enlighten the characterization of the same LbL-assembly system of (PDADMAC/PSS) coated on the real membrane support, which will be discussed in the next section.

III-B. LbL-assembled coating on membrane-like model surface

Now that we have shown in the previous section that the substrate plays an important role in the behavior of LbL-assembled film's construction in the region of zone I, it is therefore interesting and crucial to see the film buildup on the real membrane support. However, the determination of the structural properties of the LbL-assembled films on the membrane support substrate is challenging in view of its rough polymer substrate, special surface charge density and irregular sample shapes including hollow fibers and flat sheets. These uncommon properties of the membrane make the common characterization methods of LbL-assembly become nearly useless. In order to be able to employ the traditional characterization techniques such as ellipsometry that requires homogeneous and reflective surface, spin-coated membrane-like surface made from raw materials of membrane (Sulfonated poly(ethersulfone)- SPES) provided by Project partner has been prepared on Si-wafer as described in chapter II. The investigation into the LbL-assembly on these membrane-like films that mimic the real membrane's surface could reveal preliminary information of the film's growth behavior on real membranes.

III-B-1. Membrane-like surfaces

The spin-coated surfaces as well as the flat sheet membranes were characterized by Atomic force microscope (AFM) and contact angle machine.

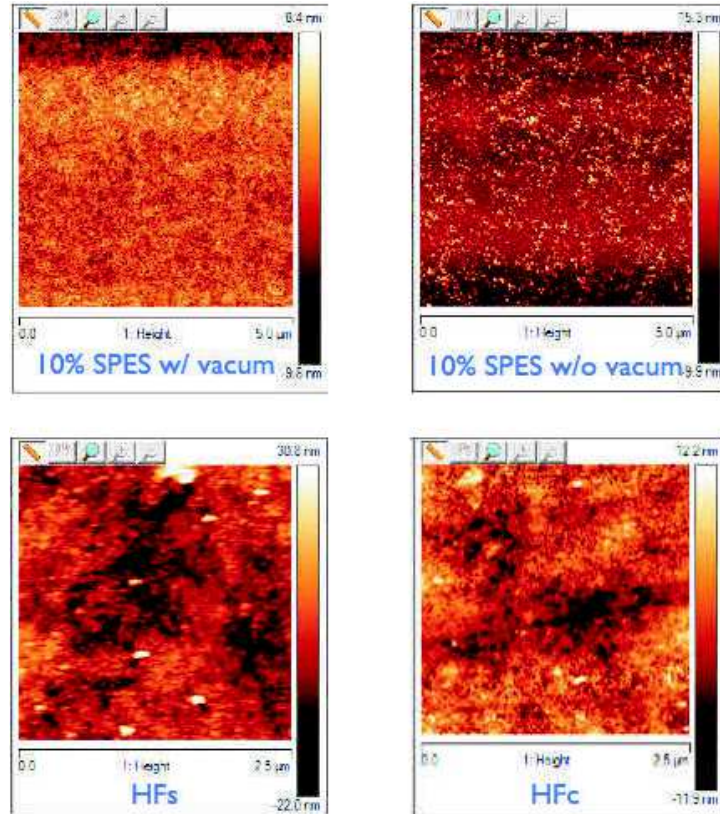


Figure III-6. AFM images of SPES films made with and without vacuum (on the top) and flat sheet membranes HF_s and HF_c (on the bottom).

Figure III-6 shows AFM pictures of the homogeneous spin-casted SPES films on the Si-wafer supports compared to the heterogeneous surfaces of two different flat sheet membranes HF_s and HF_c (provided by partner). The arithmetic average roughness (R_a) and root mean squared average roughness (R_q) of all the four surfaces were calculated and shown in

Different surfaces / Surface properties	SPES prepared without vacuum	SPES prepared with vacuum	HF _s	HF _c
R_q (nm)	3.28	2.53	6.40	3.42
R_a (nm)	2.35	2.01	4.80	2.73
Contact angle Θ_{eq} (Glycerol)	$38 \pm 1^\circ$	$45 \pm 1^\circ$	$34 \pm 1^\circ$	$34 \pm 1^\circ$

Table III-1 together with the contact angle results of these surfaces. We found that both the average roughness and equilibrium contact angle of the membrane-like surfaces are comparable with that of the surface of both flat sheet membranes HFc and HF. The SPES film prepared without vacuum has a contact angle of about 38 degrees, Rq of about 3.28 nm and Ra about 2.35nm, which are more analogous to the surfaces of flat sheet membranes compared to the film prepared under vacuum. Therefore the SPES films prepared without vacuum assistance were chosen for the study of the LbL-assembly on membrane-like surface.

Different surfaces Surface properties	SPES prepared without vacuum	SPES prepared with vacuum	HF _s	HSc
Rq(nm)	3.28	2.53	6.40	3.42
Ra(nm)	2.35	2.01	4.80	2.73
Contact angle Θ_{eq} (Glycerol)	38±1°	45±1°	34±1°	34±1°

Table III-1. Surface properties including Rq, Ra and equilibrium contact angle Θ_{eq}

III-B-2. Comparison of LbL-film growth on Si-Wafers and membrane-like surfaces by ellipsometry

Spin-assisted and spray-assisted LbL-assembled films of (PDADMAC/PSS)_n were coated on both spin-casted SPES membrane-like films and on Si-Wafers in order to compare the film growth behaviors on these two different surfaces using the convenient technique of ellipsometry.

As shown in Figure III-7, we observed that the spin-assisted LbL-assembled films on these two surfaces show a surprisingly large difference. This difference is probably due to different surface properties between SPES membrane-like film and Si-Wafer. In addition, the swelling problem caused by the residual organic solvent in the SPES film might influence the growth of the film and also increase the difficulty of measuring accurately the film thickness by ellipsometer.

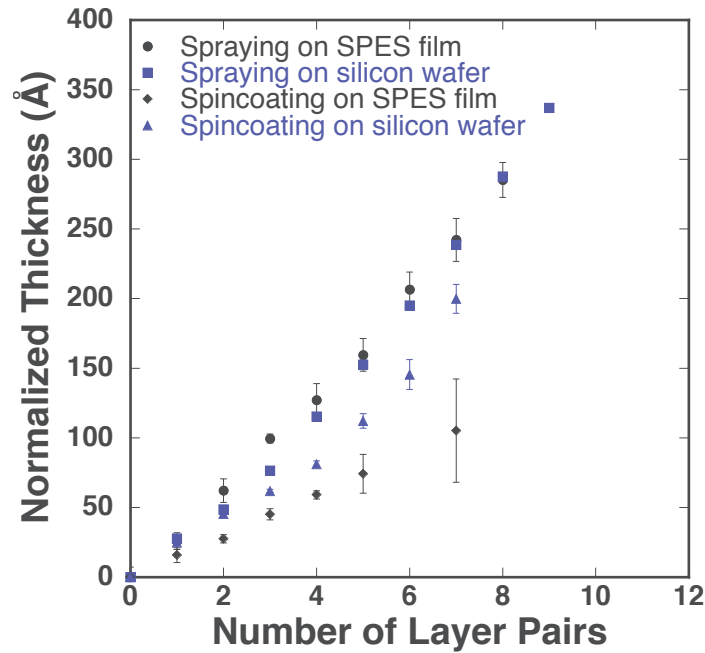


Figure III-7. Normalized thickness of the LbL-assembled films of (PDADMAC/PSS)_n on SPES film and on Si-wafer made by spin-coating and spray-assisted LbL-assembly.

Although the growth of spray-assisted LbL-assembled film on Si-Wafers seems very similar to the one on the SPES membrane-like surface, the growth of film on Si-wafer shows non-linear growth having a few layer pairs at the beginning of construction (zone I) as transitional area before film start to grow linearly, while films on SPES membrane-like substrate have much less (if any) layer pairs as transitional area before the linear growth starts. This phenomenon could be explained by the fact that after spin casting of SPES film onto the Si-wafer, the foundation for constructing LbL-assembled films has been changed from highly hydrophilic silicon dioxide to more hydrophobic and partially charged sulfonated polyether sulfone, which is considered to have considerable influence on the LbL-assembly.^{168–171} It has been suggested that polyelectrolytes form more coiled structure when they are coated on substrates with more hydrophobic property due to more hydrophobic interaction between the hydrophobic segments of polyelectrolytes and substrate, which results in a faster reaching out to the linear zone II.^{17,172–174} In consequence, the number of layer pairs of zone I is supposed to be less for LbL-assembly on the membrane and membrane-like surfaces, which will be further confirmed by direct study of LbL-assembly on real membrane with a technique called UV-Vis reflection spectroscopy in the following section III-C-1.

III-C. *LbL-assembled coating on real membrane surfaces*

After having studied the dipping LbL-assembly on model surfaces and membrane-like surfaces by dipping, we learned that the film's structural behavior of our system of (PDADMAC/PSS)_n follows the conventional zone model with similar growth rate in the linear zone II but altering number of layer pairs involved in the zone I for different substrates. It is therefore interesting and necessary to study the film's behavior on real membranes. In the previous section we have got some information of the films constructed on membrane-like surfaces which can give an idea about the film's behavior on real membranes, however, due to some limits of this method such as: dipping LbL-assembly can't be performed because of the residual organic solvent that can absorb water and then destroy the film by forming some holes, and the error bar is too big to get accurate comparison, the results on the membrane-like surfaces can merely be an indication. That's why we should now look into the film's construction on real membranes of flat sheets and hollow fibers.

III-C-1. UV-Vis reflection spectroscopy measurement of LbL-assembly on flat sheet real membrane surface

UV-Vis reflection spectroscopy is one of the few techniques that could be utilized for the characterization of LbL-assembled films on real membranes. LbL-assembled coatings of (PDADMAC/PSS)_n on flat sheet membrane were carried out and characterized by UV-Vis reflection spectroscopy as described in section II-A-7.1. .

Figure III-8B shows an UV-Vis reflection spectra of the LbL-assembled (PDADMAC/PSS)_n on flat sheet membrane HF's obtained using an integrating sphere for collecting the reflected light and the Kubelka-Munk (K-M) function for calculating F(R) that is proportional to the absorbance. We can see that the K-M spectra wavelengths (Figure III-8B) is in very well agreement with the UV-Vis absorption spectra of sulfonated polystyrene (PSS) in water solution (Figure III-8a),

indicating increasing absorbed amount of PSS chromophores with increasing number of deposited PSS layers, which proves successful LbL-assembled coating on the membrane support (HFs).

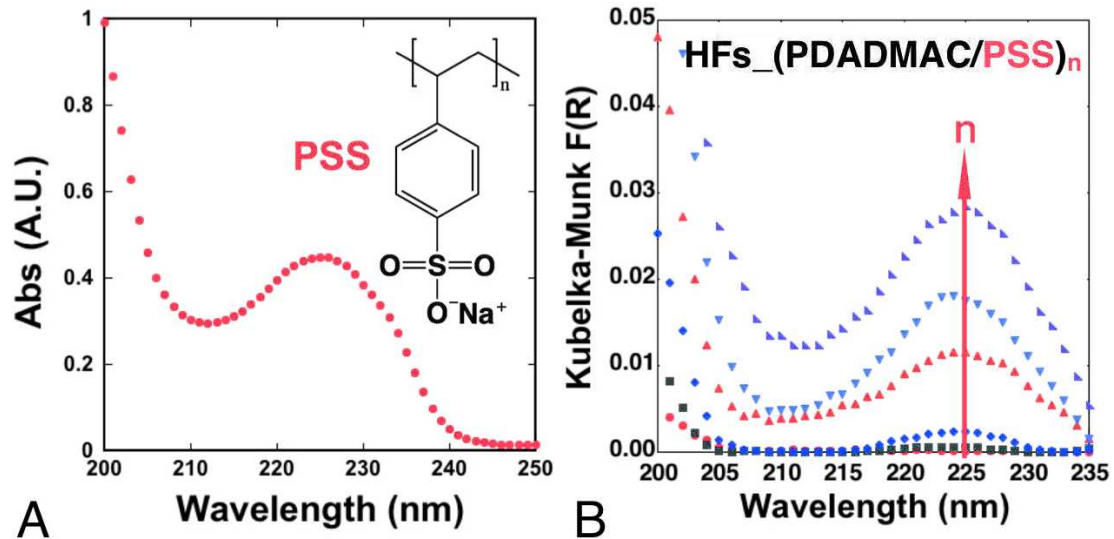


Figure III-8. A) UV-Vis absorption spectra of PSS solution in water; B) K-M indicating the increasing amount of PSS chromophores with the adding number of deposited PSS layers, which proves successful LbL-assembled coating on to the membrane support (HFs).

Figure III-9A is the raw UV-Vis reflection spectra of the LbL-assembled (PDADMAC/PSS)_n on flat sheet membrane, which indicates dropping reflection of the spectrum with increasing number of layer pairs. By using the reflection R, we can calculate $\text{Log}1/R$ that is also proportional to the absorbance. The plot of $\text{Log}1/R$ of the absorbance peaks at the wavelength of 200 and 225 nm as a function of the number of layer pairs is shown in Figure III-9B. As expected, we find likewise non-linear regime with only 3 layer pairs in the zone I, which confirms that films in zone I grow relatively faster on the flat sheet membrane HFs than on the conventional model surfaces such as Si-wafers, quartz slides or QCM sensors, because of the more hydrophobic surface of flat sheet membranes bearing less charge density and zeta potential of only about -20 mV in neutral pH environment.¹⁷⁵

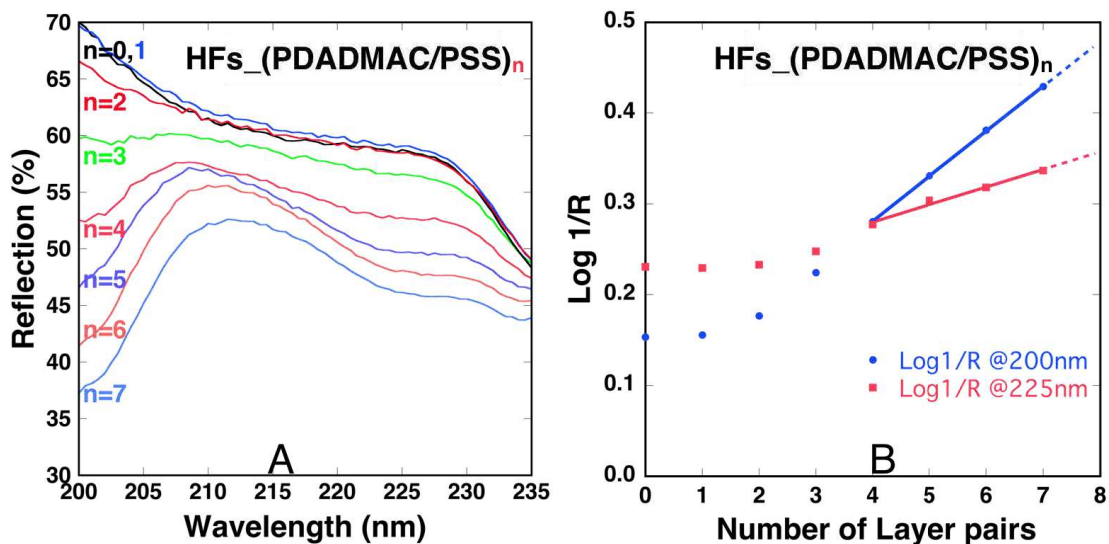


Figure III-9. A) Raw data of the UV-Vis reflection spectra showing the reflection R of a flat sheet membrane HF coated with LbL-assembled $(\text{PDADMAC/PSS})_n$ films at different wavelengths; B) variation of $\text{Log}1/R$ values (calculated from the reflection R values at the wavelength of 200 nm (blue) and 225 nm (red) obtained in spectra A) as a function of number of layer pairs spectroscopy (data for $n=4$ to 7 were linearly fitted, the slope is 0.05 A.U. (blue) and 0.02 A.U. (red) per layer pair respectively).

III-C-2. Permeability and retention measurement of LbL-assembly on hollow fiber real membrane surfaces

Another method that we can use to characterize the LbL-assembly on real membranes refers to the test of LbL-assembly coated membrane's performance, i.e., permeability and retention. The retention of MgSO_4 and water permeability were measured for the hollow fiber membranes HF coated with different number of layer pairs of (PDADMAC/PSS) with 0.5M NaCl.

Figure III-10 shows the results of retention and permeability as a function of number of layer pairs. A 'zigzag' behavior for the membrane performance was identified when the film's capping layer was alternated with PSS and PDADMAC respectively (Figure III-10B). It's not hard to find that the retention exhibited an increase when the film was capped with PSS layer and a drop after an additional PDADMAC layer is applied, vice-versa for the trend of the permeability. This can be attributed to the different swelling degree between the PSS and PDADMAC capped LbL-assembled films. It has been shown by different research groups that PDADMAC terminating

films have a higher swelling degree of up to 4 fold more than PSS terminating films. The higher swelling degree of PDADMAC terminating films caused the film to become looser which led to a higher water permeability and a lower ion selectivity.^{176–179} To ensure good retention, hereafter only films with terminating layer of PSS will be employed for other experiments of LbL-assembly modified membranes during this thesis.

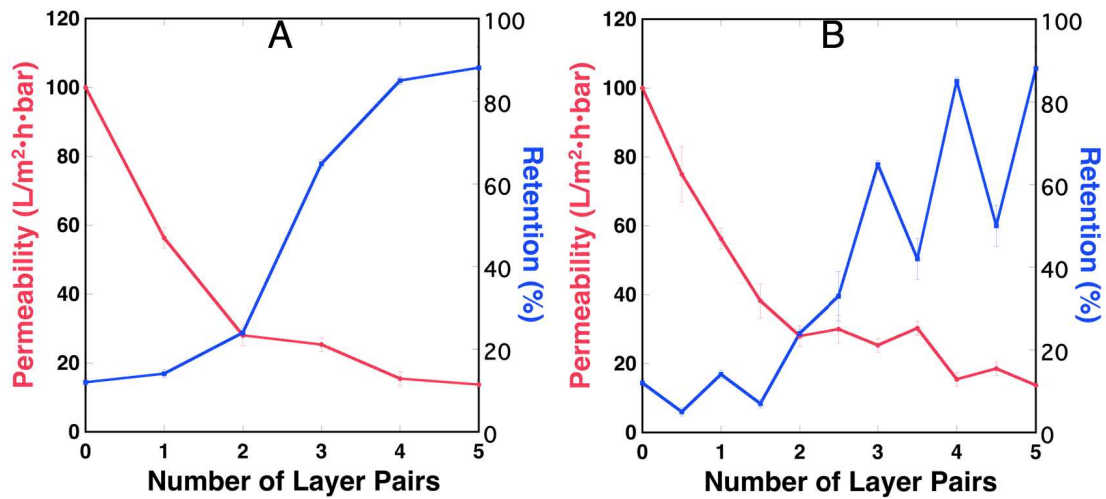


Figure III-10. A) Permeability and retention of the hollow fiber membranes HF_s modified with LbL-assembled (PDADMAC/PSS)_n as a function of integer number of layer pairs; B) Same as A) but with additional performance data of membranes coated with extra ½ layer pairs. (integer numbers of layer pairs represent films terminated with PSS, while films with an extra ½ layer pairs are terminated with PDADMAC)

In addition, we also found that the retention increased and the permeability decreased both non-linearly with increasing number of layer pairs of (PDADMAC/PSS), and that both values reached its plateau after 4 layer pairs (Figure III-10A), which is similar to previous studies on the LbL-assembly modified nanofiltration membranes.^{5,180} More detailed studies on the mechanism behind these findings of membrane performance will be discussed in the next section where we compare the membrane performance data with other abovementioned characterization data.

III-D. Comparison of different LbL-assembled film growth on real membrane surfaces and on model surfaces

III-D-1. Non-linear regime both on model surfaces and on real membranes

The fact that the retention of the (PDADMAC/PSS)_n modified membranes increased non-linearly and reached a plateau with the increasing number of layer pairs suggests a connection of the mechanism behind with the non-linear regime that we discovered in the previous sections. Several research groups have also found similar results for the LbL-assembled modified nanofiltration membrane and some have ascribed the mechanism to the different structure between the initial layers and the outer layers.^{69,181,9,182–186} We speculate that this difference in structure is probably also linked to the film's non-linear growth behavior as described by the zone model for the following reasons.

Firstly, the ion separation ability and its mechanism of the LbL-assembly modified nanofiltration membrane have been deduced mostly from electrostatic repulsive forces also called Donnan exclusion effect owing to the particular multi-bipolar architecture of the LbL-assembled film.¹⁸⁷ As the intrinsic charges don't have any excess uncompensated polyions, their Donnan exclusion effect is restricted due to the neutralization of the oppositely charged polyions. Therefore, Donnan exclusion effect of the LbL-assembled films is suggested to be mainly contributed by the uncompensated or over-compensated extrinsic charges that form in the zone II, which is commonly agreed but barely proved for the lack of accurate quantitative characterization of the LbL-assembly on real membranes.^{4,9,39,175,180,181,188–201} Thanks to our innovative application of UV-Vis reflection spectroscopic measurement to the characterization of film growth on the LbL-assembly modified membranes, we found as previously mentioned that film's growth on HF's flat sheet membranes followed as would expected the non-linear regime but with only 3 layer pairs in the zone I instead of 4 for Si-wafers or of 6 for the quartz slides. These observations just agree with the membrane performance's measurements revealing a maximum retention obtained at 4

layer pairs of (PDADMAC/PSS), which concludes that the (PDADMAC/PSS)_n films of 4 layer pairs on the hollow fiber membranes should have already extended into the steady linear zone II where Donnan exclusion effect reached and remained the maximum due to the presence of extrinsic charges. This would also explain why at 5 layer pairs the retention stopped increasing and the permeability dropped only slightly due to the increment of water diffusion distance arising from slightly increased film thickness.

Secondly, one might argue that mechanism behind the LbL-assembly modified nanofiltration membranes is only due to size-exclusion effect arising from size reduction of the membrane support's pores after the covering of defect free LbL-assembled films, and has nothing to do with the Donnan exclusion effect. This can be simply excluded by several previous observations showing that membranes coated with salt free polyelectrolytes solutions showed very limited retention compared to membranes coated with same polyelectrolytes system but containing salt in the solutions,^{5,184,187} which implied that polyelectrolytes systems with linear behavior (usually made of salt free solutions) are not suitable for making efficient nanofiltration membranes probably due to the lack of extrinsic charges that only exist in the non-linear systems. Therefore, simply covering the membrane support's pores with LbL-assembled films of linear regime can not result in membranes with good retention because of the lack of extrinsic charges which give birth to Donnan exclusion effect. This once again confirms the direct link between the non-linear film growth behavior with the high retention of LbL-assembly modified membranes.

Finally, the important and puzzling counter ions measurements were carried out by quite a few researchers who had some interesting contradictory conclusions as to whether the counter ions were present in the bulk or not, or only at the surface or also in the bulk,^{132,142,202-215} which makes it hard to conclude the contribution of counter ions to the Donnan exclusion effect. Recently, Ghostine et al published an article concerning the LbL-assembled (PDADMAC/PSS)_n film's growth mechanism and counter ions measurement using radioactive counter ions.⁴³ In this article, they confirmed that there are overcompensated extrinsic polycations only after when the film's construction extends into a steady linear state (zone II), which is in accordance with our first hypothesized reason. In addition, they revealed that the PSS-capped film formed a glassy and stoichiometric complex that provided a better ions barrier than

the much more hydrated PDADMAC-capped film, which is consistent with our findings of ‘zigzag’ behavior for the membranes’ retention and permeability (Figure III-10b).

To conclude, our studies show close connection between the non-linear growth behavior of LbL-assembled films and the resulting high retention of LbL-assembly modified membranes. The extrinsic charges present in the zone II of films with non-linear regime is the key factor of the high retention because of the resulting Donnan exclusion effect, which is important for guiding our design of new generation membranes with LbL-assembly technique.

III-D-2. Surface effect on LbL-assembled film growth

De Grooth et al showed that LbL-assembly modified membranes made with UF support of polyethersulfone (PES) reaches 83% retention of MgSO_4 after only 2 layer pairs of coating with (PDADMAC/PSS), while membranes made with UF support of partially sulfonated PES (SPES) had MgSO_4 retention of only 52% when coated with 2 layer pairs and 78% when coated with 3 layer pairs.¹⁷⁵ This indicates not only the important influence of surface properties of the membrane support to the performance of LbL-assembly modified membranes, but also confirms the existence of surface effect on the film growth which is in consistence with our previous findings of different film growth behaviors for substrates (Si-Wafers, Quartz slide, Flat sheet membranes HF_s) bearing different surface properties (see Figure III-11).

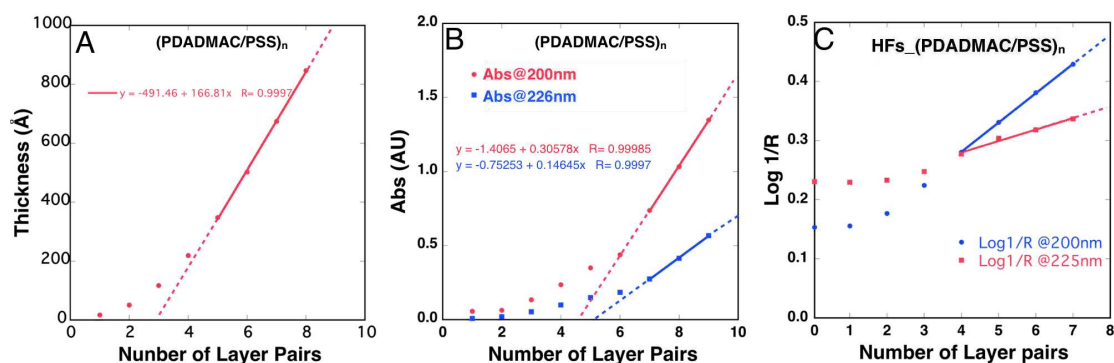


Figure III-11. Non-linear film growth of (PDADMAC/PSS)_n A) on Si-Wafers with 4 layer pairs in zone I (see **Figure III-1**), B) on quartz slide with 6 layer pairs in zone I (see **Figure III-3B**) and C) on flat sheet membrane HF_s with 3 layer pairs in zone I (see **Figure III-9B**).

As mentioned by Decher³³, the difference of film growth only exists in the first few layer pairs (zone I) where surface effect takes place, and after a few layer pairs (zone II) film grows independently of the underlying substrate at a fixed rate that is governed by the choice of polyanion/polycation pair and by the deposition conditions. Consequently, the increment rate of thickness on Si-wafers (16.7 nm/layer pair), the increment rate of absorbance at the wavelength of 200 nm on quartz slides (0.30 A.U./layer pair) and the increment rate of Log1/R at the wavelength of 200 nm on flat sheet membranes (0.05 A.U./layer pair) are proportional to each other. Therefore, we can obtain the ratio of thickness to absorbance = 55.7 nm/A.U. and the ratio of thickness to Log1/R = 334 nm/A.U., which can be used for converting the absorbance and Log1/R values to thickness. Using these two ratio values, the absorbance and Log1/R data were converted into thickness data and were plotted together with the ellipsometry data as shown in Figure III-12.

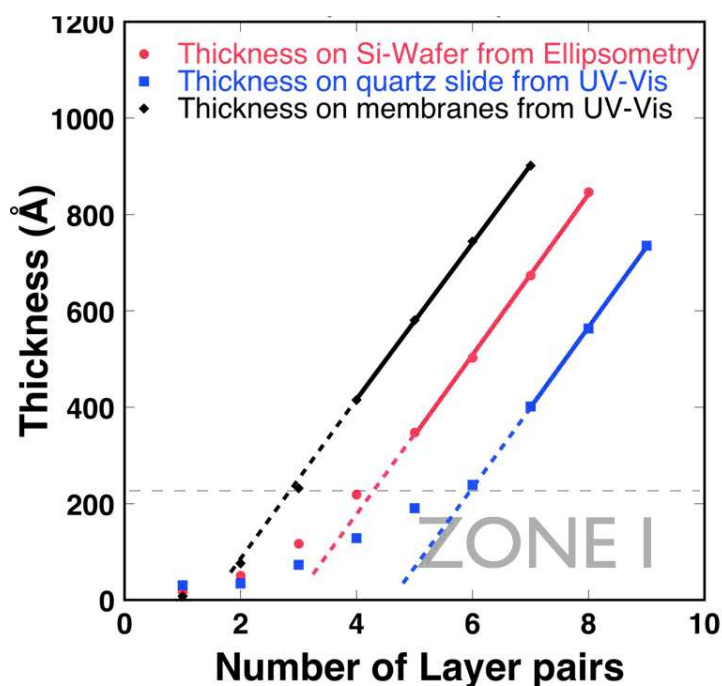


Figure III-12. Surface effect on the zone I of LbL-assembled (PDADMAC/PSS)_n demonstrated by comparing thickness values of the films assembled on three different surfaces (Si-Wafers, Quartz slides, Flat sheet membranes HF). The dotted grey line indicates the thickness under which zone I is located.

Figure III-12 shows that after different number of layer pairs of (PDADMAC/PSS)_n, the film thickness on the three different surfaces reached a shared thickness of about

22 nm, above which a similar linear growth starts. This clearly indicates strong surface effect on the film growth in zone I where different number of layer pairs of polyelectrolytes were required for different surfaces. In the zone I, the film grew the fastest on the membrane compared with that on the Si-wafer and quartz slide. As already discussed previously, this was due to the low charge density and hydrophobic property of the membrane surface that is made of partially sulfonated PES, which resulted in more coiled/less flattened polyelectrolytes conformation leading to thicker film compared to the other two more hydrophilic surfaces.^{17,172-174} Similarly, less flattened/more coiled polyelectrolytes conformation, originating from relatively lower charge density of the Si-wafer than that of the quartz slide, was attributed to the faster growth on the Si-wafer compared to that on the quartz slide. These findings not only confirm strong influence of the surface on the general build-up of LbL-assembled films, but also, more importantly, establish a link between the build-up of the film and the membrane performance of the LbL-assembly modified membranes, which can be of remarkable help in this work of making new generation membranes using the LbL-assembly technique.

Besides, the shared thickness of zone I by the three different surfaces also confirms the ‘diffusion in and out’ mechanism for the non-linear regime, which predicts that film starts to grow linearly when the initial film reach a thickness beyond the diffusion ability of the polyelectrolytes (22nm for our system of (PDADMAC/PSS)_n).^{46,47}

Summary

To conclude, by monitoring and comparing the growth of LbL-assembled films of (PDADMAC/PSS)_n on different surfaces with the help of different characterization techniques, we confirmed the non-linear regime of our system in addition to the existence of surface effect of the traditional zone model. To our knowledge, we precisely quantified for the first time the film’s growth on non-homogeneous membrane surfaces thanks to the application of UV-Vis reflection spectroscopy. As the surface effect has strong influence on membrane performance of the LbL-assembly modified membranes,¹⁷⁵ this method can be of a very powerful tool for the

investigation of LbL-assembly modified membranes for the reason that very few effective characterization methods can be employed in this field.

Now that we have thoroughly studied the growth behaviors of the selective layer system of polyelectrolytes (PDADMAC/PSS) and its link with the membrane performance, its time to start looking into the reinforcing layer that is made of nanofibers and serves for mechanical reinforcement and for enhancing membrane permeability. In next chapter, we will first investigate how to prepare stable nanofibers solutions for the LbL-assembly as well as the growth behavior of nanofibers based LbL-assembled films by different characterization methods.

IV. LbL-assembly of CNTs and CNFs based films

Carbon nanotubes (CNTs) and cellulose nanofibrils (CNFs) were selected for making a mechanically strong intermediate porous layer between the membrane support and the separation layer because of their highly strong mechanical properties. Furthermore, the intermediate layer made of these nanofibers provides very high specific surface area and forms interconnected nano-pores, which can not only enhance the permeability of the coated membranes by introducing water nanochannels, but also improve the membranes' selectivity through incorporation of active chemical or functional agents on nanoscale.^{216,217}

Before applying the nanofibers on the modification of membranes via LbL-assembly, we explored how to prepare stable nanofibers solutions for the LbL-assembly as well as the growth behavior of nanofibers based LbL-assembled films by different characterization methods.

IV-A. *LbL-assembled CNTs based films*

Carbon nanotubes (CNTs) (Figure IV-1) are ideal candidates as reinforcement fillers, owing to their extremely high Young's modulus (1.1 TPa),²¹⁸ their remarkable ultra high tensile strength (up to 63 GPa), and their unique ability to maintain high permeability and to increase chlorine resistance of membranes.²¹⁹ It was found that the incorporation of CNTs into the barrier layer increases the permeate flux by a factor of about 3 for nanocomposite membrane based on a cross-linked electrospun PVA substrate coated with a nonporous hydrophilic polymer/CNTs nanocomposite layer.⁷² Other groups also investigated the enhancement of membrane's selectivity, chemical resistance, mechanical strength and thermal stability by incorporating CNTs into the membrane through different methods.^{217,219-222} Nevertheless, studies on the application of CNTs into membrane modification by LbL-assembly remain limited.^{223,224} That's because the main bottleneck in the practical applications of

CNTs is that as-produced CNTs are held together in bundles of hundreds of individual tubes by very strong van der Waals interactions between hydrophobic walls even if attempts are made to disperse them,^{225,226} which makes the achievement of stable suspensions of individual CNTs become a major challenge for their further application. While organic solvents featuring high electron pair donicity and low hydrogen bond parameter have demonstrated the ability to form stable suspensions of CNTs,²²⁷ water suspensions of CNTs - a prerequisite for many other applications like LbL-assembly, still remains a challenge.²²⁸

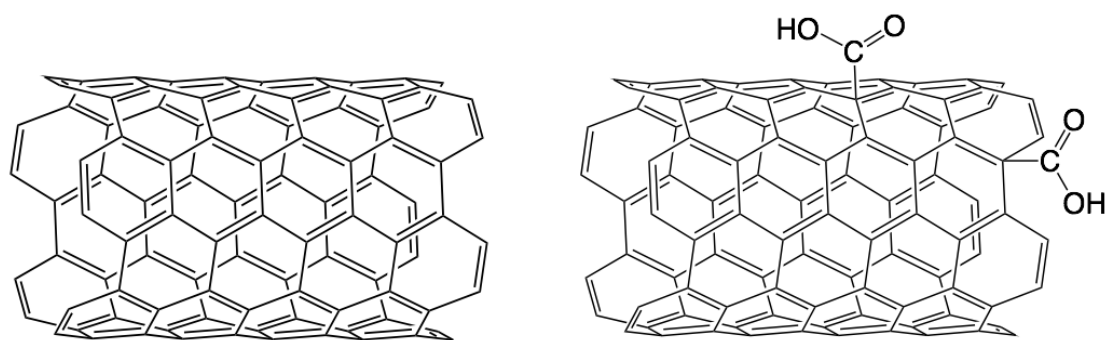


Figure IV-1. Representative structure of single wall carbon nanotube P2-CNTs (left without carboxylic group) and P3-CNTs (right with carboxylic group) bought from carbon solution, Inc. (5,5 Armchair type SWNT as an example).

Different methods for obtaining stable water suspensions of CNTs have been reported and were conventionally classified into three main categories depending on how the CNTs are treated during the initial state of the process: mechanical, physicochemical, and irradiation.²²⁸ Among these methods, physicochemical method have been most widely adopted, namely, covalent surface modification and non-covalent surface modification, depending on whether or not covalent bonding between the CNTs and the functional groups and/or modifier molecules is involved in the surface modification process. In contrast with covalent surface modifications, where local hybridization state was changed from sp^2 to sp^3 yielding defects and destruction of CNTs, non-covalent surface modifications are advantageous for being able to conserve the CNTs inherent properties including sp^2 conjugated structures and the electronic performance, high mechanical strength and smooth surface. Non-covalent surface modifications are one of the simplest and most effective ways to nondestructively enhance the dispersibility of CNTs in water.

Non-covalent surface modifications typically use surfactants and/or amphiphilic polymers that can either adsorb onto or wrap CNTs surfaces by π - π or hydrophobic interactions between their hydrophobic part and CNTs surfaces, which reduces the van der Waals interactions between CNTs and facilitates the disruption of CNTs bundles into individual tubes or smaller bundles. Meanwhile the hydrophilic part of these modifiers can further help disperse the CNTs through electrostatic and steric repulsion. Besides these hydrophilic agents endow the CNTs with better solubility in water.

Although effective suspension of CNTs with surfactants can be achieved, the CNTs concentration are severely restricted.²²⁹ O'Connell et al. invented a new technique for rendering SWNTs water soluble in the g/l concentration range.²³⁰ This approach, by wrapping water-soluble linear polymers polystyrene sulfonated (PSS) or polyvinyl pyrrolidone (PVP) around the tubes, allows for the first time pristine nanotubes to be manipulated reliably by solution-phase techniques like LbL-assembly.

IV-A-1. Preparing CNTs aqueous dispersion by physical wrapping with poly(styrene sulfonated) (PSS)

In contrast with other dispersing agents such as small surfactant molecules that disperse CNTs only by forming micellar domains on the CNT surfaces through weak hydrophobic interactions, PSS can not only adsorb onto CNT surfaces by π - π interactions due to its benzene groups, but also wrap CNTs by forming thermodynamically favorable restricted condensed wrapping state resulting in the reduction in surface energy of CNTs in water which helps the dispersion of the CNTs in water in addition to the electrostatic repulsive effect of its negatively charged SO_3^- groups. Therefore the PSS-wrapped CNTs suspensions can reach much higher concentrations than the surfactants adsorbed CNTs suspensions.²²⁸ One way to achieve the exfoliation of CNTs in water with the help of dispersing agents is the ultrasonication process by which the van der Waals interactions in the CNTs bundles can be overcome leading simultaneously to CNTs exfoliation and simultaneously the wrapping of dispersing agents like PSS onto CNTs. As a result, a stable suspensions of PSS-wrapped CNTs can be obtained and remain stable for months.²³¹

IV-A-1.1. UV-Vis spectroscopic monitoring of the PSS-wrapped CNTs suspensions

Despite the stability of the PSS-wrapped CNTs suspensions, effective qualitative and quantitative characterizations of the degree of dispersion (DD) of CNTs are missing. As the functionality of a wide range of applications depends on the dispersion of individual CNTs rather than just CNT bundles,^{232–235} the evaluation of the DD of CNTs in water is crucial and remains quite a challenge. Most early works have described the suspension state of CNTs simply in terms of photographs of vials containing a black solution,²³⁶ occasionally combined with some time-consuming AFM studies revealing only qualitative and local suspension state of CNTs, from which we can not discriminate the state of the CNTs dispersion between nanodispersion and macrodispersion.²³⁷ The dispersion state characterized by conventional microscopy, including optical, AFM, SEM, and TEM, can hardly be to be used for representing qualitatively and quantitatively the state of the CNTs dispersions due to either instrumental resolution limits or sampling problems.

It is known that all kinds of CNTs are active in the UV-Vis region and exhibit characteristic bands corresponding to additional absorption due to 1D van Hove singularities, and that contrary to completely dispersed CNTs bundled CNTs are hardly active in the wavelength region between 200 and 1200 nm, it is therefore possible to detect individual nanotubes via UV-Vis spectroscopic technique, which implies that there is a relationship between the concentration of CNTs individually suspended in solution and intensity of the corresponding spectrum.²³⁸ Grossiord et al. showed that the UV-Vis absorbance of SDS-adsorbed CNTs in an aqueous solution increases with increasing sonication time and reaches to a plateau after a certain time, which indicates that a maximal amount of individual CNTs were exfoliated although not meaning 100% of the CNTs exfoliated.²²⁶ Therefore, the UV-Vis spectroscopic technique can be used for monitoring quantitatively the degree of dispersion of CNTs in water and for determining how much time of sonication should be applied for obtaining a stable CNTs suspension with maximum exfoliation.

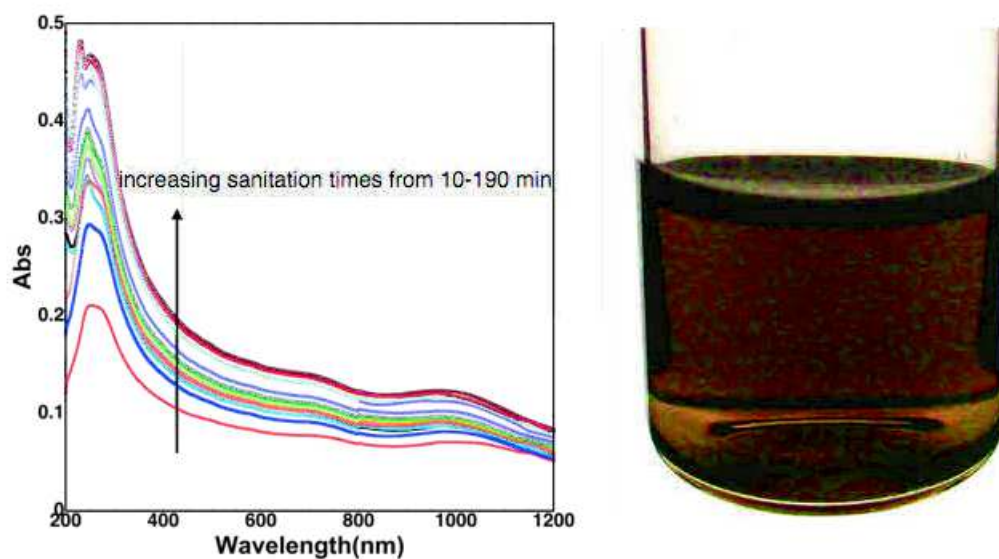


Figure IV-2. A) Evolution of the UV-Vis spectra of aqueous PSS-wrapped P3-CNTs suspensions as a function of different sonication times; B) optical graph of the final homogeneous PSS wrapped P3-CNTs suspension.

In order to ensure a maximal exfoliation of the CNTs in water by ultrasonication, UV-Vis absorbance measurements of the CNTs suspensions sonicated with different time during the ultrasonication were carried out. As shown in **Figure IV-2**, we can see that the absorbance of the CNTs suspensions in water increases with increasing sonication time and that after about 2 hours of sonication the absorbance reaches a plateau, indicating that about 2 hours of sonication is enough for effectively exfoliating the CNTs in water. AFM image of a drop of the resulting CNTs suspension was shown in Figure II-1c and proved successful exfoliation of the CNTs into individual single nanotubes.

IV-A-1.2. Purification of the PSS wrapped CNTs suspensions by ‘Salt-out’

LbL-assembled films of PSS-wrapped CNTs suspensions have been demonstrated by several studies.^{239,240} Most of these works did not apply or mention any purification of the PSS-wrapped CNTs suspensions despite of the presence of excess PSS that could

compete with the PSS-wrapped CNTs for LbL-assembly. Apparently the amount of PSS used for dispersing CNTs have been properly adjusted so that the influence of possible excess PSS could be negligible. Indeed O'Connell et al. have estimated an average of 8.1 monomer units of dispersing polymers per nm of CNT and up to 2:1 for the weight ratio of PSS to CNTs.²³⁰

Nevertheless, the purification of PSS-wrapped CNTs suspensions could be useful if we want to increase the proportion of CNTs in the films, and it becomes crucial once the amount of excess PSS is no longer negligible, preventing CNTs from adsorption during LbL-assembly process. Very few studies have been conducted on the purification of excess dispersing agents due to the unique properties of CNTs.^{241,242} As the PSS-wrapped CNTs in the suspension with colloidal state have very tiny size combined with very low density, it is impossible to separate CNTs from excess PSS by conventional methods such as direct centrifugation. Some works used filter membranes to stop and collect the CNTs while the excess of soluble dispersing agents permeate the filters and then were removed. A big disadvantage of this method is that the filter membranes used could be easily blocked by the CNTs and/or carbonaceous impurities. Moreover, the process of collecting and redispersion of the CNTs is time-consuming.

Here we present a new method called 'salt out' for purifying excess dispersing agents in CNTs suspension. The 'salt out' purification method involves two main processes, namely, coagulation and centrifugation.

The first coagulation step consists in precipitating the PSS wrapped P3-CNTs of colloidal state by adding sufficient NaCl. The counter-ions provided by the added salt can compress the electrical double layer of the colloidal PSS wrapped P3-CNTs, which destabilizes the colloidal dispersion and leads to inter-particle collision of the CNTs when the salt concentration is high enough. Photographs of PSS wrapped P3-CNTs suspensions with different amount of NaCl added are shown in Figure IV-3. It appears that the CNTs suspension stay clear and stable at 0.3M of NaCl, whereas at 0.6M and 1M of NaCl, both suspensions form aggregates almost immediately after the addition of salts. Therefore, with at least 0.6M of NaCl, coagulation can be induced in the CNTs suspensions. Since bivalent and multivalent ions have even much higher coagulating ability, it will require much less amount of multivalent salts for the coagulation to take place.

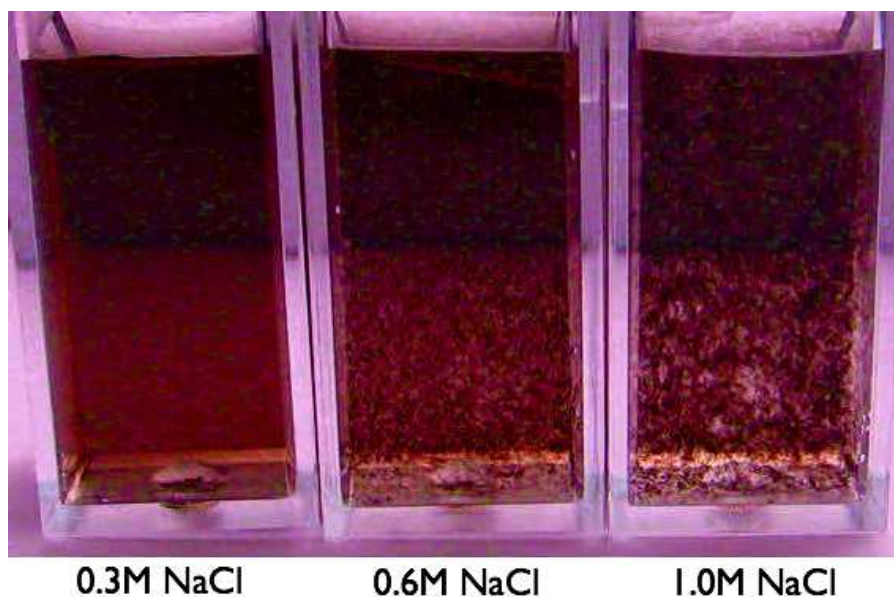


Figure IV-3. Photographs of PSS wrapped P3-CNTs suspensions with three different amount of NaCl added: 0.3M, 0.6M and 1.0M (from left to right).

The second step consists on the centrifugation of the coagulated. It is known that the bigger size of the aggregation can facilitate the settlement of the CNTs by centrifugation, we can thus separate the CNTs from the excess of PSS by several steps of centrifugation until there is no more PSS in the supernatant solution, which can be determined by UV-Vis measurement of the supernatant solution. Figure IV-4 shows the UV-Vis absorption spectra of the four consecutive centrifugations. As we can see that, after the first centrifugation, the supernatant solution shows a strong absorption band for PSS characteristic wavelength ranging from 200 nm to 250 nm, which indicates that a major amount of excess PSS was separated. There is a slight absorption in the whole UV-Vis wavelength range originating from small amount of CNTs that did not settled down after the centrifugation. After the second centrifugation, there is a significant decrease of the intensity of PSS absorption band indicating that most of the PSS excess has been removed after 2 steps of centrifugation. After the fourth centrifugation, it remains only absorption around the wavelength of 200 nm, which is ascribed to NaCl.

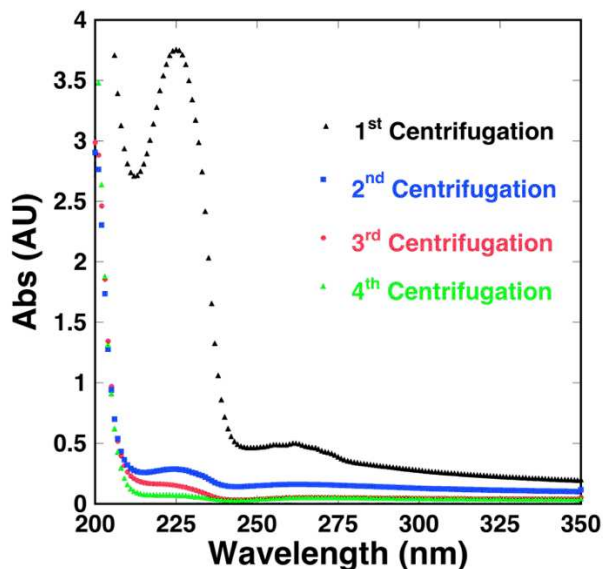


Figure IV-4. UV-Vis absorption spectra of the supernatant after four consecutive centrifugation process of 30 min at 17000Rpm.

After the centrifugation steps, the resulting purified PSS wrapped P3-CNTs sediments are redispersed in water with only 10 seconds of ultrasonication for destroying the weakly bonded CNTs aggregates. Figure IV-5 displays photographs of the resulting PSS wrapped P3-CNTs sediments redispersed in water before and after ultrasonication. The final purified PSS wrapped P3-CNTs suspensions can stay clear and stable for months without any visible precipitations.

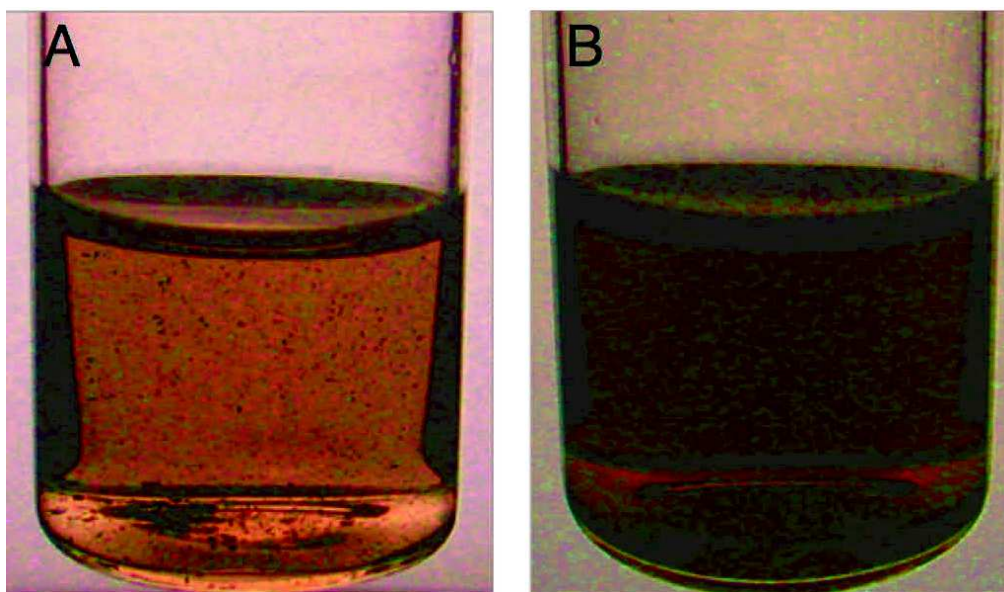


Figure IV-5. Photographs of the resulting purified PSS wrapped P3-CNTs sediments redispersed in water before A) and after B) ultrasonication.

IV-A-2. Characterization of LbL-assembled CNTs based films

Based on aforementioned results of the investigation on the preparation of stable PSS-wrapped CNTs by ultrasonication, suspensions of PSS wrapped P3-CNTs bought from Carbon Solution, Inc. were prepared as described previously in section II-A-2.1. The concentration of CNTs (PSS excluded) was adjusted to 0.5 mg/mL for all the LbL-assembly experiments. Anionic charged PSS wrapped CNTs based LbL-assembled films were fabricated together with cationic polyelectrolytes such as PVAm, PDADMAC, and PEI, and their growth behaviors were investigated with traditional characterization methods including ellipsometry, UV-Vis spectroscopy and QCM-D.

IV-A-2.1. LbL-assembly of CNTs based films on Si-wafer followed by ellipsometry

CNTs based LbL-assembled films were prepared on Si-wafer by dipping using PVAm solutions at different ionic strengths (0M and 0.5M) as polyelectrolyte partner. Film thickness of each layer pair was measured by ellipsometry (Figure IV-6).

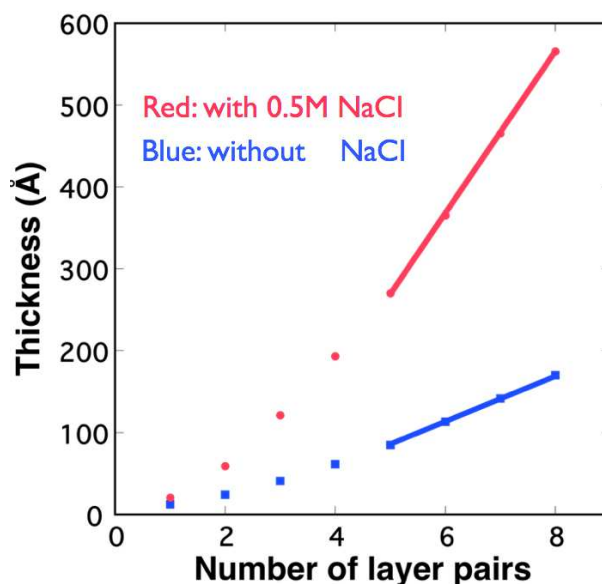


Figure IV-6. Thickness of LbL-assembled films of $(\text{PVAm/PSS wrapped P3-CNTs})_n$ at different ionic strength conditions for PVAm solutions as a function of number of layer pairs prepared by dipping. (data for $n=5$ to 8 were linearly fitted, the slope is (Red) 100 \AA per layer pair and (Blue) 28 \AA per layer pair)

We can observe that thickness of the PSS wrapped P3-CNTs based LbL-assembled films rises with increasing number of layer pairs and became linear after about 5 layer pairs in absence and presence of salt, which indicates successful assembly of PSS wrapped CNTs and PVAm on the substrate and almost same amount of PSS wrapped CNTs was loaded in each deposition step in the linear regime. At 0.5M NaCl, the increment per layer pair (PVAm/PSS wrapped CNTs) is around 100 Å, while in absence of salt it is only about 28 Å per layer pair. The reason why films made of PVAm solutions with 0.5M salt grew much faster than without salt, is that the presence of salt electrostatically screened the charged groups of PVAm polymer chains, leading to conformational changes of the adsorbed polymer chains. An increase of the ion-segment competition resulted in larger loops and longer tails of the adsorbed polymer chains and thus higher amount of polymer and CNTs absorption, which led to the thicker film at high ionic strength condition for PVAm solution^{142,243,244}

IV-A-2.2. LbL-assembly of CNTs based films on quartz slide followed by UV-Vis absorption spectroscopy

Same films of (PVAm/PSS wrapped P3-CNTs) with different ionic strength conditions were LbL-assembled on quartz slides and characterized by UV-Vis absorption spectroscopy. UV-Vis absorption spectra of these films and absorption curve at a characteristic absorption wavelength are displayed in Figure IV-7. Because carbon nanotubes have a π plasmon-originated broad spectral absorption range starting from UV to near infrared,²⁴⁵ and because the PSS that were used for dispersing CNTs by wrapping absorb from wavelength of 200 to 250 nm, there are overlaps of absorption bands of CNTs and PSS. Therefore 500nm was chosen as characteristic absorption wavelength for CNTs in order to plot the absorption variation that originates only from CNTs. Since PVAm do not adsorb in the UV-Vis wavelength range, the measured absorbance shown in Figure IV-7A is due to both CNTs and PSS. Optical absorbance was found in the whole UV-Vis wavelength range, which indicates successful deposition of CNTs. The two peaks at the wavelength of 200 nm and 225 nm respectively are characteristic adsorption of PSS, which are superposed by relevant absorbance of CNTs.

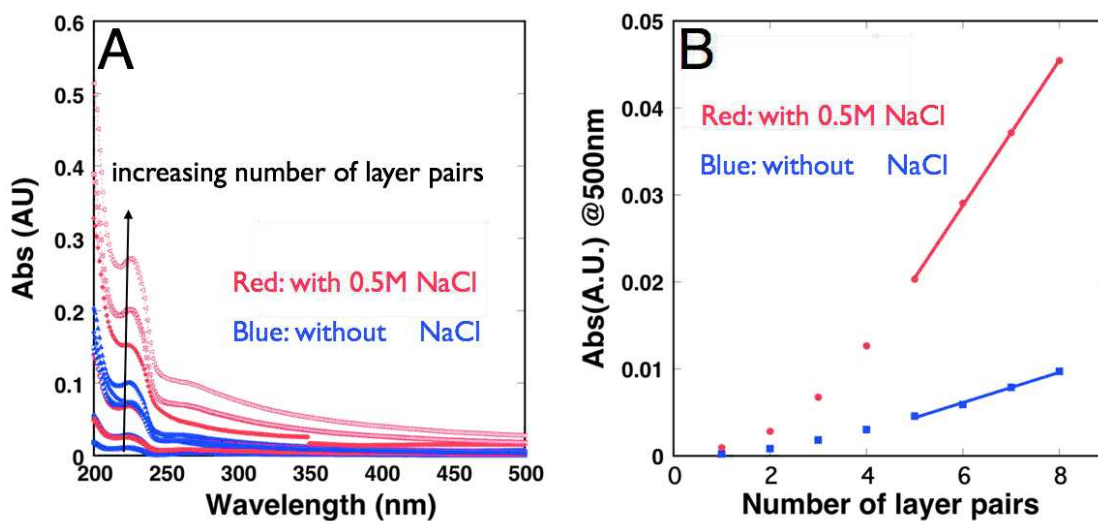


Figure IV-7. A) UV-Vis absorption spectra of LbL-assembled films of $(\text{PVAm}/\text{PSS wrapped P3-CNTs})_n$ prepared by dipping at different ionic strength conditions for PVAm solutions as a function of number of layer pairs prepared by dipping (Red dots refer to PVAm with 0.5M NaCl and Blue dots refer to PVAm without salt); B) Absorption at 500 nm as a function of the number of layer pairs (data for $n=5$ to 8 were linearly fitted, the slope is (Red) 0.0083 A.U. per layer pair and (Blue) 0.0017 A.U. per layer pair).

Similar to the thickness results shown in Figure IV-6, Figure IV-7B shows also linear growth after 5 layer pairs and faster growth when 0.5M NaCl is present in the PVAm solutions.

IV-A-2.3. LbL-assembly of CNTs based film on quartz crystal metalized with gold electrodes followed by QCM-D

Figure IV-8 displays QCM-D data of LbL-assembled $(\text{PEI}/\text{PSS wrapped P3-CNTs})_n$ and $(\text{PDADMAC}/\text{CNTs})_n$ films on gold coated quartz crystal. We can see that the adsorption of polyelectrolytes PDADMAC or PEI only results in a slight change of frequency (ΔF) compared to the large shift arising from adsorption of PSS-wrapped CNTs. Moreover, during the initial deposition steps, the adsorption of CNTs on PEI is much higher than on PDADMAC. This is probably attributed to the higher amount of PEI absorbed onto the gold surface compared to the absorption of PDADMAC, which is due to the special affinity of PEI and its branched three-dimension (3D) structure –

the same reason that makes PEI the most often used anchoring layer for the LbL-assembly. Linear behavior of the $(\text{PEI/CNTs})_n$ and superlinear behavior of the $(\text{PDADMAC/CNTs})_n$ agree with the typical linear regime of $(\text{PEI/PSS})_n$ and superlinear regime of $(\text{PDADMAC/PSS})_n$ films, which suggests similar behavior of PSS-wrapped CNTs to that of PSS. Both the linearity of the $(\text{PEI/CNTs})_n$ films and superlinearity of the $(\text{PDADMAC/CNTs})_n$ films prove homogeneous loading of the PSS-wrapped CNTs in each layer, which once again confirms successful application of the PSS-wrapped CNTs into the LbL-assembly.

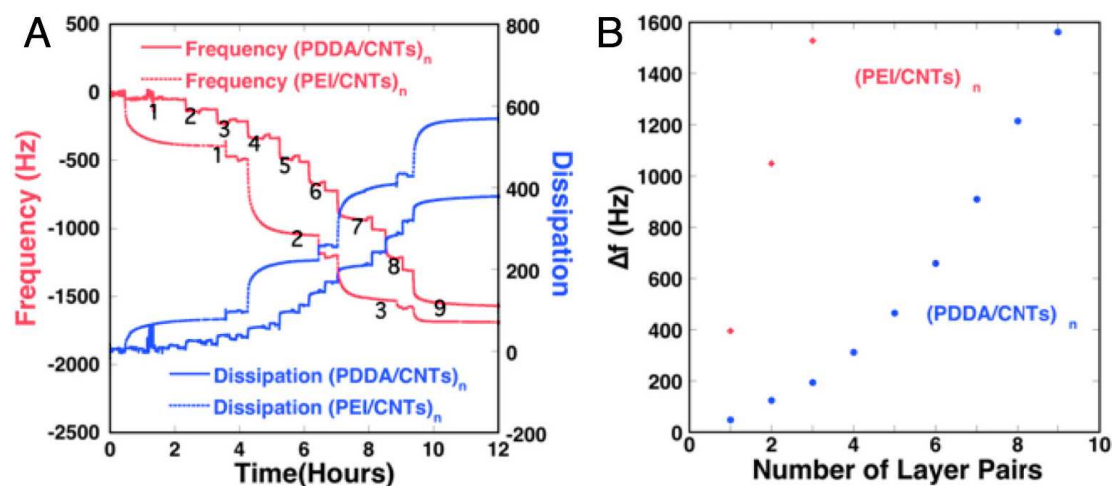


Figure IV-8. A) Raw QCM-D data showing changes in frequency and dissipation for the LbL-assembly of $(\text{PEI/PSS wrapped P3-CNTs})_n$ and $(\text{PDADMAC/PSS wrapped P3-CNTs})_n$ films built on a gold coated quartz crystal; B) QCM-d frequency shift vs number of layer pairs for $(\text{PEI/PSS wrapped P3-CNTs})_n$ and $(\text{PDADMAC/PSS wrapped P3-CNTs})_n$ films. (QCM-D data obtained at the fifth harmonic of 15 MHz)

IV-A-2.4. Micron-thick CNTs based LbL-assembled films

As mechanical tests require freestanding micron-thick films, micron-thick CNT based LbL-assembled films were prepared following the procedures described in II-A-4 on hydrophobic Si-wafers using the computer controlled dipping robot. PVAm was chosen as the polyelectrolyte partner of PSS wrapped P3-CNTs (weight ratio of P3-CNTs to PSS is 1:2) because of its high density of primary amine groups that are cross-linkable and can form hydrogen bonds with carboxylic groups carried by CNTs.

In order to characterize the thickness of as-prepared thick CNTs based films, we used both spectroscopic ellipsometry and AFM. A four-layer model (silicon, silicone

dioxide, multilayered polymer film, air) was employed for the spectroscopic ellipsometry measurements in order to determine the thickness and the refractive index of the adsorbed multilayered CNTs based films on Si-wafers. For the AFM measurements, the obtained CNTs based films on Si-wafer were carefully scratched before being imaged by AFM on the edge of the scratch. Thickness of the films can thus be obtained by the AFM profile image of the edge as shown in Figure IV-9.

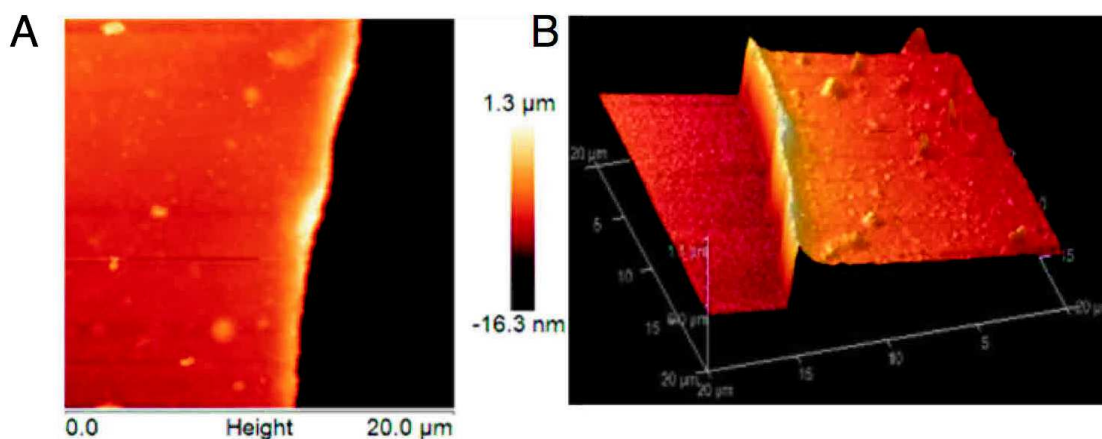


Figure IV-9. AFM images of the edge of a scratched thick film of (PVAm/PSS wrapped P3-CNTs) in A) 2d and B) 3d mode.

Thickness determined by spectroscopic ellipsometry and of AFM were compared and listed in Table IV-1. The calculated relative error between the two methods was about 4.1 ± 2.0 % in average for six different samples. The small relative error implies reliable thickness values obtained using both methods, which is important since mechanical stress will be calculated relying on the film thickness obtained.

CNTs based LbL-assembled films	AFM		Spectroscopic ellipsometry				Relative error (%)	
	Thickness(nm)	Std(nm)	Thickness(nm)	Std(nm)	n	k	Relative error	Average
Sample 1	487.1	3.9	467	3	1.605	-0.028	4.1	
Sample 2	706.5	1.3	663	8	1.673	-0.053	6.2	
Sample 3	803.8	18.8	801	22	1.603	-0.049	0.4	4.1±2.0
Sample 4	633	4.5	658	11	1.621	-0.051	3.9	
Sample 5	575.4	8.1	600	15	1.641	-0.039	4.3	
Sample 6	548	12	516	4	1.745	-0.113	5.8	

Table IV-1. Thickness measured for six thick LbL-assembled (PVAm/PSS wrapped P3-CNTs)_n films with different thickness measured by AFM and spectroscopic ellipsometry. (each thickness value determined by AFM and ellipsometry was average of 5 measurements)

IV-B. *LbL-assembled CNFs based films*

Carboxylated Cellulose nanofibrils (CNFs) (Figure IV-10A), also known as microfibrillated cellulose (MFC), are another promising candidate for the reinforcement of the LbL-assembled films owing to their wide abundance, outstanding mechanical properties, low weight, biodegradability and renewability. In contrast to hydrophobic characteristic of CNTs, CNFs possess hydrophilic properties combined with abundant charged carboxylic groups, which facilitate the preparation of stable aqueous solution or suspensions. Stable CNFs suspensions were prepared by ultrasonication in water followed by centrifugation and filtration for removing undispersed materials as described in II-A-2.2. The concentration of CNTs suspensions in water was adjusted to 0.5 mg/mL and no extra salt, apart from the counter ions to the charges on the CNFs, were added for all the LbL-assembly experiments. Cationic chitosan (CHI) (Figure IV-10B), as another abundant polysaccharide widely used for the removal of heavy, transition metals and dyes,²⁴⁶⁻²⁴⁹ was chosen for building mechanically strong LbL-assembled films with CNFs, due to its rigid linear chain conformation composed of β -1,4-D-glucose same as that of cellulose making cellulose so strong. Actually, contrary to α -1,4-D-glucose or 1-6-D-glucose carried by other polysaccharides like starch where branched chains are formed instead, the OH groups on the linear β -1,4-D-glucose units can take part in hydrogen bonds between different polymer chains, and the entire structure can make a strong planar assembly (Figure IV-11). These individual planes stack on top of each other to make a very strong three-dimensional structure. Therefore chitosan is an ideal polyelectrolyte for making robust LbL-assembled films of strong three-dimensional structure with CNFs. Chitosan (CHI) was prepared at a concentration of 1 g/L with pH adjusted to 6 as described in II-A-2.2. LbL-assembly of as-prepared CNFs suspensions and chitosan were performed by dipping and characterized with different conventional methods.

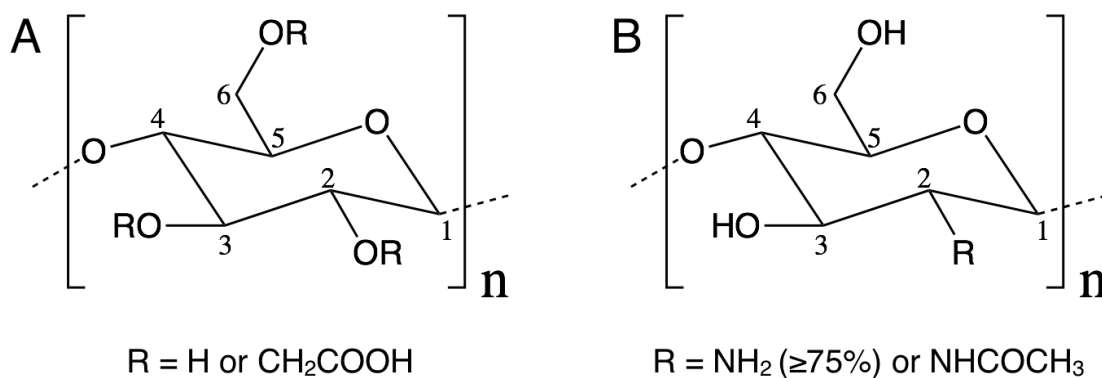


Figure IV-10. Chemical structure of CNFs A) and chitosan B).

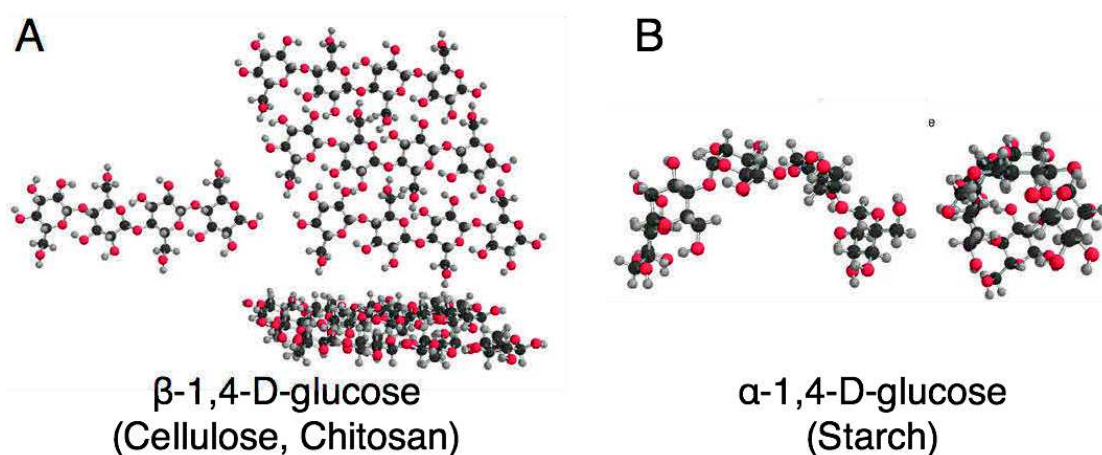


Figure IV-11. 3d chemical structure of A) linear β -1,4-D-glucose forming planar structure and B) branched α -1,4-D-glucose.

IV-B-1. LbL-assembly of CNFs based film on Si-wafer followed by ellipsometry

Although both CNFs and chitosan have outstanding properties and high potential applications especially in biobased nanocomposites, very few research works have been dedicated to studying LbL-assembly of CNFs and chitosan.^{250,251} In order to determine whether the CNFs could interact with the oppositely charged chitosan to form LbL-assembled films as previously demonstrated by the team of professor Pereira, a series of experiments were conducted where LbL-assembled films of CNFs and chitosan at different ionic strength were made by dipping on Si-wafers.

Ellipsometry was used for measuring the film's thickness and the results are summarized in Figure IV-12.

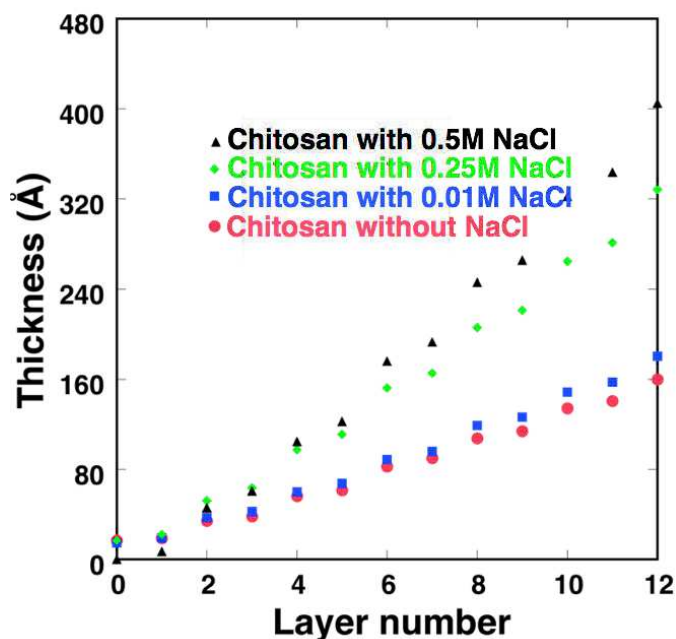


Figure IV-12. Thickness of LbL-assembled films of CNFs and chitosan at different NaCl concentrations as a function of layer number.

As we can see from Figure IV-12 that all the LbL-assembled films of CHI/CNFs shows a linear growth with increasing layer number, which suggested successful deposition of CNFs as well as chitosan on Si-wafers by dipping. The linear regime further proves inflexible rigid chain conformation of the chitosan, which is important for constructing ultra-strong mechanical films with CNFs that will be discussed in chapter VI. Meanwhile we can see that film's thickness varied with different concentration of NaCl added in the starting chitosan solution. When there is no salt or very few salt (0.01M) present in the chitosan solution, the thickness increment for each layer pair of (CHI/CNF) is about 2.7 nm. Whereas, when there is 0.25M or 0.5M of salt, each layer pair has more than twice the previous thickness increment of up to about 7 nm. To understand the reason of the influence of salt on film's thickness in this case, we have to be careful, because in contrast to the usually very flexible conventional polyelectrolytes used for LbL-assembly, chitosan has a special planar and rigid glucose polymer chain, which resulted in the linear growth regime even with salt added. Besides, compared to the differential thickness for each CNFs layer of more than 30 nm reported in the previous study where conventional cationic

polyelectrolytes like PAH and PDADMAC were used, the thickness increment for each CNFs layer in our CHI/CNFs system is less than 6 nm corresponding to one monolayer of CNFs as their diameter are about from 5nm to 15nm according to TEM pictures and previous report.¹⁰³ This finding further indicates a flat conformation of the chitosan which forms layered 3D structure with the monolayer of CNFs probably without too much interdigitation.

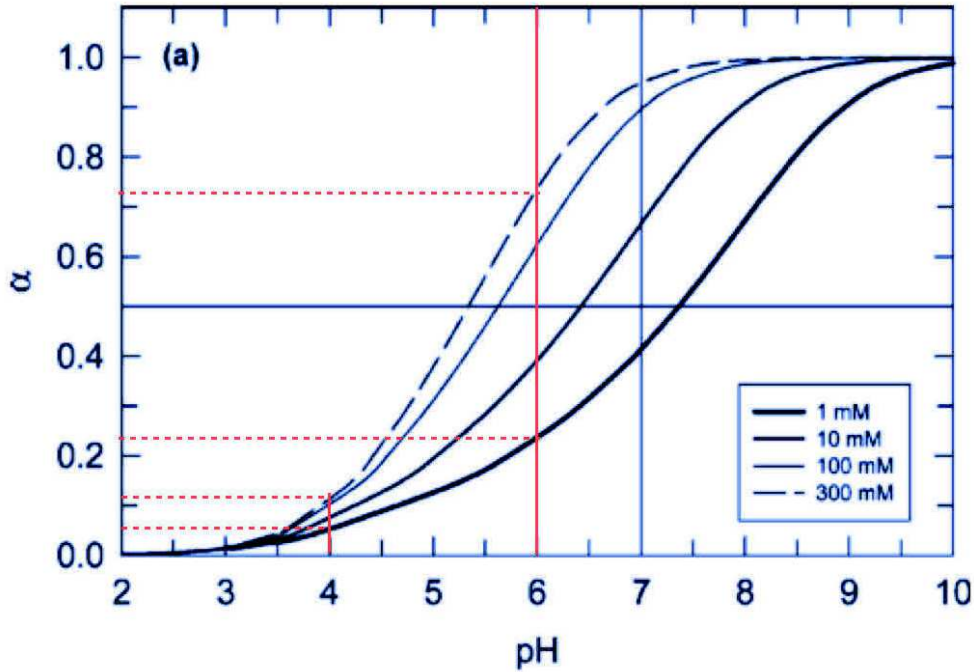


Figure IV-13. Degree of charge dissociation of CNFs as a function of pH in the bulk dispersion at different ionic strengths calculated by applying linearized Poisson-Boltzmann equation (based on curves obtained from similar samples).¹⁰³

As a result, the thickness increment by adding sufficient salt in the chitosan solution should not be only (if any) due to the conformational change of the polyelectrolytes, which, however, is the case for conventional polyelectrolytes. It is probably attributed to increase of charge density on the CNFs caused by variation of degree of charge dissociation (α) of the CNFs which is calculated by

$$\alpha = \frac{\tau^{A^-}}{\tau^{A^-} + \tau^{HA}} \quad \text{Equation IV-1}$$

where τ^{A^-} and τ^{HA} are the concentration of carboxylate and carboxylic acid respectively. Because the dissociation of carboxyl group depends significantly on

environmental pH and ionic strength, the increase of ionic strength in the PVAm solution increased the degree of charge dissociation and consequently the charge density of carboxylate on the CNFs. By applying linearized Poisson-Boltzmann equation, Wågberg et al calculated degree of charge dissociation of CNFs as a function of pH in the bulk dispersion at different ionic strengths.¹⁰³ As shown in Figure IV-13, at pH 6, which is the pH of chitosan solution, the degree of dissociation of CNFs is dramatically increased from 0.22 for the ionic strength of 1 mM to 0.72 for the ionic strength of 300 mM. The increased degree of dissociation definitely results in significantly increased charge density on the CNFs surfaces, which leads to proportional increase of chitosan loading, so as the film's thickness.

In addition, we have performed some experiments on trying to make LbL-assembled films with CNFs and chitosan at pH of 3 and 4 (data not shown), where films could not be assembled even with increased ionic strength of the solution of chitosan. Similarly the failure of making LbL-assembled films under these low pH values can also be explained by the fact that CNFs are barely charged with degree of dissociation less than 0.1 at pH of lower than 4, which is probably less than the critical minimum charge density required for possible adsorption of cationic charged chitosan on CNFs surfaces, resulting in the failure of LbL-assembly.

Larger pH of chitosan solution might further increase the degree of dissociation, which, however, is not possible for the reason that it starts to form gels when the pH of chitosan's solution becomes larger than 6. That is why pH 6 has been chosen for all the experiments during this thesis.

IV-B-2. LbL-assembly of CNFs based film on quartz crystal followed by QCM-D

QCM-D studies of LbL-assembly of CNFs and chitosan with ionic strength of 0.5M at pH 6 were also carried out by following similar procedures as described previously. Figure IV-14 shows the QCM-d results, in which stable and almost linear decrease of Δ frequency can be observed. Sauerbrey mass of the film, calculated by using the Sauerbrey equation (**Equation II-4**), shows similar linear trend, which is in great agreement with the previous results obtained by ellipsometry (see Figure IV-12). The absorption for both chitosan and CNFs were quite fast and the absorption equilibrium

was generally reached within one minute. However, the rinsing step with water for chitosan was much slower than CNFs, which could be due to two possible reasons. One possible explanation is that the CNFs have higher flexibility due to their high length-to-weight ratio, and that the chitosan chains are less flexible due to their rigid planar structures made of β -1,4-D-glucose rings. The other possibility lies on the fact that chitosan solutions prepared at pH 6, which is almost the limit maximum pH for the chitosan to be soluble in water, in addition to the presence of 0.5M of salt, had relatively high viscosity due to extensive intra and intermolecular hydrogen bonding, and gave rise to more difficult and slower rinsing step.

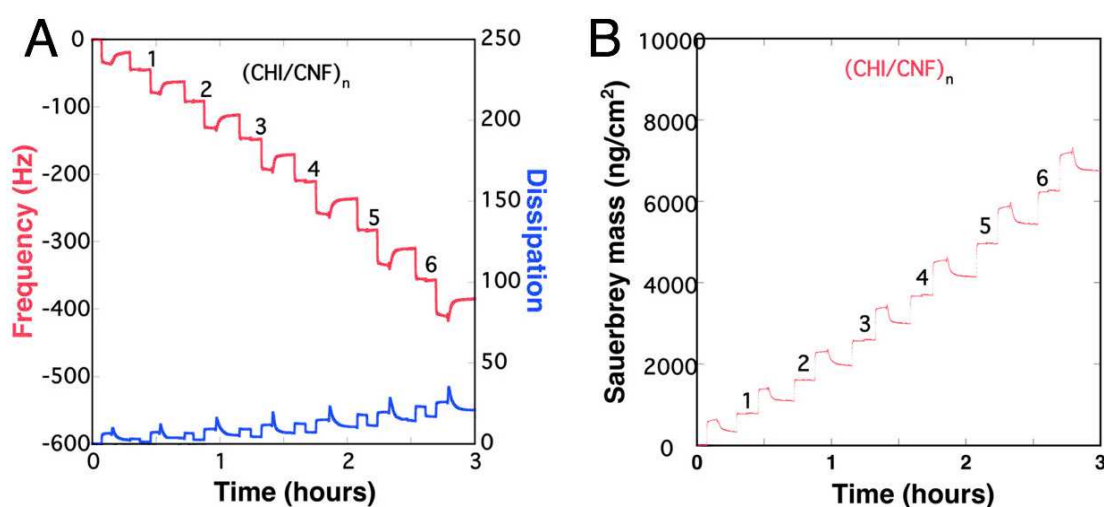


Figure IV-14. A) QCM-D data showing changes in frequency and dissipation (5th overtone) for the LbL-assembly of (CHI0.5M/CNFs)_n film on a gold coated quartz crystal as a function of time; B) Variation of calculated Sauerbrey mass of the LbL-assembled (CHI0.5M/CNFs)_n film with number of layer pairs labeled. (QCM-D data obtained at the fifth harmonic 15 MHz)

IV-B-3. Comparison between QCM-D and ellipsometry results for CNFs based LbL-assembled films

In order to be able to compare the Δ frequency data measured by QCM-d with thickness data obtained by ellipsometry, we firstly used the Sauerbrey equation (Equation II-4) to convert Δ frequency into mass that is then divided by an assumed density of 1.2 g/cm³,²⁵² which gave rise to thickness value (Sauerbrey thickness). Together with the ellipsometry thickness data, the obtained Sauerbrey thickness

values are plotted as a function of layer number in Figure IV-15A. As expected, both ellipsometry thickness and Sauerbrey thickness are somewhat linear with loaded layer number and show slightly different growth rate. The growth rate of Sauerbrey thickness is about 25 % more than that of ellipsometry thickness. Keeping in mind that real density of the wet film in the QCM-d chamber should be less than 1.2 g/cm^3 due to presence of water in the film, the real Sauerbrey thickness should be higher. On the contrary, the ellipsometry thickness was obtained by assuming refractive index of the CNFs based film to be 1.465 which should be 1.55 (determined in section IV-A-2.4.), since thickness is inversely proportional to refractive, the real or more accurate thickness should be about 5% thinner. Therefore real Sauerbrey thickness should be over 50 % more than that of real ellipsometry thickness. This is not surprising, because, in contrast to the dry state of the films assembled on Si-wafers for ellipsometry measurements, the films assembled in the QCM-D chamber is in wet state without drying, and both CNFs and chitosan are quite hygroscopic, which causes water to be trapped in the film resulting in overestimated thickness.^{253–255}

Additionally, the ratio of thickness of CNFs to that of chitosan was calculated and plotted versus layer number for both Sauerbrey thickness and ellipsometry thickness in Figure IV-15B, where the ratio for ellipsometry thickness is about 2.96 whereas the ratio for Sauerbrey thickness is only about 1.64. The reason for the big difference in the ratio of thickness of CNFs to that of chitosan might be attributed to the fact that CNFs form porous film layers whose density is much smaller than what we assumed (1.2 g/cm^3), which leads to underestimation of the thickness of CNFs layer and hence much smaller ratio of CNFs to chitosan for Sauerbrey thickness.

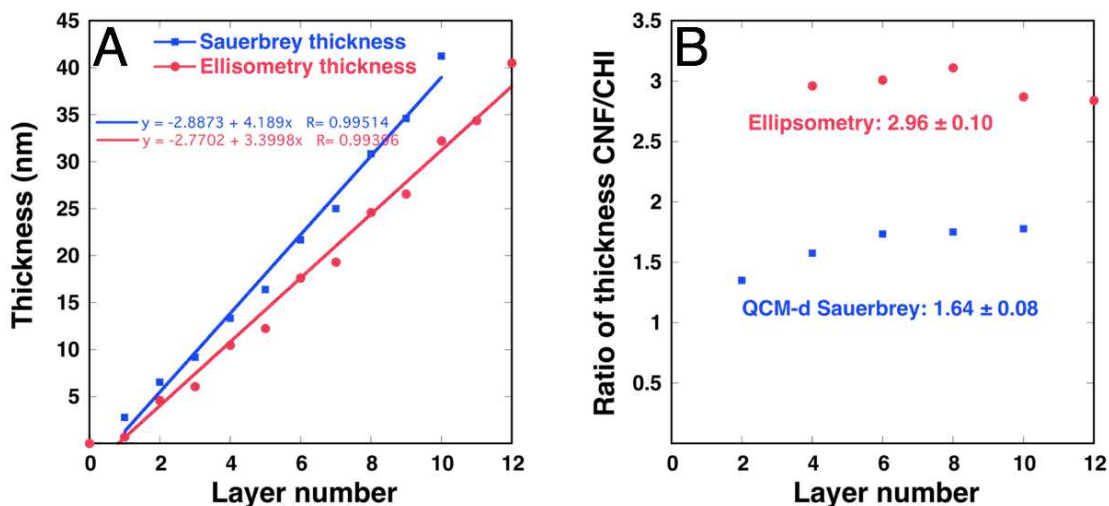


Figure IV-15. A) Thickness variation of LbL-assembled (CHI/CNFs) films as a function of layer number measured by ellipsometry (ellipsometry thickness in red points) and by calculating using Sauerbrey equation assuming a density of 1.2 g/cm^3 for the film (Sauerbrey thickness in blue points), respectively (both thickness data were linearly fitted, the slope for Sauerbrey thickness and ellipsometry thickness is 8.4 nm and 6.8 nm per layer pair respectively); B) Plot of the ratio of thickness of CNFs to that of chitosan versus layer number for both Sauerbrey thickness and ellipsometry thickness.

IV-B-4. Micron-thick CNFs based LbL-assembled films

Like CNTs, micron-thick CNFs based LbL-assembled films of $(\text{CHI/CNFs})_n$ were prepared on hydrophobic Si-wafer by robot assisted dipping. Film of 150 layer pair of (CHI/CNFs) , namely $(\text{CHI/CNFs})_{150}$, was constructed and its thickness was measured by three different methods including SEM, AFM, and spectroscopic ellipsometry.

Figure IV-16 shows a cross-sectional image of the $(\text{CHI/CNFs})_{150}$ film obtained by SEM, which gives a film thickness of $1.13 \pm 0.03 \mu\text{m}$. The white dots are broken CNFs fibers, we can see that these CNFs are homogeneously incorporated in the film, which is crucial for getting films with good mechanical reinforcements with CNFs.

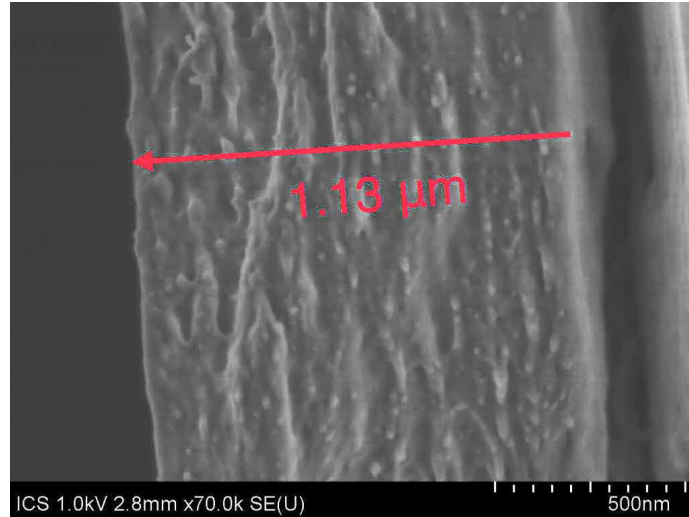


Figure IV-16. SEM cross-sectional image of (CHI/CNFs)₁₅₀ film.

The same (CHI/CNFs)₁₅₀ film was also characterized by AFM with the scratching method (Figure IV-17). By taking the height of the AMF profile image, we obtained a mean thickness of $1.148 \pm 0.006 \mu\text{m}$ for the film, which is in agreement with the thickness obtained by SEM, indicating reliability of these two techniques for measuring thick LbL-assembled films.

However, both SEM and AFM methods are of time consuming and can destroy the measured samples. We need another fast and non-destructive method. Spectroscopic ellipsometry is an ideal candidate owing to its fast and non-contact optical technique for measuring thickness of thin films (thinner than $10 \mu\text{m}$).

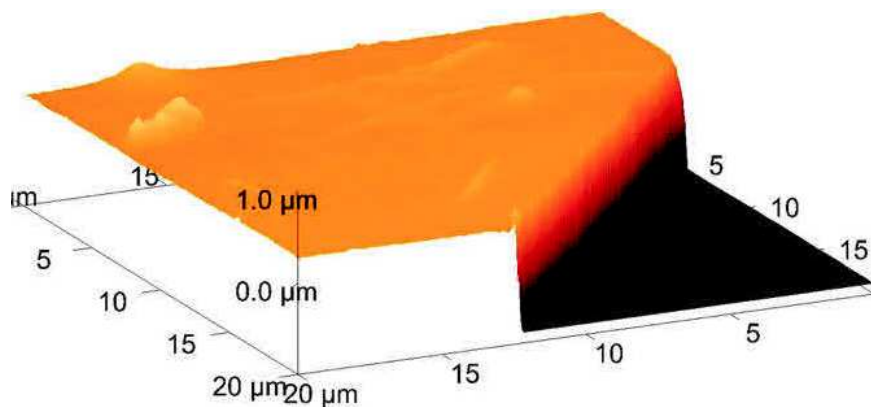


Figure IV-17. AFM image of the edge of the scratched (CHI/CNFs)₁₅₀ film shown in 3D mode.

Figure IV-18 shows psi and delta spectra of the (CHI/CNFs)₁₅₀ film (blue lines) obtained by a Sentech spectroscopic ellipsometer. The red curves are fitted results using the 4 layers model (silicon, silicone dioxide, multilayered film, air), of which 1.55 was used as fixed value for the refractive index of the layer of tested multilayered film of (CHI/CNFs)_n (Table IV-2).⁹³ We can see that the fitted spectra are very well superposed with the blue spectra of experimental measurements, which implies high accuracy of our model. As shown in Table IV-2, a representative thickness of 1131.8 nm was given by the model, which is very convincing since it is in excellent agreement with the SEM and AFM data. Therefore this model was routinely employed for measuring thick CNFs based LbL-assembled films during the thesis, except for the cases of very thin films (less than 20 layer pairs) where the single wavelength ellipsometer with fixed refractive index of 1.465 was used.

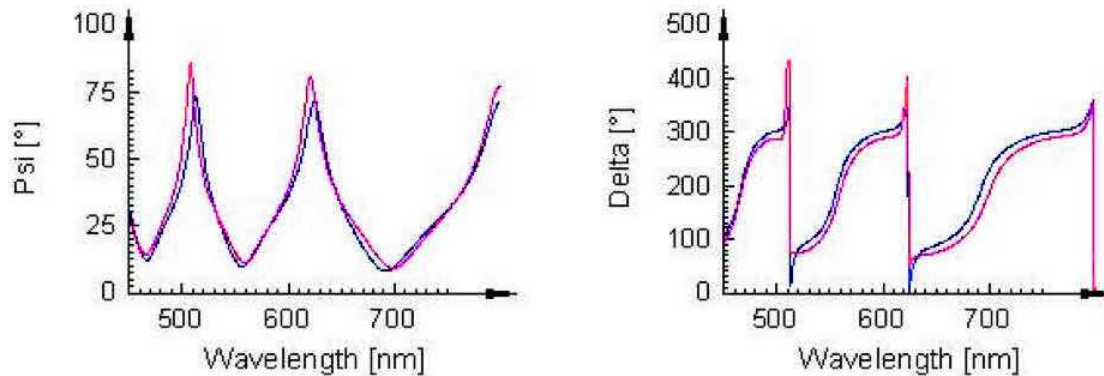


Figure IV-18. Psi and Delta spectra of the (CHI/CNFs)₁₅₀ film measured with a Sentech spectroscopic ellipsometer (blue lines are the measured data, red lines are corresponding fits)

Layer Name	Thickness [nm]	Th. fitted	n(632.8 nm)	n fitted
Freestanding Film	1131.8	yes	1.550	yes
SiO ₂ (Silicon dioxide)	3.0	no	no	no
Si (Silicon)	Substrate	no	no	no

Table IV-2. Spectroscopic ellipsometer results of the (CHI/CNFs)₁₅₀ film including thickness and refractive index (n) fitted using the 4 layers model (silicon, silicone dioxide, multilayered film, air).

Summary

In this chapter, we systematically studied the LbL-assembled films composed of nanofibers including CNTs and CNFs. An essential prerequisite to LbL-assembly was the preparation of stable aqueous dispersions of both nanofibers. Then we could successfully prepared nanofiber based LbL-assembled films by dipping and followed their growth using different characterization methods. The thickness of the micron-thick nanofibers based films was obtained through various methods including AFM, spectroscopic ellipsometry and SEM. It was found that the thickness values given by these methods were consistent to each other and that the most convenient method was the spectroscopic ellipsometry which was therefore chosen for routine measurements. These studies of the nanofibers based LbL-assembled films provide basic supporting information for the investigations of the nanofibers reinforced LbL-assembly modified membranes which will be discussed in the next chapter that is focused on the membrane performance.

V. Nanofibers reinforced LbL-assembly modified nanofiltration membranes

After having thoroughly studied the traditional three zone model of LbL-assembly and their connection with Donnan effect of nanofiltration membranes (Chapter III), as well as CNTs and CNFs based LbL-assembly (Chapter IV), we started investigating LbL-assembly on real membranes and the performance of these LbL-assembled and nanofibers reinforced nanofiltration membranes, which is presented in this chapter.

V-A. Selection of polyelectrolytes for making nanofiltration membranes

One of the main advantages of LbL-assembly technique is the composition of the film can be optimized with respect to the targeted properties. For instance, by choosing proper polyelectrolytes that are resistant to chlorine, we are able to produce nanofiltration membranes with chlorine resistant properties, which has been long desired but barely achieved by traditional techniques of making nanofiltration membranes.⁵⁴

Within the frame of our project, a very early step of work was to decide the best polyelectrolytes combination that could be used for making chlorine resistant LbL-assembly modified nanofiltration membranes. Regarding polyanion, PSS was employed for its various qualities: relatively cheap and commercial availability, excellent chemical resistance, widely studied, etc. As for the polycation, a study of chlorine resistance on six different polycations including poly(allylamine hydrochloride) (PAH), poly(ethyleneimine) (PEI), poly(4-N-methylvinylpyridinium bromide) (PVMPB), poly(vinylbenzyltrimethyl-ammonium chloride) (PVBTMAC), poly(di-allyldimethylammonium chloride) (PDADMAC), poly(acryloyloxyethyltrimethyl-ammonium chloride) (PAOETMAC) was performed within the project. Chemical structures of these polyelectrolytes candidates are displayed in Figure V-1.

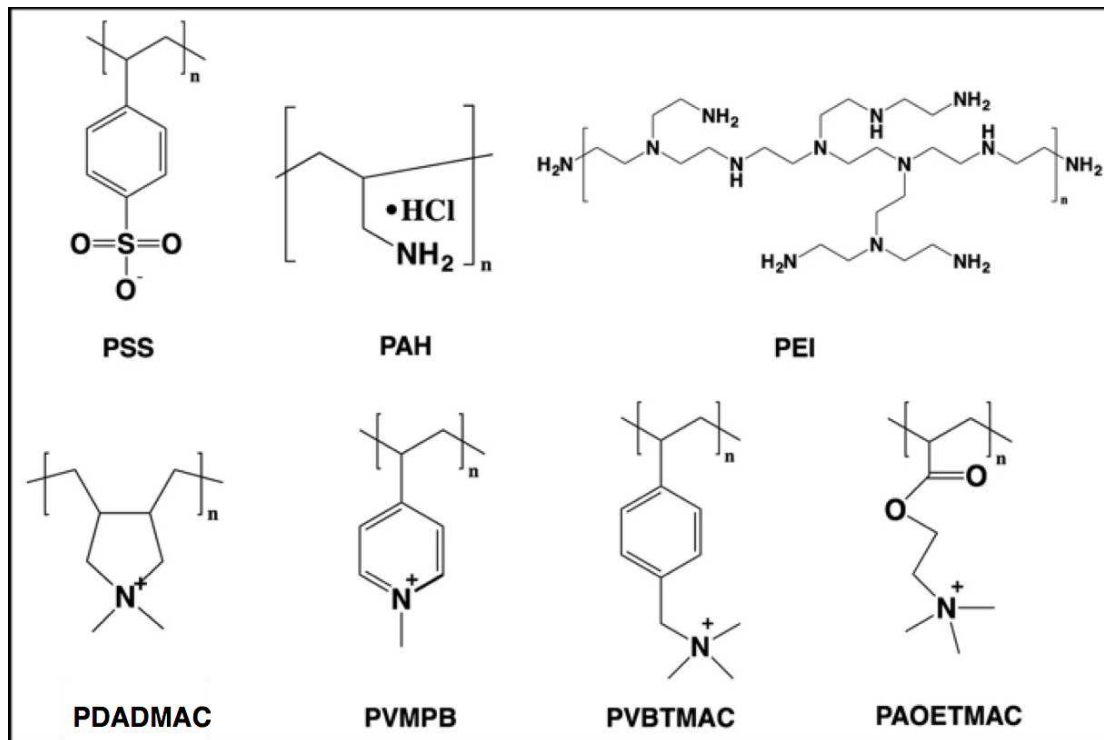


Figure V-1. Chemical structures of different polyelectrolytes candidates.

Figure V-2 shows optical pictures of the six originally transparent polycations solutions mixed with transparent hypochlorite (NaOCl) solution at pH 8,¹⁵⁶ from which we can easily find that PAH and PEI solutions showed visible turbidity after 5 min of mixing. The turbidity indicated existence of reactions of PAH and PEI with NaOCl, which was further supported by comparing the UV-Vis absorption spectra of the solutions before and after mixing with NaOCl as shown in Figure V-3.

Influence of hypochlorite solution for various polycations

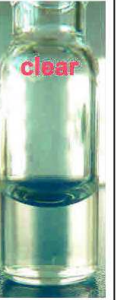
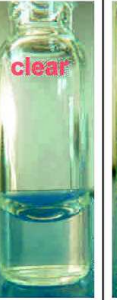
Polycation +	PAH (Polyallylamine hydrochloride 1g/L in water)	PEI (Polyethyleneimine 1g/L in water)		PDDA Polydiallyldimet hylammonium chloride 1g/L	PVBTMA Polyvinylben- zyltrimethyl- ammonium chloride 1g/L	PVMPE Polyvinyl- methylpyridine bromide 1g/L	PAOETMA Polymethacryl- oxyethyltri- methylammo- nium bromide 1g/L)
NaClO ₄	pH 8	pH 8		pH 8	pH 8	pH 8	pH 8
Concentration	1%	0.1%	1%	1%	1%	1%	1%
Reaction							

Figure V-2. Optical pictures of various polycations solutions mixed with hypochlorite solution exhibiting different degree of reaction.¹⁵⁶

From Figure V-3, we can see that before the mixing, NaOCl has strong absorption between the wavelength of 250 and 350 nm with a maximum at approximately 300 nm, and that after the mixing, both the solutions of PAH and PEI exhibit a diminished absorption at the same wavelength region and disappearance of the absorption peak at 300 nm arising from original NaOCl. Consequently, we can conclude that there has been reactions in the solutions of PAH and PEI after mixing with NaOCl, which led to the turbidity and the diminishment of UV-Vis absorbance arising from NaOCl. Actually, the reactions, taking place between PAH and NaOCl or between PEI and NaOCl, were reasonable and under our estimation considering the presence of primary amines groups in PAH and of all the primary, secondary and tertiary amines groups in branched PEI. It is known that primary, secondary and tertiary amines are prone to be oxidized by oxidizing agents like NaOCl, where oxidation of the amines may lead to loss of charges and also defragmentation of the polyelectrolytes.²⁵⁶ During the oxidation process, NaOCl is decomposed to smaller reduction products like Cl₂ and OH⁻ which do not absorb in the UV-Vis spectral region mentioned above and result in the aforementioned decrease of absorption.

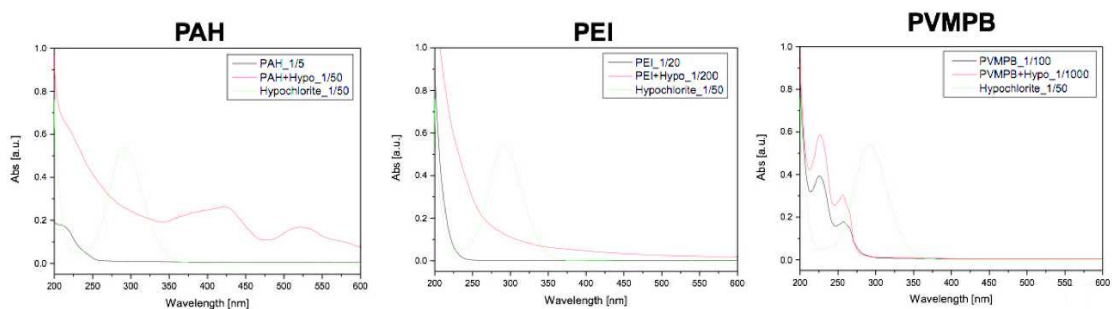


Figure V-3. UV-Vis absorbance curves of PAH, PEI and PVMPB (from left to right) solutions in reaction with NaClO_4 at a concentration of 0.1%.¹⁵⁶

Although, as shown in Figure V-2, the solutions of PVMPB stay clear after mixing with NaOCl , the UV-Vis data of the PVMPB before and after the mixing shown in Figure V-3 indicates the existence of reactions probably between the ternary amines and NaOCl which led to the decomposition of NaOCl and consequently loss of absorption in the characteristic spectra region between the wavelength of 250 and 300 nm. It is likely that the reaction between PVMPB and NaOCl produced oxidation products that remain soluble in solution, which is why there is no turbidity recorded. Therefore, the pictures in Figure V-2 can only serve as a reference, in order to determine whether the polycations are resistant to NaOCl , the UV-Vis absorption measurements were required and necessary.

While these primary, secondary and tertiary amines have appeared unstable against oxidizing agents like NaOCl , quaternary amines are considered to be resistant to NaOCl because of the lack of weak C-H bond and the lone pair of electrons which are prone to oxidation. The absence of turbidity in the three polycations solutions (PDADMAC, PVBTMAC, POETMAC) containing quaternary amines after mixing with NaOCl , as shown in Figure V-2, implied possible resistance to NaOCl . However, UV-Vis absorption curves of these three polycations solutions shown in Figure V-4 suggest that only PDADMAC was stable against NaOCl with no decrease or disappearance of characteristic absorption. A decrease of absorbance of NaOCl in the cases of PAOETMAC and PVBTMAC indicates instability against NaOCl . The oxidation of PAOETMAC must have taken place on the methacryloxy and ester groups rather than on the quaternary ammonium groups. However, the oxidation of PVBTMAC is hard to explain. A possible explanation is that it could have happened

either by an oxidative α -cleavage between the phenyl ring and the polymer backbone or by a β -cleavage leading to smaller PVBTMAC chains.²⁵⁶

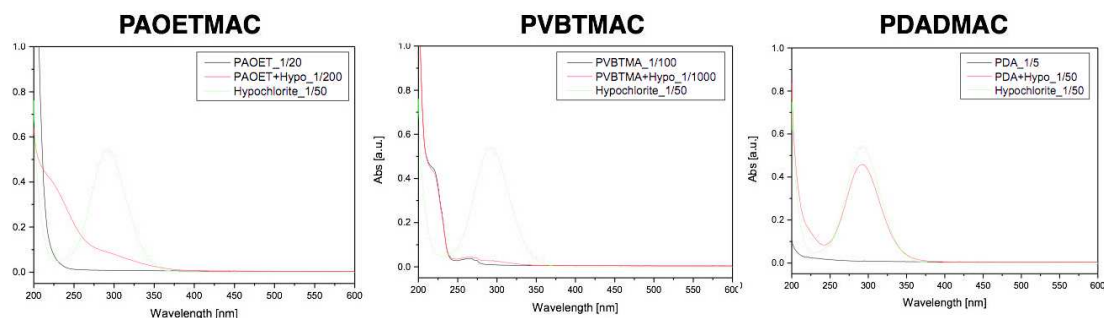


Figure V-4. UV-Vis absorbance curves of PAOETMAC, PVBTMAC and PDADMAC solutions (from left to right) in reaction with NaClO_4 at a concentration of 0.1%.

To conclude, after UV-Vis absorption studies of different polycations bearing different types of amines groups, it was found that PDADMAC containing quaternary amines groups was the most stable polycation that is resistant to NaOCl . Therefore, together with the chlorine-resistant polyanion PSS, PDADMAC was selected as the polyelectrolytes component for making LbL-assembly modified nanofiltration membranes.

V-B. *LbL-assembled coatings for the membranes*

After having chosen PSS and PDADMAC as the polyelectrolytes combination for making the selective layer of the LbL-assembly modified nanofiltration membranes, LbL-assembly behaviors of this system of selective layer of $(\text{PDADMAC/PSS})_n$ and the nanofibers reinforcing system were studied and discussed as described in chapter III and chapter IV respectively. All these studies were performed prior to making LbL-assembled coatings on real membrane porous supports so as to obtain membranes with best performance, which will be discussed in this chapter. Before investigating the different performance of the LbL-assembly modified membranes, three different methods were used for determining whether the coatings were successfully assembled on the membranes porous supports (HFs).

V-B-1. SEM characterization

The first method used was SEM characterization of the membranes. LbL-assembled film of 4 layer pairs of (PDADMAC/PSS) were deposited on hollow fiber membrane HF's following the procedure described in II-A-7.2. before being characterized on the cross-section by SEM. Figure V-5 shows cross-sectional SEM images of an untreated HF's membrane support and the HF's membrane coated via LbL-assembly of 4 layer pairs of (PDADMAC/PSS). Despite resolution limitation of SEM, the thin layer of LbL-assembled coating having denser structure than the polymeric porous membrane support can still be seen on top of the porous HF's membrane support, which indicates successful deposition of LbL-assembled coating on the membrane support.

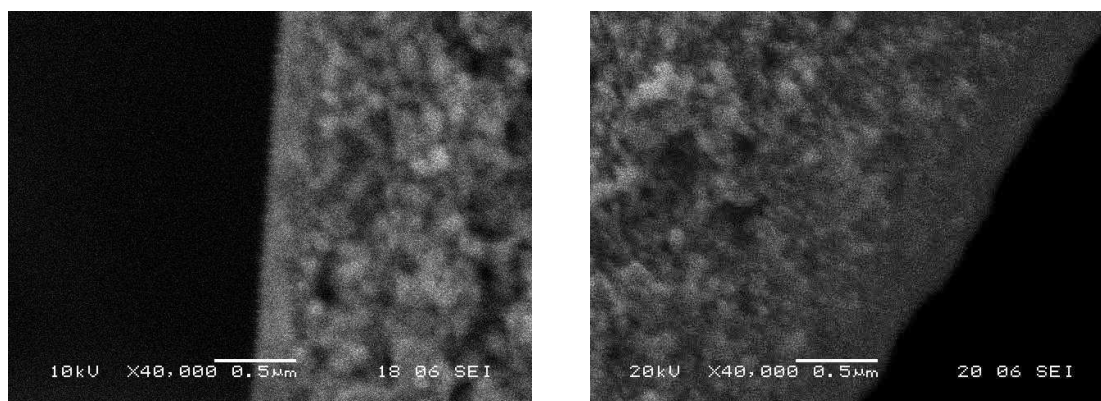


Figure V-5. Cross-sectional SEM image of the inner side of (figure on the left) an untreated HF's membrane and (figure on the right) a HF's membrane coated with 4 layer pairs of LbL-assembled (PDADMAC/PSS).

V-B-2. Small dye molecules separation by LbL-assembly modified nanofiltration membranes

The second method used was through a comparison of the untreated hollow fiber membrane support HF's ability of filtering a small dye molecules with that of LbL-assembly coated HF's. A red organic acid dye of Nylosan Red E-BL150 was used. Its molecular weight is 548.57 g/mol and its chemical structure is displayed in Figure V-6. Water solution of this dye was prepared at a concentration of 5mM.

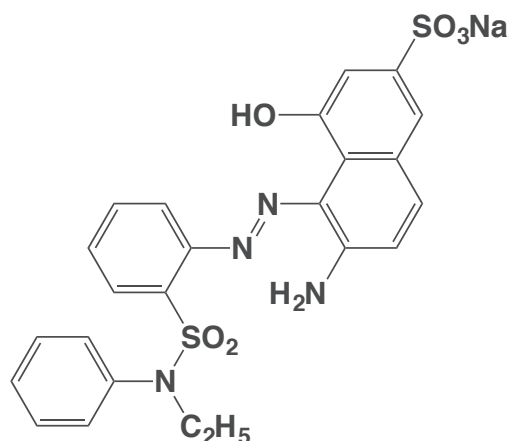


Figure V-6. Chemical structure of Nylosan Red E-BL150.

Two single fiber modules of HF membranes were made according to the procedure described in II-A-5.1. One module was left intact, while the other one was coated with 4 layer pairs of (PDADMAC/PSS) by LbL-assembly following the procedure protocol (II-A-7.2.). Then filtrations of the dye solutions were carried out for both membranes modules until the module chambers were filled with permeated solutions. As the untreated membrane porous support is basically an ultrafiltration membrane whose molecular weight cut-off (MWCO) is larger than 10kDa, it should not be able to filtrate the small red dye of only 548.57 Da. This is confirmed by Figure V-7 showing the module chamber of the untreated membrane filled with permeated red color solution that is very much the same as the feed red dye solution, which indicates that the untreated membrane could not retain the small red dye molecules. On the contrary, the module chamber of LbL-assembly coated membrane is filled with colorless solution that was confirmed to be purely water by UV-Vis spectra (data not shown), which not only proves successful modification of the membrane support by LbL-assembly but also suggests realization of making LbL-assembly modified nanofiltration membranes with the ability to retain small organic dye molecules having molecular weight less than 1000 Da.

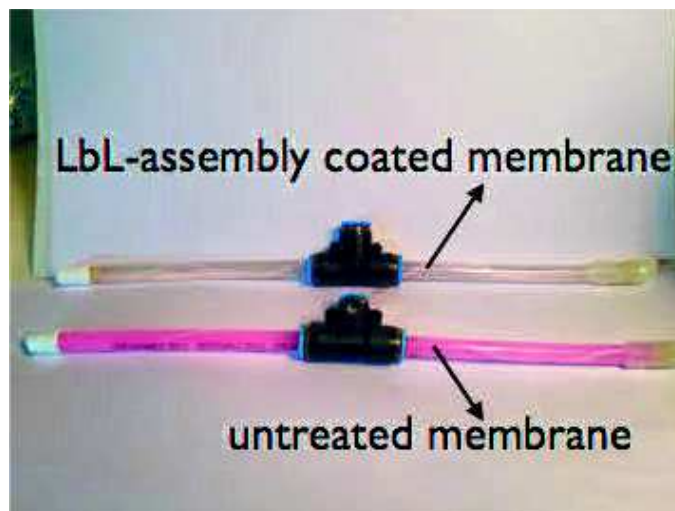


Figure V-7. Optical pictures of the two membranes modules filled with permeated solutions after filtration of the red dye solutions.

V-B-3. UV-Vis reflection spectroscopy measurements

The last method involves UV-Vis reflection spectroscopy measurements. As the hollow fiber membranes have curved and small surfaces, it is almost impossible to make UV-Vis reflection spectroscopy measurements on them. That's why flat sheet membranes made of same raw polymers were prepared by tape-casting and provided by our partner so as to make LbL-assembly coatings and UV-Vis reflection spectroscopy measurements on the flat surfaces of these membranes. LbL-assembled coatings of $(\text{PDADMAC/PSS})_n$ on flat sheet membranes were carried out and characterized by UV-Vis reflection spectroscopy following the procedure described in section II-A-7.1. The raw reflection spectra were already displayed Figure III-9A.

As shown in Figure III-9A, the spectrum labeled as $n=0$ refers to the untreated membrane support HFs, while the spectra of LbL-assembly modified membranes with n layer pairs of (PDADMAC/PSS) were labeled with $n = 1$ to 7. We can easily see that reflections of the modified membrane decreased with increasing number of layer pairs n in the characteristic wavelength range of PSS from 200 to 235 nm, which implies once again successful deposition of LbL-assembly coating of (PDADMAC/PSS) on the membrane support.

V-C. Performance of LbL-assembly modified membranes

Since successful modification of membranes by LbL-assembly has been achieved, it's important to investigate the performance of these membranes. Retention of divalent ions and water permeability are the two most important properties of nanofiltration membranes. MgSO_4 retention and water permeability were measured following the procedure described in section II-B-5.1 and were calculated using the Equation I-3 and the Equation I-1 respectively.

LbL-assembly modification of Hollow fiber membranes HFs started always with PDADMAC as first layer for better adhesion with the negatively charged HFs surface through electrostatic interactions. Several HFs membranes were coated with different layer pairs of (PDADMAC/PSS) whose MgSO_4 retention and water permeability were measured and plotted in Figure V-8A. In the mean time, UV-Vis reflection spectroscopy measurements were carried out for LbL-assembly modified flat sheet membranes also coated with an increasing number of layer pairs of (PDADMAC/PSS), and the absorption characteristic values of $\log 1/R$ were calculated and then plotted as a function of number of layer pairs in Figure V-8B.

As already discussed in section III-D-1. , Figure V-8B shows that the first 4 layer pairs belong to the transitional zone I, and that steady linear regime (zone II) starts only from the fourth layer pairs, where Donnan exclusion effect reaches and remains the maximum owing to the presence of extrinsic charges in zone II. This finding is consistent with the retention and permeability results shown in Figure V-8A, which shows that water permeability decreased and MgSO_4 retention increased with increasing number of layer pairs for the first 4 layer pairs, and that retention stops increasing and permeability drops slightly due to probably the increment of water diffusion distance that is inversely proportional to permeability.

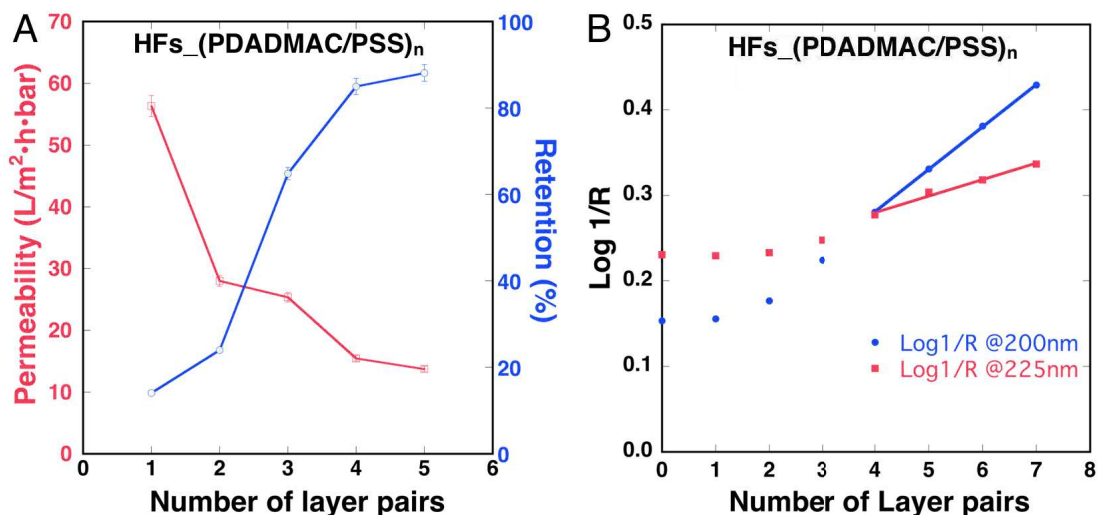


Figure V-8. A) MgSO_4 retentions and water permeability for LbL-assembly modified hollow fiber membranes coated with n layer pairs as a function of number of layer pairs; B) $\text{Log } 1/R$ as a function of number of layer pairs obtained from UV-Vis reflection spectroscopy measurements data.

Briefly, LbL-assembly modified membranes coated with different number of layer pairs of (PDADMAC/PSS) were successfully prepared and their MgSO_4 retention and water permeability were measured. The 4 layer pairs coated membranes exhibited the best MgSO_4 retention of $85.5 \pm 2.1\%$ combined with optimal water permeability of about $13.5 \pm 1.5 \text{ L/m}^2 \cdot \text{h} \cdot \text{bar}$ which is almost twice that of commercial nanofiltration membranes due to much thinner selective coating made by LbL-assembly.¹⁰ In addition, the possibility of tailoring the MgSO_4 retention by varying the number of layer pairs, as well as the ability of adjusting the membranes' charge by selecting either polyanions or polycations as the top terminating layer, are very attractive for making a wide range of membranes with customizable properties.

Furthermore, chlorine resistance of the LbL-assembly modified membranes coated with optimal 4 layer pairs of (PDADMAC/PSS) were studied by our project partners (results not shown), who showed that the as-prepared LbL-assembly modified nanofiltration membranes have more than 100000ppm-hrs of chlorine resistance. For comparison, the best commercial nanofiltration membranes have chlorine resistance of less than 1000ppm-hrs.⁵⁰ The excellent chlorine resistance of the (PDADMAC/PSS)_n coated LbL-assembly modified nanofiltration membranes is

ascribed to the good chlorine resistant properties of the selected polyelectrolytes as previously discussed in section V-A.

V-D. Performance of LbL-assembly modified membranes reinforced with nanofibers

Nanofibers have received much attention due to their unique properties such as large surface area, high porosity, small pore size, superior mechanical properties and ease of addition of surface functionalities on nanoscale compared to other material. Carbon nanotubes (CNTs) and cellulose nanofibrils (CNFs) have found their applications in fabricating membranes with high flux owing to the formation of interconnected nanopores and nano waterchannels, and with high retention thanks to the numerous nanoscaled functionalities attached on the nanofibers.^{216,217} In this thesis, we try to improve the filtration and mechanical performance of LbL-assembly modified membranes by incorporating CNTs and CNFs in an intermediate layers between the porous membrane support and the selective polyelectrolytes multilayers via LbL-assembly.

As pointed out in previous chapter, we studied the preparation of aqueous suspensions of CNTs and CNFs followed by the fabrication and characterization of LbL-assembled films with these suspensions. Stable aqueous suspensions of CNTs and CNFs were obtained and homogeneous CNTs and CNFs based LbL-assembled films were achieved. Taking advantage of these studies, we study in this section the influence of the incorporation of these nanofibers on the LbL-assembly modified membranes by measuring their membrane performance including MgSO_4 retention and water permeability.

V-D-1. Performance of LbL-assembly modified membranes reinforced with CNTs

Carbon nanotubes (CNTs) are ideal reinforcing nanofibers candidates for their extremely strong mechanical strength and high surface area. Besides, the inherent rigidity of CNTs allows formation of reticular nanofibers network on the porous membrane support which helps to avoid blockage of the support and reinforce the

mechanical properties of the LbL-assembly coating on it. In order to coat CNTs via LbL-assembly, stable aqueous suspensions of individual CNTs are pre-required, which, however is difficult to achieve because as-produced CNTs tend to aggregate together in bundles by strong van der Waals interactions. We managed to prepare stable aqueous suspensions of CNTs by physical wrapping of PSS with help of ultrasonication which can disperse the CNTs bundles into individual nanotubes due to reduction in surface energy of the PSS-wrapped CNTs in water. PSS wrapped P3-CNTs suspensions were prepared following the protocol defined in II-A-2.1. and pH of the suspensions was maintained at 6.0 ± 0.5 .

Before utilizing the CNTs suspensions for reinforcing the LbL-assembly modified membranes, we had to investigate the influence of incorporation of CNTs on the growth behavior of LbL-assembled films $(\text{PDADMAC/PSS})_n$ that serve as selective layer. For this purpose, LbL-assembled films of (PDADMAC/PSS) reinforced with one layer of CNTs were prepared on Si-wafers and were characterized by ellipsometry.

As our CNTs suspensions are negatively charged, two different polycations solutions of PVAm ($\text{pH}=8$) and PDADMAC were used as first layer prior to the deposition of the CNTs. On top of the first CNTs based layer pair of (PVAm/CNTs) or (PDADMAC/CNTs) , increasing layer pairs of (PDADMAC/PSS) were coated, herein referring to $(\text{PVAm/CNTs})_1(\text{PDADMAC/PSS})_n$ and $(\text{PDADMAC/CNTs})_1(\text{PDADMAC/PSS})_n$ respectively. Film thickness of these two films and their thickness increment for each even layer were compared with that of pure polyelectrolytes film of (PDADMAC/PSS) namely $(\text{PDADMAC/PSS})_1(\text{PDADMAC/PSS})_n$, which are all plotted in Figure V-9.

The thickness increment of even layers corresponds to thickness of each layer of PSS except for the first layer of the CNTs based films that corresponds to thickness of CNTs layer. Figure V-9 clearly shows that the incremental thickness of CNTs for both CNTs based films is much thicker than the incremental thickness of the first layer of PSS for the film of pure polyelectrolytes $(\text{PDADMAC/PSS})_1(\text{PDADMAC/PSS})_n$, which suggests successful incorporation of CNTs. Larger thickness of CNTs on PVAm ($42.98 \pm 1.42 \text{ \AA}$) than on PDADMAC ($31.01 \pm 0.70 \text{ \AA}$) may be explained by the effects of charge stoichiometry.²⁵⁷ As degree of charge dissociation/ionization of weak polyelectrolytes depends strongly on its

environmental pH and ionic strength, the charge stoichiometry brings about higher amount of absorption of weak polyelectrolytes for compensating the charge when the degree of ionization is lower. PDADMAC is a strong polyelectrolyte bearing quaternary ammonium groups, thus its degree of ionization doesn't change with the environmental pH. Whereas, PVAm is a weak polyelectrolyte having high density of primary amine groups whose pKa is about 10.5, and its degree of ionization is close to 0.3 at pH 8 that was used for our experiments.²⁵⁸ Consequently, the absorption of PVAm is higher than PDADMAC, leading to more CNTs absorption and thus thicker layer of CNTs on PVAm compared to PDADMAC.

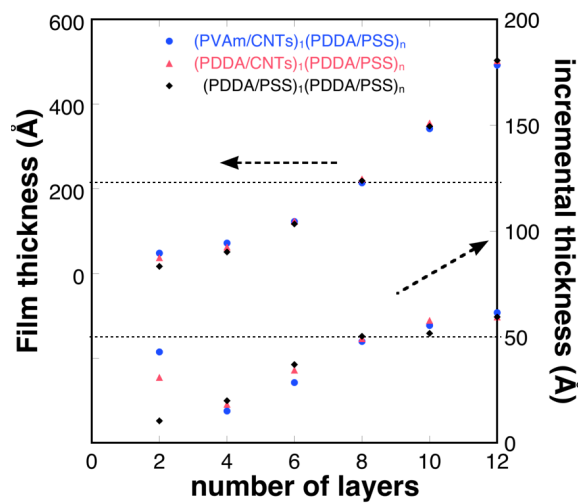


Figure V-9. Plot of film thickness (left axis) and incremental thickness of each even layer (right axis) as a function of number of layers for CNTs based films of $(\text{PVAm/CNTs})_1(\text{PDADMAC/PSS})_n$ and $(\text{PDADMAC/CNTs})_1(\text{PDADMAC/PSS})_n$ compared with films of $(\text{PDADMAC/PSS})_n$ as a function of number of layers.

Figure V-9 also shows that after 6 layer or 3 layer pairs, both the CNTs based films have similar film growth and thickness increment of the even layer (PSS) compared to the $(\text{PDADMAC/PSS})_n$ film, which implies that the incorporation of the CNTs might not have changed too much the upper film's growth behavior and thus neither its Donnan exclusion effect. In order to verify this hypothesis, we turned to investigate performance of LbL-assembly modified membranes coated with these CNTs based structure. As previously discussed, optimal $(\text{PDADMAC/PSS})_n$ modified membranes system was obtained by coating 4 layer pairs of $(\text{PDADMAC/PSS})_n$, namely, $(\text{PVAm/CNTs})_1(\text{PDADMAC/PSS})_3$, which is used for comparison. Therefore we prepared LbL-assembly modified membranes with coatings of one layer of CNTs

based films which are $(\text{PDADMAC/CNTs})_1(\text{PDADMAC/PSS})_3$ and $(\text{PVAm/CNTs})_1(\text{PDADMAC/PSS})_3$ respectively. The coating procedure is the same as other membrane coating procedure.

LbL-assembly modified nanofiltration membranes	Film thickness (Å)	Incremental thickness of 1 st even layer (Å)	MgSO ₄ Retention (%)	Water permeability (L/m ² •h•bar)
$(\text{PDADMAC/PSS})_1(\text{PDADM AC/PSS})_3$	218.82±1.49	10.44±0.47	85.5±2.1	13.5±1.5
$(\text{PDADMAC/CNTs})_1(\text{PDAD MAC/PSS})_3$	223.02±2.89	31.01±0.70	84.7±3.1	20.8±0.5
$(\text{PVAm/CNTs})_1(\text{PDADMAC/ PSS})_3$	214.31±6.92	42.98±1.42	84.3±1.4	18.8±1.0

Table V-1. Film thickness and incremental thickness of first even layer of the CNTs based films $(\text{PDADMAC/CNTs})_1(\text{PDADMAC/PSS})_3$, $(\text{PVAm/CNTs})_1(\text{PDADMAC/PSS})_3$ and compared with that of $(\text{PDADMAC/PSS})_1(\text{PDADMAC/PSS})_3$ in addition to MgSO₄ retention and water permeability of LbL-assembly modified membranes coated with these films.

Table V-1 shows that membrane coated with both CNTs based films have similar MgSO₄ retention as that of membrane coated without CNTs, which confirms our hypothesis of intact structure of the upper selective film when one layer of CNTs is incorporated. Moreover, compared to the pure polyelectrolytes modified membranes, the water permeability of both membranes reinforced with CNTs rose more than 40%. Since both CNTs based films have very close thickness to that of pure (PDADMAC/PSS) film, the increase of permeability must arise from the incorporation of CNTs that generates mesh structure and nano-scaled porous water transportation channel leading to a higher flux. Therefore, the concept of using nanofibers for increasing permeability of LbL-assembly modified membranes without compromise at the cost of reducing membranes' retention is validated. Based on the principle of not reducing membranes' retention, more layers of CNTs were not employed due to possible decline of retention. However, more layers of CNTs should bring more nano-scaled water channels leading to higher permeability as shown in Table V-2. Thus our concept of nanofibers reinforced membranes could be applied to

other membranes fabrication systems especially for TFC membranes that bear dense and thick selective coatings.

LbL-assembly modified membranes	MgSO ₄ Retention (%)	Water permeability (L/m ² •h•bar)
(PDADMAC/PSS) ₂	24.1±1.1	28.0±1.5
(PDADMAC/CNTs) ₂ (PDADMAC/PSS) ₂	22.0±1.4	46.7±1.0

Table V-2. Performance of LbL-assembly modified membranes reinforced with two layers of CNTs on which 2 layer pairs of (PDADMAC/PSS) were added, compared with LbL-assembly modified membranes coated with only 2 layer pairs of (PDADMAC/PSS). It shows that two layers of CNTs coated membranes has similar MgSO₄ as that of membranes modified with two layer pairs of (PDADMAC/PSS), but much higher permeability can be observed for the CNTs based membranes.

In contrast to traditional TFC nanofiltration membranes whose selective coating layer has a thickness of generally far much thicker than 50 nm, the LbL-assembled coating for our optimal nanofiltration membranes is only about 22 nm, which endows the LbL-assembly modified membranes with much higher permeability. Moreover, the ease of preparation and various possibilities of customization make LbL-assembly technique highly interesting for making new generation membranes.

V-D-2. Performance of LbL-assembly modified membranes reinforced with CNFs

Although CNTs reinforced LbL-assembly modified membranes have demonstrated prominent performance including high MgSO₄ retention and improved water permeability comparing with unreinforced membranes, potential toxicity, relatively high cost and difficulty in preparation of aqueous suspension of CNFs may impede their real applications in commercial membranes. That's why we were also interested in another nontoxic, relatively low cost and also mechanically strong nanofibers - cellulose nanofibrils (CNFs). Cellulose is the most abundant material in the biosphere

bearing long polysaccharide chains composed of β -1,4-D-glucose rings. CNFs are usually produced by high-pressure homogenizer combined with chemical pre-treatments such as enzymatic pre-treatment or TEMPO oxidation pre-treatment.^{259,260} The CNFs never-dried pulp that we used was a gift from professor Wagberg and Innventia AB (Stockholm, Sweden). They made the carboxymethylated CNFs in an innovative way, which involved a carboxymethylation pretreatment step before high-pressure homogenization.^{103,261} The CNFs produced in this new manner have fewer large fragments and require lower energy consumption. Stable suspension of CNFs were prepared as described in section II-A-2.2 for LbL-assembly.

LbL-assembly modified membranes	MgSO ₄ Retention (%)	Water permeability (L/m ² •h•bar)
(PDADMAC/PSS) ₂	24.1±1.1	28.0±1.5
(PDADMAC/CNFs) ₂ (PDADMAC/PSS) ₂	62.0±1.2	29.4±1.0

Table V-3. Comparison of MgSO₄ retention and water permeability between 2 layers of CNFs reinforced LbL-assembly modified membranes and membranes modified with 2 layer pairs of (PDADMAC/PSS).

CNFs reinforced LbL-assembly modified membranes coated with two layers of CNFs followed by two layer pairs of (PDADMAC/PSS) were prepared and their MgSO₄ retention and water permeability are determined and compared with membranes coated with two layer pairs of (PDADMAC/PSS) (**Table V-3**). Surprisingly, in contrast with CNTs, the CNFs reinforced membrane didn't change too much in term of water permeability compared to membrane without nanofibers, whereas the MgSO₄ retention dramatically increased from 24% to 62%. Two possible explanations could be drawn for the unchanged water permeability. The first explanation involves flexibility of nanofibers. CNFs are more flexible than CNTs due to presence of amorphous compositions leading to densely packed structure with very few pores if any. This is consistent with reported excellent gas barrier properties of CNFs based membranes,²⁶² which was ascribed to the dense structure formed by the nanofibrils through intra and intermolecular hydrogen bonding. This however needs to be further studied to confirm. Another explanation lies on the hydrophilic property of CNFs.

Based on experimental and computational results of ultra fast water transport in the cores of carbon nanotubes²⁶³ and protein channels², Ma et al.²⁶⁴ predicted that nanofibers with hydrophobic surface should lead to greater permeability improvement than hydrophilic fibers. This could explain why highly hydrophilic CNFs could not improve permeability as the hydrophobic CNTs did. Although the possible densely packed film structure of hydrophilic CNFs based films prohibit their role as water nanochannels promoter, the high specific area of CNFs could provide great number of active sites on the surface, which could immobilize contaminant ions especially multivalent ions, leading to the increased retention.^{265,266} Therefore, the incorporation of CNFs in the LbL-assembly modified membranes might not increase membranes' permeability but might improve membranes' retention with their changeable function sites. Because of limited time provided by our project, we did not further investigate membrane performance of CNFs reinforced membranes, but rather focused more on mechanical reinforcing role of CNFs which will be pointed out in next chapter.

VI. Mechanical properties of LbL-assembled films reinforced with nanofibers

Apart from making LbL-assembly modified nanofiltration membranes and enhancing the membranes' performance by incorporating nanofibers as intermediate reinforcing layer of porous mesh structure, another aim of the present work is to reinforce the mechanical properties of LbL-assembled films by introducing the very nanofibers that we use for enhancing membrane performance, for the reason that the LbL-assembled coatings on the membranes require high mechanical strength for spanning over and without blocking the membrane support's holes, as well as for resisting harsh membrane operating conditions.¹

In order to test the mechanical properties of LbL-assembled films, thick freestanding films were constructed with the help of a dipping robot or spin-coater in the case of spin-assisted LbL-assembly, and then samples of these films were prepared and tested by a custom-made tensile testing machine recording the displacement and applied force. Stress-strain curves were obtained after tensile tests and data treatment as described in section II-B-5. In addition to the tensile tests of the freestanding LbL-assembled films, nanoindentation tests on similar thick films LbL-assembled on hydrophilic silicon wafer were also carried out to provide supplementary information of the mechanical properties of the LbL-assembled films.

VI-A. Mechanical properties of LbL-assembled films of polyelectrolytes

Before looking into mechanical properties of nanofibers reinforced LbL-assembled films, we explored the mechanical strength of LbL-assembled films composed of only polyelectrolytes. For this purpose, thick freestanding (PDADMAC/PSS)₁₀₀ film was constructed via LbL-assembly using a computer controlled dipping robot. Then tensile tests were carried out for measuring their mechanical properties. Film thickness was obtained by ellipsometry and used for calculating the stress. Stress-strain curve was obtained and plotted as shown in Figure VI-1. The LbL-assembled

film of (PDADMAC/PSS)₁₀₀ has a Young's modulus of about 2.4 GPa and a tensile strength of about 58 MPa, which are quite remarkable compared to previously reported tensile strength of 9 MPa for films of (PEI/PAA), whereas the elongation-to-break of about 3.5% is similar to that of (PEI/PAA) film.¹⁵ Compared to another study, where similar tensile strength of about 70MPa was reported for LbL-assembled films of (PDADMAC/PAA), this time the films' elongation-to-break was much smaller (10% for the film of (PDADMAC/PAA)).²⁶⁷ These differences might be attributed to different polyelectrolytes components of the tested films. As the selective layer of our LbL-assembly modified membranes are made of (PDADMAC/PSS), we only focused on the obtained mechanical properties data of the (PDADMAC/PSS) system and we didn't further explore the exact reasons for these differences in mechanical properties of LbL-assembled films made of different polyelectrolytes, which although could be interesting for future studies.

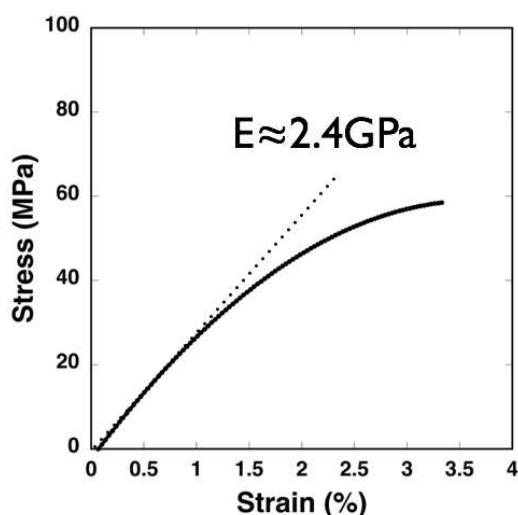


Figure VI-1. Typical stress-strain curve (polynomial fit) of LbL-assembled film of (PDADMAC/PSS)₁₀₀ (the Young's modulus deduced at low deformation is about 2.4 GPa).

VI-B. Mechanical properties of LbL-assembled films reinforced with CNTs

Knowing the mechanical properties of LbL-assembled films composed solely of polyelectrolytes of (PDADMAC/PSS), we started to investigate the reinforcement of mechanical properties of LbL-assembled films by nanofibers. CNTs based LbL-

assembled films have shown promising strong mechanical properties in several previous studies.^{15,268,269} Here we prepared thick freestanding CNTs based LbL-assembled films together with PVAm using the same method as that of making freestanding films of (PDADMAC/PSS) with the help of a dipping robot. Stable aqueous suspensions of CNTs were prepared by physical wrapping of PSS with the weight ratio of CNTs to PSS at 1:2 as described previously in section II-A-2.1 (for the sake of simplification, all the P3-CNTs and P2-CNTs represents PSS wrapped P3-CNTs and PSS wrapped P2-CNTs in this study). Various important factors that influence mechanical properties of CNTs based films were investigated including: salt present in the starting PVAm solutions, type of CNTs (functionalized or not), alignment of CNTs, and interfacial interactions between CNTs and the PVAm matrix.

VI-B-1. Effect of salt on the mechanical properties of film

As it is known that the amount of nanofibers present in the nanofibers reinforced nanocomposites is one of the most important factors among others that determine the mechanical properties of nanocomposites.²⁷⁰ The ratio of the amount of CNTs (PSS included) to that of PVAm in the films of (PVAm/P3-CNTs)_n could be approximately evaluated by measuring differential thickness of each layer in the steady linear growth zone. Figure VI-2 shows calculated ratio of differential thickness of each layer CNTs to that of PVAm for the LbL-assembled films of (PVAm/P3-CNTs)_n at different concentration of NaCl used in PVAm solutions (C[NaCl]). Very close ratio about 3.0 ± 0.6 was found for all the different C[NaCl] starting from 0 to 1M, which implies that the ionic strength of PVAm solutions do not influence too much if any the absorption ratio of CNTs to PVAm during LbL-assembly. This is probably due to the charge stoichiometry of the LbL-assembled films.¹³² As the CNTs are PSS wrapped and the amount of PSS is 2 times that of carbon nanotubes, and because the density of carbon nanotubes are similar to that of polyelectrolytes around 1.1 g/cm^{-3} ,¹⁵ we can calculate the approximate percentage of carbon nanotubes (v) contained in the films of (PVAm/P3-CNTs)_n by the following equation

$$v = \frac{\psi}{\psi + 1} \cdot \frac{\rho}{\rho + 1} \quad \text{Equation VI-1}$$

where ψ is the ratio of differential thickness of PSS wrapped CNTs to that of PVAm and ρ is the ratio of carbon nanotubes to PSS for the preparation of PSS wrapped CNTs, which are 3.0 ± 0.6 and 0.5 respectively. Therefore the approximate percentage of carbon nanotubes in the films of $(\text{PVAm}/\text{P3-CNTs})_n$ is about 25%.

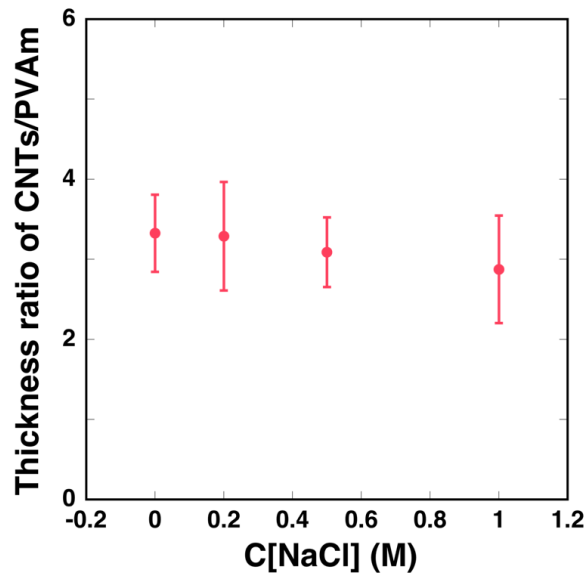


Figure VI-2. Differential thickness ratio of each layer of PSS wrapped CNTs and PVAm of films $(\text{PVAm}/\text{P3-CNTs})_n$ at different concentration of NaCl present in the starting PVAm solutions.

The similar percentage of carbon nanotubes contained in the CNTs based films of $(\text{PVAm}/\text{P3-CNTs})_n$ prepared at different amount of salt in the starting PVAm solutions might lead to similar mechanical properties for these films. Since adding salt in PVAm solutions can result in much faster growth of the CNTs based LbL-assembled films of $(\text{PVAm}/\text{P3-CNTs})_n$ (IV-A-2.), it is naturally interesting to confirm whether the presence of salt will influence mechanical properties of the final CNTs based films. For this purpose, thick freestanding films of $(\text{PVAm}/\text{P3-CNTs})_n$ made with and without presence of 0.5M NaCl in the starting PVAm solutions were fabricated and their mechanical properties were studied by tensile tests.

Figure VI-3 shows stress-strain curves of the LbL-assembled films of $(\text{PVAm}/\text{P3-CNTs})_n$ made with and without salt in the PVAm solutions. As expected, by adding

salt in the starting solution of PVAm, the ending film of (PVAm/P3-CNTs)_n has quite similar stress-strain curve compared to films made without salt. Both films have Young's modulus of 9 GPa and yield stress of about 150 MPa. The same mechanical properties of both films could be easily understood by the fact that the content of CNT in the film dose not change when the amount of salt in the solution of PVAm changes. Regarding the conformational change of PVAm chains caused by the presence of salt, its influence on the mechanical properties is negligible compared to the influence of amount of nanofibers.

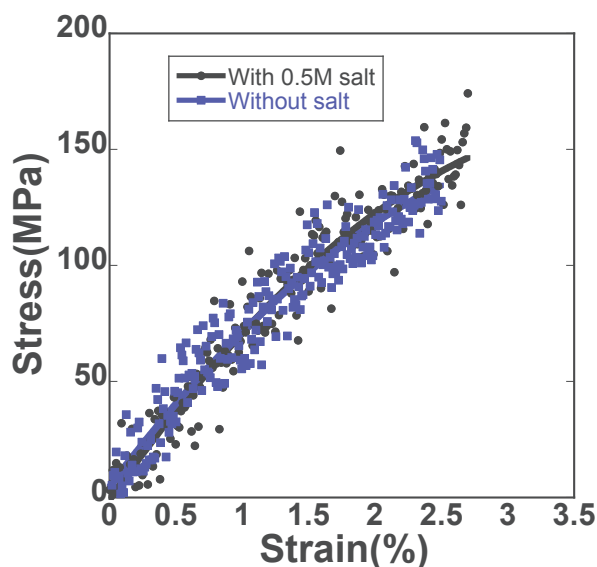


Figure VI-3. Stress-strain curves of LbL-assembled films of (PVAm/P3-CNTs)_n made with and without adding salt in the PVAm solution (blue and black dots represent without salt and with 0.5M NaCl respectively, the blue and black lines are polynomial fit of same color data).

In addition, the similar amount of carbon nanotubes present in both (PVAm/P3-CNTs)_n films made with and without 0.5M salt can be further confirmed by verifying characteristic UV-Vis absorbance of CNTs per layer pair for both films. Figure VI-4 shows the UV-Vis absorbance of the two films at the 500 nm arising solely from carbon nanotubes absorption and their thickness per layer pair in the steady linear zone. We can see that the UV-Vis absorbance of each layer pair is almost proportional to the thickness of each layer pair which varied due to presence of salt as previously shown in section IV-A-2. The amount of carbon nanotubes can be represented by dividing the UV-Vis absorbance by the thickness, which is 0.000083 A.U./nm for

film with salt and 0.000061 A.U./nm for film without salt. The slight difference could have been caused by experimental errors of the UV-Vis measurements.

As time required for the construction of micron-thick freestanding films is proportional to the number of layer pairs needed to obtain a certain thickness, films prepared with salt in the PVAm solutions should take less time since they grow much faster than films prepared without using salt. Considering the negligible difference in mechanical properties, we decided to build all freestanding films with 0.5M of salt in the polyelectrolyte solution for all other tests, so that we could build freestanding films much more quickly.

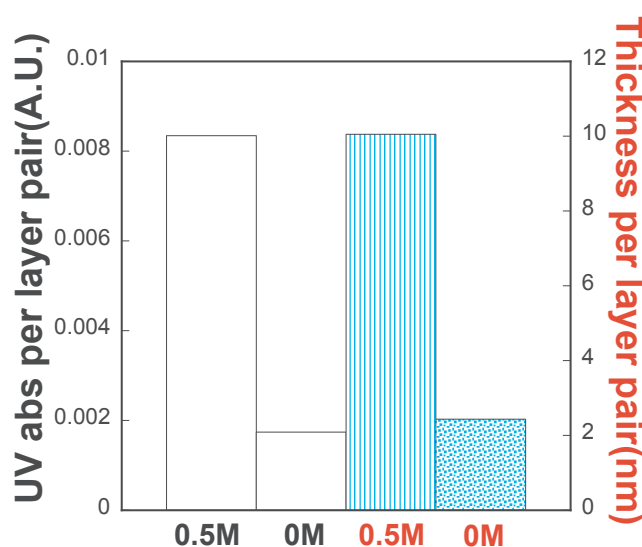


Figure VI-4. UV-Vis absorbance per layer pair at wavelength of 500 nm (left vertical axis in black) and thickness per layer pair at steady linear region for both films $(\text{PVAm}/\text{P3-CNTs})_n$ made with and without 0.5M NaCl in PVAm solutions.

VI-B-2. Comparing mechanical properties of LbL-assembled films made with and without CNT

Figure VI-5 shows the typical stress-strain curve of CNTs based film $(\text{PVAm}/\text{P3-CNTs})_{120}$ in comparison with that of film made of solely polyelectrolytes $(\text{PDADMAC}/\text{PSS})_{100}$. We can easily find that the incorporation of CNTs dramatically improves the mechanical properties of LbL-assembled films due to the transfer of the CNTs strength to the entire film. The remarkable Young's modulus of CNTs reinforced films is about 9 GPa that is almost 3-fold higher than that of films made

without CNTs. The CNTs based films also exhibited tensile strength of as high as 150 MPa, which approaches that of SWNTs reinforced LbL-assembled films reported in previous study.¹⁵ In contrast to this previous research where CNTs had a film volume fraction of about 50%, our (PVAm/P3-CNTs)₁₂₀ films have only about 25%. This could be ascribed to more efficient dispersion of carbon nanotubes with PSS wrapping than the chemical dispersion method used in that study. However, compared to the tensile strength values of SWNTs that were experimentally determined to be between 13 and 50 GPa,^{271,272} the obtained much lower tensile strength of the CNTs based LbL-assembled films should be mainly attributed to weak interfacial interactions between PSS wrapped CNTs and the polyelectrolytes matrix, which results in slippage of CNTs and matrix-CNTs interfacial breaking dominant failure of films. This will be further discussed in the section VI-C-1.1.

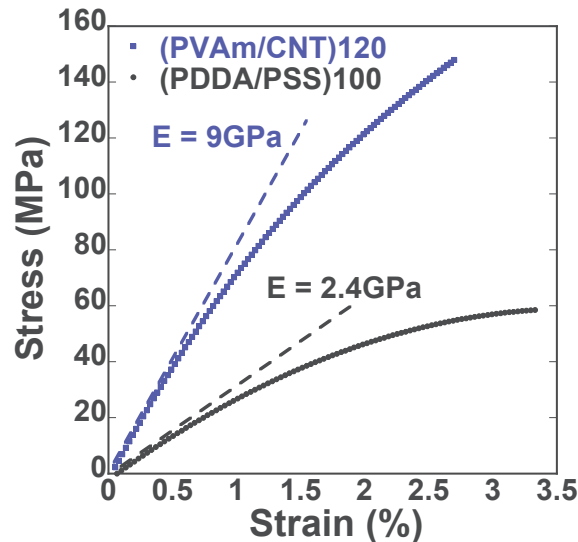


Figure VI-5. Representative Stress-strain curves of LbL-assembled film made of solely polyelectrolytes of (PDADM/PSS)₁₀₀ (polynomial fit in black line) and of CNTs reinforced LbL-assembled films of (PVAm/P3-CNTs)₁₂₀ (polynomial fit in blue line); The modulus deduced at low deformation is about 9 GPa for films of (PVAm/P3-CNTs)₁₂₀ and 2.4 GPa for films of (PDADM/PSS)₁₀₀.

VI-B-3. Alignment of CNTs by LbL-assembly

More and more attention has been paid to assembling nanocomposites of aligned nanofibers for obtaining anisotropic materials with higher degree of inheritance from the excellent properties of the nanofibers such as high electrical conductivity, high

mechanical properties, or even high membrane performance.^{273,274} CNTs can be aligned in a matrix polymer film by blown bubble film process,²⁷⁵ mechanical stretching,^{275–277} electrical field,²⁷⁸ and magnetic field.²⁷⁹ LbL-assembly has also been successfully used for aligning CNTs,²⁸⁰ however, to our knowledge, mechanical properties of LbL-assembled films of aligned CNTs haven't yet been studied. Here, in this section we demonstrate the alignment of CNTs by LbL-assembly assisted by two different methods, which are grazing-incidence spraying and spin-coating respectively. Then influence of the alignment of CNTs on the mechanical properties of CNTs based LbL-assembled freestanding films will be investigated.

VI-B-3.1. Alignment of CNTs by grazing-incidence spray-assisted LbL-assembly

Grazing-incidence spraying is a method of LbL-assembly first developed by Blell during her thesis.²⁹ It is about high airflow assisted spraying with a low spraying angle, namely, grazing-incidence spraying. Similarly to the 'combing' method used for aligning CNTs in the work of Shim et al.,²⁸⁰ where the alignment of CNTs was caused by pressurized airflow combing after water rinsing step of LbL-assembly of PSS-wrapped CNTs, the grazing-incidence spraying binds the LbL-assembly coating and high airflow to a single step, which means that the CNTs are aligned during the LbL-assembly deposition under pressurized air. The high shear force arising from pressurized airflow induces alignment of CNTs in the airflow direction during the LbL-assembly. Figure VI-6a is AFM image of aligned PSS wrapped P3-CNTs prepared by grazing-incidence spray-assisted LbL-assembly of one layer pair of (PEI/PSS wrapped P3-CNTs) on Si-wafer under airflow rate of 35 L/min and liquid flow rate of 2 mL/min. We can see that individual PSS wrapped CNTs are deposited on the surface and preferentially aligned in the direction of spraying. Figure VI-6b is fast fourier transform of the AFM image, which shows an elongated pattern vertical to the alignment direction, indicating high degree of orientation.

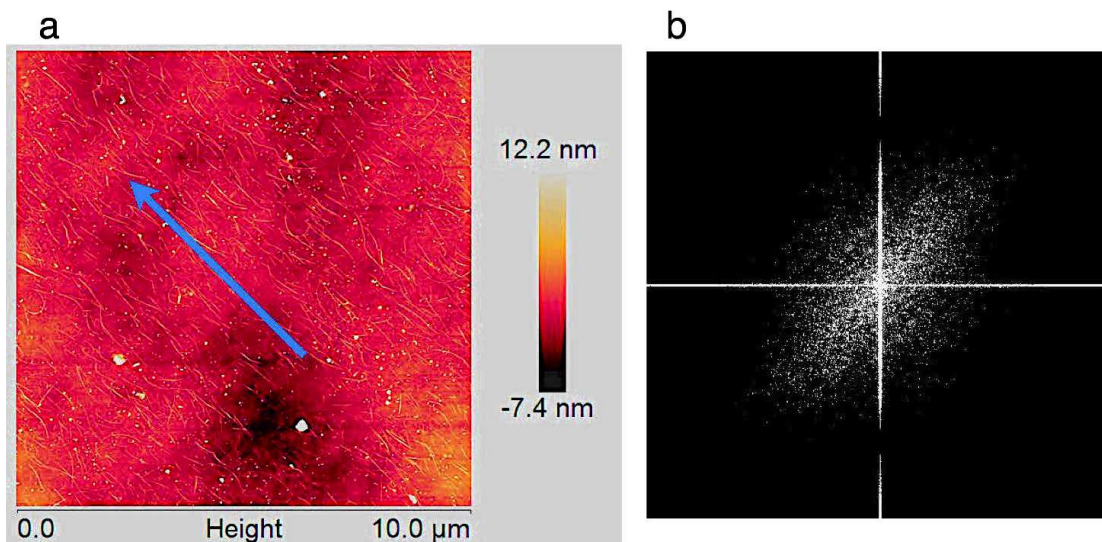


Figure VI-6. a) AFM image of aligned CNTs by grazing-incidence spray-assisted LbL-assembly of one layer pair of (PEI/PSS wrapped P3-CNTs) on Si-wafer (blue arrow indicates spraying direction); b) Fast fourier transform of image a in 32-bit showing an elongated pattern vertical to the alignment direction.

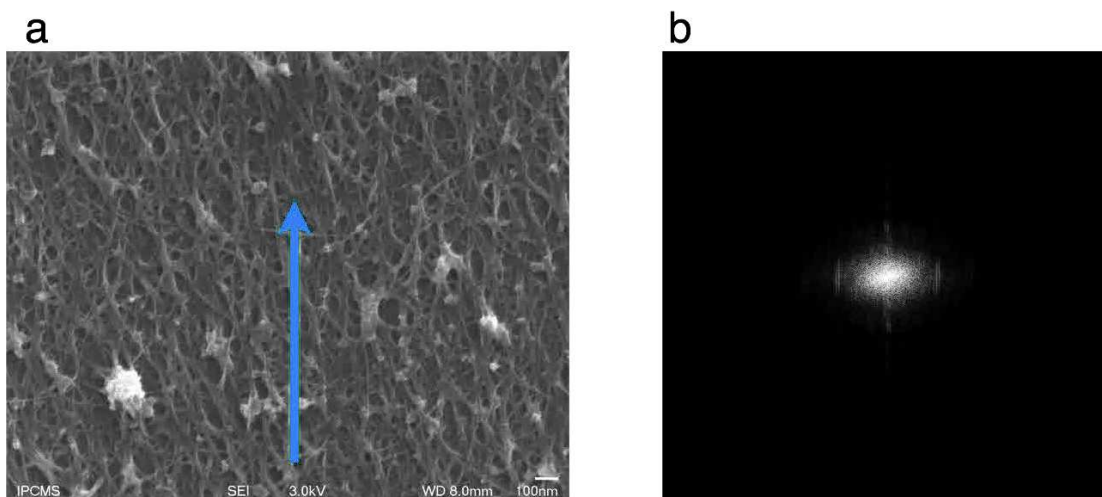


Figure VI-7. a) SEM image of grazing-incidence spray-assisted LbL-assembly of 20 layer pairs of (PAH/PSS wrapped P3-CNTs) (blue arrow indicates spraying direction); b) Fast fourier transform of image a in 32-bit showing an elongated pattern vertical to the alignment direction.²⁸¹

Figure VI-7 shows SEM image and its fast fourier transform pattern of grazing-incidence spray-assisted LbL-assembly of 20 layer pairs of (PAH/PSS wrapped P3-CNTs) prepared under same conditions. Similarly, the SEM image reveals a preferential alignment direction of the CNTs parallel to the spraying direction resulting in elongated fast fourier transform pattern with its long axis vertical to the

alignment direction, which confirms alignment of CNTs in the spraying direction by the grazing-incidence method.

VI-B-3.2. Alignment of CNTs by spin-assisted LbL-assembly

Despite the highly aligned CNTs obtained by grazing-incidence spray-assisted LbL-assembly, this method has some disadvantages such as restrained area of the assembled films by spraying nozzle size or requirement of relatively high volume of solutions. In order to construct enough area of freestanding LbL-assembled films of aligned CNTs for the tensile tests, another method for fabricating aligned CNTs was employed, which is spin-assisted LbL-assembly.

Spin-coating is a technique that has been done for almost a century for making thin films through deposition of organic material on a spinning substrate.²⁸² It was successfully combined with LbL-assembly technique in order to accelerate the construction of films and to fabricate films with ordered structures.^{25–28} Alignment of one layer of CNTs was already demonstrated by LeMieux et al.,²⁸³ while in this part, we explore production of multilayered films composed of aligned CNTs through so called spin-assisted LbL-assembly technique. Stable suspensions of PSS wrapped P3-CNTs and PAH solutions were spin-assisted LbL-assembled at the speed of 8000 Rpm using a spin-coater following the procedure that is described in section II-A-6.2.

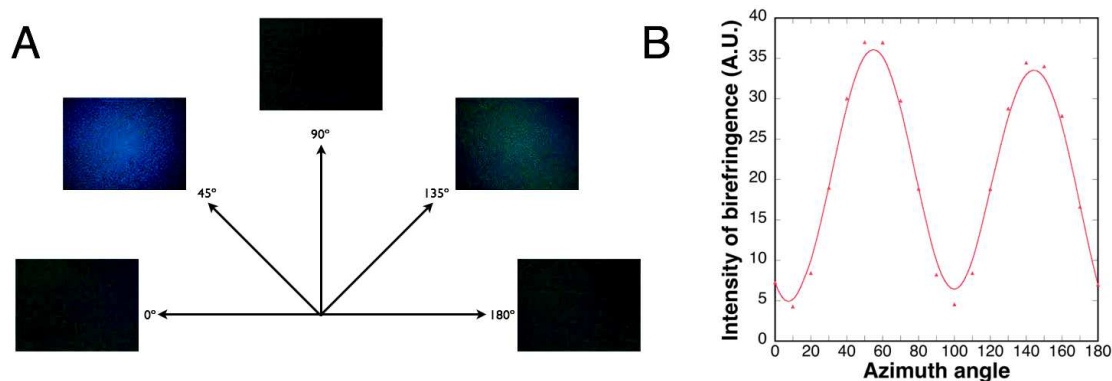


Figure VI-8. A) Cross-polarized microscopy optical micrographs of spin-assisted LbL-assembly of 20 layer pairs of (PAH/PSS wrapped P3-CNTs) at different azimuth angles; B) Intensity of birefringence calculated based on the light intensity of the micrographs in A) as a function of the azimuth rotation angle of the sample; When the azimuth rotation angle is 0°, the alignment direction of CNTs is parallel to one of the crossed polarizer.

Films of 20 layer pairs of (PAH/P3-CNTs), namely (PAH/P3-CNTs)₂₀, were constructed by spin-assisted LbL-assembly. We used cross-polarized microscopy to

examine the anisotropy of the aligned CNTs. The reflected light intensity depended on the relative orientation of the CNTs with respect to the optical axis of the polarizers (azimuth angle) (II-B-4.4.). **Figure VI-8** shows the obtained micrographs under cross-polarized microscope and their intensity of birefringence calculated based on the light intensity at different azimuth rotation angle of the sample. As expected, light intensity or intensity of birefringence of the sample show anisotropic properties. When the azimuth rotation angle of the sample is either parallel (0°) or vertical (90°) to one of the two polarizers, the obtained micrographs appear dark, which is due to maximum degree of light extinction by the two crossed polarizers. Whereas, the intensity of birefringence or light intensity of the micrographs reach to the maximum when the azimuth rotation angle comes to 45° or 135° , where maximum transmission of light is achieved due to birefringence properties of the films with aligned CNTs. This observation confirms that the CNTs have been aligned by the spin-assisted LbL-assembly. The alignment of CNTs was further proved by the AFM image and its elongated fast Fourier transform image as shown in **Figure VI-9**.

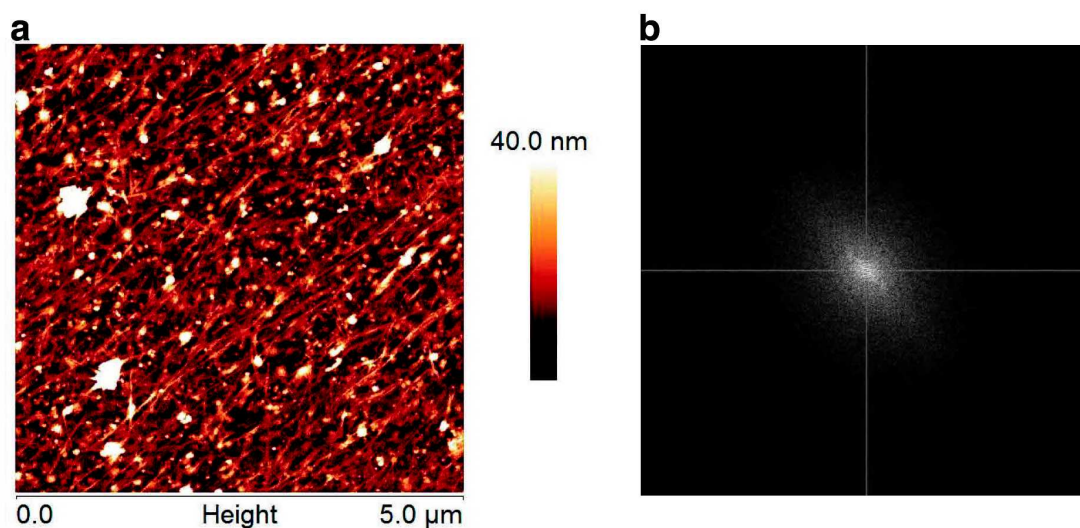


Figure VI-9. AFM picture of a spin-coated (PAH/P3-CNTs)₂₀ LbL-assembled film a) and its fast Fourier transform image.

To conclude, it can be stated that orientation of CNTs was achieved either by grazing-incidence or by spin-assisted LbL-assembly. As it is interesting to look into the mechanical properties of these LbL-assembled films of aligned CNTs, freestanding CNTs based films were prepared by spin-assisted LbL-assembly in order to make samples for tensile tests.

VI-B-3.3. Impact of CNTs alignment on the mechanical properties

To investigate the impact of CNTs alignment on the mechanical properties of the CNTs based films, both spin-assisted and dipping LbL-assembly techniques were employed for making films of (PVAm/PSS wrapped P3-CNTs)_n with oriented and disordered CNTs respectively. After the tensile tests, we obtained the stress-strain curves as shown in Figure VI-10. It shows that film with oriented CNTs made by spin-assisted LbL-assembly has tensile strength of about 215 MPa which is 50% higher than that of disordered CNTs made by dipping LbL-assembly. The Young's modulus was also improved from 9 GPa to 12.5GPa arising from oriented CNTs. The enhancement of mechanical properties by the aligned CNTs can be explained by the fact that the alignment of CNTs render the film of CNTs with more densely packed structure which in turn enhance the interfacial interactions between PSS wrapped CNTs and PVAm matrix. The very few increase of Young's modulus makes us believe, once again, that interfacial failure rather than carbon nanotubes breaking dominates the rupture of (PVAm/P3-CNT)_n films, which restrict the effect of orientation of CTNs on the mechanical properties. Otherwise, the Young's modulus of both films of disordered and aligned CNTs should be much higher according to the mixing law of fiber reinforced composite materials.²⁸⁴

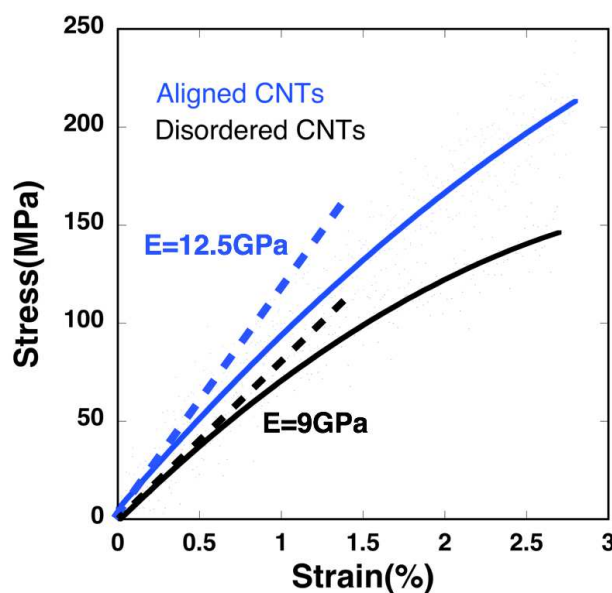


Figure VI-10. Representative stress-strain curves for films of (PVAm/PSS wrapped P3-CNTs)_n with oriented CNTs by spin-assisted LbL-assembly (Blue) and that with disordered CNTs by

dipping LbL-assembly (Black). Both curves were obtained after polynomial fitting, and the modulus deduced at low deformation is about 12.5 GPa for spin-assisted LbL-assembled film and 9 GPa for dipping LbL-assembled film.

The weak interfacial interactions between the PSS wrapped CNTs and PVAm matrix could lead to the failure of CNTs-Polyelectrolyte matrix interfaces instead of breaking of CNTs whose tensile strength is much stronger. Figure VI-11 shows a cross-sectional SEM image of a ruptured film of (PVAm/PSS wrapped P3-CNTs) made by dipping LbL-assembly. We can see that unbroken fibers or fiber bundles of 10-25 nm width and near micron length present all over the cross-section of the film. Since individual PSS wrapped P3-CNTs has only about 5 nm width (from AFM image Figure II-1C), these fibers should be bundles of the PSS wrapped P3-CNTs rather than pristine P3-CNTs or single PSS wrapped P3-CNTs. These suspended PSS wrapped CNTs fiber bundles indicate slippage of the PSS wrapped CNTs from the polyelectrolyte matrix during film's rupture process, instead of CNTs breaking or slippage of pristine P3-CNTs from PSS, which confirms our hypothesis of the interfacial failure dominating film's rupture for the CNTs based LbL-assembled films.

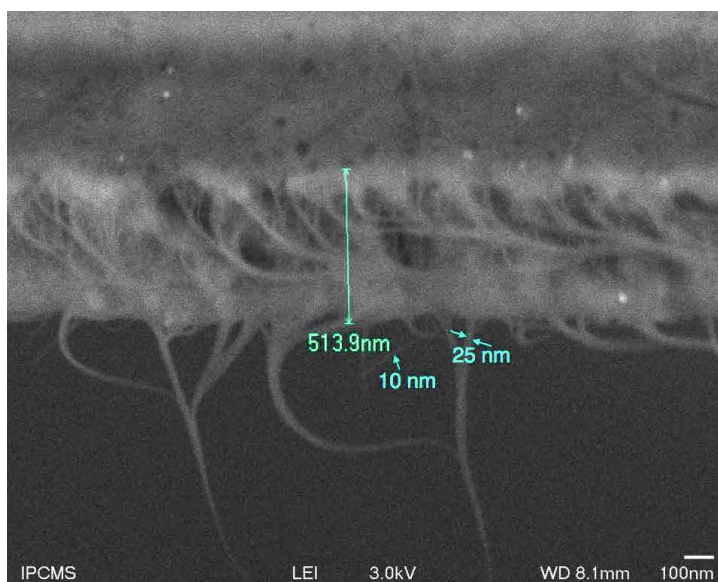


Figure VI-11. Representative cross-sectional SEM image of a ruptured film of (PVAm/ PSS wrapped P3-CNTs)_n with a thickness of about 514 nm. (for the cross-sectional SEM imaging: freestanding films were broken by hand pulling using a tweezer)

The interfacial interactions between PVAm matrix and PSS wrapped CNTs are mainly weak electrostatic interactions arising from amine groups of PVAm and sulfonate groups of PSS that wrap CNTs for dispersing in water. Although the functionalized P3-CNTs have 1-3 atomic% of carboxylic acid groups which might form hydrogen bonds with amines groups of PVAm, however their contribution to the interfacial interactions are negligible. This can be confirmed by the similar stress-strain curves obtained for both (PVAm/PSS wrapped CNTs)_n films made of CNTs with (P3-CNTs) and without (P2-CNTs) functionalized carboxylic acid groups (Figure VI-12). Therefore, despite the fact that remarkable mechanical properties have been obtained for the LbL-assembled films made of PSS wrapped carbon nanotubes, the weak electrostatic interfacial interactions prohibits the achievement of stronger CNTs based films. One possible way to prevent the weak interfacial interactions is by using chemical functionalized CNTs without physical wrapping so that post cross-linking process can be employed for enhancing the interfacial interactions. However, as previously shown by Mamedov et al.,¹⁵ where only 220 MPa of tensile strength was obtained for LbL-assembled films made with chemical functionalized CNTs, which is still way too far from theoretically possible value. Another possibility of improvement of interfacial interactions has been demonstrated by Shim et al.,²⁶⁸ where specific interactions between non-charged polyvinyl alcohol (PVA) and CNTs was inferred to have a key role in the mechanical properties, and cross-linking using glutaraldehyde (GA) further improved the mechanical properties. Unfortunately, we failed in repeating similar experiments of making (PVA/CNTs)_n films by LbL-assembly, which is still hard to explain. One possible reason could be that the hydrogen bonding interactions between PVA and CNTs are difficult to achieve and require certain crucial steps that we haven't figured out yet.

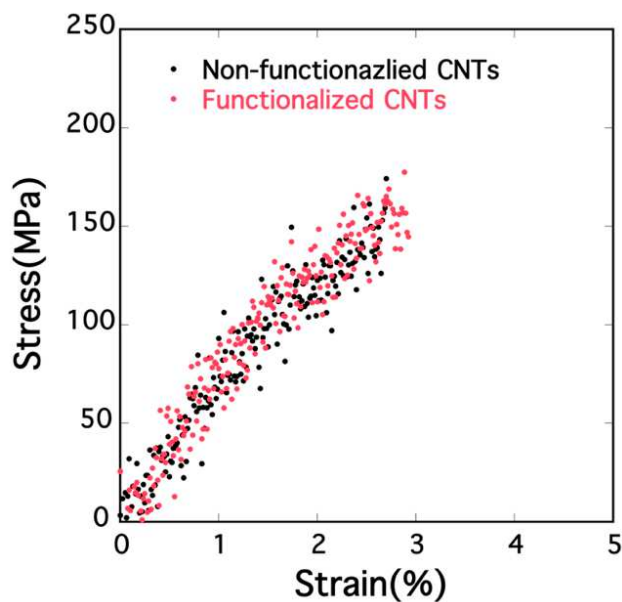


Figure VI-12. Representative stress-strain curves of dipping LbL-assembled films of (PVAm/PSS wrapped CNTs)_n with functionalized P3-CNTs (red) and non-functionalized P2-CNTs (black) showing similar results.

Briefly, in this section, alignment of CNTs was explored by two different LbL-assembly methods which are grazing-incidence spraying and spin-assisted respectively. The achievement of aligned CNTs by these two methods was confirmed by different characterization methods including AFM and fast Fourier transform, SEM, and cross-polarized microscopy. Mechanical properties of films (PVAm/CNTs)_n prepared by spin-assisted LbL-assembly were investigated and compared with same films made by dipping. It was found that alignment of CNTs imparted the films with 50% higher tensile strength and larger Young's modulus compared to the films made of disordered CNTs. We believe that the CNTs-PVAm matrix interfacial failure is responsible for film's fracture during tests, which restrained their mechanical properties to reach to theoretically much higher values in view of the extremely high Young's modulus and tensile strength of carbon nanotubes.

VI-C. Mechanical properties of LbL-assembled films reinforced with CNFs

Indeed, the inherent hydrophobic properties of carbon nanotubes not only make preparation of stable CNTs suspension become difficult, but also cause low compatibility with hydrophilic polyelectrolyte matrix, which results in LbL-assembled films of restrained mechanical properties. It is therefore interesting to seek strong nanofibers of hydrophilic structure in order to build LbL-assembled films with higher-order interfacial interactions between reinforcing nanofibers and matrix which could lead to films of superior mechanical properties.

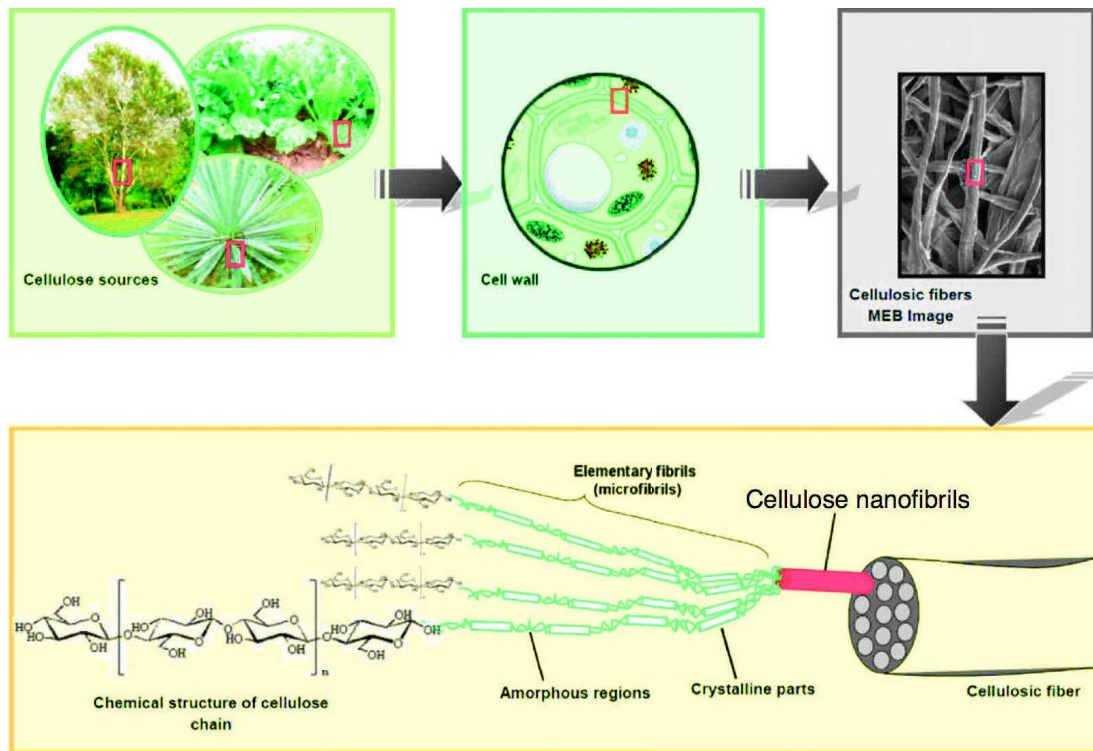


Figure VI-13. From the cellulose sources to the cellulose molecules: details of the cellulosic fiber structure with emphasis on the cellulose nanofibrils in red color.²⁸⁵

Cellulose nanofibrils (CNFs) are ideal candidates for this, owing to their high strength and stiffness combined with low weight, biodegradability and renewability.²⁸⁶ As shown in Figure VI-13, cellulose nanofibrils are the basic mechanical reinforcing elements of cellulosic fibers composed of nanosized cellulose fibrils with high aspect ratio. CNFs usually have a typical diameter of 3-100 nm and a wide range of length

from hundreds nanometer up to several microns depending on preparation methods and source of cellulose.²⁸⁷ The CNFs used in this thesis were made by high-pressure homogenization with microfluidizers after carboxymethylation pretreatments.²⁶⁰ The negatively charged carboxymethyl CNFs produced using this innovative method have a degree of substitution (DS) of 0.083 and a uniform diameter of 5-15nm combined with a length of over 1 μm , which results in an aspect ratio of at least 100. The high strength and stiffness, high surface area-to-volume ratio and high aspect ratio, biodegradability and sustainability, and intra-intermolecular hydrogen bond donors and acceptors, all these properties of the CNFs together can endow CNFs based LbL-assembled films with excellent mechanical properties. The focus of this part of the thesis was set on reinforcing mechanical properties of LbL-assembled films by incorporating CNFs in the assembly.

To study mechanical properties of CNFs based LbL-assembled films, thick LbL-assembled films of $(\text{CHI}/\text{CNFs})_{150}$ were prepared as already described in previous sections on hydrophobic Si-wafer surfaces with the help of a dipping robot. Chitosan solutions were chosen as LbL-assembly partner of CNFs for their similar molecular structures. Both CNFs and chitosan contain linearly bonded β -1,4-D-glucopyrane which can lead to rigid planar and more densely packed structure. The similar planar chain structure and abundant hydrogen bond functions (OH, NH_2 , $\text{C}=\text{O}$) of both materials could result in films with remarkable mechanical properties. The obtained mechanical properties of $(\text{CHI}/\text{CNFs})_{150}$ films will be compared with that of films $(\text{PVAm}/\text{CNFs})_n$ reported previously.⁹³

Figure VI-14a shows optical photograph of a freestanding $(\text{CHI}/\text{CNFs})_{150}$ film, from which we can see clearly the ICS logo behind the film, indicating high transparency and homogeneity of the film. Besides, UV-Vis transmittance spectra were obtained for the films of $(\text{CHI}/\text{CNFs})_{150}$ in the range of wavelength between 200 and 800 nm (Figure VI-14b), which confirm the high transparency of the film with over 85% transmittance in the entire visible spectrum, while the low transmittance below 225 nm arises from the absorption of acetic acid groups of CNFs and the periodic fringes refer to the so called 'Fabry-Perot' fringes.²⁸⁸ The Fabry-Perot fringes stem from the multiple interferences between beams transmitted and partially reflected at the interfaces (film-air in our case of freestanding films), which could be used for precisely calculating film's thickness. According to Equation VI-2:

$$\theta = \frac{1}{2n_e \cdot (1/\lambda_p - 1/\lambda_{p+1})} \quad \text{Equation VI-2}$$

Where θ is the film thickness, n_e is the refractive index of the film, and the two adjacent wavelength, λ_p and λ_{p+1} , of which λ_p is the wavelength where absorbance of the fringes is maximal. Base on UV-Vis transmittance data, λ_p and λ_{p+1} are 225 and 240 nm respectively. As discussed in section IV-B-4. where we determined the refractive index of film (CHI/CNFs)₁₅₀ to be 1.55 through several techniques. Thus we obtain the film thickness θ equal to 1.16 μm , which is exactly consistent with the values obtained by SEM, AFM, and spectroscopic ellipsometer. Consequently, the Fabry-Perot fringes validate once again thickness of the CNFs based LbL-assembled films, which could be a supplementary convenient method for measuring thick LbL-assembled films' thickness. Moreover, these fringes suggest as well the homogeneity of the film, which is important for fabricating films with strong mechanical properties.

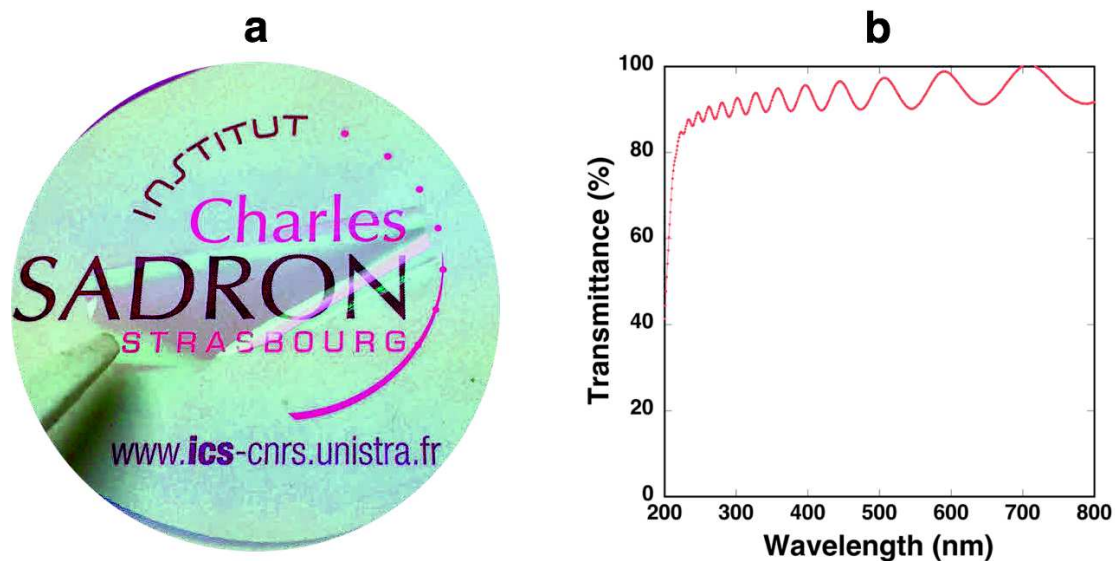


Figure VI-14. a) Optical photograph of a freestanding LbL-assembled film of (CHI/CNFs)₁₅₀ built from a chitosan solution with 0.5M NaCl, the film thickness measured by spectroscopic ellipsometry is $1.13 \pm 0.03 \mu\text{m}$; b) UV-Vis spectra of the very freestanding film of (CHI/CNFs)₁₅₀.

Tensile tests were carried out on samples of laminated dipping LbL-assembled (CHI/CNFs)₁₅₀ films. The obtained stress-strain curves were compared with similar films (PVAm/CNFs)_n studied by our team members Merindol et al.⁹³ In addition to

the study on dipping LbL-assembled films, spin-assisted LbL-assembled films of (CHI/CNFs)₁₂₀ were also prepared for investigating on the alignment of CNFs of the spin-coating assembled films and its impact on films' mechanical properties. Supplementary nanoindentation tests were performed on the same films prepared on hydrophilic Si-wafer surfaces, so as to investigate influence of humidity on the films' mechanical properties.

VI-C-1. Mechanical properties of CNFs based film

Figure VI-15 shows representative stress-strain curve of the dipping LbL-assembled films of chitosan and CNFs (coded (CHI/CNFs)_n, n refers to number of layer pair) that were tested under ambient humidity (less than 50%). The CNFs based films show fascinating mechanical properties of Young's modulus of 14 GPa combined with tensile strength of up to 450 MPa, which is comparable to that of steel,²⁸⁹ yet at much lower density. Compared with CNTs based films, CNFs based films have higher tensile strength and slightly superior Young's modulus, which is unexpected in view of the much stiffer CNTs than CNFs. In order to explain this, we have to look into the mechanism of reinforcement of these nanofibers based nanocomposites.

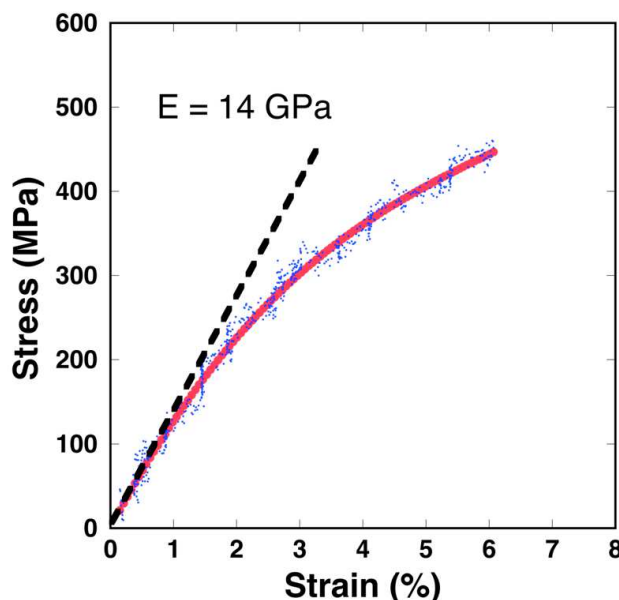


Figure VI-15. Representative stress-strain curve for films of dipping LbL-assembled film (CHI/CNFs)₁₅₀ tested under ambient humidity (polynomial fitting in red line). The Young's modulus estimated graphically at low deformation is about 14 GPa.

The fracture of nanofibers reinforced films can originate from anywhere of films including the matrix, the fibers-matrix interfaces and the fibers, depending on the reinforcing mechanism of the fibers.

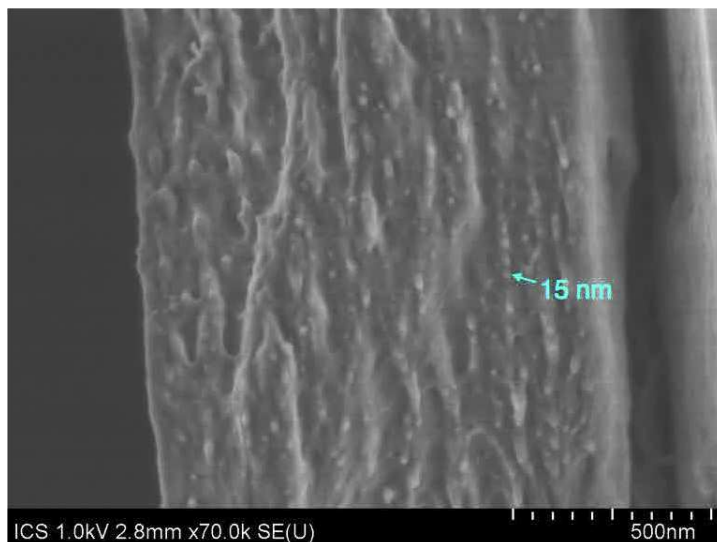


Figure VI-16. Representative cross-sectional SEM images (out of at least 5 samples) of fractured CNFs reinforced LbL-assembled film of $(\text{CHI}/\text{CNFs})_{150}$ showing broken CNFs or CNFs-matrix bundles. (for the cross-sectional SEM imaging: samples of micron thick films together with Si-wafer substrates were broken with diamond cutter)

From Figure VI-16 we can observe that in contrast to the fibers pull-out mechanics of the rupture of CNTs based films (Figure VI-11), which indicates weak fiber-matrix interfacial interactions, the cross-section of the ruptured CNFs based films shows individual broken CNFs or CNFs bundled with matrix, which indicates fibers rupture induced failure mechanics of the rupture of CNFs based films. In order to understand and explain the mechanics of the rupture of CNFs based films, simple shear-lag model (see the Appendix 1) can be applied.^{284,290}

There are two basic modes for the fracture of nanofibers reinforced films (Figure VI-17). When the fiber's aspect ratio S is higher than the critical aspect ratio of the film S_c , film's rupture is caused by the fragmentation of the nanofibers (Figure VI-17A). On the other hand, if S is lower than S_c , the film's fracture is dominated by the matrix's rupture which leads to the fibers pull-out without fragmentation (Figure VI-17B).

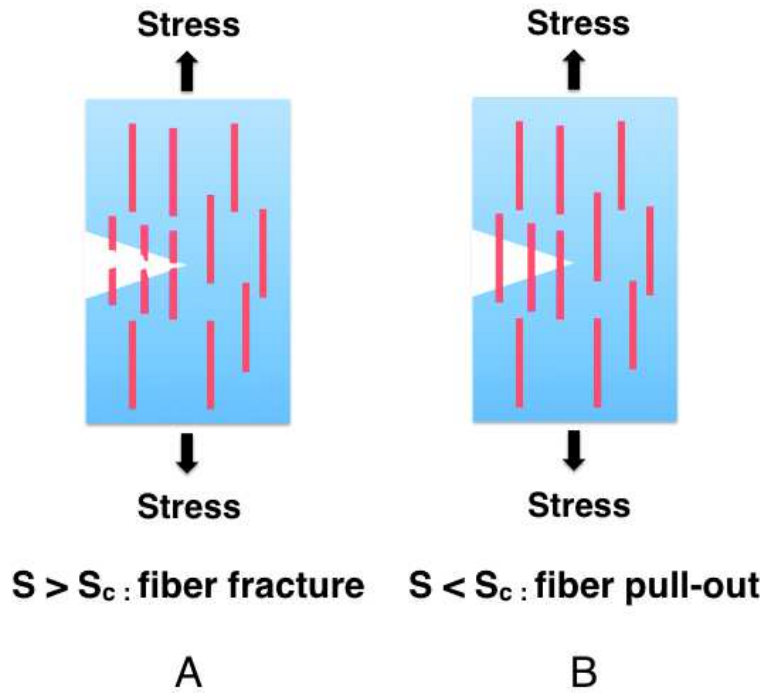


Figure VI-17. A) when $S > S_c$, nanofibers' fragmentation causes nanocomposite's fracture; B) when $S < S_c$, nanocomposite's fracture is caused by the matrix's rupture leading to fibers pull-out.

As for the CNFs based LbL-assembled films, the aspect ratio of CNFs S is about $1000/5=200$. And the critical aspect ratio S_c is equal to $\frac{\sigma_{fu}}{2\tau_i}$ where τ_i is the shear stress (see Appendix 1), assuming σ_{fu} between 800MPa and 2GPa for the CNFs and $\tau_i = 40\text{MPa}$,²⁹¹ we expect a relatively low S_c in the range from 10 to 25 for the CNFs based films. Therefore the aspect ratio of CNFs S is much higher than the S_c of the CNFs based LbL-assembled films, which should result in strong films with fiber fracture dominating film failure.

Since S is much higher than S_c and the tensile strength of the matrix chitosan σ_m is low compared to the tensile strength of the CNFs σ_f , Equation 0-9 (see Appendix 1)

$$\sigma_c = \bar{\sigma}_{fu} v_f + \sigma'_m (1 - v_f) = \sigma_{fu} \left(1 - \frac{S_c}{2S}\right) v_f + \sigma'_m (1 - v_f)$$

where:

σ_c : Tensile strength of the CNFs based LbL-assembled film;

σ_{fu} : Ultimate tensile strength of the fiber;

σ'_m : Stress of matrix when the film breaks;

v_f : Volume fraction of the fibers;

can be simplified to

$$\sigma_c = \sigma_{fu} v_f \quad \text{Equation VI-3}$$

Knowing that the CNFs' volume fraction can be appropriately estimated using the ellipsometry thickness results of each layer of CNFs and chitosan (assuming same density of CNFs and chitosan), we can obtain the volume fraction of the fibers $v_f = \text{thickness of CNFs layer} / (\text{thickness of CNFs layer} + \text{thickness of chitosan layer}) = 0.75$. Equation VI-3 becomes

$$450 \text{ MPa} = 0.75 \sigma_{fu}$$

Equation VI-4

which gives the fiber's ultimate tensile strength σ_{fu} of about 600 MPa.

Raw material	Preparation procedure	Max. Stress (MPa)	Modulus of elasticity (GPa)	Strain at break (%)	References
Sugar beet pulp	Casting	ND	2.5–3.2	ND	Dufresne et al. (1997)
Softwood sulfite pulp	Casting	80–100	~6 ^a	~1 mm ^a	Zimmermann et al. (2004, 2005a, b)
Swede root pulp	Filtering	100	7	ND	Bruce et al. (2005)
Softwood dissolving pulp	Vacuum filtering	104	14.0	2.6	Henriksson and Berglund (2007)
Sugar beet pulp chips	Casting	104	9.3	3.2	Leitner et al. (2007)
Bleached sulfite softwood cellulose pulp	Casting	180	13.0	2.1	Svagan et al. (2007)
Softwood dissolving pulp; bleached sulfite softwood	Vacuum filtering	129–214	10.4–13.7	3.3–10.1	Henriksson et al. (2008)
Wood powder, holocellulose pulp	Vacuum filtering	213–240	12.8–15.1	3.2–4.4	Iwamoto et al. (2008)
Commercial MFC (Daicel Chemical Industries)	Vacuum filtering	140–160	8.5–10.5 ^a	5–11	Nakagaito and Yano (2008a, b)
Never-dried softwood and hardwood bleached kraft pulp	Vacuum filtering	222–233	6.2–6.9	7.0–7.6	Fukuzumi et al. (2009)
Commercial MFC (Daicel Chemical Industries)	ND	67–68 ^a	ND	2.7–2.8 ^a	Iwatake et al. (2008)
Bleached spruce sulfite pulp	Vacuum filtering	104–154	15.7–17.5	5.3–8.6	Syverud and Stenius (2009)
Hardwood bleached kraft pulp	Vacuum filtering	222–312	6.2–6.5	7.0–11.5	Saito et al. (2009)

Table VI-1. Mechanical properties of CNFs based films.²⁹¹

Although the tensile strength of 450 MPa defeats most CNFs based materials in the previous studies (Table VI-1),²⁹¹ the calculated relevant fiber tensile strength σ_{fu} of 600 MPa is still far from that of individual cellulose crystal.^{292,293} Many attributed this to two main reasons. Karabulut et al. argued that the relatively low tensile strength of freestanding LbL-assembled CNTs based film was due to weak interactions between fibers, which is not our case, otherwise the failure of our films would have been fibers pull-out mechanics instead of fibers rupture.¹⁶ The other reason was proposed by Håkansson et al. who attribute the commonly reported lower values of tensile strength of CNFs based materials to the random distribution of CNFs, and they improved the tensile strength of CNFs based filaments up to more than 490 MPa by a process combining hydrodynamic alignment with a dispersion–gel transition that produces homogeneous and smooth filaments from a low-concentration dispersion of cellulose nanofibrils in water.²⁹⁴ However the improved tensile strength is still far below that of a composite with aligned CNFs predicted by the rule of mixture or shear-lag model, in addition they did not mention or explain why the Young's modulus of these materials

were not enhanced compared to other random CNFs based materials. Therefore, we believe that either lack of strong interfacial interactions or the randomly distributed CNFs could not completely explain the relatively lower tensile strength of our films compared to models-predicted values based on the mechanical properties of crystalline cellulose fibers. One strong hint goes to the structure of the CNFs that we used. Indeed, according to previous study on similar CNFs by Aulin et al.,²⁹⁵ the CNFs have a degree of crystallinity of about 60%. In another work the same authors calculated Young's modulus of amorphous part of CNFs using the lower-bound model (Reuss model) and obtained a value of about 48 GPa, which is about from 1/4 to 1/3 of the crystalline part of CNFs depending on different reported values.^{291,292} Assuming same strain for both amorphous and crystalline part of CNFs when ruptured, and taking the reported value of tensile strength of crystalline cellulose fiber $\sigma_{fu} = 1.75$ GPa, we can obtain the tensile strength of amorphous part of cellulose fiber ranging from 438 to 583 MPa. This value is in good agreement with the calculated fiber ultimate tensile strength of 600 MPa in our case, indicating that the failure of our CNFs based films are amorphous part rupture dominated, which may hint that even better mechanical properties could be possibly obtained using CNFs with higher amount of crystalline part. This agreement proves our hypothesized fibers rupture induced film failure mechanics based on SEM image, however, it still can not explain why our films have much higher tensile strength than other reported data.

We attribute the high tensile strength to two main reasons. Firstly, the hierarchically layered structures mimic the structures of natural materials such as wood and nacre, which can avoid fibers aggregations and render our films more tolerant to flaws. Secondly, the abundant groups of -OH, -COO, -CO, -NH, -O- that are present on both chitosan and CNFs form considerable intra and intermolecular hydrogen bonds in addition to the electrostatic interactions, which in turn enhance chitosan-CNFs interfacial interactions.

VI-C-1.1. Influence of polyelectrolyte matrix on the mechanical properties of the film

Fiber-matrix interfacial interaction is so important for the mechanical properties of the fiber-reinforced composite materials that sometimes its effect can be crucial. For instance, LbL-assembled nacre-like films of high performance have been first

introduced by Kotov et al,¹⁵ and then the same team improved the film's tensile strength by four times simply by replacing the original polymer adhesive poly(diallyldimethylammonium chloride) (PDADMAC) with poly(vinyl alcohol) (PVA) that can form hydrogen bonding and covalent linkages with the stiffening agent Montmorillonite (MTM) clay.⁸⁹ The dramatic enhance of mechanical properties was ascribed mainly to the reinforcement of fiber-matrix interfacial interactions, which was due to the presence of hydrogen bonds and possible crystallization of PVA.

Knowing that the β -1,4-D-glucopyrane suprastructures and the intra- and intermolecular hydrogen bonds are responsible for the considerable high mechanical properties of cellulose, in this thesis, for forming LbL-assembled strong CNFs based films, we chose a natural biopolymer chitosan as the LbL-assembly partner of CNFs for the reason that chitosan has same rigid laminar β -1,4-D-glucopyrane structures as the CNFs. We expected that these rigid structures combined with the abundant hydrogen bonding groups on both chitosan and CNFs could enhance chitosan-CNFs interfacial interactions by forming hydrogen bonds in addition to the electrostatic interactions, so as to improve the tensile strength of the films.

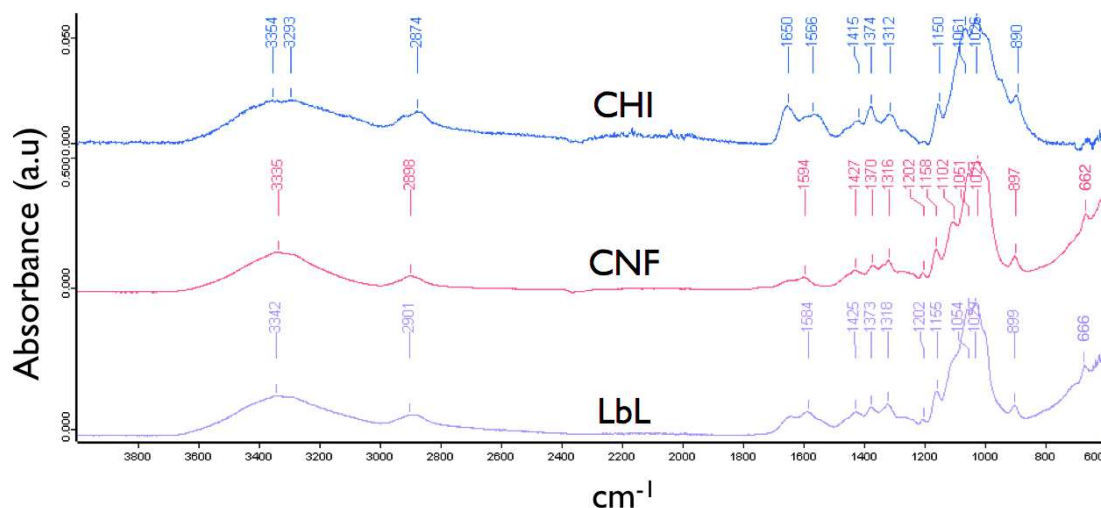


Figure VI-18. ATR infrared absorption spectra of chitosan (CHI), CNF and the dipping LbL-assembled (CHI/CNFs)_n (LbL).

For confirming the formation of hydrogen bonds in the LbL-assembled films, ATR-IR absorption spectra were measured for chitosan, CNFs, and the assembled films respectively (Figure VI-18). In none of the three spectra was there any sharp

absorption at circa 3500 cm^{-1} , which confirms that the hydroxyl groups in both chitosan and CNFs are involved in intra- and intermolecular hydrogen bonds. The broad peak at the wavelengths from 3000 to 3700 cm^{-1} for both chitosan and CNFs are due to the O-H stretching vibration and their intra- and intermolecular hydrogen bonding interactions. The C-O stretching at 1051 and 1021 cm^{-1} , and the OH out of plane bending at 662 cm^{-1} for the CNFs were all shifted to 1054 , 1029 and 666 cm^{-1} respectively for the LbL-assembled films, indicating once again that hydrogen bonds were formed on these groups after the LbL-assembly.

The band at 897 cm^{-1} , assigned to motions of atoms attached to C_1 (Figure IV-10), indicates the amorphous structure. The band at 1427 cm^{-1} (CH_2 symmetrical bending) should respond to changes in the environment of the C_6 group, such as the formation (or breaking) of an intramolecular hydrogen bond involving O_6 . O'Connor et al. found that when the degree of crystallinity of the cellulose increases the absorption at 897 cm^{-1} increases and the band at 1427 cm^{-1} decreases.²⁹⁶ Thus they defined a term called crystallinity index that is the ratio of the absorbance of the band maximum at about 1427 cm^{-1} to the absorbance of the maximum at about 897 cm^{-1} . They demonstrated that the larger the crystallinity index is the higher degree of crystallinity the cellulose has.

Materials	Chitosan	CNFs	(CHI/CNFs) ₁₅₀
Crystallinity index	0.48	0.58	0.72

Table VI-2. Crystallinity index (CI) of chitosan, CNFs and LbL-assembled (CHI/CNFs)₁₅₀. The CI is defined as the ratio of the absorbance of the band maximum at about 1427 cm^{-1} to the absorbance of the maximum at about 897 cm^{-1} . Absorbances used to calculate the index were obtained from measurements at these two wavelengths by the usual baseline technique. (these values of CI were calculated for the data evaluation, we remain however skeptical of using this technique; to validate this method, other measurements should be performed in the future e.g. X-ray diffraction characterization of the crystallinity)

Table VI-2 lists the calculated crystallinity index (CI) of pure chitosan, pure CNFs, and the LbL-assembled film of (CHI/CNFs)₁₅₀, showing increased CI after the assembly of the film, which indicates enhanced crystallinity or ordered structures for the LbL-assembled films. This is most probably due to the crystallization of chitosan molecules during assembly, which was also indicated by Bonderer et al.²⁹⁰ who

ascribed an increase of interfacial shear stress to a possible crystallization of chitosan molecules on the surface of alumina platelets. Similar explanations were also given by Coleman et al. who demonstrated that the presence of interfacial crystallinity of matrix (polyvinyl alcohol) has a large bearing on the mechanical properties of carbon nanotubes composites.²⁹⁷

To conclude, the ultra-high tensile strength of the LbL-assembled films of chitosan/CNFs is attributed to a combination of several reasons:

1. The high volume fraction (75%) and homogeneous distribution of the strong CNFs in the chitosan matrix;
2. The rigid laminar β -1,4-D-glucopyrane structures present both on the CNFs and chitosan might lead to more ordered laminar structures;
3. The abundant hydrogen bond donors and acceptors present on the CNFs and chitosan molecules results in strong intra- and intermolecular hydrogen bonds
4. Possible crystallization of chitosan might further enhance the interfacial interactions and thus the mechanical properties of the films.

This combination effect may explain why we got almost twice tensile stress for the chitosan/CNFs films compared to polyvinyl amine (PVAm)/CNFs films obtained by Merindol et al.(Figure VI-19).⁹³ At both relative humidity of dry condition (<5% RH) and ambient condition (<50% RH), the films of chitosan/CNFs exhibited much higher tensile strength than PVAm/CNFs films. At ambient condition, the Young's modulus of chitosan/CNFs films is also higher than that of PVAm/CNFs films, although at dry condition, both films show similar trend and similar Young's modulus. This indicates that the chitosan/CNFs films are more resistant to the influence of the environmental humidity than the PVAm/CNFs films, which might be ascribed to possibly higher degree of crystallinity of the chitosan/CNFs films.

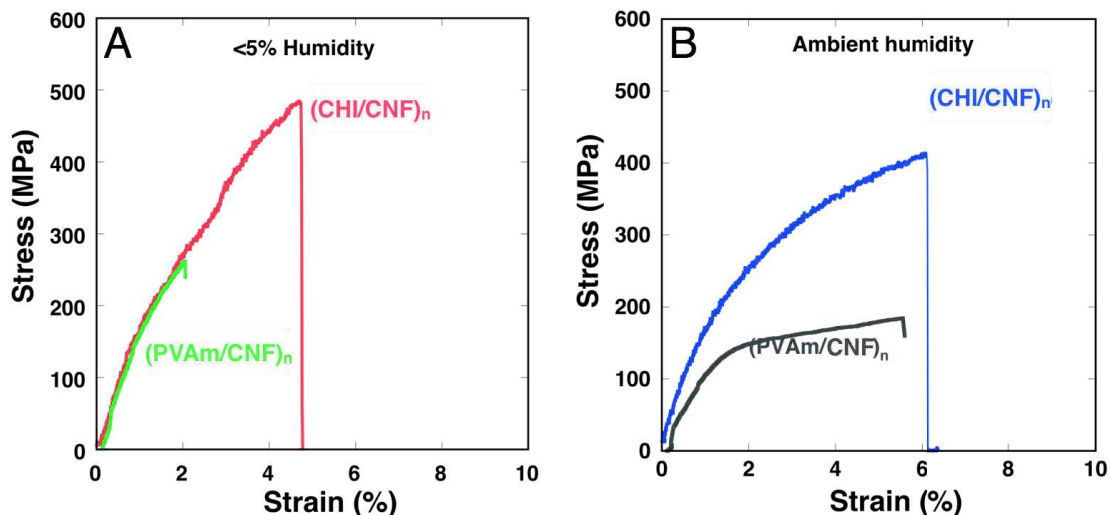


Figure VI-19. A) Typical stress-strain curves obtained under condition of < 5% humidity of (red) dipping LbL-assembled film (CHI/CNF)₁₅₀ compared with (green) dipping LbL-assembled film (PVAm/CNF)_n; B) Typical stress-strain curves obtained under condition of ambient humidity of (blue) dipping LbL-assembled film (CHI/CNF)₁₅₀ compared with (grey) dipping LbL-assembled film (PVAm/CNF)_n. All curves were obtained after polynomial fitting. The curves of (PVAm/CNF)_n were obtained from previous study of Merindol et al.⁹³

VI-C-1.2. Influence of humidity on the mechanical properties of CNFs based films

From Figure VI-19, we can see that the humidity has influence on the mechanical properties of the LbL-assembled CNFs based films, which has already been pointed out by several studies.⁹³ Merindol et al. showed that, as humidity increased, strength and Young's modulus of the film decreased while the strain at break increased, which was attributed to the plasticizing effect of water (Figure VI-20). As mentioned in the previous section, we also studied this effect by performing the tensile tests under dry and ambient conditions of humidity. Similarly, we found drop of tensile stress and rise of strain at break under ambient humidity compared to dry conditions (Figure VI-19).

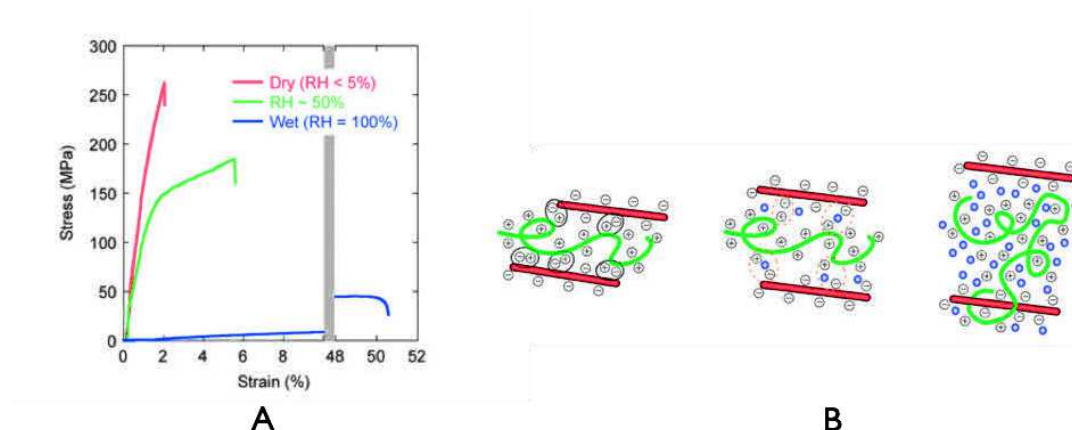


Figure VI-20. Typical stress-strain curves obtained for $(\text{PVAm}/\text{CNF})_n$ thick films built from PVAm solution at $\text{pH}=10$ in various humidity conditions; (B) Simplified molecular sketch of the effect of hydration on the interactions between CNF and PVAm. The green lines represent PVAm; the red sticks correspond to CNF, and the blue dots represent the water molecules in the film; + and - symbols represent, respectively, pending ammonium and carboxylates groups (counter ions have been omitted for clarity).⁹³

In order to confirm this plasticizing effect of water, nanoindentation tests at different relative humidity conditions (from 5% to 33%) were carried out on micron-thick chitosan/CNFs films. In order to avoid unintentional probing of the properties of the substrate during the nanoindentation tests, micron thick dipping LbL-assembled films of $(\text{CHI}/\text{CNFs})_{300}$ with a thickness about $2.1 \mu\text{m}$ were prepared on hydrophilic Si-wafers. Nanoindentation tests on these films were performed by following the procedures described in section II-B-6 and the load-displacement curves were obtained.

Figure VI-21A shows representative load-displacement curves of the nanoindentation tests, from which we can see that the slope S of the load-displacement curves during the beginning stage of unloading dropped with increasing relative humidity. This is quantified by the calculated Young's modulus of these nanoindentation tests at different relative humidity shown in Figure VI-21B, which shows gradual drop of Young's modulus with increasing humidity. This is consistent with previous studies showing humidity influence on the mechanical properties of LbL-assembled films arising from water plasticizing effect. These results also emphasize that the nanoindentation technique permits to assess quantitatively and accurately the Young's modulus of the samples in such specific experimental conditions.

In addition to these nanoindentation tests of static mode, more sophisticated dynamic measurements involving sinusoidal force nanoindentation with relatively high frequency of partial unloading were later carried out at different relative humidity conditions on similar CNFs based LbL-assembled films of (CHI/CNFs)₃₀₀ following the procedure described in section II-B-6.3.2.

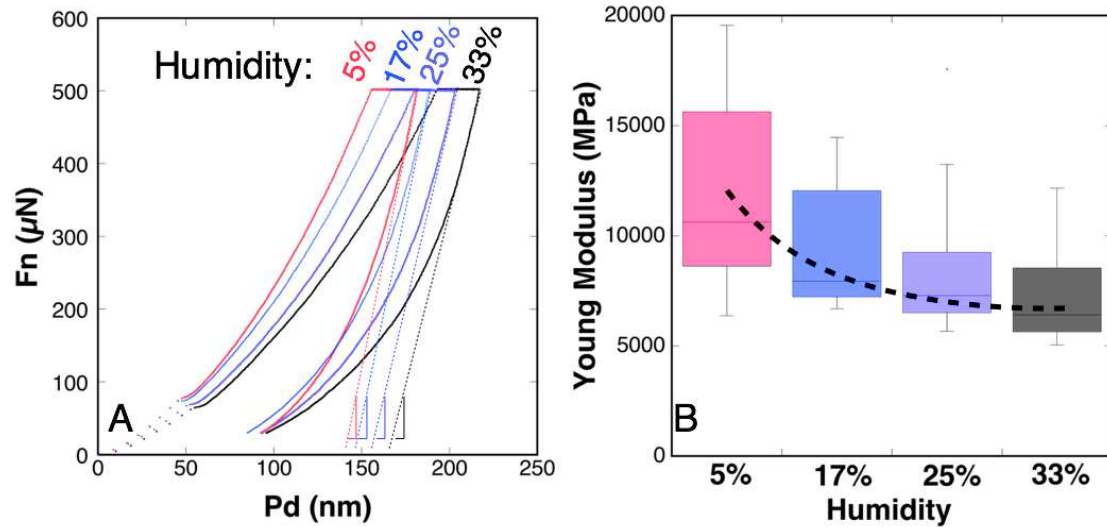


Figure VI-21. A) Load-displacement curve of nanoindentation tests at different humidity conditions of CNFs based films (of thickness about $2.1 \mu\text{m}$) coated on Si-wafers (from left to the right: 5% (red), 17% (blue), 25% (violet), 33% (black); the dotted lines are slopes (S) at the beginning of unloading stage for each humidity condition); B) Young's modulus as a function of different humidity under which the samples were conditioned and measured (the dash black curve is drawn to guide the eyes).

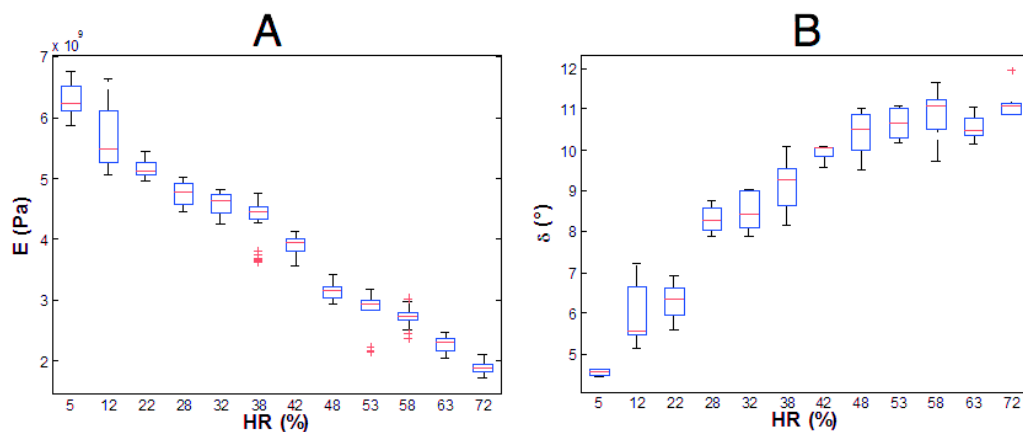


Figure VI-22. A) Young's modulus and B) Load-displacement phase shift (δ) versus relative humidity RH (from 5% to 72%) obtained with dynamic nanoindentation tests on the (CHI/CNFs)₃₀₀ of a thickness about $2.1 \mu\text{m}$.

The resulting values of Young's modulus were plotted as a function of relative humidity (Figure VI-22A). Once again, we found continuous decrease of the Young's modulus with increasing RH. The Young's modulus dropped from about 6 GPa in dry condition to about 2 GPa at 72% RH. The relatively lower Young's modulus in dry condition of about 6 GPa compared to that of 14 GPa obtained by tensile test on similar CNFs based films, could be explained by the fact that the LbL-assembled films are highly anisotropic between the lateral (x-y) and depth (z) direction. The bonding interactions on the vertical z direction are generally lower than the lateral direction. Since the tensile tests and nanoindentation tests measure the films' Young's modulus in the lateral and vertical directions respectively, the obtained Young's modulus with these two methods should be different due to the anisotropy of the LbL-assembled films. This anisotropic effect is further enhanced for the CNFs based films because of the inherent anisotropy of the cellulose nanofibrils. Despite the difference, these values are still comparable or even stronger than most common polymer films.²⁹⁸ The load-displacement phase shifts (δ) were also plotted as a function of relative humidity (Figure VI-22B). We observed that the phase shift δ tends to increase with increasing RH and reaches a plateau at RH of about from 50% to 70%, which indicated a transition in RH where water absorption and plasticization of the film's network reached to a critical point. Both results of Young's modulus and phase shift at different RH conditions obtained by dynamic nanoindentation tests confirmed the existence of water plasticizing effect to the mechanical properties of CNFs based LbL-assembled films. This is in agreement with the results of static nanoindentation tests and tensile tests. Furthermore, the nanoindentation technique informs us about the probable existence of a saturation phenomenon for high RH values (typically above 50%). For the future study, the analysis of viscoelastic properties as a function of temperature at different relative humidity conditions could be investigated in order to determinate the glass transition temperature (T_g) of the LbL-assembled films although it was estimated out of scope in this work.

VI-C-1.3. Influence of fiber alignment on the mechanical properties

Due to the anisotropic mechanical properties of the CNFs, it's interesting to make LbL-assembled films with aligned CNFs and study the influence of the fiber alignment on the mechanical properties of the films. Spin-assisted LbL-assembly is known to be able to align anisotropic objects by the dynamic shearing force.²⁹⁹ Thick LbL-assembled films of (CHI/CNFs)₁₂₀ were constructed using spin-coating method following the procedure described in the section II-A-6.2.

Figure VI-23 shows the linear thickness variation of the spin-coating LbL-assembled films of (CHI/CNFs) as a function of the number of layer pairs during build-up and optical graph of relevant films on Si-wafer with different interference colors. The birefringence originating from the alignment of CNFs of the as-prepared spin-coating LbL-assembled film of 120 layer pairs of (CHI/CNFs) was characterized by the cross-polarized light microscope (cPIM) (see section II-B-4.4). Similarly to the results of aligned CNTs based films (Figure VI-8), Figure VI-24 shows birefringence of the film of spin-assisted LbL-assembled film (CHI/CNFs)₁₂₀ caused by the alignment of CNFs, which led to variation of film's light intensity as a function of the azimuth rotating angle of the film.

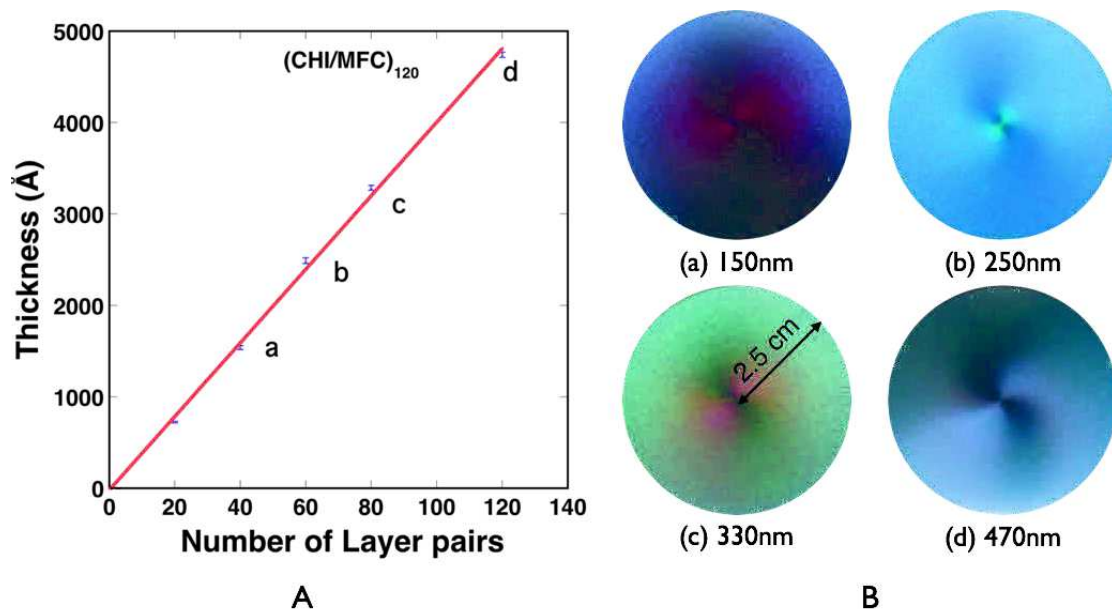


Figure VI-23. A) Build-up of (CHI/MFC)_n using spin-assisted LbL-assembly with rotation

speed of 8000 Rpm followed by spectroscopic ellipsometry with fixed refractive n equal to 1.55; B) Reflection pictures showing the interference colors of the film at different thicknesses indicated below each sample (scale bar shows the radius of the Si-wafer = 2.5 cm).

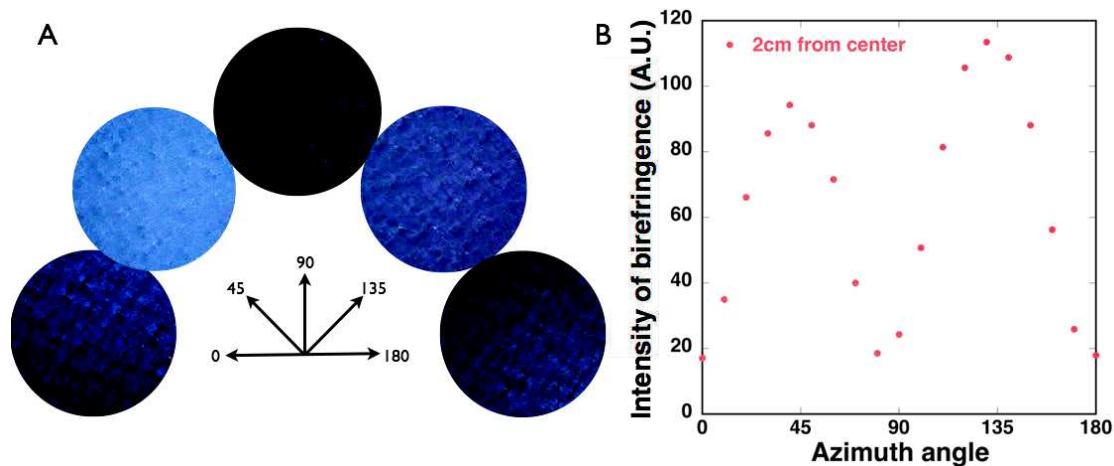


Figure VI-24. A) Reflection optical micrographs taken every 20 degrees of sample's azimuth rotation under cross-polarizer of the spin-assisted LbL-assembled film (CHI/MFC)₁₂₀ with rotation speed of 8000 (pictures were taken on a spot at a distance of 2 cm from the center of the same sample shown in Figure VI-23); B) Intensity of the birefringence calculated based on the light intensity of the micrographs in A as a function of the azimuth rotation angle of the sample.

Apart from the macroscopic characterization of the alignment of the CNFs in the spin-assisted LbL-assembled films of (CHI/CNFs) by the cPIM, microscopic characterization of the alignment of CNFs by AFM was also carried out. AFM image of one layer pair of spin-assisted LbL-assembled chitosan/CNFs on Si-wafer was obtained and analyzed with Image-J using a plugin - Orientation-J developed by the Biomedical Imaging Group in the EPFL which allows to visualize and quantify the degree of orientation of each pixel of an image (Figure VI-25).³⁰⁰ As expected, we observed a dominant distribution of the fibers in main the alignment direction (0 degree) and gradually decreasing distribution with increasing deviation degree from the alignment direction (Figure VI-25B), which indicates again the alignment of the CNFs by spin-assisted LbL-assembly. Using the software, the alignment of the CNFs in the AFM image of can be visualized by labeling the fibers with different color depending on their alignment direction (Figure VI-25D). From Figure VI-25C, we

can observe a major vertical (0 degree) alignment direction of the fibers labeled with red color combined with small amount of fibers bearing alignment direction deviated from the main alignment direction at 0 degree which are colored mainly in green and blue.

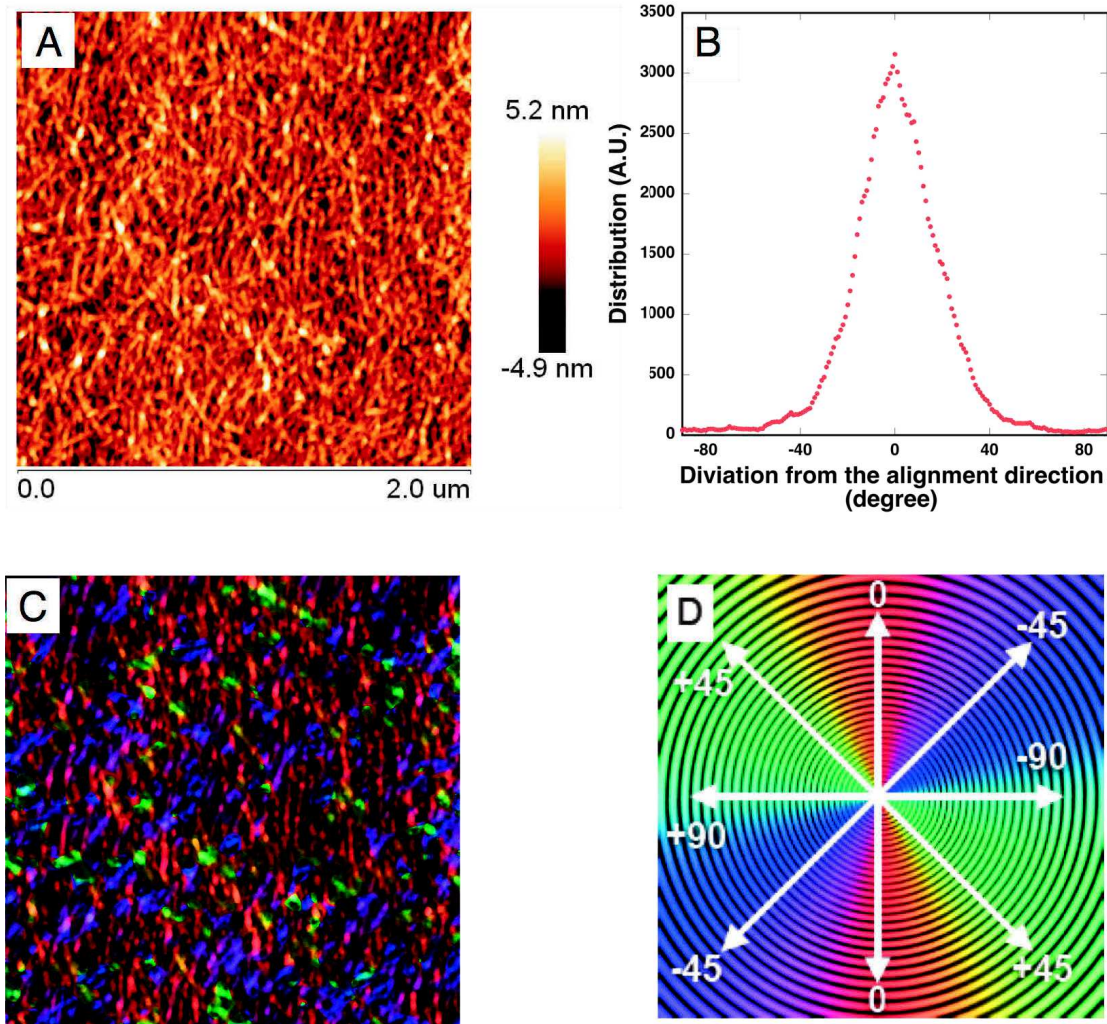


Figure VI-25. A) AFM image of one layer pair of spin-assisted LbL-assembled chitosan/CNFs on Si-wafer; B) Distribution of orientation obtained after analyzing the AFM image A with software Image-J using a plugin called Orientation-J from the Biomedical Imaging Group in EPFL;⁹³ C) Colored image after orientation analysis and visual representation of AFM image A with Orientation-J; D) Color map of the colored image C showing different orientation as a function of color.

In order to quantify the alignment of the fibers, we used an order parameter (S) corresponding to the average of the second Legendre polynomial which is usual

employed to characterize the degree of orientation of the nematic phase for liquid crystals. The order parameter S can be calculated using the equation:

$$S = \left\langle \frac{3 \cos^2(\theta) - 1}{2} \right\rangle \quad \text{Equation VI-5}$$

where θ is the deviation angle between an element and the main alignment direction of the sample. The average is weighed by the distribution intensity (Figure VI-25B) measured at each angle. This parameter of value between 0 and 1 defines the degree of orientation of a sample. The value 0 refers to non-oriented samples, while 1 refers to perfectly oriented samples. Using the distribution intensity data of Figure VI-25B, we obtained the order parameter $S = 0.84$ for the spin-assisted LbL-assembled film of (CHI/CNFs)₁₂₀, which confirms the alignment of the CNFs by spin-assisted LbL-assembly.

After having characterized the alignment of CNFs in the spin-assisted LbL-assembled films of (CHI/CNFs), we started investigating the mechanical properties of these aligned CNFs based LbL-assembled films. Stripes of spin-assisted LbL-assembled films of (CHI/CNFs)₁₂₀ were cut in parallel to the direction of orientation of the fibers (along the direction of circle sample's radius) and characterized by tensile tests. Figure VI-26 shows representative stress-strain curves of the spin-assisted LbL-assembled films of (CHI/CNFs) compared with that of dipping LbL-assembled films. The tensile stress of the spin-assisted LbL-assembled film was increased to higher than 540 MPa and the Young's modulus reached up to 50 GPa. The tensile stress is in agreement with previously calculated ultimate stress for our CNFs of 600 MPa. These remarkable and better mechanical properties compared to the dipping LbL-assembled films of random CNFs, are probably due to the alignment effect of the CNFs, which reinforce the film's mechanical properties in the direction of fiber alignment.

Using the simple rule of mixtures:

$$E_c = E_f v_f + E_m (1 - v_f) \quad \text{Equation VI-6}$$

Where E_c , E_f , E_m , are the Young's modulus of composite material, fibers and matrix, respectively, and the volume fraction of the CNFs fibers $v_v = 0.75$, we obtained E_f of about 70 GPa, which is slightly higher than the previously calculated Young's modulus for the amorphous part of the CNFs about 48 GPa. This indicates possibly different fibers rupture mechanics between the films of aligned CNFs and that of

random CNFs. Nevertheless, the obtained Young's modulus of 50 GPa for the LbL-assembled films of aligned CNFs is comparable to some Kevlar composites, and to our knowledge it concerns the strongest CNFs based material.²⁹¹

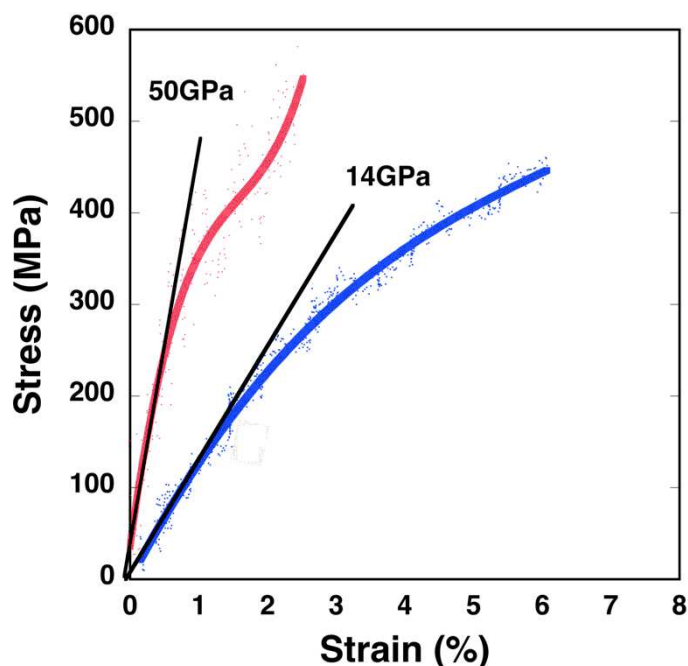


Figure VI-26. Typical stress-strain curves of (red) spin-assisted LbL-assembled film (CHI/MFC)₁₂₀ and (blue) dipping LbL-assembled film (CHI/MFC)₁₅₀. Both curves were obtained after polynomial fitting, and the modulus deduced at low deformation is about 50 GPa for spin-assisted LbL-assembled film and 14 GPa for dipping LbL-assembled film.

Summary

In summary, in this chapter, we studied the mechanical reinforcement of the LbL-assembled films with CNTs and CNFs by testing mechanical properties nanofibers based films through tensile tests and nanoindentation tests. Both CNTs and CNFs based films showed considerably improved tensile strength and Young's modulus compared to polyelectrolytes films, which confirms the mechanical reinforcement effect of the nanofibers in addition to their effect in enhancing membrane's permeability. In addition, different factors impacting the nanofibers based films' mechanical properties were also studied including ionic strength of the solutions, alignment of the nanofibers, influence of interfacial interactions and effect of relative humidity, which provide theoretical and experimental basis for constructing robust LbL-assembled films and LbL-assembly modified nanofiltration membranes.

Conclusions and perspectives

It is known that traditional TFC nanofiltration membranes made by forming selective polyamide thin film on porous membrane support through interfacial polymerization has several fatal issues such as high fouling potential, high-cost or poor chlorine resistance.¹ Fortunately these issues can be solved by producing new generation nanofiltration membranes via the versatile LbL-assembly technique that has numerous features such as:

- Ease of film construction in aqueous and environmentally friendly conditions;
- Customizable membrane properties (e.g. chemical resistance) via designing and alternating various parameters of LbL-assembly such as type of polyelectrolytes, ionic strength, choice of charge type of capping polyelectrolyte, etc...
- Ultra-thin, defect-free and homogeneous selective coating resulting in membranes with high permeability and retention;
- Possibility of incorporating nanofibers as intermediate layer for improving membrane permeability and reinforcing mechanical properties.

Therefore the goal of this thesis was to construct new generation nanofiltration membranes with high membrane performance and of mechanical robustness using LbL-assembly technique within a European cooperation project.

1. Film growth behaviors and their link to membrane performance

To achieve this goal, fundamental study of the film growth behaviors of the LbL-assembled films were firstly carried out in order to understand and establish the link between film growth behaviors and the membrane performance of LbL-assembly modified NF membranes. LbL-assembly of (PDADMAC/PSS) was chosen as main system for the membrane modification for the reason that both PDADMAC and PSS were proved to be highly resistant to chlorine oxidation. By studying LbL-assembly of (PDADMAC/PSS) system on different surfaces including conventional tool surfaces (Si-wafers, quartz slides, quartz crystal metalized with gold), spin-coated membrane-like surface and real membrane surface (flat sheet membranes and hollow

fiber membranes), we confirmed successful LbL-assembly on these surfaces and observed non-linear growth regime as well as important surface effect on the film growth.

1.1. Surface effect on the film growth behavior

It was observed that the surface effect resulted in different growth behaviors in the zone I of the conventional zone model for substrates bearing different surface properties such as hydrophilicity or charge density/zeta potential (Figure C-1). For the films to pass the zone I and to enter the linear zone II, different number of layer pairs was needed for different surfaces. 4 layer pairs was required for films constructed on Si-wafers, whereas 6 layer pairs was needed for films on quartz slides, which was ascribed to higher zeta potential of quartz slides than Si-wafers. Besides, more interestingly, only 3 layer pairs was needed for the films on real membranes support, which was probably due to the hydrophobic and low charge density/surface potential of the membrane surfaces made of partially charged PES. This study showed strong influence of the surface properties on the film growth of LbL-assembly. This is important for understanding the dependence of membrane performance of LbL-assembly modified membranes on the number of layer pairs of LbL-coating.

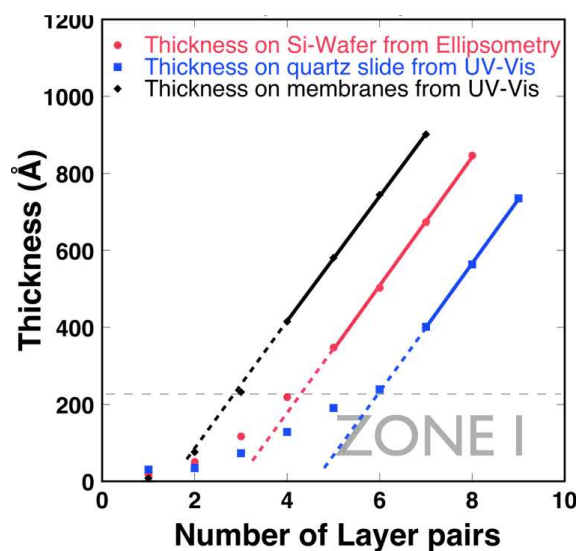


Figure C-2. Surface effect on the zone I of LbL-assembled (PDADMAC/PSS)_n demonstrated by comparing thickness values of the films assembled on three different surfaces (Si-Wafers, Quartz slides, Flat sheet membranes HF_s). The dotted grey line indicates the thickness under which zone I is located.

1.2. Non-linear growth behavior and Donnan exclusion effect

The excellent ion separation ability of the LbL-assembly modified nanofiltration membrane have been deduced mostly from electrostatic repulsive forces also called Donnan exclusion effect owing to the particular multi-bipolar architecture of the LbL-assembled film.¹⁸⁷ While Donnan exclusion effect of the LbL-assembled films is suggested to be mainly contributed by the uncompensated or over-compensated extrinsic charges that form in the zone II, which is commonly agreed but barely proved for the lack of accurate quantitative characterization of the LbL-assembly on real membranes.^{4,9,39,175,180,181,188–201}

Using UV-Vis reflection spectroscopy, we successfully monitored the film growth on flat sheet membranes and confirmed non-linear growth behavior on the membranes support. It was found that film started growing linearly (zone II) from the fourth layer pairs of coating, which is exactly in agreement with the membrane performance results obtained later on where best MgSO_4 retention was achieved with 4 layer pairs of coating (Figure C-2). This confirmed the direct link of non-linear growth mechanism to the high membrane retention arising from Donnan exclusion effect, which has already been pointed out by Ghostine et al.⁴³ who showed that Donnan exclusion effect reached to maximum at the zone II of the non-linear growth regime films.

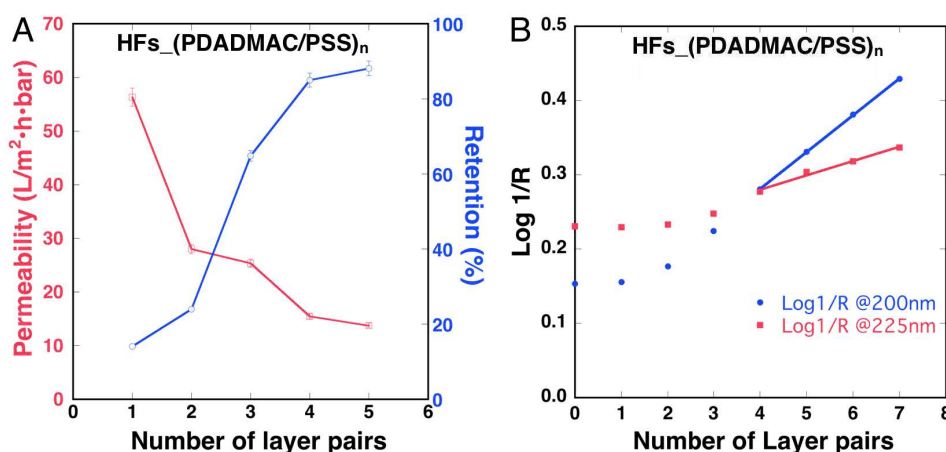


Figure C-2. A) MgSO_4 retentions and water permeability for LbL-assembly modified hollow fiber membranes coated with n layer pairs as a function of number of layer pairs; B) $\text{Log } 1/R$ as a function of number of layer pairs obtained from UV-Vis reflection spectroscopy measurements data.

In summary, non-linear growth regime and its Donnan exclusion effect originating from extrinsic charges in the zone II were confirmed to be the reasons why membrane coated with such films can achieve excellent performance. This was very important finding for our later investigation on the LbL-assembly modified membranes and the nanofibers reinforced membranes.

2. LbL-assembly modified NF membranes and nanofibers reinforced membranes

2.1. LbL-assembly modified NF membranes

After having studied the fundamental film growth behavior of LbL-assembled films of (PDADMAC/PSS), we turned to investigating the membrane performance of the LbL-assembly modified NF membranes by coating different number of layer pairs of (PDADMAC/PSS) on hollow fiber membrane supports and testing their MgSO_4 retention and water permeability. It was found that the retention of MgSO_4 increased and the water permeability dropped with increasing number of layer pairs of coating until they reached to a plateau at 4 layer pairs. With 4 layer pares of coating, the obtained MgSO_4 retention of $85.5 \pm 2.1\%$ combined with optimal water permeability of about $13.5 \pm 1.5 \text{ L/m}^2 \cdot \text{h} \cdot \text{bar}$ which is almost twice that of commercial nanofiltration membranes due to much thinner selective coating made by LbL-assembly.¹⁰ Furthermore, the same coated membranes exhibited more than 100000ppm-hrs of chlorine resistance which is orders of magnitude higher than traditional TFC polyamide nanofiltration membranes.⁵⁰

2.2. Three layers structure for improving membrane permeability

As described in the state of the art, owing to the introduction of water nanochannels, LbL-assembly modified membranes of three layers structure with intermediate layer of nanofibers between the top selective layer and membrane support on the bottom was employed for improving membrane permeability. CNTs and CNFs, two strong nanofibers were chosen for the construction of the intermediate layer. Prior to making LbL-assembly modified membranes with these nanofibers, fundamental investigations on the LbL-assembly of nanofibers based films on tool surfaces were carried out after successful preparation of stable nanofibers aqueous suspensions.

LbL-assembly modified membranes with one layer of CNTs as intermediate layer showed 40% higher permeability while retaining similar MgSO_4 retention compared

to membranes modified with pure polyelectrolytes of (PDADMAC/PSS), which proved our concept of three layer structure for improving membrane permeability. This concept can be potentially useful for improving permeability of traditional TFC membranes that have also dense selective layer limiting their flux. CNFs reinforced membranes showed improved MgSO_4 retention, however, did not show any improvement of permeability, which might be due to the hydrophilic properties of the CNFs surfaces that was suggested to have less improvement of water transport than hydrophobic nanofibers like CNTs.²⁶⁴

3. Nanofibers reinforcement on mechanical properties of LbL-assembled films

Apart from the effect in improving membrane permeability, the intermediate layer of nanofibers serves also as strong mechanical support for the selective layer of polyelectrolytes. Therefore, another main goal of this thesis was to study the mechanical reinforcement of nanofibers to the LbL-assembled films. In order to test the mechanical properties of LbL-assembled films, micron-thick freestanding films were prepared with help of a programmed automatic robot machine and then tensile tests on the samples made of these films were performed.

- It was found that, compared to LbL-assembled films of pure polyelectrolytes (PDADMAC/PSS), CNTs and CNFs based films both exhibited far much better tensile strength and young modulus. The mechanical properties of the nanofibers based films could even be further improved by in plane alignment of nanofibers.

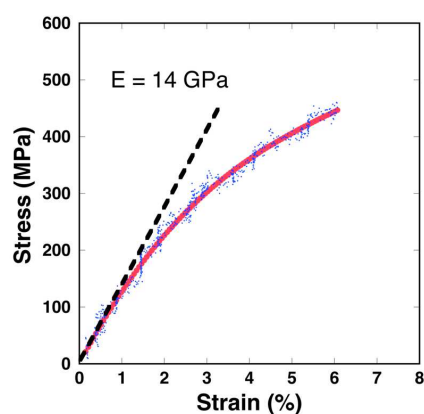


Figure C-3. Representative stress-strain curve for films of dipping LbL-assembled film $(\text{CHI/CNFs})_{150}$ tested under ambient humidity (polynomial fitting in red line). The Young's modulus estimated graphically at low deformation is about 14 GPa.

- The importance of the interfacial interactions between the nanofibers and the polyelectrolytes matrix on the film's mechanical properties was also investigated. It was shown that weaker interfacial interactions could lead to fibers pull-out dominant film failure which resulted in relatively lower tensile strength for the CNTs based films compared with CNFs based films. In contrast, for CNFs based films, tensile strength of up to 450 MPa (Figure C-3) and fiber-breaking dominant film failure was observed, which was mainly attributed to the inherent rigid structure of β -1,4-D-glucopyrane of the chitosan and its high affinity with CNFs by forming intra- and intermolecular hydrogen bonds, high volume fraction of nanofibers of up to 75% and possible crystallization of chitosan.

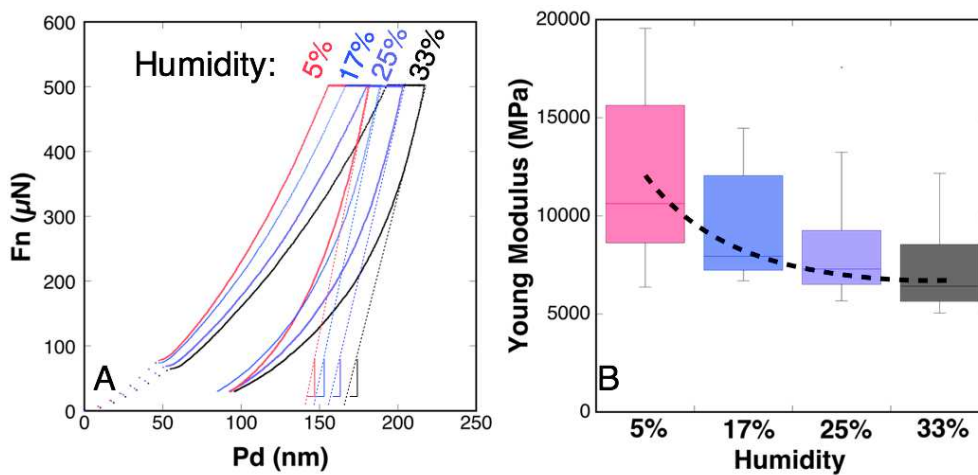


Figure C-4. A) Load-displacement curve of nanoindentation tests at different humidity conditions of CNFs based films (of thickness about 2.1 μ m) coated on Si-wafers (from left to the right: 5% (red), 17% (blue), 25% (violet), 33% (black); the dotted lines are slopes (S) at the beginning of unloading stage for each humidity condition); B) Young's modulus as a function of different humidity under which the samples were conditioned and measured (the dash black curve is drawn to guide the eyes).

- Relative humidity was found to have an effect on the mechanical properties of the CNFs based films (Figure C-4). Higher relative humidity led to lower tensile strength, which is consistent with previous study by Merindol et al.⁹³ This was further explored by complementary tests of both static and dynamic nanoindentation, where continuous dropping of the Young's modulus with increasing RH was found. Despite the inconsistency in obtained Young's

modulus between the nanoindentation tests and the tensile tests, which originated from the anisotropy of the LbL-assembly and the CNFs, the effect of relative humidity on the mechanical properties of CNFs based films was confirmed.

To conclude, in this thesis work involved in a European project, we systematically studied the fundamental film growth behaviors of LbL-assembly and their connection with LbL-assembly modified membrane's performance. We studied and understood the non-linear growth regime, and successfully explained the results of membrane retention and permeability with the zone model and the Donnan exclusion effect originating from the extrinsic charges present in the zone II of films with non-linear growth regime. Inspired by the works of Chu et al.⁷² and of Blell²⁹, three layers structured system with intermediate layer of nanofibers was studied in two aspects, which are improvement of membrane performance and reinforcement of mechanical properties of LbL-assembled films respectively.

This work opens the possibility to preparing new generation membranes with high attractive features such as low cost, customizable performance or high chemical resistance using LbL-assembly technique. Extra work could be carried out on making LbL-assembly modified membranes with other systems particularly systems with non-linear growth regime. More works should be performed on the investigation on three layers structured membranes in order to understand why incorporation of CNFs could not improve the permeability.

The obtained record mechanical properties for the chitosan and CNFs based films approached that of Kevlar and could lead to an interesting extension of this work (Figure C-5), which is the possibility of constructing purely biobased nanocomposites of ultrastrong mechanical properties with the LbL-assembly of chitosan and CNFs that could lead to various applications, e.g. personal armor with biodegradable property. Besides, extra studies of the effects of relative humidity and ambient temperature on the mechanical properties of LbL-assembled films by nanoindentation technique are also highly interesting for better understanding of the mechanism behind these effects on the mechanical properties of LbL-assembled films. Actually, some of these works have been already started in cooperation with the team of Gauthier at the Institut Charles Sadron.

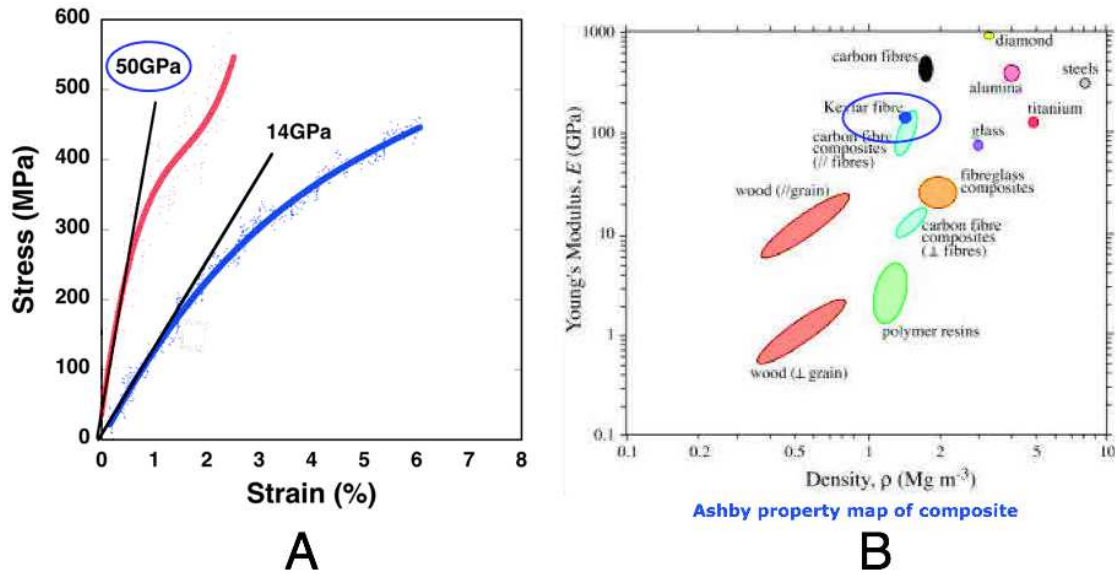


Figure C-5. A) Typical stress-strain curves of (red) spin-assisted LbL-assembled film (CHI/MFC)₁₂₀ and (blue) dipping LbL-assembled film (CHI/MFC)₁₅₀. Both curves were obtained after polynomial fitting, and the modulus deduced at low deformation is about 70 GPa for spin-assisted LbL-assembled film and 14 GPa for dipping LbL-assembled film. B) Ashby property map of composite material where Kevlar fiber (purple circle) shows similar Young's modulus compared to the oriented LbL-assembled film (CHI/MFC)₁₅₀ shown in A.

References

1. Singh, R. *Membrane Technology and Engineering for Water Purification*. (Elsevier, 2015).
2. Peng, X. S., Jin, J., Nakamura, Y., Ohno, T. & Ichinose, I. Ultrafast permeation of water through protein-based membranes. *Nat. Nanotechnol.* **4**, 353–357 (2009).
3. Krasemann, L. & Tieke, B. Ultrathin self-assembled polyelectrolyte membranes for pervaporation. *J. Memb. Sci.* **150**, 23–30 (1998).
4. Harris, J. J., Stair, J. L. & Bruening, M. L. Layered polyelectrolyte films as selective, ultrathin barriers for anion transport. *Chem. Mater.* **12**, 1941–1946 (2000).
5. Ng, L. Y., Mohammad, A. W. & Ng, C. Y. A review on nanofiltration membrane fabrication and modification using polyelectrolytes: Effective ways to develop membrane selective barriers and rejection capability. *Adv. Colloid Interface Sci.* **197–198**, 85–107 (2013).
6. Decher, G. Fuzzy Nanoassemblies: Toward Layered Polymeric Multicomposites. *Science* **277**, 1232–1237 (1997).
7. Miller, M. D. & Bruening, M. L. Controlling the nanofiltration properties of multilayer polyelectrolyte membranes through variation of film composition. *Langmuir* **20**, 11545–11551 (2004).
8. Ulbricht, M. Advanced functional polymer membranes. *Polymer (Guildf)*. **47**, 2217–2262 (2006).
9. Hong, S. U., Malaisamy, R. & Bruening, M. L. Optimization of flux and selectivity in $\text{Cl}^-/\text{SO}_4^{2-}$ separations with multilayer polyelectrolyte membranes. *J. Memb. Sci.* **283**, 366–372 (2006).
10. Hong, S. U., Malaisamy, R. & Bruening, M. L. Separation of fluoride from other monovalent anions using multilayer polyelectrolyte nanofiltration membranes. *Langmuir* **23**, 1716–1722 (2007).
11. Sanyal, O., Sommerfeld, A. N. & Lee, I. Design of ultrathin nanostructured polyelectrolyte-based membranes with high perchlorate rejection and high permeability. *Sep. Purif. Technol.* **145**, 113–119 (2015).
12. Ma, H., Burger, C., Hsiao, B. S. & Chu, B. Ultra-fine cellulose nanofibers: new nano-scale materials for water purification. *J. Mater. Chem.* **21**, 7507 (2011).
13. Decher, G., Lehr, B., Lowack, K., Lvov, Y. & Schmitt, J. New nanocomposite films for biosensors: Layer-by-layer adsorbed films of polyelectrolytes, proteins or DNA. in *Biosensors and Bioelectronics* **9**, 677–684 (1994).
14. Mamedov, A., Ostrander, J., Aliev, F. & Kotov, N. A. Stratified assemblies of magnetite nanoparticles and montmorillonite prepared by the layer-by-layer assembly. *Langmuir* **16**, 3941–3949 (2000).
15. Mamedov, A. A. *et al.* Molecular design of strong single-wall carbon nanotube/polyelectrolyte multilayer composites. *Nat. Mater.* **1**, 190–194 (2002).
16. Karabulut, E. & Wågberg, L. Design and characterization of cellulose nanofibril-based freestanding films prepared by layer-by-layer deposition technique. *Soft Matter* **7**, 3467 (2011).
17. Kharlampieva, E., Kozlovskaya, V. & Sukhishvili, S. A. Layer-by-Layer Hydrogen-Bonded Polymer Films: From Fundamentals to Applications. *Adv. Mater.* **21**, 3053–

- 3065 (2009).
18. Shimazaki, Y., Mitsuishi, M., Ito, S. & Yamamoto, M. Preparation of the Layer-by-Layer Deposited Ultrathin Film Based on the Charge-Transfer Interaction. *Langmuir* **13**, 1385–1387 (1997).
 19. Serizawa, T. *et al.* Stepwise Stereocomplex Assembly of Stereoregular Poly(methyl methacrylate)s on a Substrate. *J. Am. Chem. Soc.* **122**, 1891–1899 (2000).
 20. Serizawa, T., Hashiguchi, S. & Akashi, M. Stepwise Assembly of Ultrathin Poly(vinyl alcohol) Films on a Gold Substrate by Repetitive Adsorption/Drying Processes. *Langmuir* **15**, 5363–5368 (1999).
 21. Decher, G. & Schlenoff, J. B. *Multilayer Thin Films: Sequential Assembly of Nanocomposite Materials*. (WILEY-VCH Verlag GmbH, 2006).
 22. Zhang, X., Chen, H. & Zhang, H. Layer-by-layer assembly: from conventional to unconventional methods. *Chem. Commun.* 1395 (2007).
 23. Xiong, H., Cheng, M., Zhou, Z., Zhang, X. & Shen, J. A New Approach to the Fabrication of a Self-Organizing Film of Heterostructured Polymer/Cu₂S Nanoparticles. *Adv. Mater.* **10**, 529–532 (1998).
 24. Schlenoff, J. B., Dubas, S. T. & Farhat, T. Sprayed polyelectrolyte multilayers. *Langmuir* **16**, 9968–9969 (2000).
 25. Chiarelli, P. a. *et al.* Controlled fabrication of polyelectrolyte multilayer thin films using spin-assembly. *Adv. Mater.* **13**, 1167–1171 (2001).
 26. Cho, J., Char, K., Hong, J. D. & Lee, K. B. Fabrication of highly ordered multilayer films using a spin self-assembly method. *Adv. Mater.* **13**, 1076–1078 (2001).
 27. Dubas, S. T. & Schlenoff, J. B. Factors Controlling the Growth of Polyelectrolyte Multilayers. *Macromolecules* **32**, 8153–8160 (1999).
 28. Lee, S. S. *et al.* Layer-by-layer deposited multilayer assemblies of ionene-type polyelectrolytes based on the spin-coating method. *Macromolecules* **34**, 5358–5360 (2001).
 29. Blell, R. Microfibrillated cellulose based nanomaterials. (2012).
 30. Ferreira, M., Rubner, M. F. & Hsieh, B. R. Luminescence Behavior of Self-Assembled Multilayer Heterostructures of Poly (Phenylenevinylene). *MRS Proc.* **328**, 119 (2011).
 31. Schrof, W. *et al.* Nonlinear Optical Properties of Polyelectrolyte Thin Films Containing Gold Nanoparticles Investigated by Wavelength Dispersive Femtosecond Degenerate Four Wave Mixing (DFWM). *Adv. Mater.* **10**, 338–341 (1998).
 32. Farhat, T. R. & Schlenoff, J. B. Corrosion control using polyelectrolyte multilayers. *Electrochem. Solid State Lett.* **5**, B13–B15 (2002).
 33. Hattori, H. Anti-Reflection Surface with Particle Coating Deposited by Electrostatic Attraction. *Adv. Mater.* **13**, 51–54 (2001).
 34. Hiller, J., Mendelsohn, J. D. & Rubner, M. F. Reversibly erasable nanoporous anti-reflection coatings from polyelectrolyte multilayers. *Nat. Mater.* **1**, 59–63 (2002).
 35. Cheng, J. H., Fou, A. F. & Rubner, M. F. Molecular self-assembly of conducting polymers. *Thin Solid Films* **244**, 985–989 (1994).
 36. Müller, M., Rieser, T., Lunkwitz, K. & Meier-Haack, J. Polyelectrolyte complex layers: a promising concept for anti-fouling coatings verified by in-situ ATR-FTIR spectroscopy. *Macromol. Rapid Commun.* **20**, 607–611 (1999).
 37. Kou, R.-Q. *et al.* Surface Modification of Microporous Polypropylene Membranes by Plasma-Induced Graft Polymerization of α -Allyl Glucoside. *Langmuir* **19**, 6869–6875

- (2003).
38. Ouyang, L., Malaisamy, R. & Bruening, M. L. Multilayer polyelectrolyte films as nanofiltration membranes for separating monovalent and divalent cations. *J. Memb. Sci.* **310**, 76–84 (2008).
 39. Stanton, B. W., Harris, J. J., Miller, M. D. & Bruening, M. L. Ultrathin, multilayered polyelectrolyte films as nanofiltration membranes. *Langmuir* **19**, 7038–7042 (2003).
 40. Lavallo, P. *et al.* Comparison of the structure of polyelectrolyte multilayer films exhibiting a linear and an exponential growth regime: An in situ atomic force microscopy study. *Macromolecules* **35**, 4458–4465 (2002).
 41. Elbert, D. L., Herbert, C. B. & Hubbell, J. A. Thin Polymer Layers Formed by Polyelectrolyte Multilayer Techniques on Biological Surfaces. *Langmuir* **15**, 5355–5362 (1999).
 42. Tang, K. & Besseling, N. A. M. Formation of polyelectrolyte multilayers: ionic strengths and growth regimes. *Soft Matter* **12**, 1032–40 (2016).
 43. Ghostine, R. A., Markarian, M. Z. & Schlenoff, J. B. Asymmetric growth in polyelectrolyte multilayers. *J. Am. Chem. Soc.* **135**, 7636–7646 (2013).
 44. Picart, C. *et al.* Buildup Mechanism for Poly(l-lysine)/Hyaluronic Acid Films onto a Solid Surface. *Langmuir* **17**, 7414–7424 (2001).
 45. Picart, C. *et al.* Molecular basis for the explanation of the exponential growth of polyelectrolyte multilayers. *Proc. Natl. Acad. Sci. U. S. A.* **99**, 12531–5 (2002).
 46. Lavallo, P. *et al.* Modeling the Buildup of Polyelectrolyte Multilayer Films Having Exponential Growth. *J. Phys. Chem. B* **108**, 635–648 (2003).
 47. Lavallo, P. *et al.* Direct evidence for vertical diffusion and exchange processes of polyanions and polycations in polyelectrolyte multilayer films. *Macromolecules* **37**, 1159–1162 (2004).
 48. Ghostine, R. A., Markarian, M. Z. & Schlenoff, J. B. Asymmetric growth in polyelectrolyte multilayers. *J. Am. Chem. Soc.* **135**, 7636–7646 (2013).
 49. S, P., Perry, R. H., Green, D. W. & Maloney, J. O. *Chemical Engineers' Handbook Seventh. Society* **27**, (1997).
 50. Li, N. N., Fane, A. G., Ho, W. S. W. & Matsuura, T. Advanced Membrane Technology and Applications. *John Wiley & Sons, Inc.* (2008).
 51. Loeb, S. & Sourirajan, S. *Sea water demineralization by means of a semipermeable membrane.* (University of California, Department of Engineering, 1963).
 52. Elimelech, M. & Phillip, W. A. The future of seawater desalination: energy, technology, and the environment. *Science* **333**, 712–717 (2011).
 53. Strathmann, H. & Kock, K. The formation mechanism of phase inversion membranes. *Desalination* **21**, 241–255 (1977).
 54. Glater, J., Hong, S. & Elimelech, M. The search for a chlorine-resistant reverse osmosis membrane. *Desalination* **95**, 325–345 (1994).
 55. Schäfer, A. *et al.* *Fouling in Nanofiltration.* (2004).
 56. Zhao, C., Xue, J., Ran, F. & Sun, S. Modification of polyethersulfone membranes – A review of methods. *Prog. Mater. Sci.* **58**, 76–150 (2013).
 57. Marchese, J. *et al.* Fouling behaviour of polyethersulfone UF membranes made with different PVP. *J. Memb. Sci.* **211**, 1–11 (2003).
 58. Sun, M., Su, Y., Mu, C. & Jiang, Z. Improved Antifouling Property of PES Ultrafiltration Membranes Using Additive of Silica–PVP Nanocomposite. *Ind. Eng.*

- Chem. Res.* **49**, 790–796 (2010).
59. Wu, L., Sun, J. & Wang, Q. Poly(vinylidene fluoride)/polyethersulfone blend membranes: Effects of solvent sort, polyethersulfone and polyvinylpyrrolidone concentration on their properties and morphology. *J. Memb. Sci.* **285**, 290–298 (2006).
 60. Stewart, I. Design, Energy and Cost Analyses of Membrane Processes. (2015).
 61. Sedath, R. H., Taylor, D. R. & Li, N. N. Reduced Fouling of Ultrafiltration Membranes Via Surface Fluorination. *Sep. Sci. Technol.* **28**, 255–269 (1993).
 62. Yoon, K. *et al.* High flux ultrafiltration membranes based on electrospun nanofibrous PAN scaffolds and chitosan coating. *Polymer* **47**, 2434–2441 (2006).
 63. Ulbricht, M. & Belfort, G. Surface modification of ultrafiltration membranes by low temperature plasma II. Graft polymerization onto polyacrylonitrile and polysulfone. *J. Memb. Sci.* **111**, 193–215 (1996).
 64. Boributh, S., Chanachai, A. & Jiratananon, R. Modification of PVDF membrane by chitosan solution for reducing protein fouling. *J. Memb. Sci.* **342**, 97–104 (2009).
 65. Kim, E.-S., Yu, Q. & Deng, B. Plasma surface modification of nanofiltration (NF) thin-film composite (TFC) membranes to improve anti organic fouling. *Appl. Surf. Sci.* **257**, 9863–9871 (2011).
 66. Decher, G., Hong, J. D. & Schmitt, J. Buildup of ultrathin multilayer films by a self-assembly process: III. Consecutively alternating adsorption of anionic and cationic polyelectrolytes on charged surfaces. *Thin Solid Films* **210-211**, 831–835 (1992).
 67. Zhao, Q., An, Q. F., Ji, Y., Qian, J. & Gao, C. Polyelectrolyte complex membranes for pervaporation, nanofiltration and fuel cell applications. *J. Memb. Sci.* **379**, 19–45 (2011).
 68. Krasemann, L. & Tieke, B. Highly efficient composite membranes for ethanol-water pervaporation. *Chem. Eng. Technol.* **23**, 211–213 (2000).
 69. Malaisamy, R. & Bruening, M. L. High-flux nanofiltration membranes prepared by adsorption of multilayer polyelectrolyte membranes on polymeric supports. *Langmuir* **21**, 10587–10592 (2005).
 70. Loh, K. J., Lynch, J. P. & Kotov, N. A. Mechanical-Electrical Characterization of Carbon Nanotube Thin Films for Structural Monitoring Applications. *Proc. SPIE* **6174**, 61741Z (2006).
 71. Wang, X., Fang, D., Yoon, K., Hsiao, B. S. & Chu, B. High performance ultrafiltration composite membranes based on poly(vinyl alcohol) hydrogel coating on crosslinked nanofibrous poly(vinyl alcohol) scaffold. *J. Memb. Sci.* **278**, 261–268 (2006).
 72. Wang, X. *et al.* High flux filtration medium based on nanofibrous substrate with hydrophilic nanocomposite coating. *Environ. Sci. Technol.* **39**, 7684–7691 (2005).
 73. Yoon, K., Hsiao, B. S. & Chu, B. High flux nanofiltration membranes based on interfacially polymerized polyamide barrier layer on polyacrylonitrile nanofibrous scaffolds. *J. Memb. Sci.* **326**, 484–492 (2009).
 74. Dahlin, R. L., Kasper, F. K. & Mikos, A. G. Polymeric nanofibers in tissue engineering. *Tissue Eng. Part B. Rev.* **17**, 349–64 (2011).
 75. Pham, Q. P., Sharma, U. & Mikos, A. G. Electrospinning of polymeric nanofibers for tissue engineering applications: a review. *Tissue Eng.* **12**, 1197–211 (2006).
 76. Kim, J. Y. *et al.* Formation of Nanoparticle-Containing Multilayers in Nanochannels via Layer-by-Layer Assembly. *Chem. Mater.* **22**, 6409–6415 (2010).
 77. Wang, Y. & Caruso, F. Template Synthesis of Stimuli-Responsive Nanoporous

- Polymer-Based Spheres via Sequential Assembly. *Chem. Mater.* **18**, 4089–4100 (2006).
78. Wang, Y., Yu, A. & Caruso, F. Nanoporous polyelectrolyte spheres prepared by sequentially coating sacrificial mesoporous silica spheres. *Angew. Chem. Int. Ed. Engl.* **44**, 2888–92 (2005).
79. Mallwitz, F. & Laschewsky, A. Direct Access to Stable, Freestanding Polymer Membranes by Layer-by-Layer Assembly of Polyelectrolytes. *Adv. Mater.* **17**, 1296–1299 (2005).
80. Stroock, A. D., Kane, R. S., Weck, M., Metallo, S. J. & Whitesides, G. M. Synthesis of Free-Standing Quasi-Two-Dimensional Polymers. *Langmuir* **19**, 2466–2472 (2003).
81. Rehage, H. & Veyssié, M. Two-Dimensional Model Networks. *Angew. Chemie Int. Ed. English* **29**, 439–448 (1990).
82. Caruso, F. Nanoengineering of Inorganic and Hybrid Hollow Spheres by Colloidal Templating. *Science* **282**, 1111–1114 (1998).
83. Jiang, C., Markutsya, S., Pikus, Y. & Tsukruk, V. V. Freely suspended nanocomposite membranes as highly sensitive sensors. *Nat. Mater.* **3**, 721–8 (2004).
84. Ko, H., Jiang, C., Shulha, H. & Tsukruk, V. V. Carbon Nanotube Arrays Encapsulated into Freely Suspended Flexible Films. *Chem. Mater.* **17**, 2490–2493 (2005).
85. Ono, S. S. & Decher, G. Preparation of ultrathin self-standing polyelectrolyte multilayer membranes at physiological conditions using pH-responsive film segments as sacrificial layers. *Nano Lett.* **6**, 592–8 (2006).
86. Markutsya, S., Jiang, C., Pikus, Y. & Tsukruk, V. V. Freely Suspended Layer-by-Layer Nanomembranes: Testing Micromechanical Properties. *Adv. Funct. Mater.* **15**, 771–780 (2005).
87. Patro, T. U. & Wagner, H. D. Layer-by-layer assembled PVA/Laponite multilayer free-standing films and their mechanical and thermal properties. *Nanotechnology* **22**, 455706 (2011).
88. Mamedov, A. a. & Kotov, N. a. Free-standing layer-by-layer assembled films of magnetite nanoparticles. *Langmuir* **16**, 5530–5533 (2000).
89. Podsiadlo, P. *et al.* Ultrastrong and stiff layered polymer nanocomposites. *Science* **318**, 80–83 (2007).
90. Hua, F., Cui, T. & Lvov, Y. M. Ultrathin cantilevers based on polymer-ceramic nanocomposite assembled through layer-by-layer adsorption. *Nano Lett.* **4**, 823–825 (2004).
91. Liang, Z., Susha, A. S., Yu, A. & Caruso, F. Nanotubes Prepared by Layer-by-Layer Coating of Porous Membrane Templates. *Adv. Mater.* **15**, 1849–1853 (2003).
92. Landel, R. F. & Nielsen, L. E. *Mechanical Properties of Polymers and Composites, Second Edition.* (1993).
93. Merindol, R. *et al.* Bio-inspired multiproperty materials: strong, self-healing, and transparent artificial wood nanostructures. *ACS Nano* **9**, 1127–36 (2015).
94. Fischer-Cripps, A. C. *Nanoindentation.* (Springer New York, 2011).
95. Oliver, W. C. & Pharr, G. M. An improved technique for determining hardness and elastic modulus using load and displacement sensing indentation experiments. *J. Mater. Res.* **7**, 1564–1583 (2011).
96. Fan, X., Park, M.-K., Xia, C. & Advincula, R. Surface Structural Characterization and Mechanical Testing by Nanoindentation Measurements of Hybrid Polymer/clay

- Nanostructured Multilayer Films. *J. Mater. Res.* **17**, 1622–1633 (2011).
97. Lehaf, A. M., Hariri, H. H. & Schlenoff, J. B. Homogeneity, modulus, and viscoelasticity of polyelectrolyte multilayers by nanoindentation: Refining the buildup mechanism. *Langmuir* **28**, 6348–6355 (2012).
 98. Hariri, H. H., Lehaf, A. M. & Schlenoff, J. B. Mechanical Properties of Osmotically Stressed Polyelectrolyte Complexes and Multilayers: Water as a Plasticizer. *Macromolecules* **45**, 9364–9372 (2012).
 99. Wang, J. *et al.* Thickness dependence of elastic modulus and hardness of on-wafer low-k ultrathin polytetrafluoroethylene films. *Scr. Mater.* **42**, 687–694 (2000).
 100. Zhao, W. *et al.* Dispersion and noncovalent modification of multiwalled carbon nanotubes by various polystyrene-based polymers. *J. Appl. Polym. Sci.* **109**, 3525–3532 (2008).
 101. Dobbins, T., Chevious, R. & Lvov, Y. Behavior of Na⁺-Polystyrene Sulfonate at the Interface with Single-Walled Carbon Nanotubes (SWNTs) and Its Implication to SWNT Suspension Stability. *Polymers* **3**, 942–954 (2011).
 102. Hill, D. E., Lin, Y., Rao, A. M., Allard, L. F. & Sun, Y. P. Functionalization of Carbon Nanotubes with Polystyrene. *Macromolecules* **35**, 9466–9471 (2002).
 103. Wågberg, L. *et al.* The build-up of polyelectrolyte multilayers of microfibrillated cellulose and cationic polyelectrolytes. *Langmuir* **24**, 784–795 (2008).
 104. Wågberg, L., Winter, L., Ödberg, L. & Lindström, T. On the charge stoichiometry upon adsorption of a cationic polyelectrolyte on cellulosic materials. *Colloids and Surfaces* **27**, 163–173 (1987).
 105. Maoz, R., Frydman, E., Cohen, S. R. & Sagiv, J. Constructive nanolithography: Site-defined silver self-assembly on nanoelectrochemically patterned monolayer templates. *Adv. Mater.* **12**, 424–429 (2000).
 106. Zeman, L. & Fraser, T. Formation of air-cast cellulose acetate membranes Part II. Kinetics of demixing and microvoid growth. *J. Memb. Sci.* **87**, 267–279 (1994).
 107. Zeman, L. & Fraser, T. Formation of air-cast cellulose acetate membranes. Part I. Study of macrovoid formation. *J. Memb. Sci.* **84**, 93–106 (1993).
 108. Kim, I.-C., Yun, H.-G. & Lee, K.-H. Preparation of asymmetric polyacrylonitrile membrane with small pore size by phase inversion and post-treatment process. *J. Memb. Sci.* **199**, 75–84 (2002).
 109. H. STRATHMANN. *Materials Science of Synthetic Membranes.* **269**, (1985).
 110. van de Witte, P., Dijkstra, P. J. J., van den Berg, J. W. a. W. a & Feijen, J. Phase separation processes in polymer solutions in relation to membrane formation. *J. Memb. Sci.* **117**, 1–31 (1996).
 111. Arahman, N. Structure Change of Polyethersulfone Hollow Fiber Membrane Modified with Pluronic F127, Polyvinylpyrrolidone, and Tetronic 1307. *Mater. Sci. Appl.* **03**, 72–77 (2012).
 112. Figoli, A. *et al.* Towards non-toxic solvents for membrane preparation: a review. *Green Chem.* **16**, 4034 (2014).
 113. Finch, C. A. Synthetic polymer membranes - a structural perspective, 2nd edition. *Br. Polym. J.* **18**, 211–211 (1986).
 114. Azzam, R. M. A. & Bashara, N. M. Ellipsometry and polarized light. (1987).
 115. Anderson, R. J., Bendell, D. J. & Groundwater, P. W. *Organic Spectroscopic Analysis.* **22**, (Royal Society of Chemistry, 2004).

116. Sauerbrey, G. Use of crystal oscillators for weighing thin films and for microweighing. *Zeitschrift fuer Phys.* **155**, 206–222 (1959).
117. Marx, K. A. Quartz crystal microbalance: A useful tool for studying thin polymer films and complex biomolecular systems at the solution - Surface interface. *Biomacromolecules* **4**, 1099–1120 (2003).
118. Rodahl, M., Höök, F., Krozer, A., Brzezinski, P. & Kasemo, B. Quartz crystal microbalance setup for frequency and Q-factor measurements in gaseous and liquid environments. *Rev. Sci. Instrum.* **66**, 3924 (1995).
119. Rodahl, M. & Kasemo, B. A simple setup to simultaneously measure the resonant frequency and the absolute dissipation factor of a quartz crystal microbalance. *Rev. Sci. Instrum.* **67**, 3238 (1996).
120. Hansma, H. G., Laney, D. E., Bezanilla, M., Sinsheimer, R. L. & Hansma, P. K. Applications for atomic force microscopy of DNA. *Biophys. J.* **68**, 1672–1677 (1995).
121. Pyne, A., Thompson, R., Leung, C., Roy, D. & Hoogenboom, B. W. Single-Molecule Reconstruction of Oligonucleotide Secondary Structure by Atomic Force Microscopy. *Small* **10**, 3257–3261 (2014).
122. Kasas, S. & Thomson, N. Biological applications of the AFM: from single molecules to organs. *Int. J. Imaging Syst. Technol.* **8**, 151–161 (1997).
123. Binnig, G. & Quate, C. F. Atomic Force Microscope. *Phys. Rev. Lett.* **56**, 930–933 (1986).
124. Siperko, L. M. & Landis, W. J. Atomic Force Microscopic Imaging of Biologically Important Materials. *MRS Proc.* **295**, 243 (2011).
125. Drake, B. *et al.* Imaging crystals, polymers, and processes in water with the atomic force microscope. *Science* **243**, 1586–1589 (1989).
126. Y. Martin C. C. Williams & Wickramasinghe, H. K. Atomic force microscope-force mapping and profmng on a sub 100A scale. *J. Appl. Phys.* *61*, 4723 ; (7 pages) **61**, 4723 (1987).
127. Zhong, Q., Inniss, D., Kjoller, K. & Elings, V. B. Fractured polymer/silica fiber surface studied by tapping mode atomic force microscopy. *Surf. Sci. Lett.* **290**, L688–L692 (1993).
128. Egerton, R. F. *Physical Principles of Electron Microscopy*. (Springer US, 2005).
129. Watt, I. M. *The Principles and Practice of Electron Microscopy*. (Cambridge University Press, 1997).
130. Hild, F. & Roux, S. Digital image correlation: From displacement measurement to identification of elastic properties - A review. *Strain* **42**, 69–80 (2006).
131. Chu, T. C., Ranson, W. F. & Sutton, M. A. Applications of digital-image-correlation techniques to experimental mechanics. *Exp. Mech.* **25**, 232–244 (1985).
132. Schlenoff, J. B. & Dubas, S. T. Mechanism of Polyelectrolyte Multilayer Growth: Charge Overcompensation and Distribution. *Macromolecules* **34**, 592–598 (2001).
133. Farhat, T., Yassin, G., Dubas, S. T. & Schlenoff, J. B. Water and ion pairing in polyelectrolyte multilayers. *Langmuir* **15**, 6621–6623 (1999).
134. Ladam, G. *et al.* In Situ Determination of the Structural Properties of Initially Deposited Polyelectrolyte Multilayers. *Langmuir* **16**, 1249–1255 (2000).
135. Decher, G. & Schmitt, J. Fine-Tuning of the film thickness of ultrathin multilayer films composed of consecutively alternating layers of anionic and cationic polyelectrolytes. *Prog. Colloid Polym. Sci.* **89**, 160–164 (1992).
136. Caruso, F., Rodda, E., Furlong, D. N., Niikura, K. & Okahata, Y. Quartz Crystal

- Microbalance Study of DNA Immobilization and Hybridization for Nucleic Acid Sensor Development. *Anal. Chem.* **69**, 2043–2049 (1997).
137. Lvov, Y., Decher, G. & Moehwald, H. Assembly, structural characterization, and thermal behavior of layer-by-layer deposited ultrathin films of poly(vinyl sulfate) and poly(allylamine). *Langmuir* **9**, 481–486 (1993).
138. McAloney, R. a., Sinyor, M., Dudnik, V. & Cynthia Goh, M. Atomic force microscopy studies of salt effects on polyelectrolyte multilayer film morphology. *Langmuir* **17**, 6655–6663 (2001).
139. Mashl, R. J., Gronbeck-Jensen, N., Fitzsimmons, M. R. & Li, D. Q. Theoretical and experimental adsorption studies of polyelectrolytes on an oppositely charged surface. *J. Chem. Phys.* **110**, 2219–2225 (1999).
140. Gregory, J. Polymers at interfaces. *Polym. Int.* **36**, 102–102 (1995).
141. Raposo, M. & Oliveira Osvaldo N, J. Adsorption mechanisms in layer-by-layer films. *Brazilian J. Phys.* **28**, 0 (1998).
142. Schlenoff, J. B., Ly, H. & Li, M. Charge and Mass Balance in Polyelectrolyte Multilayers. *J. Am. Chem. Soc.* **120**, 7626–7634 (1998).
143. Raposo, M., Pontes, R. S., Mattoso, L. H. C. & Oliveira, O. N. Kinetics of Adsorption of Poly(o-methoxyaniline) Self-Assembled Films. *Macromolecules* **30**, 6095–6101 (1997).
144. Tsukruk, V. V. *et al.* Electrostatic Deposition of Polyionic Monolayers on Charged Surfaces †. *Macromolecules* **30**, 6615–6625 (1997).
145. Porcel, C. *et al.* From exponential to linear growth in polyelectrolyte multilayers. *Langmuir* **22**, 4376–83 (2006).
146. Lefaux, C. J., Zimmerlin, J. A., Dobrynin, A. V. & Mather, P. T. Polyelectrolyte spin assembly: Influence of ionic strength on the growth of multilayered thin films. *J. Polym. Sci. Part B Polym. Phys.* **42**, 3654–3666 (2004).
147. Nepal, D., Balasubramanian, S., Simonian, A. L. & Davis, V. A. Strong Antimicrobial Coatings: Single-Walled Carbon Nanotubes Armored with Biopolymers. *Nano Lett.* **8**, 1896–1901 (2008).
148. Cheung, J. H., Stockton, W. B. & Rubner, M. F. Molecular-Level Processing of Conjugated Polymers. 3. Layer-by-Layer Manipulation of Polyaniline via Electrostatic Interactions. *Macromolecules* **30**, 2712–2716 (1997).
149. Caruso, F., Niikura, K., Furlong, D. N. & Okahata, Y. 1. Ultrathin Multilayer Polyelectrolyte Films on Gold: Construction and Thickness Determination. *Langmuir* **13**, 3422–3426 (1997).
150. Zhang, M. *et al.* Electrostatic Layer-by-Layer Assembled Carbon Nanotube Multilayer Film and Its Electrocatalytic Activity for O₂ Reduction. *Langmuir* **20**, 8781–8785 (2004).
151. Olek, M. *et al.* Layer-by-Layer Assembled Composites from Multiwall Carbon Nanotubes with Different Morphologies. *Nano Lett.* **4**, 1889–1895 (2004).
152. Laschewsky, A. *et al.* A new route to thin polymeric, non-centrosymmetric coatings. *Thin Solid Films* **284-285**, 334–337 (1996).
153. Priolo, M. A., Gamboa, D., Holder, K. M. & Grunlan, J. C. Super Gas Barrier of Transparent Polymer–Clay Multilayer Ultrathin Films. *Nano Lett.* **10**, 4970–4974 (2010).
154. Stockton, W. B. & Rubner, M. F. Molecular-Level Processing of Conjugated Polymers. 4. Layer-by-Layer Manipulation of Polyaniline via Hydrogen-Bonding Interactions. *Macromolecules* **30**, 2717–2725 (1997).

155. Saarinen, T., Osterberg, M. & Laine, J. Adsorption of polyelectrolyte multilayers and complexes on silica and cellulose surfaces studied by QCM-D. *Colloids Surfaces a-Physicochemical Eng. Asp.* **330**, 134–142 (2008).
156. Gregurec, D. *et al.* Stability of polyelectrolyte multilayers in oxidizing media: a critical issue for the development of multilayer based membranes for nanofiltration. *Colloid Polym. Sci.* **293**, 381–388 (2014).
157. Serizawa, T. & Akashi, M. A novel approach for fabricating ultrathin polymer films by the repetition of the adsorption/drying processes. *J. Polym. Sci. Part A Polym. Chem.* **37**, 1903–1906 (1999).
158. Zhao, Q., Qian, J., An, Q. & Du, B. Speedy fabrication of free-standing layer-by-layer multilayer films by using polyelectrolyte complex particles as building blocks. *J. Mater. Chem.* **19**, 8448 (2009).
159. Wang, Y. *et al.* Dispersion of single-walled carbon nanotubes in poly(diallyldimethylammonium chloride) for preparation of a glucose biosensor. *Sensors Actuators B Chem.* **130**, 809–815 (2008).
160. Serizawa, T., Yamamoto, K. & Akashi, M. A novel fabrication of ultrathin poly(vinylamine) films with a molecularly smooth surface. *Langmuir* (1999).
161. Ke, B.-B., Wan, L.-S., Li, Y., Xu, M.-Y. & Xu, Z.-K. Selective layer-by-layer self-assembly on patterned porous films modulated by Cassie–Wenzel transition. *Phys. Chem. Chem. Phys.* **13**, 4881 (2011).
162. Serizawa, T., Kamimura, S., Kawanishi, N. & Akashi, M. Layer-by-Layer Assembly of Poly(vinyl alcohol) and Hydrophobic Polymers Based on Their Physical Adsorption on Surfaces. *Langmuir* **18**, 8381–8385 (2002).
163. Dodoo, S., Balzer, B. N., Hugel, T., Laschewsky, A. & Klitzing, R. von. Effect of Ionic Strength and Layer Number on Swelling of Polyelectrolyte Multilayers in Water Vapour. *Soft Mater.* **11**, 157–164 (2013).
164. Rooij, N. F. D. E., Corporation, M. D., Park, M., Chemistry, T. & Germany, W. Zeta Potential Measurements of Ta₂O₅ and SiO₂ Thin Films. *J. Colloid Interface Sci.* **147**, 22–32 (1991).
165. Zembala, M. & Déjardin, P. Streaming potential measurements related to fibrinogen adsorption onto silica capillaries. *Colloids Surfaces B Biointerfaces* **3**, 119–129 (1994).
166. Fuerstenau, D. W. Streaming Potential Studies on Quartz in Solutions of Amminium Acetates in Relation to the Formation of Hemimicelles at the Quartz- Solution Interface. *Jorunal Phys. Chem.* **60**, 981–985 (1956).
167. Skinner, B. & Appleman, D. Melanophlogite, a cubic polymorph of silica. *Am. Mineral.* **48**, 854–867 (1963).
168. Zhou, D. *et al.* Influence of the foundation layer on the layer-by-layer assembly of poly-L-lysine and poly(styrenesulfonate) and Its usage in the fabrication of 3D microscale features. *Langmuir* **20**, 9089–9094 (2004).
169. Tien, J., Terfort, A. & Whitesides, G. M. Microfabrication through Electrostatic Self-Assembly. *Langmuir* **13**, 5349–5355 (1997).
170. Jiang, X., Ortiz, C. & Hammond, P. T. Exploring the rules for selective deposition: Interactions of model polyamines on acid and oligoethylene oxide surfaces. *Langmuir* **18**, 1131–1143 (2002).
171. Clark, S. L. & Hammond, P. T. Role of secondary interactions in selective electrostatic multilayer deposition. *Langmuir* **16**, 10206–10214 (2000).
172. Schoeler, B., Sharpe, S., Hatton, T. A. & Caruso, F. Polyelectrolyte multilayer films of

- different charge density copolymers with synergistic nonelectrostatic interactions prepared by the layer-by-layer technique. *Langmuir* **20**, 2730–2738 (2004).
173. Schoeler, B., Poptoshev, E. & Caruso, F. Growth of Multilayer Films of Fixed and Variable Charge Density Polyelectrolytes: Effect of Mutual Charge and Secondary Interactions. *Macromolecules* **36**, 5258–5264 (2003).
174. Kotov, N. a. Layer-by-layer self-assembly: the contribution of hydrophobic interactions. *NanoStructured Mater.* **12**, 789–796 (1999).
175. de Groot, J. *et al.* Long term physical and chemical stability of polyelectrolyte multilayer membranes. *J. Memb. Sci.* **489**, 153–159 (2015).
176. Salomäki, M. & Kankare, J. Specific Anion Effect in Swelling of Polyelectrolyte Multilayers. *Macromolecules* **41**, 4423–4428 (2008).
177. Köhler, K., Shchukin, D. G., Möhwald, H. & Sukhorukov, G. B. Thermal behavior of polyelectrolyte multilayer microcapsules. 1. The effect of odd and even layer number. *J. Phys. Chem. B* **109**, 18250–9 (2005).
178. Adusumilli, M. & Bruening, M. L. Variation of ion-exchange capacity, zeta potential, and ion-transport selectivities with the number of layers in a multilayer polyelectrolyte film. *Langmuir* **25**, 7478–85 (2009).
179. Miller, M. D. & Bruening, M. L. Correlation of the Swelling and Permeability of Polyelectrolyte Multilayer Films. *Chem. Mater.* **17**, 5375–5381 (2005).
180. von Klitzing, R. & Tiede, B. Polyelectrolyte membranes. *Adv. Polym. Sci.* **165**, 177–210 (2004).
181. Harris, J. J. & Bruening, M. L. Electrochemical and in situ ellipsometric investigation of the permeability and stability of layered polyelectrolyte films. *Langmuir* **16**, 2006–2013 (2000).
182. Dai, J. H., Jensen, A. W., Mohanty, D. K., Erndt, J. & Bruening, M. L. Controlling the permeability of multilayered polyelectrolyte films through derivatization, cross-linking, and hydrolysis. *Langmuir* **17**, 931–937 (2013).
183. Fadhilah, F. *et al.* Development of multilayer polyelectrolyte thin-film membranes fabricated by spin assisted layer-by-layer assembly. *J. Appl. Polym. Sci.* **126**, 1468–1474 (2012).
184. Toutianoush, A. & Tiede, B. Pervaporation separation of alcohol/water mixtures using self-assembled polyelectrolyte multilayer membranes of high charge density. *Mater. Sci. Eng. C-Biomimetic Supramol. Syst.* **22**, 459–463 (2002).
185. Malaisamy, R., Talla-Nwafo, A. & Jones, K. L. Polyelectrolyte modification of nanofiltration membrane for selective removal of monovalent anions. *Sep. Purif. Technol.* **77**, 367–374 (2011).
186. SU, B., Wang, T., Wang, Z., Gao, X. & Gao, C. Preparation and performance of dynamic layer-by-layer PDADMAC/PSS nanofiltration membrane. *J. Memb. Sci.* **423-424**, 324–331 (2012).
187. Krasemann, L. & Tiede, B. Selective ion transport across self-assembled alternating multilayers of cationic and anionic polyelectrolytes. *Langmuir* **16**, 287–290 (2000).
188. Lowack, K. & Helm, C. A. Molecular Mechanisms Controlling the Self-Assembly Process of Polyelectrolyte Multilayers. *Macromolecules* **31**, 823–833 (1998).
189. Zhang, G., Song, X., Ji, S., Wang, N. & Liu, Z. Self-assembly of inner skin hollow fiber polyelectrolyte multilayer membranes by a dynamic negative pressure layer-by-layer technique. *J. Memb. Sci.* **325**, 109–116 (2008).
190. Mi, Y.-F., Zhao, Q., Ji, Y.-L., An, Q.-F. & Gao, C.-J. A novel route for surface zwitterionic functionalization of polyamide nanofiltration membranes with improved

- performance. *J. Memb. Sci.* **490**, 311–320 (2015).
191. Bruening, M. L., Dotzauer, D. M., Jain, P., Ouyang, L. & Baker, G. L. Creation of functional membranes using polyelectrolyte multilayers and polymer brushes. *Langmuir* **24**, 7663–7673 (2008).
 192. Bertrand, P., Jonas, a, Laschewsky, a & Legras, R. Ultrathin polymer coatings by complexation of polyelectrolytes at interfaces: suitable materials, structure and properties. *Macromol. Rapid Commun.* **21**, 319–348 (2000).
 193. Liu, Y. & Bruening, M. Multilayer Dendrimer–Polyanhydride Composite Films on Glass, Silicon, and Gold Wafers. *Angew. Chemie Int. Ed.* **36**, 2114–2116 (1997).
 194. Serizawa, T. *et al.* Stepwise preparation and characterization of ultrathin hydrogels composed of thermoresponsive polymers. *Macromolecules* **37**, 6531–6536 (2004).
 195. Tripathi, B. P., Dubey, N. C. & Stamm, M. Functional polyelectrolyte multilayer membranes for water purification applications. *J. Hazard. Mater.* (2013).
 196. Jin, W. Q., Toutianoush, A. & Tieke, B. Use of polyelectrolyte layer-by-layer assemblies as nanofiltration and reverse osmosis membranes. *Langmuir* **19**, 2550–2553 (2003).
 197. Stair, J. L., Harris, J. J. & Bruening, M. L. Enhancement of the ion-transport selectivity of layered polyelectrolyte membranes through cross-linking and hybridization. *Chem. Mater.* **13**, 2641–2648 (2001).
 198. Duong, P. H. H., Zuo, J. & Chung, T. S. Highly crosslinked layer-by-layer polyelectrolyte FO membranes: Understanding effects of salt concentration and deposition time on FO performance. *J. Memb. Sci.* **427**, 411–421 (2013).
 199. Sullivan, D. M. & Bruening, M. L. Ultrathin, ion-selective polyimide membranes prepared from layered polyelectrolytes. *J. Am. Chem. Soc.* **123**, 11805–11806 (2001).
 200. Lu, O. Y., Malaisamy, R. & Bruening, M. L. Multilayer polyelectrolyte films as nanofiltration membranes for separating monovalent and divalent cations. *J. Memb. Sci.* **310**, 76–84 (2008).
 201. Sullivan, D. M. & Bruening, M. L. Ultrathin, gas-selective polyimide membranes prepared from multilayer polyelectrolyte films. *Chem. Mater.* **15**, 281–287 (2003).
 202. Farhat, T. R. & Schlenoff, J. B. Doping-controlled ion diffusion in polyelectrolyte multilayers: mass transport in reluctant exchangers. *J. Am. Chem. Soc.* **125**, 4627–36 (2003).
 203. Lourenço, J. M. C. *et al.* Counterions in poly(allylamine hydrochloride) and poly(styrene sulfonate) layer-by-layer films. *Langmuir* **20**, 8103–9 (2004).
 204. Dubas, S. T. & Schlenoff, J. B. Polyelectrolyte Multilayers Containing a Weak Polyacid: Construction and Deconstruction. *Macromolecules* **34**, 3736–3740 (2001).
 205. Laurent, D. & Schlenoff, J. B. Multilayer Assemblies of Redox Polyelectrolytes. *Langmuir* **13**, 1552–1557 (1997).
 206. Hoogeveen, N. G., Cohen Stuart, M. A., Fleer, G. J. & Böhmer, M. R. Formation and Stability of Multilayers of Polyelectrolytes. *Langmuir* **12**, 3675–3681 (1996).
 207. Riegler, H. & Essler, F. Polyelectrolytes. 2. Intrinsic or Extrinsic Charge Compensation? Quantitative Charge Analysis of PAH/PSS Multilayers. *Langmuir* **18**, 6694–6698 (2002).
 208. Ladam, G. *et al.* In Situ Determination of the Structural Properties of Initially Deposited Polyelectrolyte Multilayers. *Langmuir* **16**, 1249–1255 (2000).
 209. Guzmán, E., Ritacco, H., Rubio, J. E. F., Rubio, R. G. & Ortega, F. Salt-induced changes in the growth of polyelectrolyte layers of poly(diallyl-dimethylammonium

- chloride) and poly(4-styrene sulfonate of sodium). *Soft Matter* **5**, 2130 (2009).
210. Jaber, J. A. & Schlenoff, J. B. Counterions and water in polyelectrolyte multilayers: a tale of two polycations. *Langmuir* **23**, 896–901 (2007).
211. Zan, X., Hoagland, D. A., Wang, T. & Su, Z. Ion Dispositions in Polyelectrolyte Multilayer Films. *Macromolecules* **45**, 8805–8812 (2012).
212. Tanchak, O. M. *et al.* Ion distribution in multilayers of weak polyelectrolytes: A neutron reflectometry study. *J. Chem. Phys.* **129**, 084901 (2008).
213. Lösche, M., Schmitt, J., Decher, G., Bouwman, W. G. & Kjaer, K. Detailed Structure of Molecularly Thin Polyelectrolyte Multilayer Films on Solid Substrates as Revealed by Neutron Reflectometry. *Macromolecules* **31**, 8893–8906 (1998).
214. Kellogg, G. J. *et al.* Neutron Reflectivity Investigations of Self-Assembled Conjugated Polyion Multilayers. *Langmuir* **12**, 5109–5113 (1996).
215. Schmitt, J. *et al.* Internal structure of layer-by-layer adsorbed polyelectrolyte films: a neutron and x-ray reflectivity study. *Macromolecules* **26**, 7058–7063 (1993).
216. BARHATE, R. & RAMAKRISHNA, S. Nanofibrous filtering media: Filtration problems and solutions from tiny materials. *J. Memb. Sci.* **296**, 1–8 (2007).
217. Faccini, M. *et al.* Electrospun Carbon Nanofiber Membranes for Filtration of Nanoparticles from Water. **2015**, (2014).
218. Baughman, R. H., Zakhidov, A. A. & de Heer, W. A. Carbon nanotubes--the route toward applications. *Science* **297**, 787–92 (2002).
219. Park, J. *et al.* Carbon nanotube-based nanocomposite desalination membranes from layer-by-layer assembly. *Desalin. Water Treat.* **15**, 76–83 (2013).
220. Dumée, L. *et al.* Fabrication of thin film composite poly(amide)-carbon-nanotube supported membranes for enhanced performance in osmotically driven desalination systems. *J. Memb. Sci.* **427**, 422–430 (2013).
221. Ahn, C. H. *et al.* Carbon nanotube-based membranes: Fabrication and application to desalination. *J. Ind. Eng. Chem.* **18**, 1551–1559 (2012).
222. Sears, K. *et al.* Recent Developments in Carbon Nanotube Membranes for Water Purification and Gas Separation. *Materials* **3**, 127–149 (2010).
223. Park, J. *et al.* Carbon nanotube-based nanocomposite desalination membranes from layer-by-layer assembly. *Desalin. Water Treat.* **15**, 76–83 (2013).
224. Tang, H., Zhang, G. & Ji, S. Rapid assembly of polyelectrolyte multilayer membranes using an automatic spray system. *AIChE J.* **59**, 250–257 (2013).
225. Thess, A. *et al.* Crystalline Ropes of Metallic Carbon Nanotubes. *Science* **273**, 483–487 (1996).
226. Grossiord, N., Regev, O., Loos, J., Meuldijk, J. & Koning, C. E. Time-dependent study of the exfoliation process of carbon nanotubes in aqueous dispersions by using UV-visible spectroscopy. *Anal. Chem.* **77**, 5135–5139 (2005).
227. Ausman, K. D., Piner, R., Lourie, O., Ruoff, R. S. & Korobov, M. Organic solvent dispersions of single-walled carbon nanotubes: Toward solutions of pristine nanotubes. *J. Phys. Chem. B* **104**, 8911–8915 (2000).
228. Kim, S. W. *et al.* Surface modifications for the effective dispersion of carbon nanotubes in solvents and polymers. *Carbon N. Y.* **50**, 3–33 (2012).
229. Vigolo, B. *et al.* Macroscopic Fibers and Ribbons of Oriented Carbon Nanotubes. *Science* **290**, 1331–1334 (2000).
230. O’Connell, M. J. *et al.* Reversible water-solubilization of single-walled carbon

- nanotubes by polymer wrapping. *Chem. Phys. Lett.* **342**, 265–271 (2001).
231. Islam, M. F., Rojas, E., Bergey, D. M., Johnson, A. T. & Yodh, A. G. High Weight Fraction Surfactant Solubilization of Single-Wall Carbon Nanotubes in Water. *Nano Lett.* **3**, 269–273 (2003).
232. Zhu, J. *et al.* Improving the Dispersion and Integration of Single-Walled Carbon Nanotubes in Epoxy Composites through Functionalization. *Nano Lett.* **3**, 1107–1113 (2003).
233. Hammel, E. *et al.* Carbon nanofibers for composite applications. *Carbon N. Y.* **42**, 1153–1158 (2004).
234. Song, Y. S. & Youn, J. R. Influence of dispersion states of carbon nanotubes on physical properties of epoxy nanocomposites. *Carbon N. Y.* **43**, 1378–1385 (2005).
235. Liu, T., Phang, I. Y., Shen, L., Chow, S. Y. & Zhang, W. De. Morphology and mechanical properties of multiwalled carbon nanotubes reinforced nylon-6 composites. *Macromolecules* **37**, 7214–7222 (2004).
236. Wang, Z., Shirley, M. D., Meikle, S. T., Whitby, R. L. D. & Mikhalovsky, S. V. The surface acidity of acid oxidised multi-walled carbon nanotubes and the influence of in-situ generated fulvic acids on their stability in aqueous dispersions. *Carbon N. Y.* **47**, 73–79 (2009).
237. Green, M. J. Analysis and measurement of carbon nanotube dispersions: Nanodispersion versus macrodispersion. *Polym. Int.* **59**, 1319–1322 (2010).
238. Jiang, L., Gao, L. & Sun, J. Production of aqueous colloidal dispersions of carbon nanotubes. *J. Colloid Interface Sci.* **260**, 89–94 (2003).
239. Shim, B. S. *et al.* Nanostructured thin films made by dewetting method of layer-by-layer assembly. *Nano Lett.* **7**, 3266–3273 (2007).
240. Shim, B. S. *et al.* Integration of Conductivity, Transparency, and Mechanical Strength into Highly Homogeneous Layer-by-Layer Composites of Single-Walled Carbon Nanotubes for Optoelectronics. *Chem. Mater.* **19**, 5467–5474 (2007).
241. O’Connell, M. J. Band Gap Fluorescence from Individual Single-Walled Carbon Nanotubes. *Science* **297**, 593–596 (2002).
242. Hou, P.-X., Liu, C. & Cheng, H.-M. Purification of carbon nanotubes. *Carbon N. Y.* **46**, 2003–2025 (2008).
243. Van de Steeg, H. G. M., Cohen Stuart, M. a., De Keizer, A. & Bijsterbosch, B. H. Polyelectrolyte adsorption: a subtle balance of forces. *Langmuir* **8**, 2538–2546 (1992).
244. Shubin, V. & Linse, P. Effect of Electrolytes on Adsorption of Cationic Polyacrylamide on Silica: Ellipsometric Study and Theoretical Modeling. *J. Phys. Chem.* **99**, 1285–1291 (1995).
245. Kataura, H. *et al.* Optical properties of single-wall carbon nanotubes. *Synth. Met.* **103**, 2555–2558 (1999).
246. Vieira, R. S. & Beppu, M. M. Interaction of natural and crosslinked chitosan membranes with Hg(II) ions. *Colloids Surfaces A Physicochem. Eng. Asp.* **279**, 196–207 (2006).
247. Jean, B., Heux, L., Dubreuil, F., Chambat, G. & Cousin, F. Non-electrostatic building of biomimetic cellulose-xyloglucan multilayers. *Langmuir* **25**, 3920–3923 (2009).
248. Juang, R.-S. & Ju, C.-Y. Equilibrium Sorption of Copper(II)–Ethylenediaminetetraacetic Acid Chelates onto Cross-Linked, Polyaminated Chitosan Beads. *Ind. Eng. Chem. Res.* **36**, 5403–5409 (1997).
249. Crini, G. Non-conventional low-cost adsorbents for dye removal: a review. *Bioresour.*

- Technol.* **97**, 1061–85 (2006).
250. De Mesquita, J. P., Donnici, C. L. & Pereira, F. V. Biobased nanocomposites from layer-by-layer assembly of cellulose nanowhiskers with chitosan. *Biomacromolecules* **11**, 473–480 (2010).
251. De Mesquita, J. P., Donnici, C. L., Teixeira, I. F. & Pereira, F. V. Bio-based nanocomposites obtained through covalent linkage between chitosan and cellulose nanocrystals. *Carbohydr. Polym.* **90**, 210–217 (2012).
252. Rodenhause, K. B. *et al.* Combined optical and acoustical method for determination of thickness and porosity of transparent organic layers below the ultra-thin film limit. *Rev. Sci. Instrum.* **82**, 103111 (2011).
253. Caruso, F., Furlong, D. N. & Kingshott, P. Characterization of Ferritin Adsorption onto Gold. *J. Colloid Interface Sci.* **186**, 129–140 (1997).
254. Hook, F., Rodahl, M., Brzezinski, P. & Kasemo, B. Energy dissipation kinetics for protein and antibody-antigen adsorption under shear oscillation on a quartz crystal microbalance. *Doktorsavhandlingar vid Chalmers Tek. Hogsk.* **7463**, 729–734 (1997).
255. Muratsugu, M. *et al.* Quartz crystal microbalance for the detection of microgram quantities of human serum albumin: relationship between the frequency change and the mass of protein adsorbed. *Anal. Chem.* **65**, 2933–7 (1993).
256. Moya, S. *et al.* Polyelectrolyte multilayer capsules templated on biological cells: core oxidation influences layer chemistry. *Colloids Surfaces A Physicochem. Eng. Asp.* **183-185**, 27–40 (2001).
257. Choi, J. & Rubner, M. F. Influence of the degree of ionization on weak polyelectrolyte multilayer assembly. *Macromolecules* **38**, 116–124 (2005).
258. Feng, X., Pelton, R., Leduc, M. & Champ, S. Colloidal complexes from poly(vinyl amine) and carboxymethyl cellulose mixtures. *Langmuir* **23**, 2970–2976 (2007).
259. Saito, T., Nishiyama, Y., Putaux, J. L., Vignon, M. & Isogai, A. Homogeneous suspensions of individualized microfibrils from TEMPO-catalyzed oxidation of native cellulose. *Biomacromolecules* **7**, 1687–1691 (2006).
260. Pääkko, M. *et al.* Enzymatic hydrolysis combined with mechanical shearing and high-pressure homogenization for nanoscale cellulose fibrils and strong gels. *Biomacromolecules* **8**, 1934–1941 (2007).
261. J.A.Walecka. An Investigation of Low Degree of Substitution Carboxymethylcelluloses. *TAPPI* 458 (1956).
262. Syverud, K. & Stenius, P. Strength and barrier properties of MFC films. *Cellulose* **16**, 75–85 (2009).
263. Holt, J. K. *et al.* Fast mass transport through sub-2-nanometer carbon nanotubes. *Science* **312**, 1034–1037 (2006).
264. Ma, H., Burger, C., Hsiao, B. S. & Chu, B. Highly Permeable Polymer Membranes Containing Directed Channels for Water Purification. *ACS Macro Lett.* **1**, 723–726 (2012).
265. Volesky, B. Biosorption and me. *Water Res.* **41**, 4017–29 (2007).
266. Carpenter, A. W., de Lannoy, C.-F. & Wiesner, M. R. Cellulose Nanomaterials in Water Treatment Technologies. *Environ. Sci. Technol.* **49**, 5277–5287 (2015).
267. Podsiadlo, P. Layer-By-Layer Assembly of Nanostructured Composites: Mechanics and Applications. (2008).
268. Shim, B. S. *et al.* Multiparameter structural optimization of single-walled carbon nanotube composites: toward record strength, stiffness, and toughness. *ACS Nano* **3**,

- 1711–1722 (2009).
269. Podsiadlo, P., Shim, B. S. & Kotov, N. A. Polymer/clay and polymer/carbon nanotube hybrid organic–inorganic multilayered composites made by sequential layering of nanometer scale films. *Coord. Chem. Rev.* **253**, 2835–2851 (2009).
270. Moniruzzaman, M. & Winey, K. I. Polymer Nanocomposites Containing Carbon Nanotubes. *Macromolecules* **39**, 5194–5205 (2006).
271. Yu, M., Files, B., Arepalli, S. & Ruoff, R. Tensile loading of ropes of single wall carbon nanotubes and their mechanical properties. *Phys. Rev. Lett.* **84**, 5552–5 (2000).
272. Li, F., Cheng, H. M., Bai, S., Su, G. & Dresselhaus, M. S. Tensile strength of single-walled carbon nanotubes directly measured from their macroscopic ropes. *Appl. Phys. Lett.* **77**, 3161 (2000).
273. Hinds, B. J. *et al.* Aligned multiwalled carbon nanotube membranes. *Science* **303**, 62–65 (2013).
274. Guo, W., Liu, C., Sun, X., Yang, Z. & Kia, H. G. Aligned carbon nanotube/polymer composite fibers with improved mechanical strength and electrical conductivity. *J. Mater. Chem.* **22**, 903–908 (2012).
275. Yu, G., Cao, A. & Lieber, C. M. Large-area blown bubble films of aligned nanowires and carbon nanotubes. *Nat. Nanotechnol.* **2**, 372–7 (2007).
276. Akima, N. *et al.* Strong Anisotropy in the Far-Infrared Absorption Spectra of Stretch-Aligned Single-Walled Carbon Nanotubes. *Adv. Mater.* **18**, 1166–1169 (2006).
277. Shoji, S., Suzuki, H., Zaccaria, R. P., Sekkat, Z. & Kawata, S. Optical polarizer made of uniaxially aligned short single-wall carbon nanotubes embedded in a polymer film. *Phys. Rev. B* **77**, 153407 (2008).
278. Park, C. *et al.* Aligned single-wall carbon nanotube polymer composites using an electric field. *J. Polym. Sci. Part B Polym. Phys.* **44**, 1751–1762 (2006).
279. Kimura, T. *et al.* Polymer Composites of Carbon Nanotubes Aligned by a Magnetic Field. *Adv. Mater.* **14**, 1380–1383 (2002).
280. Shim, B. S. B. S. & Kotov, N. A. N. A. Single-walled carbon nanotube combing during layer-by-layer assembly: from random adsorption to aligned composites. *Langmuir* **21**, 9381–9385 (2005).
281. jonas, B. *Nanoscale Polyelectrolyte Multilayer Films Containing Carbon Nanotubes, Alignment and Material Properties.* (2014).
282. P.H.WALKER & J.G.THOMPSON. Proceedings - American Society for Testing Materials. *Nabu Press* 464 (2010).
283. LeMieux, M. C. *et al.* Self-Sorted, Aligned Nanotube Networks for Thin-Film Transistors. *Science* **321**, 101–104 (2008).
284. P.K.Mallick. *Fiber-reinforced composites.* (CRC Press, 2009).
285. Lavoine, N., Desloges, I., Dufresne, A. & Bras, J. Microfibrillated cellulose – Its barrier properties and applications in cellulosic materials: A review. *Carbohydr. Polym.* **90**, 735–764 (2012).
286. Siró, I. & Plackett, D. Microfibrillated cellulose and new nanocomposite materials: A review. *Cellulose* **17**, 459–494 (2010).
287. Klemm, D. *et al.* Nanocelluloses: A new family of nature-based materials. *Angewandte Chemie - International Edition* **50**, 5438–5466 (2011).
288. Guan, Y. *et al.* Fabry-Perot fringes and their application to study the film growth, chain rearrangement, and erosion of hydrogen-bonded PVPON/PAA films. *J. Phys. Chem. B* **110**, 13484–90 (2006).

289. Cool, T., Bhadeshia, H. K. D. H. & MacKay, D. J. C. The yield and ultimate tensile strength of steel welds. *Mater. Sci. Eng. A* **223**, 186–200 (1997).
290. Bonderer, L. J., Studart, A. R. & Gauckler, L. J. Bioinspired Design and Assembly of Platelet Reinforced Polymer Films. *Science* **319**, 1069–1073 (2008).
291. Siró, I. & Plackett, D. Microfibrillated cellulose and new nanocomposite materials: A review. *Cellulose* **17**, 459–494 (2010).
292. Page, D. H. & El-Hosseiny, F. Mechanical properties of single wood pulp fibres. Part VI. Fibril angle and the shape of the stress-strain curve. *J. Pulp Pap. Sci.* **9**, 99–100 (1983).
293. Eder, M., Arnould, O., Dunlop, J. W. C., Hornatowska, J. & Salmén, L. Experimental micromechanical characterisation of wood cell walls. *Wood Sci. Technol.* **47**, 163–182 (2012).
294. Håkansson, K. M. O. *et al.* Hydrodynamic alignment and assembly of nanofibrils resulting in strong cellulose filaments. *Nat. Commun.* **5**, 4018 (2014).
295. Aulin, C. *et al.* Nanoscale cellulose films with different crystallinities and mesostructures--their surface properties and interaction with water. *Langmuir* **25**, 7675–85 (2009).
296. O'Connor, R. T., DuPre, E. F. & Mitcham, D. Applications of Infrared Absorption Spectroscopy to Investigations of Cotton and Modified Cottons: Part I: Physical and Crystalline Modifications and Oxidation. *Text. Res. J.* **28**, 382–392 (1958).
297. Coleman, J. N., Khan, U., Blau, W. J. & Gun'ko, Y. K. Small but strong: A review of the mechanical properties of carbon nanotube–polymer composites. *Carbon N. Y.* **44**, 1624–1652 (2006).
298. Briscoe, B. J., Fiori, L. & Pelillo, E. Nano-indentation of polymeric surfaces. *J. Phys. D. Appl. Phys.* **31**, 2395–2405 (1998).
299. Pradhan, B., Kohlmeyer, R. R. & Chen, J. Fabrication of in-plane aligned carbon nanotube–polymer composite thin films. *Carbon N. Y.* **48**, 217–222 (2010).
300. Rezakhaniha, R. *et al.* Experimental investigation of collagen waviness and orientation in the arterial adventitia using confocal laser scanning microscopy. *Biomech. Model. Mechanobiol.* **11**, 461–73 (2012).

Appendix 1

Simple Shear lag model

In order to explain the fracture mechanics of nanocomposite materials, several models are in common use, ranging from fairly simple analytical methods to complex numerical packages. The simplest is the so-called "shear lag" mode, which is based on the assumption that all of the load transfer from matrix to fibers occurs via shear stresses acting on the cylindrical interface between the two constituents. The build-up of tensile stress in the fiber is related to these shear stresses by applying a force balance to an incremental section of the fiber (Figure 0-1).²⁸⁴

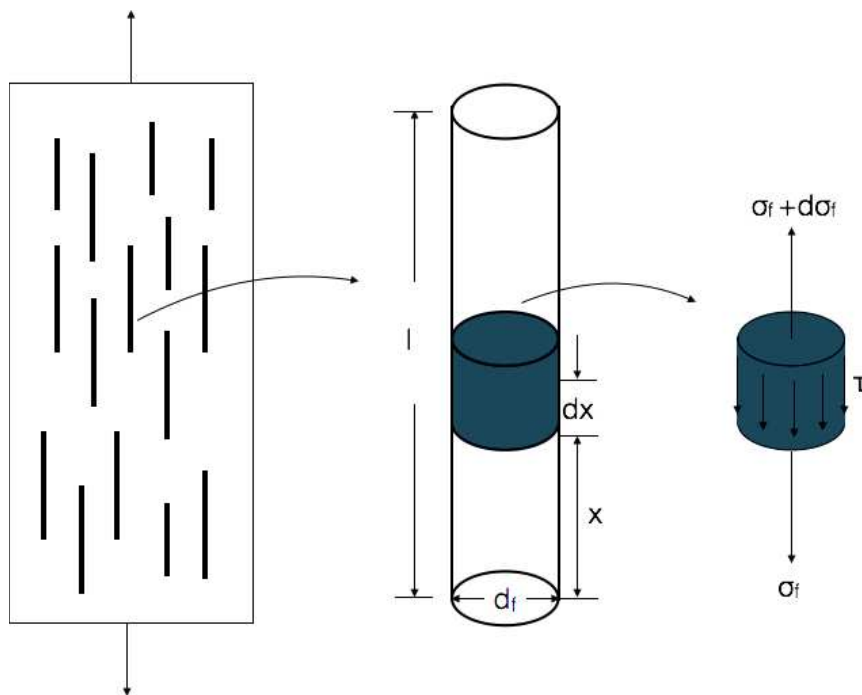


Figure 0-1. Longitudinal tensile loading of a unidirectional discontinuous fiber lamina

As shown in Figure 0-1, considering an infinitesimal length dx at a distance x from one of the fiber ends, the force equilibrium equation for this length is

$$\left(\frac{\pi}{4}d_f^2\right)(\sigma_f + d\sigma_f) - \left(\frac{\pi}{4}d_f^2\right)\sigma_f - (\pi d_f d_x)\tau = 0 \quad \text{Equation 0-1}$$

which on simplification gives

$$\frac{d\sigma_f}{dx} = \frac{4\tau}{d_f} \quad \text{Equation 0-2}$$

where

σ_f = longitudinal stress in the fiber at a distance x from one of its ends

τ = shear stress at the fiber-matrix interface

d_f = fiber diameter

Assuming no stress transfer at the fiber ends, that is, $\sigma_f=0$ at $x=0$, and integrating Equation 0-2, we can determine the longitudinal stress distribution in the fiber as

$$\sigma_f = \frac{4}{d_f} \int_0^x \tau d_x \quad \text{Equation 0-3}$$

For simple analysis, we assume that the interfacial shear stress is constant and is equal to τ_i . Thus, integration of Equation 0-3 gives –

$$\sigma_f = \frac{4\tau_i}{d_f} x \quad \text{Equation 0-4}$$

From Equation 0-4, it can be observed that for a nanocomposite lamina containing discontinuous nanofibers, the fiber stress is not uniform, instead it is zero at each end of the fiber and it increases linearly with x . The maximum fiber stress occurs at the central portion of the fiber, which can be achieved at a given load being

$$\sigma_{f_m} = 2\tau_i \frac{l_t}{d_f} \quad \text{Equation 0-5}$$

where $x=l_t/2$ =load transfer length from each fiber end and σ_{f_m} = maximum fiber stress obtained. Therefore the load transfer length, l_t , is the minimum fiber length in which the maximum fiber stress is achieved. Hereby, for a given fiber diameter and fiber-matrix interfacial condition, we get the critical aspect of ratio s_c and the critical fiber length l_c which have the following relationship

$$S_c = \frac{l_c}{d_f} = \frac{\sigma_{fu}}{2\tau_i} \quad \text{Equation 0-6}$$

where

σ_{fu} = ultimate tensile strength of the fiber

l_c = minimum fiber length required for the maximum fiber stress to be equal to the ultimate tensile strength of the fiber at its midlength

τ_i = shear strength of the fiber-matrix interface or the shear strength of the matrix adjacent to the interface, whichever is less

The average fiber stress is

$$\bar{\sigma}_f = \frac{1}{l_f} \int_0^{l_f} \sigma_f dx \quad \text{Equation 0-7}$$

which leads to two main different situations of fracture. The first one is when the fiber aspect ratio S is larger than the critical aspect ratio S_c , thus $l_c < l_f$, which means a loading of ultimate tensile strength σ_{fu} on the fiber at its midlength where $x > l_c/2$. In other words, the fibers will be fractured which results in a brittle catastrophic rupture of the material (Figure VI-17A). This gives the following equation after the integration of Equation 0-7

$$\bar{\sigma}_f = \frac{2}{l_f} \left(\int_0^{\frac{l_c}{2}} \frac{4\tau_i}{d_f} x dx + \int_{\frac{l_c}{2}}^{\frac{l_f}{2}} \sigma_{fu} dx \right) = \sigma_{fu} \left(1 - \frac{l_c}{2l_f} \right) = \sigma_{fu} \left(1 - \frac{S_c}{2S} \right) \quad \text{Equation 0-8}$$

which can lead to the equation for calculating the composite's tensile strength

$$\sigma_c = \bar{\sigma}_{fu} v_f + \sigma'_m (1 - v_f) = \sigma_{fu} \left(1 - \frac{S_c}{2S} \right) v_f + \sigma'_m (1 - v_f) \quad \text{Equation 0-9}$$

where $\bar{\sigma}_{fu}$ and σ'_m are stress of fiber and matrix respectively when the composite material breaks. In this case, $\bar{\sigma}_{fu}$ equals to ultimate tensile strength of the fiber σ_{fu} since $l_c < l_f$ and fibers fractured before matrix.

On the other hand, for $S < S_c$, thus $l_c > l_f$, the average fiber stress becomes

$$\bar{\sigma}_f = \frac{2}{l_f} \left(\int_0^{\frac{l_f}{2}} \frac{4\tau_i}{d_f} x dx \right) = \tau_i \frac{l_f}{d_f} \quad \text{Equation 0-10}$$

which indicates that continuous matrix yields before the fibers break, thus leading to toughening mechanisms such as fibers pull-out and matrix plastic flow before the complete rupture of the composite (Figure VI-17B). Therefore the tensile strength of the composite material is

$$\sigma_c = \bar{\sigma}_{fu} v_f + \sigma'_m (1 - v_f) = \tau_i \frac{l_f}{d_f} v_f + \sigma_{mu} (1 - v_f) \quad \text{Equation 0-11}$$

where, in this case, σ'_m equals to the ultimate tensile strength of the matrix σ_{mu} as the matrix breaks in prior to the fibers (assuming strong interfacial interactions).

Appendix 2

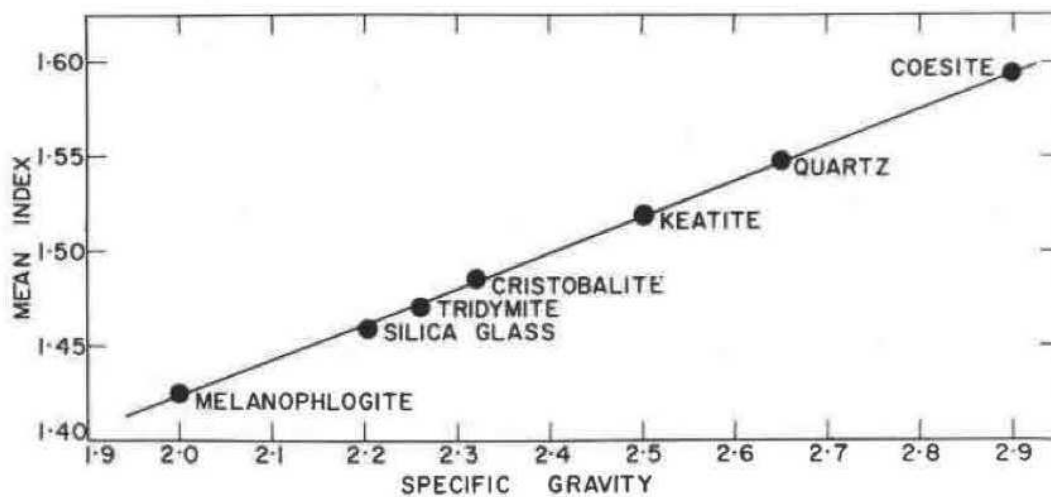


Figure 0-1. A plot of mean index of refraction versus specific gravity, showing that mean index of refraction and specific gravity for the quartz are higher than silica.¹⁶⁷